https://ntrs.nasa.gov/search.jsp?R=19910007997 2020-03-19T19:53:22+00:00Z

NASA-TP-3061 19910007997

NASA Technical Paper 3061

February 1991

Relative Efficiency and Accuracy of Two Navier-Stokes Codes for Simulating Attached Transonic Flow Over Wings

Daryl L. Bonhaus and Stephen F. Wornom

LIBRARY COPY

FEB 2 1 1991

LANGLEY RESEARCH CENTER
LIBRARY NASA
HAMPTON, VIRGINIA

NASA

NASA Technical Paper 3061

1991

Relative Efficiency and Accuracy of Two Navier-Stokes Codes for Simulating Attached Transonic Flow Over Wings

Daryl L. Bonhaus and Stephen F. Wornom
Langley Research Center
Hampton, Virginia

NASA
National Aeronautics and Space Administration
Office of Management
Scientific and Technical Information Division

Summary

In the present study, two codes that solve the three-dimensional thin-layer Navier-Stokes equations are used to compute the steady-state flow for two test cases representing typical finite wings at transonic conditions. Several grids of *C-O* topology and varying point densities are used to determine the effects of grid refinement. After a description of each code and test case, standards for determining code efficiency and accuracy are defined and applied to determine the relative performance of the two codes in predicting turbulent transonic wing flows. Computed surface pressure distributions are compared with experimental data.

Symbols

C_D	total drag coefficient
C_{D_p}	pressure drag coefficient
C_{D_v}	viscous drag coefficient
C_L	lift coefficient
C_f	skin friction coefficient
C_m	pitching-moment coefficient
C_p	pressure coefficient
b	wingspan
c	local chord length
q	dynamic pressure
x	chordwise coordinate
y	spanwise coordinate
z	vertical coordinate
η	nondimensional spanwise coordinate
ξ	nondimensional chordwise coordinate

Subscripts:

∞	free-stream conditions

Introduction

This paper is intended to serve three purposes. First, with the increase in available codes for solving the Reynolds-averaged Navier-Stokes (RANS) equations, and given the high cost of the computer resources required to run these codes routinely, it becomes necessary to evaluate their relative ability to achieve a given accuracy with the least cost in terms of computer resources. Second, the study serves as a code-on-code validation and has considerably increased our confidence in both codes. Third, the results obtained during the course of this study point to several areas of research that should be considered in the future so that better tools can be developed. As computational fluid dynamics (CFD) moves closer to being used in the aircraft design process, these determinations will become increasingly important.

The authors would like to acknowledge the contributions of James Thomas and Veer Vatsa of Langley Research Center for guidance in using CFL3D and TLNS3D. The authors would also like to thank Manuel Salas, also of Langley Research Center, for suggesting the idea of comparing the two codes and for fruitful discussion of the results.

Code Descriptions

There are many codes available at different research facilities to compute viscous transonic flow over wings. These codes are based on two classes of numerical methods. The first class uses central differencing for the flux differences, with explicitly added artificial dissipation to eliminate the odd/even decoupling associated with the central-difference method. The second class are methods that introduce dissipation naturally and are referred to as upwind methods. In order to compare the various codes, it would be necessary to have these codes executing on the same computer and to have the code developers present to provide guidance and make code modifications where required. Since this was not possible for all available codes, the study here was limited to two codes developed at NASA Langley where the code developers were present to monitor the results.

The codes analyzed in the present study are referred to as CFL3D and TLNS3D, and both codes are state of the art for the upwind and central-difference methods, respectively. Both use a finite volume formulation, with flow quantities stored at cell centers, to integrate the three-dimensional time-dependent thin-layer Navier-Stokes equations (TLNS) in time until a steady-state solution is reached. To accelerate convergence, both codes can make use of grid sequencing, multigrid, and local time-stepping techniques.

CFL3D uses the Pulliam-Chaussee diagonal ADI (alternating direction implicit) time-marching algorithm (ref. 1) with third-order upwind-biased differences for the spatial derivatives of the inviscid terms. The upwind method used is the Roe flux-difference-splitting scheme (ref. 2). A min-mod flux limiting scheme is employed to obtain smooth solutions in the vicinity of discontinuities. During the investigations conducted here, it was determined that the multigrid feature did not improve convergence for the

Navier-Stokes equations and it was not used. Details on the formulation of this code can be found in references 3–7.

TLNS3D uses an explicit five-stage Runge-Kutta time-marching algorithm, with second-order central differences for the spatial derivatives. A blend of second- and fourth-order artificial dissipation terms are added to maintain numerical stability. The artificial dissipation terms are scalar. In addition to the previously mentioned convergence acceleration techniques, TLNS3D utilizes a multigrid technique and implicit residual smoothing to improve convergence to steady state. Details on the formulation of this code can be found in references 7–16.

For turbulent attached flows, both codes use the Baldwin-Lomax algebraic turbulence model (ref. 17). TLNS3D also has the option to use the Johnson-King nonequilibrium turbulence model, which has been shown to be more accurate for separated flows than the Baldwin-Lomax model is (ref. 18).

With the exception of the downstream boundary, the boundary conditions in both codes are mathematically the same. The wing surface is modeled as a viscous surface with a no-slip condition on velocity and a zero normal pressure gradient. The treatment of the far-field boundaries are based on Riemann invariants for one-dimensional flow normal to the boundaries, as described in reference 19. These conditions are also used for the downstream boundary in CFL3D. In TLNS3D, the flow quantities at the downstream boundary are determined by extrapolation. Symmetry conditions are imposed on the grid plane at the wing root plane. The only other difference between the codes was the location of the transition point. For CFL3D, the turbulence model was used everywhere. For TLNS3D, the transition point was set at 2 percent chord on both the upper surface and the lower surface.

The values of the input parameters for both codes can be found in the appendix. The inputs were adjusted for the best performance on the finest grid for each wing and held fixed on all other grids.

Test Case Descriptions

The test cases used for analysis are the ONERA M6 wing (ref. 20) and the Lockheed Wing B (ref. 21) configuration. The experimental data for the ONERA M6 have very small wind-tunnel wall effects in contrast to the data for the Lockheed Wing B, which contain significant wind-tunnel wall effects. The geometric characteristics of the ONERA M6 wing are given in table 1(a). The M6 wing was developed specifically for experimental support of three-dimensional transonic and subsonic flow-field studies, and an extensive data base of surface pressure distributions is available over a range of transonic Mach numbers at angles of attack up to 6°. The particular case analyzed in this study is for a Mach number of 0.84 and an angle of attack of 3.06°.

The geometric characteristics of the Lockheed Wing B configuration are given in table 1(b). This wing was also tested for the purpose of CFD code evaluation. In addition to a data base of surface pressure distributions similar to that available for the ONERA M6, experimental force and moment coefficients and spanwise lift distributions are also available for Wing B. The case examined in this study is for a Mach number of 0.851 and an angle of attack of 2.95°.

Because CFL3D does not have the option of using the Johnson-King turbulence model, which has been shown to be more accurate for separated flows, only attached flow cases were selected, and both codes used the Baldwin-Lomax turbulence model.

Four computational grids were generated for each wing by using a two-boundary transfinite interpolation technique (ref. 22). These grids are of C-O topology (C in the streamwise direction and O in the spanwise direction). The finest grid contains 289 points in the streamwise direction, 65 points in the direction normal to the wing surface, and 49 points in the cross-flow direction (i.e., $289 \times 65 \times 49$). The other grids are (in decreasing order by size) $193 \times 49 \times 33$, $145 \times 33 \times 25$, and $97 \times 25 \times 17$. On the surface of the wing, the trailing edge was located at $i = 33$, 25, 17, and 13, respectively. On the upper surface, the trailing edge was located at 257, 169, 129, and 85, respectively. This translates into the following number of cells on each surface: 21 728, 9216, 5376, and 2304.

The physical geometric coordinates are scaled so that the semispan of the wing in the computational domain is of unit length. Sample plots showing the symmetry plane and far-field boundary of the computational domain and the wing surface mesh for each wing are given in figures 1 and 2. The surface grid for the ONERA M6 wing shows better definition of the wingtip. The calculations for the Lockheed Wing B are reported here for the first time, and the wingtip region will need to be better defined in future calculations.

The outer boundary of the computational domain extends approximately 6.25 semispans vertically (above and below the wing), 6.5 semispans upstream, 7.5 semispans downstream, and 6.5 semispans horizontally outward from the wingtip.

The primary computer used was the Cray-2 S supercomputer at the NASA Langley Research Center. Because of core memory limitations, the finer

grids were run on the Cray-2 supercomputer at the National Aerodynamic Simulator (NAS). The Langley Cray-2 S is approximately 28 percent faster than the NAS Cray-2. All cpu times given in this paper are relative to the Langley Cray-2 S. Both codes were compiled under FORTRAN 77 using the same options.

During final editing of this report, it was discovered that an error was made in generating the grids for the Lockheed Wing B. The quarter-chord sweep angle of the computational geometry exceeds that of the wind-tunnel model by approximately 6°. This does not change any of the conclusions drawn from this study, since the same grids were used to run both codes. TLNS3D calculations have recently been made on the actual wind-tunnel geometry.[1]

Results

We begin by examining the effect of grid refinement on the wing section pressure coefficients. Next we examine the iteration history and the accuracy for a given grid. After examining the boundary-layer profiles, skin friction, spanwise lift distributions, and surface pressure contours, we close with a discussion and evaluation of relative efficiency to achieve a given accuracy for the test cases considered herein.

Surface Pressure

Figure 3 shows the effect of grid refinement on the pressure distributions for CFL3D and TLNS3D for the ONERA M6 wing. The spanwise distance Y is normalized with respect to the semispan length $B/2$. Figure 4 shows the corresponding results for the Lockheed Wing B. Figures 3 and 4 show distinctively different solution convergence patterns between TLNS3D and CFL3D due to grid refinement. For the ONERA M6 wing, CFL3D predicts approximately the same shock location on each grid. The changes that do occur with grid refinement are to sharpen the shock. For TLNS3D, the effect of grid refinement is to move the the center of the shock downstream and to sharpen the shock as well as to resolve the region of accelerated flow at the leading edge.

For the Lockheed Wing B, both CFL3D and TLNS3D predict shock midpoint locations that move downstream and sharpen as the grid is refined.

Figures 5–8 show comparisons of the computed pressure distributions on each individual wing. There is excellent agreement for the ONERA M6 wing on the finest mesh. For the Lockheed Wing B, there are noticeable differences on the finest grid. It is also noted in the latter that there is not the agreement with experimental data seen for the ONERA M6 wing. Reference 21 gives estimated Mach number and angle-of-attack corrections required for this case, but they have not been used here.

Iteration History

In order to examine the relative efficiency and accuracy of the codes, the values of the force coefficients are stored at each iteration. To understand the convergence process better, the drag is further broken into components due to pressure and viscosity, and these components are analyzed separately. Using these data, the percent change in the force coefficients at each iteration is calculated using their final converged values as reference. The cpu time is stored at the end of each grid sequence. This time includes the time required to read and write data files and the time required to perform the calculations. It does not include code compilation time or postprocessing time. Since both codes read and write in binary format, the time spent on file input and output is small relative to the total run time. In this manner, the amount of cpu time required for the force coefficients to converge to a given percentage of their final values is determined. The cpu times are relative to the Langley Cray-2 S.

The convergence histories for the continuity equation residual, lift coefficient, and pressure and viscous drag coefficients, as the grid is refined, are presented in figures 9–12 for both wings. In each case, the residual for CFL3D drops approximately three orders of magnitude before leveling off and exhibiting high frequency oscillations, which are attributed to the use of the flux limiter. For TLNS3D, the residual continues to decrease to the end of the run.

Figures 9–12 clearly illustrate the strong point of TLNS3D, that is, fast convergence of the residual and the integrated force coefficients (lift, viscous drag, and pressure drag) as the grid is refined. As can be seen in figures 9 and 10, which show the convergence histories for the $97 \times 25 \times 17$ and the $145 \times 33 \times 25$ grids, the rate of convergence for both codes is about the same. As the number of grid points becomes large, the $193 \times 49 \times 33$ and $289 \times 65 \times 49$ grids, TLNS3D is more efficient than CFL3D. This is an important advantage for TLNS3D since run times for fine grids are measured in hours as opposed to minutes for the coarser meshes.

To quantify the relative efficiency for a given grid, let us assume convergence to be acceptable when the percent change in the lift, viscous drag, and

[1] These calculations were made as part of a joint NASA-CAE study on wall interference assessment and correction for three-dimensional semispan wings. Participants included J. A. Garriz, Q. Zhang, P. A. Newman, S. Wang, V. N. Vatsa, and K. J. Haigler.

pressure drag convergence histories remains less than approximately 0.5 percent. To reach this criteria, CFL3D requires on the order of two to three times the cpu time of TLNS3D for the two finest grids. For the 193 × 49 × 33 grid, this translates into approximately 40–50 minutes additional cpu time. For the 289 × 65 × 49 grid, this translates into 2–3 hours additional cpu time.

Accuracy

The values of the coefficients of lift, pitching moment, total drag, viscous drag, pressure drag, and their errors are given in tables 2 and 3. To estimate errors, reference values for the force coefficients must be known. These can be the experimental values or the values from a numerical solution using a very fine grid. For these test cases, the experimental values are not known. Limits on computer resources did not permit solutions on more refined meshes. The errors shown in tables 2 and 3 are based on the infinite grid prediction for each code obtained from a second-order Richardson extrapolation (extrapolating the values from the finest two grids). The percent difference in the predicted infinite grid values for the lift, pitching moment, total drag, viscous drag, and pressure drag, are shown in table 4. These errors are referenced with respect to the values of CFL3D.

In tables 2 and 3, the force coefficients using TLNS3D are converged to five significant figures. The values of the force coefficients using CFL3D are only valid to four significant figures for drag and three significant figures for lift on the 193 × 49 × 33 and 289 × 65 × 49 grids.

Figure 13 shows the force coefficients, and figure 14 shows the percentage error in the lift, pitching moment, and total drag. For a given grid, figure 14 shows CFL3D to be the more accurate scheme for predicting the lift, pitching moment, and total drag.

For the ONERA M6 wing, figure 14 shows CFL3D to be significantly more accurate than TLNS3D for the total drag, and relatively insensitive to grid refinement. Since this same behavior is not observed for the Lockheed Wing B test case where the total drag error predictions for the two codes are virtually identical, we believe that it is related to the accurately predicted shock location on each grid obtained with CFL3D for the ONERA M6 wing. For the Lockheed Wing B, both codes predict shock midpoint locations that move downstream as the mesh is refined leading to total drag error predictions of the same order.

Figure 15 shows the lift-to-drag ratios and their errors with grid refinement. This is an important quantity for the wing designer. As can be seen from these figures, TLNS3D is significantly more accurate than CFL3D in predicting the lift-to-drag ratio for the ONERA M6 wing. That is, although CFL3D predicts more accurate individual values of the lift, pitching moment, and total drag on a given grid, TLNS3D predicts the more accurate value of the lift-to-drag ratio!

A similar anomaly can be seen if one examines figure 16 and tables 2(d) and (e) and tables 3(d) and (e), which show the errors in the total drag components—viscous drag and pressure drag. One observes that, in general, the error in the total drag is smaller than the error in each of the individual components that are added to determine the total drag.

Boundary-Layer Profiles—ONERA M6 Wing

The effect of grid refinement on the boundary-layer total velocity profiles (q/q_∞) is examined in this section. Velocity profiles were plotted at 0, 50, and 80 percent span and at 25 and 75 percent chord for the upper and lower surfaces. Figures 17–22 show the influence of grid refinement on the upper-surface velocity profiles for each code. The boundary-layer profiles are plotted in two forms: the first being a linear scale that accentuates differences away from the boundary, and the second being a semilog scale that accentuates differences near the wing surface. In most cases, the near-wall profiles computed by CFL3D converge from the left as the plot is viewed, while the profiles computed by TLNS3D converge from the right. At 80 percent span and 25 percent chord on the upper surface, both sets of velocity profiles lack grid convergence. The reason is that this location is in the region of the upper surface where two shocks are coalescing to form a lambda shock. Since the pressure distribution is much more sensitive to grid resolution in this region, the edge velocities are still changing on even the finest grids. The same location on the lower surface does not experience this problem.

Figures 23–26 show comparisons of velocity profiles on the same grid. The differences between codes are much larger on the coarser grids because they approach the grid-independent profile from opposite directions. The codes are also in much better agreement at the 25-percent-chord points than at the 75-percent-chord points, again with the exception of the lambda shock region.

Shown in figures 27–32 are the boundary-layer profiles with grid refinement for the lower surface. These are followed in figures 33–36 with comparisons on the same grid.

We summarize this section by saying that there are numerical differences between the two codes, but

the profile distributions on each grid are qualitatively the same.

Boundary-Layer Profiles—Lockheed Wing B

Figures 37–42 show the influence of grid refinement on the upper-surface velocity profiles for each code. For this case, the near-wall profiles computed by both codes converge from the right as the plot is viewed. Figures 43–46 show comparisons of velocity profiles on the same grid.

Shown in figures 47–52 are the boundary-layer profiles for the lower surface as the grid is refined. These are followed with figures 53–56, which show comparisons of the codes using the same grid.

For the ONERA M6 wing, the predicted trends on each grid were the same; we note that this is not true for the Lockheed Wing B. On the $289 \times 65 \times 49$ grid, both codes predict the same trend. However, TLNS3D does not predict this trend on any other grid, whereas CFL3D predicts the trend on the $193 \times 49 \times 33$ and $145 \times 25 \times 17$ grids.

Skin Friction

ONERA M6 wing. The effect of grid refinement on the symmetry plane skin friction distributions is shown in figure 57. The skin friction is not grid converged. The improvement of shock resolution is noted; however, CFL3D seems to smear the shock more than TLNS3D. The different behavior at the leading edge is due to the different treatment there. TLNS3D computes a laminar flow solution over a small region with transition specified near the leading edge, while CFL3D is fully turbulent. Code comparisons for the same grid are presented in figure 58.

These plots show that as the grid is refined, skin friction levels achieve better agreement. The $193 \times 49 \times 33$ grid for CFL3D exhibits oscillations just upstream of the shock. These do not seem to be caused by a lack of convergence, as running the code further does not change the shape of the curve. No reason has been found for this behavior which also occurs for the Lockheed Wing B.

Lockheed Wing B. Grid convergence of skin friction distribution is shown in figure 59. Code comparisons for the same grid are presented in figure 60. We note significant differences between the two codes.

Postprocessing of the numerical data indicates that the value of Y^+ at the first node point off the surface is approximately 5.

Spanwise Lift Distributions

Figures 61 and 62 show the convergence of the lift distributions with grid refinement. CFL3D shows less variation than TLNS3D with grid refinement. In figures 63 and 64, distributions for each code on the same grid are plotted.

One noticeable difference between the two codes is the symmetry plane values of the lift coefficient. CFL3D shows very little variation at the symmetry plane in comparison with TLNS3D. Also, CFL3D shows a change in the slope of the lift distribution curve as the symmetry plane is approached.

Surface Pressure Contours

A comparison of the upper-surface pressure contours is shown in figures 65 and 66. No significant differences are observed.

Relative Efficiency for a Given Accuracy

One of the goals of this work was to examine the relative efficiency of TLNS3D and CFL3D to achieve a given accuracy. This task became difficult because of the distinctly different trends observed for the two test cases and the lack of exact values of the force coefficients on which to base the error estimates.

In order to determine the relative efficiency for a given accuracy, we examine relative accuracy in terms of the L_2 norm computed using the percent errors in lift, pitching moment, total drag, and lift-to-drag ratio based on the infinite grid extrapolated values. These are shown in figure 67.

Using this norm, CFL3D is the more accurate code for a given grid. To quantify this for the ONERA M6 wing, the accuracy achieved with TLNS3D using the $289 \times 65 \times 49$ grid (884 736 cells) for the ONERA M6 could have been obtained with CFL3D with 511 113 cells or 42 percent fewer cells. We do not have a calculation for this grid. However, we do have a calculation on a grid with 67 percent fewer cells ($193 \times 49 \times 33$ grid), and we can use that solution to estimate the relative efficiency on a grid with 42 percent fewer cells.

Shown in figure 68 are the convergence histories for CFL3D using the $193 \times 49 \times 33$ grid (67 percent fewer cells) and TLNS3D using the $289 \times 65 \times 49$ grid. Comparing the convergence history for the continuity equation residual would lead to the conclusion that CFL3D is the more efficient code. We conclude that TLNS3D is as efficient as CFL3D even though the CFL3D calculation was made on a grid that contained 67 percent fewer cells. For equivalent accuracy, we estimate that CFL3D requires 1.73 more cpu time than TLNS3D. For the Lockheed Wing B, the ratio is on the order of 2.

Conclusions

Based on the numerical results for the ONERA M6 wing and the Lockheed Wing B for attached transonic flow, the following conclusions are made:

1. In general, CFL3D is the more accurate code for a given grid.

2. For a given grid, TLNS3D is the more efficient code, especially as the number of grid points becomes large, where it is two to three times as efficient.

3. For equivalent accuracy, TLNS3D is the more efficient code. The ratio of cpu time of CFL3D to TLNS3D is on the order of 1.73–2.

All error estimates were based on the infinite grid values obtained using a Richardson extrapolation. For the ONERA M6 wing, the pressure coefficients showed excellent agreement on the finest grid, and the differences between the infinite grid values were small. For the Lockheed Wing B, there were significant differences in the pressure coefficients, which in turn are reflected in significant differences in the infinite grid values. For these reasons, further comparisons with other codes and experimental data are suggested.

NASA Langley Research Center
Hampton, VA 23665-5225
December 14, 1990

Appendix

Input Parameters

The input parameters for both test cases are given here; they were chosen to give the best performance on the finest grid. Both codes required many runs in order to select the best parameters for the finest grid. Since both codes are sensitive to the input parameters, it is conceivable that if not carefully done, different relative values could be obtained. The authors benefited greatly from the code developers' suggestions and experience.

```
TLNS3D: inputs for ONERA M6 test case
fmesh     fstrt     fsave     fplot     cpplot    fseq
1.        2.        1.        0.        0.        3.
ncyc      pltout    convout   step      iprnt     lprnt     grids     iter
150.      1.        1.        1.        0.        0.        3.        2.
cflf      bc        hmf       vis2      vis4      mscale
-6.5       0.       .0        0.25      1.0       0.
c(1)      c(2)      c(3)      c(4)      c(5)      c(6)
.25       .16667    .375      .5        1.0       0.
qfil(1)   qfil(2)   qfil(3)   qfil(4)   qfil(5)   qfil(6)
-1.       0.        -1.       0.        -1.       0.
beta(1)   beta(2)   beta(3)   beta(4)   beta(5)   beta(6)
 1.       0.          .56     0.        .44       0.
iter(1)   iter(2)   iter(3)   iter(4)
1.        2.        2.        2.
smoopi    smoopj    smoopk    zeta
0.01      2.50      3.5       .50
cflc      fbc       hmc       vis0      fcoll     fadd
0.         0.       0.        12.        1.        1.
rm        al        cd0       xref      yref      sref
.84       3.06      0.        0.        0.        0.
ivis      yvis      nturb     jstart    ystop
2.        .7500     1.        .12       .7500
rey/l     pr        prt       iwtran    iftran
21.66     1.0       1.        .100      0.
'/scr4/bonhaus/Tab1/m6a3.g289'    *** input co grid
'/scr4/bonhaus/Tab1/m6a3.s289.2' *** restart file
```

```
TLNS3D: inputs for Lockheed Wing B  test case
fmesh     fstrt     fsave     fplot     cpplot    fseq
1.        2.        1.        0.        0.        3.
ncyc      pltout    convout   step      iprnt     lprnt     grids     iter
150.      1.        1.        1.        0.        0.        3.        2.
cflf      bc        hmf       vis2      vis4      mscale
-6.5       0.       .0        1.0       2.0       0.
c(1)      c(2)      c(3)      c(4)      c(5)      c(6)
.25       .16667    .375      .5        1.0       0.
qfil(1)   qfil(2)   qfil(3)   qfil(4)   qfil(5)   qfil(6)
-1.       0.        -1.       0.        -1.       0.
beta(1)   beta(2)   beta(3)   beta(4)   beta(5)   beta(6)
 1.       0.          .56     0.        .44       0.
iter(1)   iter(2)   iter(3)   iter(4)
1.        2.        2.        2.
smoopi    smoopj    smoopk    zeta
0.01      2.50      3.5       .50
cflc      fbc       hmc       vis0      fcoll     fadd
0.         0.       0.        12.        1.        1.
rm        al        cd0       xref      yref      sref
.84       3.06      0.        0.        0.        0.
ivis      yvis      nturb     jstart    ystop
2.        .7500     1.        .12       .7500
rey/l     pr        prt       iwtran    iftran
21.66     1.0       1.        .100      0.
'/scr4/bonhaus/Tab1/m6a3.g289'   *** input co grid
'/scr4/bonhaus/Tab1/m6a3.s289.2' *** restart file
```

```
CFL3D: inputs for ONERA M6 test case
     XMACH      ALPHA       BETA  REUE,MIL    TINF,DR       ISND      C2SPE
    0.8400     03.060        0.0    21.660      540.0          0        0.0
      SREF       CREF       BREF       XMC        YMC        ZMC
   0.53080    1.00000     3.9249   0.00000       0.00       0.00
        DT      IREST    IFLAGTS       FMAX      IUNST      RFREQ     ALPHAU       CLOC
   -08.000          0        000     1.0000          0    0.39600    0.02200    0.50000
     NGRID    NPLOT3D     NPRINT     NWREST
         1          0          0        100
       NCG        IEM  IADVANCE     IFORCE      IMESH  IVISC(I)  IVISC(J)  IVISC(K)
         1          0          0          0         12         0         0         2
      IDIM       JDIM       KDIM       ITE1       ITE2       JTE1       JTE2
        49        289         65          1         49         33        257
     INEWG     IGRIDC         IS         JS         KS         IE         JE        KE
         1          0          0          0          0          0          0         0
  IDIAG(I)   IDIAG(J)   IDIAG(K)   IFLIM(I)   IFLIM(J)   IFLIM(K)       IAFA
         1          1          1          2          2          2          1
   IFDS(I)    IFDS(J)    IFDS(K)  RKAP0(I)   RKAP0(J)   RKAP0(K)
         1          1          1      .3333      .3333      .3333
 MTYPEI(1)  MTYPEI(2)  MTYPEJ(1)  MTYPEJ(2)  MTYPEK(1)  MTYPEK(2)
        12         12         12         12         12         12
      MSEQ     MGFLAG     ICONSF        MTT       NGAM
         2          1          0          0         02
      NCYC     MGLEVG      NEMGL      NITFO
      0050         01         00        000
      0200         02         00        000
      MIT1       MIT2       MIT3       MIT4       MIT5
        01         01         01         01         01
        02         01         01         01         01
  PLOT3D OUTPUT:
  BLOCK ISTART   IEND   IINC JSTART   JEND   JINC KSTART   KEND   KINC
  PRINT OUT:
  BLOCK ISTART   IEND   IINC JSTART   JEND   JINC KSTART   KEND   KINC
```

```
CFL3D: inputs for Lockheed Wing B  test case
     XMACH      ALPHA       BETA   REUE,MIL    TINF,DR       ISND      C2SPE
    0.8510      2.950        0.0     17.960      540.0          0        0.0
      SREF       CREF       BREF        XMC        YMC        ZMC
   0.52711    1.00000     3.9249    0.00000       0.00       0.00
        DT      IREST    IFLAGTS       FMAX      IUNST      RFREQ     ALPHAU       CLOC
   -08.000          0        000     1.0000          0    0.39600    0.02200    0.50000
     NGRID    NPLOT3D     NPRINT     NWREST
         1          0          0        100
       NCG        IEM   IADVANCE     IFORCE      IMESH   IVISC(I)   IVISC(J)   IVISC(K)
         2          0          0          0         12          0          0          2
      IDIM       JDIM       KDIM       ITE1       ITE2       JTE1       JTE2
        49        289         65          1         49         33        257
     INEWG     IGRIDC         IS         JS         KS         IE         JE         KE
         1          0          0          0          0          0          0          0
   IDIAG(I)   IDIAG(J)   IDIAG(K)   IFLIM(I)   IFLIM(J)   IFLIM(K)       IAFA
         1          1          1          2          2          2          1
    IFDS(I)    IFDS(J)    IFDS(K)   RKAP0(I)   RKAP0(J)   RKAP0(K)
         1          1          1      .3333      .3333      .3333
 MTYPEI(1)  MTYPEI(2)  MTYPEJ(1)  MTYPEJ(2)  MTYPEK(1)  MTYPEK(2)
        12         12         12         12         12         12
      MSEQ     MGFLAG     ICONSF        MTT       NGAM
         3          0          0          0         02
      NCYC     MGLEVG      NEMGL     NITFO
      0500         01         00       000
      0500         01         00       000
      0300         01         00       000
      MIT1       MIT2       MIT3       MIT4       MIT5
        01         01         01         01         01
        01         01         01         01         01
        01         01         01         01         01
  PLOT3D OUTPUT:
  BLOCK ISTART   IEND   IINC JSTART   JEND   JINC KSTART   KEND   KINC
  PRINT OUT:
  BLOCK ISTART   IEND   IINC JSTART   JEND   JINC KSTART   KEND   KINC
```

References

1. Pulliam, T. H.; and Chaussee, D. S.: A Diagonal Form of an Implicit Approximation-Factorization Algorithm. *J. Comp. Phys.*, vol. 39, no. 2, 1981, pp. 347–363.
2. Roe, P. L.: Characteristic-Based Schemes for the Euler Equations. *Annual Review of Fluid Mechanics,* Volume 18, Milton van Dyke, J. V. Wehausen, and John L. Lumley, eds., Annual Reviews Inc., 1986, pp. 337–365.
3. Thomas, James L.; Van Leer, Bram; and Walters, Robert W.: Implicit Flux-Split Schemes for the Euler Equations. AIAA-85-1680, July 1985.
4. Thomas, J. L.; Taylor, S. L.; and Anderson, W. K.: Navier-Stokes Computations of Vortical Flows Over Low Aspect Ratio Wings. AIAA-87-0207, Jan. 1987.
5. Van Leer, Bram; Thomas, James L.; Roe, Philip L.; and Newsome, Richard W.: A Comparison of Numerical Flux Formulas for the Euler and Navier-Stokes Equations. *A Collection of Technical Papers—AIAA 8th Computational Fluid Dynamics Conference,* 1987, pp. 36–41. (Available as AIAA-87-1104.)
6. van Leer, Bram: Upwind-Difference Methods for Aerodynamic Problems Governed by the Euler Equations. *Large-Scale Computations in Fluid Mechanics, Volume 22-Part 2 of Lectures in Applied Mathematics,* Bjorn E. Engquist, Stanly Osher, and Richard C. J. Sommerville, eds., American Mathematical Soc., 1985, pp. 327–336.
7. Vatsa, V. N.; Thomas, J. L.; and Wedan, B. W.: Navier-Stokes Computations of Prolate Spheroids at Angle of Attack. *Technical Papers—AIAA Atmospheric Flight Mechanics Conference,* Aug. 1987, pp. 488–506. (Available as AIAA-87-2627.)
8. Jameson, A.; Schmidt, Wolfgang; and Turkel, Eli: Numerical Solution of the Euler Equations by Finite Volume Methods Using Runge Kutta Time Stepping Schemes. AIAA-81-1259, June 1981.
9. Jameson, A.; and Baker, T. J.: Improvements to the Aircraft Euler Method. AIAA-87-0452, Jan. 1987.
10. Swanson, R. C.; and Turkel, Eli: A Multistage Time-Stepping Scheme for the Navier-Stokes Equations. AIAA-85-0035, Jan. 1985.
11. Vatsa, V. N.: Accurate Numerical Solutions for Transonic Viscous Flow Over Finite Wings. *J. Aircr.,* vol. 24, no. 6, June 1987, pp. 377–385.
12. Vatsa, V. N.; and Wedan, B. W.: Navier-Stokes Solutions for Transonic Flow Over a Wing Mounted in a Tunnel. AIAA-88-0102, Jan. 1988.
13. Martinelli, Luigi: *Calculations of Viscous Flows With a Multigrid Method.* Ph.D. Diss., Princeton Univ., Oct. 1987.
14. Abid, Ridha; Vatsa, Veer N.; Johnson, Dennis A.; and Wedan, Bruce W.: Prediction of Separated Transonic Wing Flows With a Non-Equilibrium Algebraic Model. AIAA-89-0558, Jan. 1989.
15. Vatsa, Veer N.; and Wedan, Bruce W.: Development of an Efficient Multigrid Code for 3-D Navier-Stokes Equations. AIAA-89-1791, June 1989.
16. Turkel, Eli; and Vatsa, Veer N.: Effect of Artificial Viscosity on Three-Dimensional Flow Solutions. AIAA-90-1444, June 1990.
17. Baldwin, Barrett; and Lomax, Harvard: Thin-Layer Approximation and Algebraic Model for Separated Turbulent Flows. AIAA Paper 78-257, Jan. 1978.
18. Johnson, D. A.; and King, L. S.: A Mathematically Simple Turbulence Closure Model for Attached and Separated Turbulent Boundary Layers. *AIAA J.,* vol. 23, no. 11, Nov. 1985, pp. 1684–1692.
19. Thomas, James L.; and Salas, M. D.: Far-Field Boundary Conditions for Transonic Lifting Solutions to the Euler Equations. *AIAA J.,* vol. 24, no. 7, July 1986, pp. 1074–1080.
20. Schmitt, V.; and Charpin, F.: Pressure Distributions on the ONERA-M6-Wing at Transonic Mach Numbers. *Experimental Data Base for Computer Program Assessment,* AGARD-AR-138, May 1979, pp. B1-1–B1-44.
21. Hinson, B. L.; and Burdges, K. P.: *Acquisition and Application of Transonic Wing and Far-Field Test Data for Three-Dimensional Computational Method Evaluation.* AFOSR-TR-80-0421, U.S. Air Force, Mar. 1980. (Available from DTIC as AD A085 258.)
22. Eriksson, Lars-Erik: *Transfinite Mesh Generation and Computer-Aided Analysis of Mesh Effects.* Ph.D. Diss., Uppsala Univ., 1984.

Table 1. Geometric Characteristics

(a) ONERA M6 wing

Mean aerodynamic chord, m	0.64607
Semispan, m	1.1963
Reference area, m^2	0.7532
Leading edge sweep angle, deg	30.0
Trailing edge sweep angle, deg	15.8
Aspect ratio	3.8
Taper ratio	0.562

(b) Lockheed Wing B

Mean aerodynamic chord, m	0.1771
Semispan, m	0.318
Reference area, m^2	0.053
Quarter-chord sweep angle, deg	30.0
Aspect ratio	3.8
Taper ratio	0.4

Table 2. Effect of Grid Convergence on Force and Moment Coefficients for ONERA M6 Wing

(a) Lift coefficient C_L

Grid	C_L		Percentage error* in C_L	
	TLNS3D	CFL3D	TLNS3D	CFL3D
$97 \times 25 \times 17$	0.25385	0.26550	6.63	2.76
$145 \times 33 \times 25$	.26041	.26794	4.22	1.86
$193 \times 49 \times 33$	.26517	.26952	2.47	1.28
$289 \times 65 \times 49$	.26865	.27134	1.19	.62
Infinite grid	.27187	.27303	0	0

*Errors based on infinite-grid value for each particular code.

(b) Pitching-moment coefficient C_m

Grid	C_m		Percentage error* in C_m	
	TLNS3D	CFL3D	TLNS3D	CFL3D
$97 \times 25 \times 17$	−0.09701	−0.10212	7.08	2.78
$145 \times 33 \times 25$	−.09938	−.10275	4.81	2.18
$193 \times 49 \times 33$	−.10128	−.10343	2.99	1.54
$289 \times 65 \times 49$	−.10290	−.10426	1.44	.74
Infinite grid	−.10440	−.10504	0	0

*Errors based on infinite-grid value for each particular code.

(c) Total drag coefficient C_D

Grid	C_D		Percentage error* in C_D	
	TLNS3D	CFL3D	TLNS3D	CFL3D
$97 \times 25 \times 17$	0.01658	0.01744	5.38	0.44
$145 \times 33 \times 25$	.01658	.01744	5.38	.45
$193 \times 49 \times 33$	.01706	.01762	2.64	.61
$289 \times 65 \times 49$	.01730	.1756	1.27	.30
Infinite grid	.01752	.01751	0	0

*Errors based on infinite-grid value for each particular code. The infinite grid value of the total drag was obtained by extrapolating the total drag values as opposed to extrapolating its components and then adding them to get the total drag.

Table 2. Concluded

(d) Viscous drag coefficient C_{D_v}

Grid	C_{D_v}		Percentage error* in C_{D_v}	
	TLNS3D	CFL3D	TLNS3D	CFL3D
$97 \times 25 \times 17$	0.00322	0.00426	43.46	24.92
$145 \times 33 \times 25$	.00420	.00511	26.25	9.88
$193 \times 49 \times 33$	.00504	.00557	11.50	1.77
$289 \times 65 \times 49$	.00538	.00563	5.53	.85
Infinite grid	.00570	.00567	0	0

*Errors based on infinite-grid value for each particular code.

(e) Pressure drag coefficient C_{D_p}

Grid	C_{D_p}		Percentage error* in C_{D_p}	
	TLNS3D	CFL3D	TLNS3D	CFL3D
$97 \times 25 \times 17$	0.01336	0.01318	−12.96	−11.18
$145 \times 33 \times 25$	.01238	.01232	−4.67	−4.07
$193 \times 49 \times 33$	.01202	.01205	−1.63	−1.76
$289 \times 65 \times 49$	.01192	.01194	−.78	−.84
Infinite grid	.01183	.01184	0	0

*Errors based on infinite-grid value for each particular code.

Table 3. Effect of Grid Convergence on Force and Moment Coefficients for Lockheed Wing B

(a) Lift coefficient C_L

Grid	C_L		Percentage error* in C_L	
	TLNS3D	CFL3D	TLNS3D	CFL3D
$97 \times 25 \times 17$	0.42087	0.44483	7.71	2.94
$145 \times 33 \times 25$	.43602	.45207	4.39	1.36
$193 \times 49 \times 33$	.44856	.45470	1.64	0.78
$289 \times 65 \times 49$	.45245	.45656	.79	.38
Infinite grid	.45605	.45828	0	0

*Errors based on infinite-grid value for each particular code.

(b) Pitching-moment coefficient C_m

Grid	C_m		Percentage error* in C_m	
	TLNS3D	CFL3D	TLNS3D	CFL3D
$97 \times 25 \times 17$	−0.24980	−0.26213	6.35	1.77
$145 \times 33 \times 25$	−.25741	−.26588	3.50	.36
$193 \times 49 \times 33$	−.26366	−.26737	1.16	.19
$289 \times 65 \times 49$	−.26526	−.26710	.56	.09
Infinite grid	−.26674	−.26685	0	0

*Errors based on infinite-grid value for each particular code.

(c) Total drag coefficient C_D

Grid	C_D		Percentage error* in C_D	
	TLNS3D	CFL3D	TLNS3D	CFL3D
$97 \times 25 \times 17$	0.02937	0.02770	14.30	9.58
$145 \times 33 \times 25$	.02784	.02689	8.35	6.39
$193 \times 49 \times 33$	.02685	.02631	4.50	4.09
$289 \times 65 \times 49$	.02625	.02578	2.16	1.97
Infinite grid	.02570	.02528	0	0

*Errors based on infinite-grid value for each particular code. The infinite grid value of the total drag was obtained by extrapolating the total drag values as opposed to extrapolating its components and then adding them to get the total drag.

Table 3. Concluded

(d) Viscous drag coefficient C_{D_v}

Grid	C_{D_v}		Percentage error* in C_{D_v}	
	TLNS3D	CFL3D	TLNS3D	CFL3D
$97 \times 25 \times 17$	0.00373	0.00507	33.69	3.55
$145 \times 33 \times 25$	.00466	.00547	17.16	−4.01
$193 \times 49 \times 33$	.00524	.00543	6.85	−3.35
$289 \times 65 \times 49$	.00544	.00534	3.29	−1.61
Infinite grid	.00563	.00526	0	0

*Errors based on infinite-grid value for each particular code.

(e) Pressure drag coefficient C_{D_p}

Grid	C_{D_p}		Percentage error* in C_{D_p}	
	TLNS3D	CFL3D	TLNS3D	CFL3D
$97 \times 25 \times 17$	0.02564	0.02263	−27.76	−13.02
$145 \times 33 \times 25$	.02318	.02143	−15.50	−7.01
$193 \times 49 \times 33$	.02161	.02088	−7.68	−4.29
$289 \times 65 \times 49$	.02081	.02044	−3.69	−2.06
Infinite grid	.02007	.02002	0	0

*Errors based on infinite-grid value for each particular code.

Table 4. Percent Difference in Infinite Grid Solutions

[Percent based on infinite-grid value for CFL3D]

	ONERA M6 wing	Lockheed Wing B
C_L	−0.4	−0.5
C_M	−.6	0
C_D	.1	1.6
C_{D_v}	.3	7.1
C_{D_p}	−.1	.2

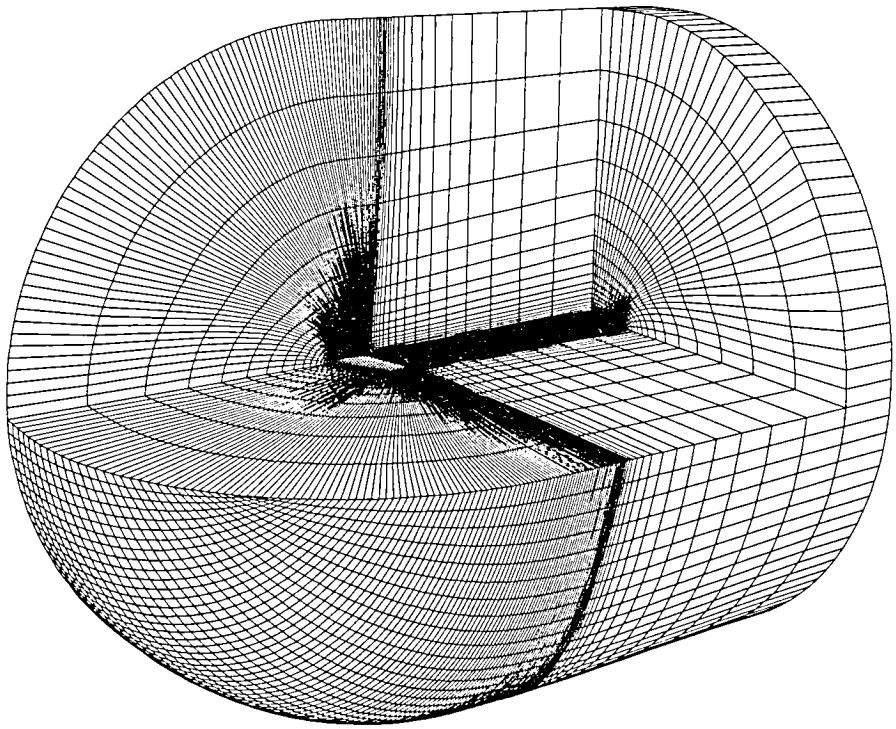

(a) Grid.

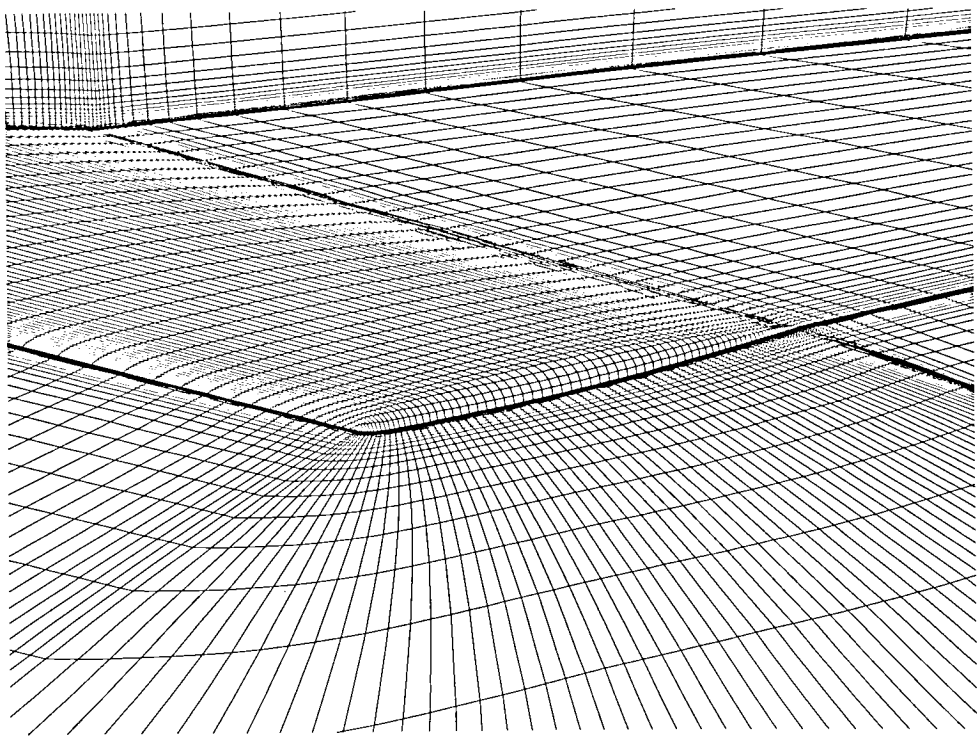

(b) Detail of grid near wingtip. $193 \times 49 \times 33$ grid.

Figure 1. Grid for ONERA M6 wing.

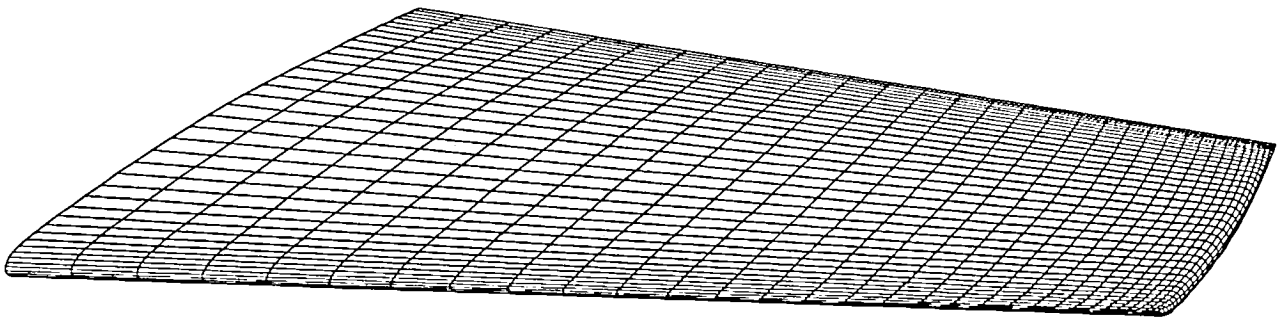

(a) ONERA M6 wing.

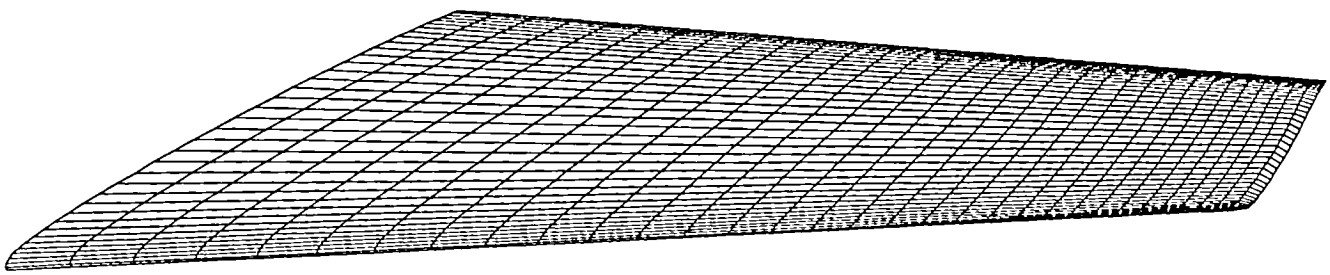

(b) Lockheed Wing B.

Figure 2. Surface grids.

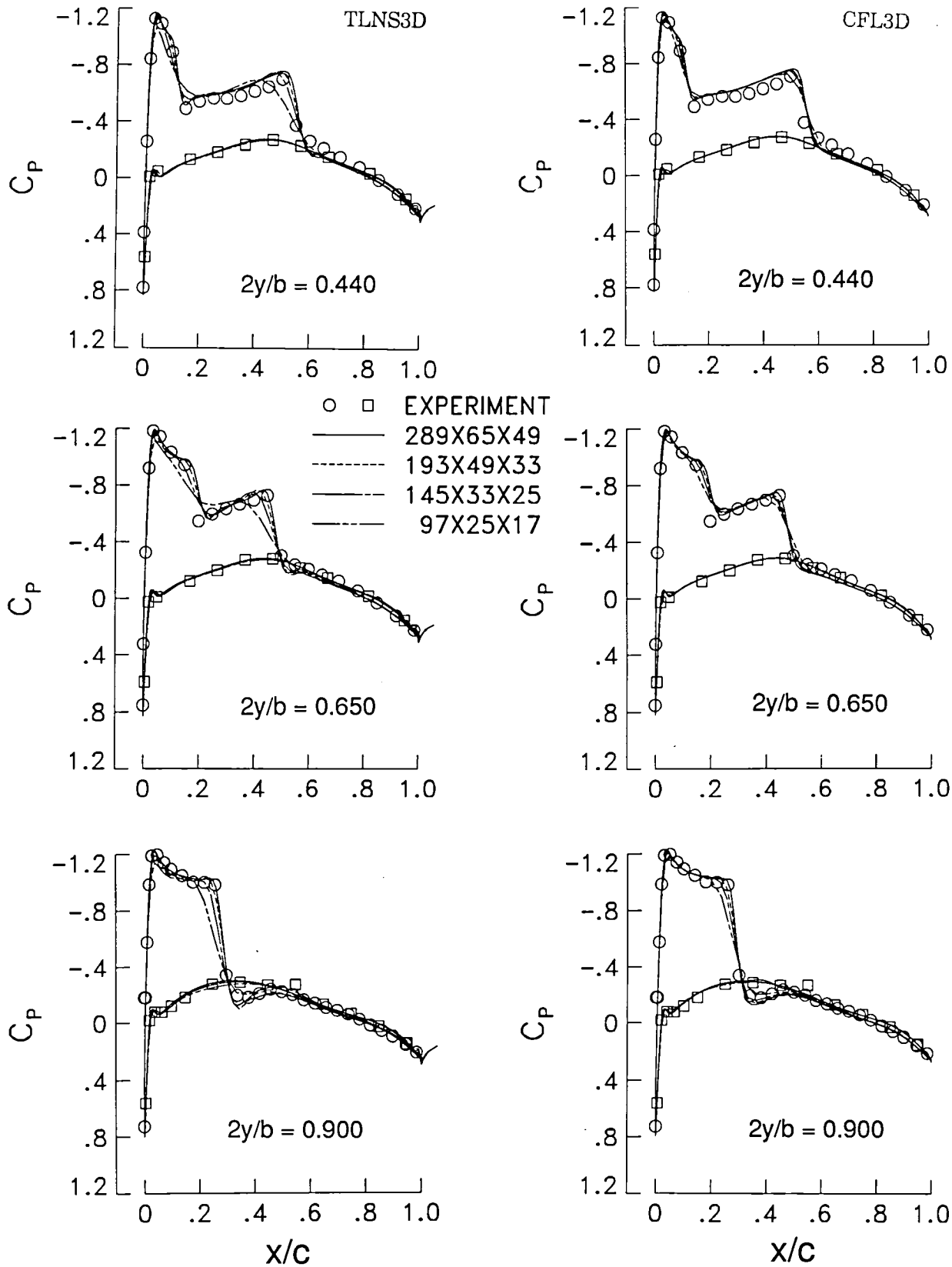

Figure 3. Effect of grid refinement on C_p for ONERA M6 wing.

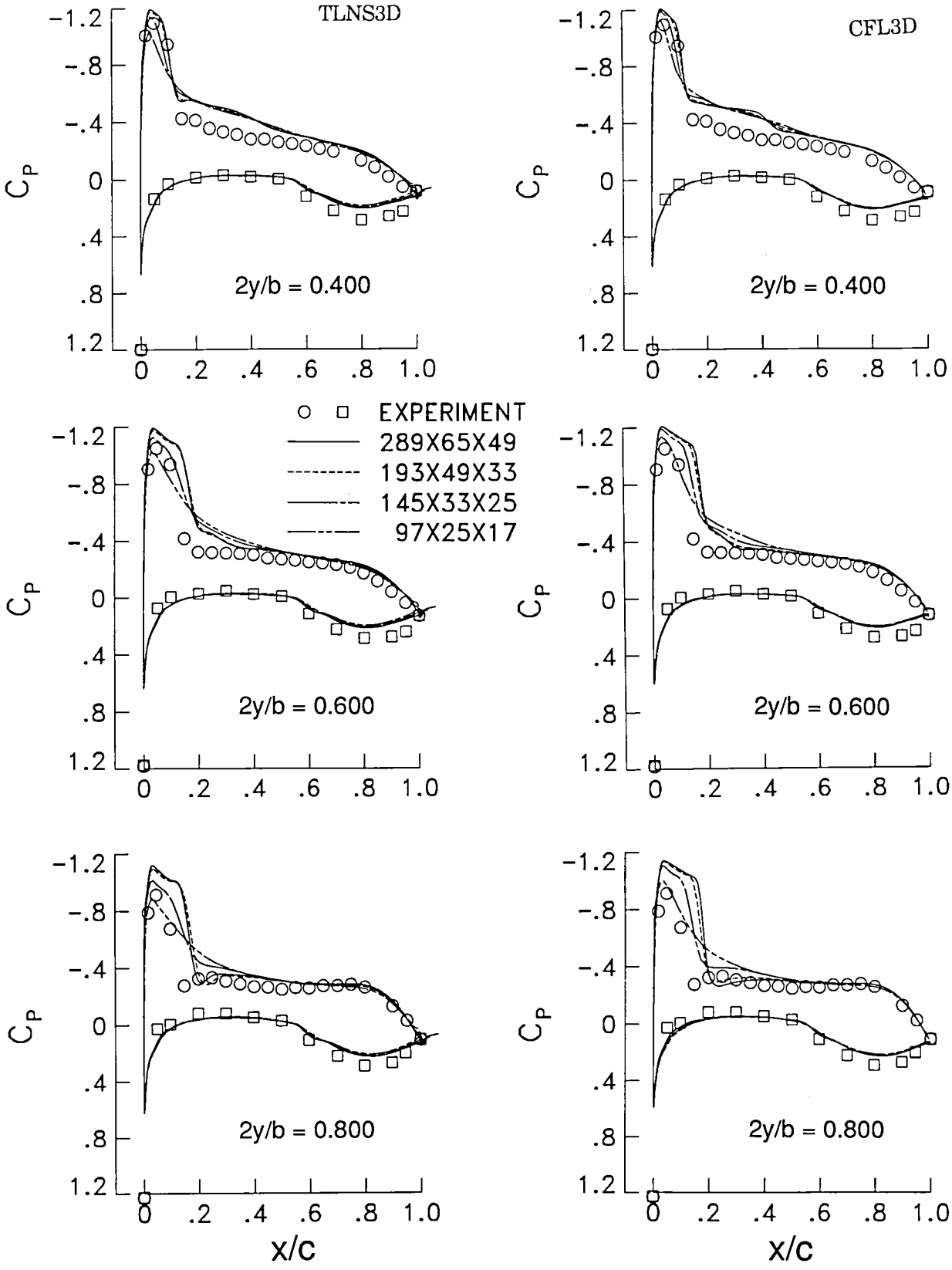

Figure 4. Effect of grid refinement on C_p for Lockheed Wing B.

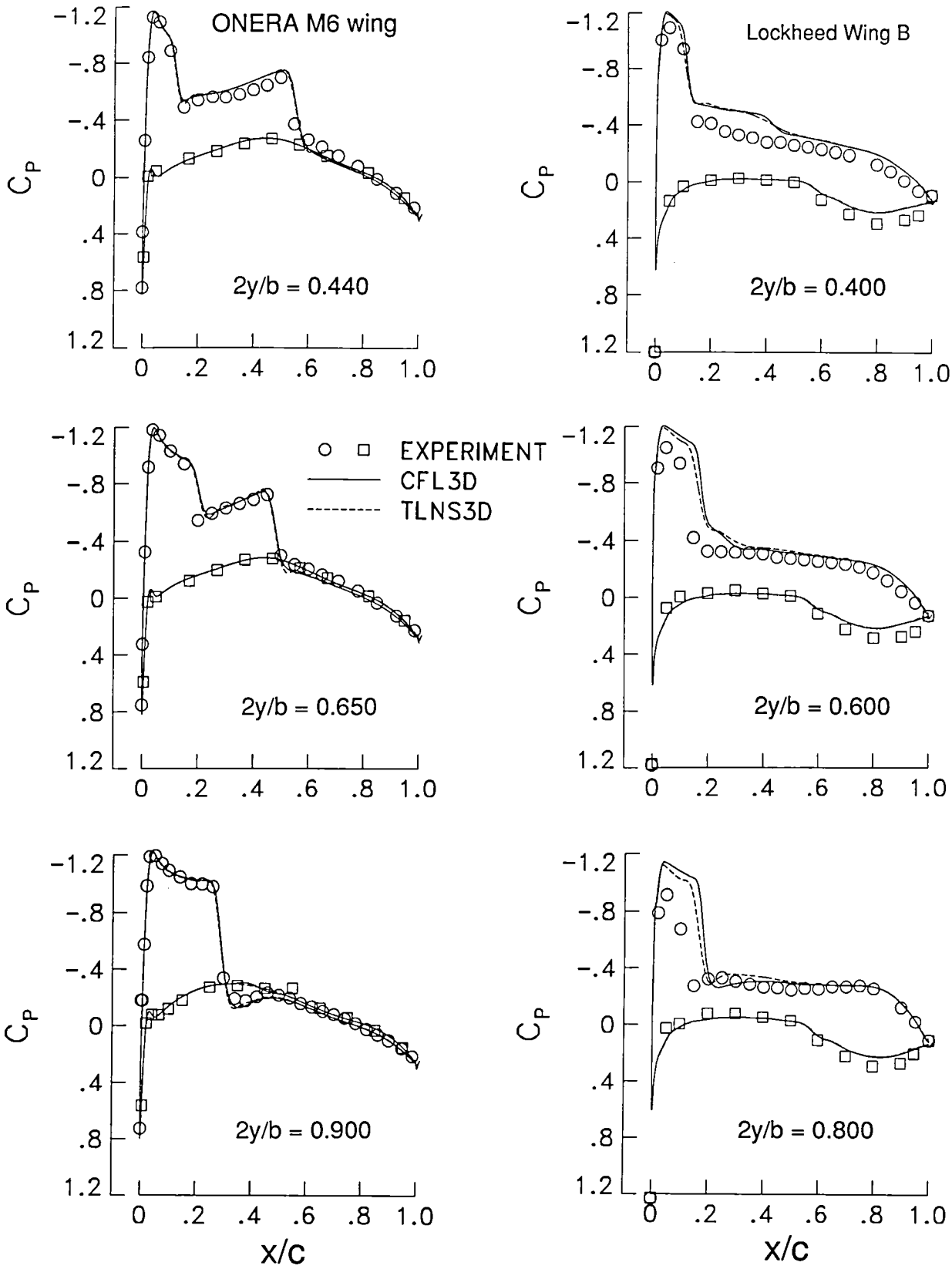

Figure 5. Comparison of C_p on the $289 \times 65 \times 49$ grid.

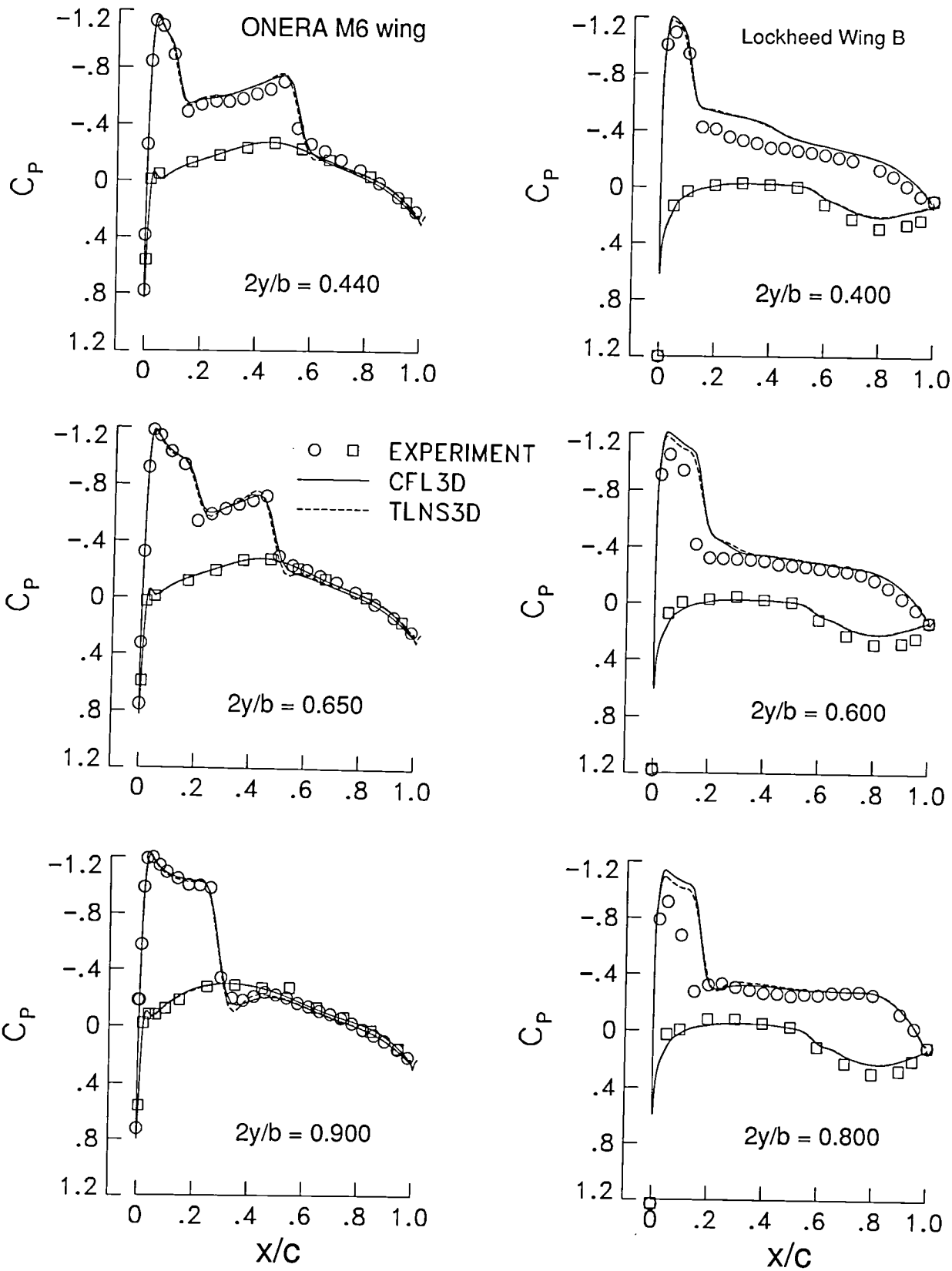

Figure 6. Comparison of C_p on the $193 \times 49 \times 33$ grid.

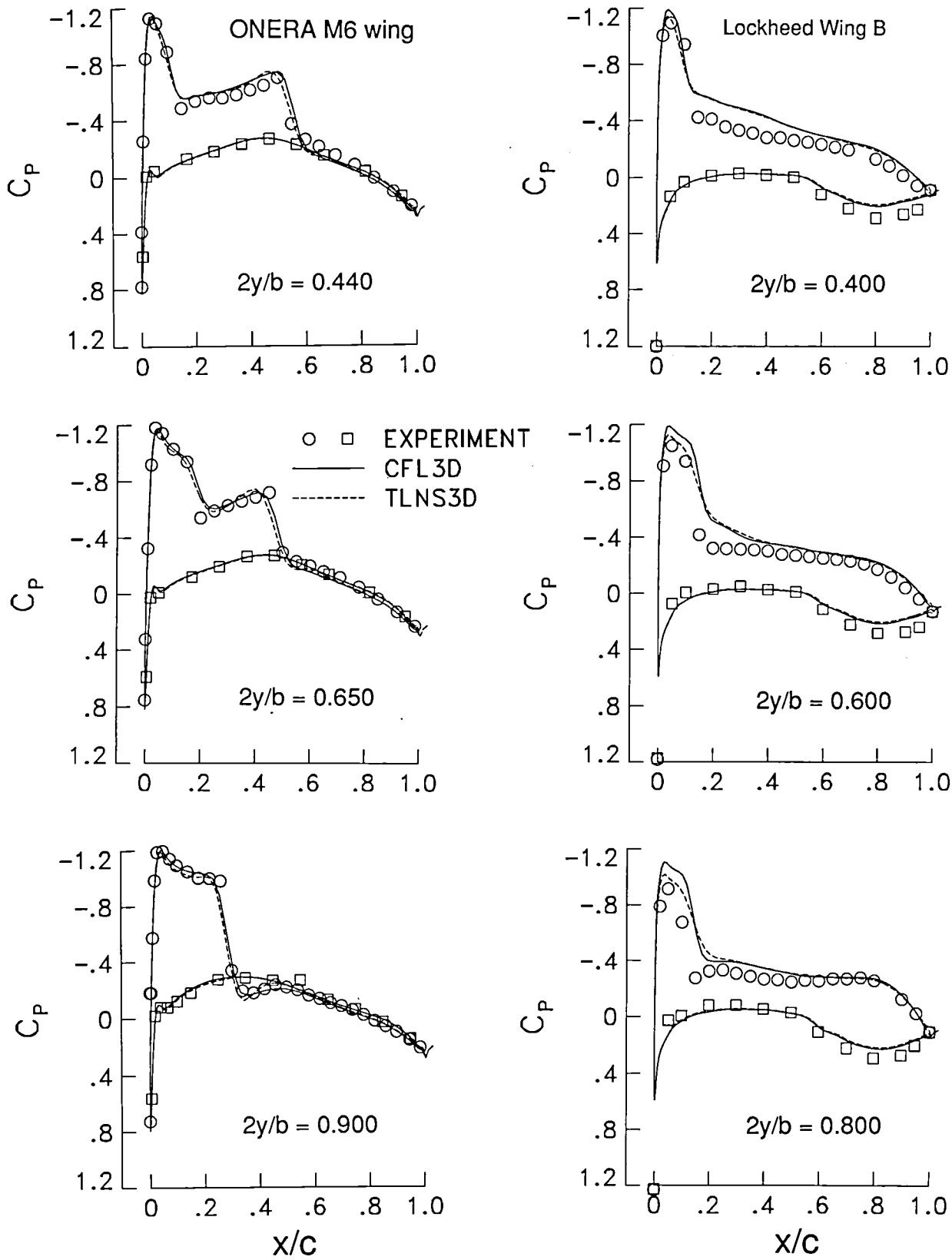

Figure 7. Comparison of C_p on the $145 \times 33 \times 25$ grid.

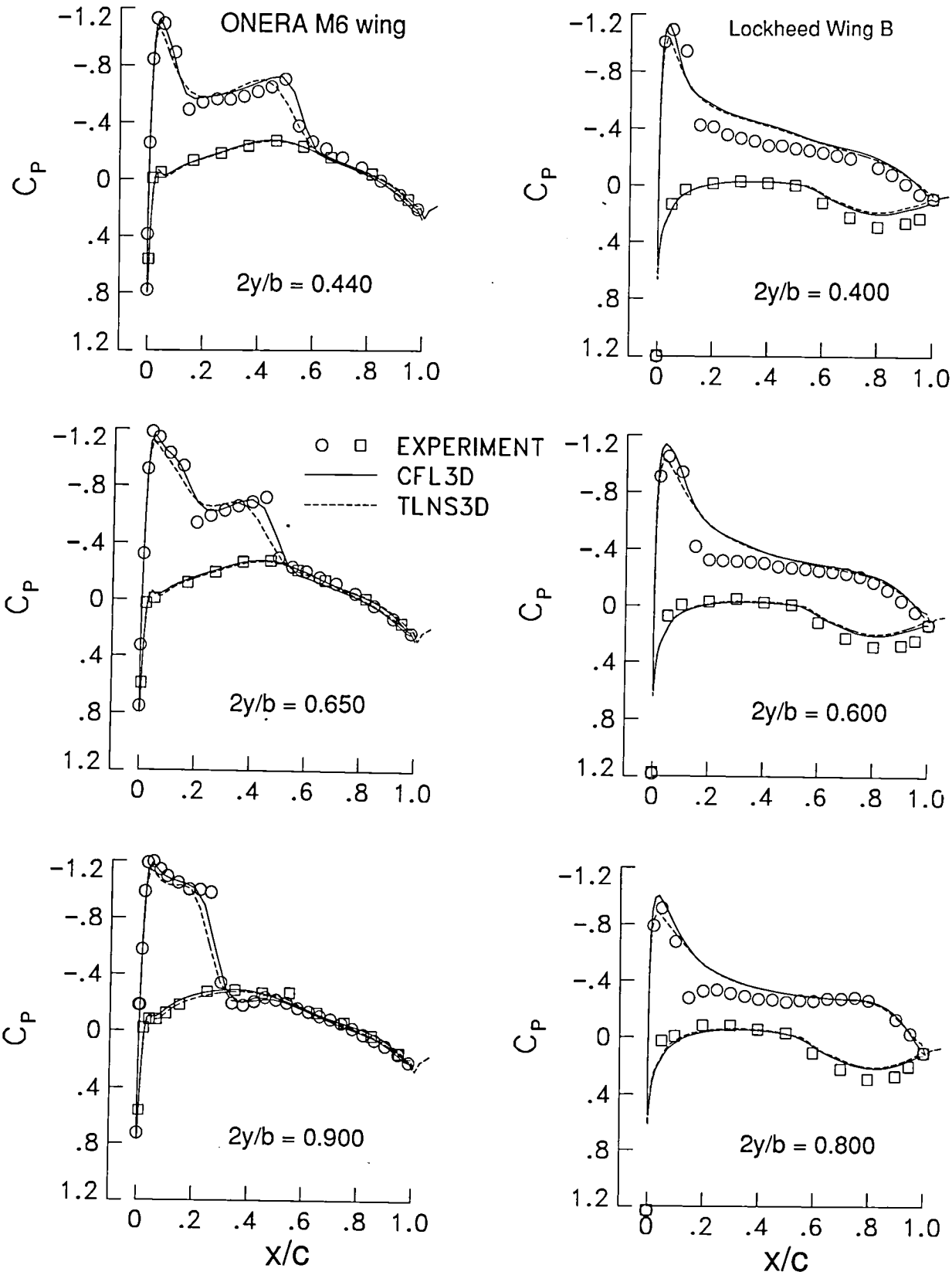

Figure 8. Comparison of C_p on the $97 \times 25 \times 17$ grid.

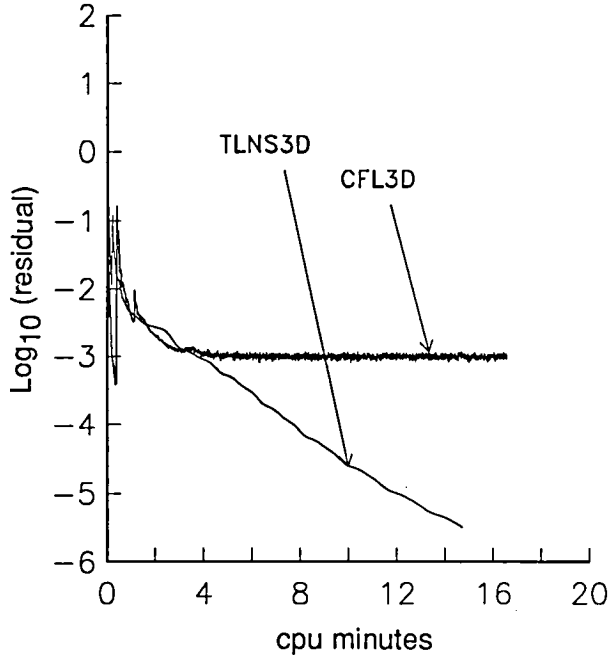

(a) Residual for ONERA M6 wing.

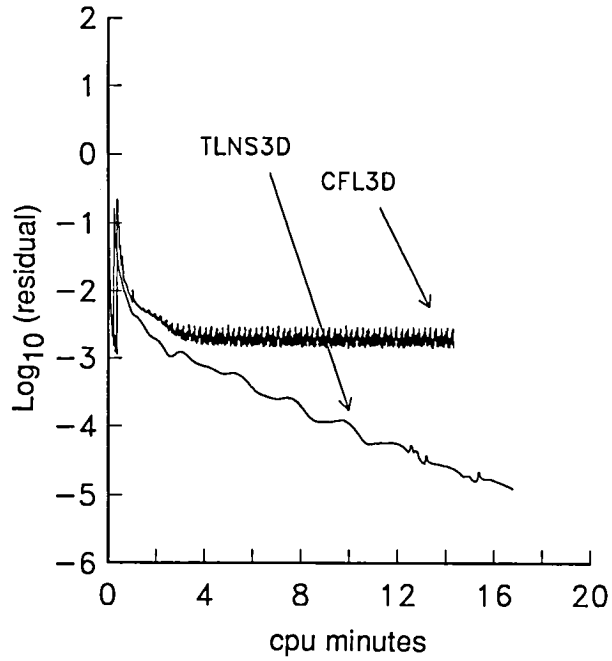

(b) Residual for Lockheed Wing B.

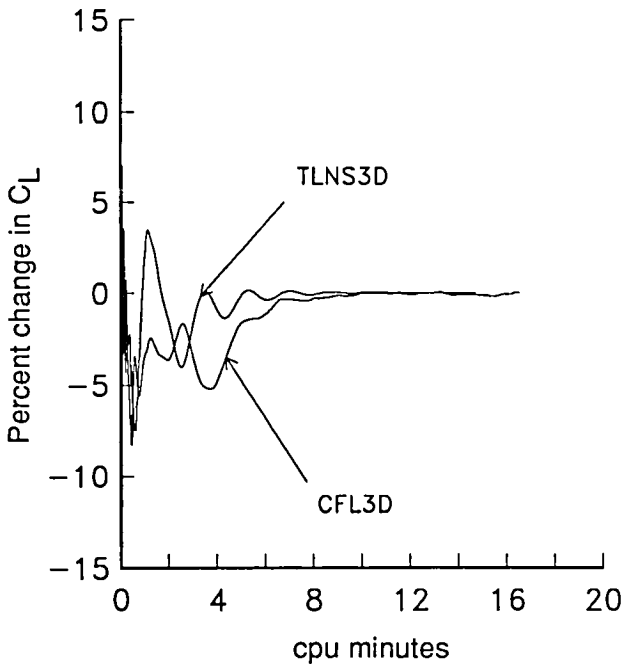

(c) Lift history for ONERA M6 wing.

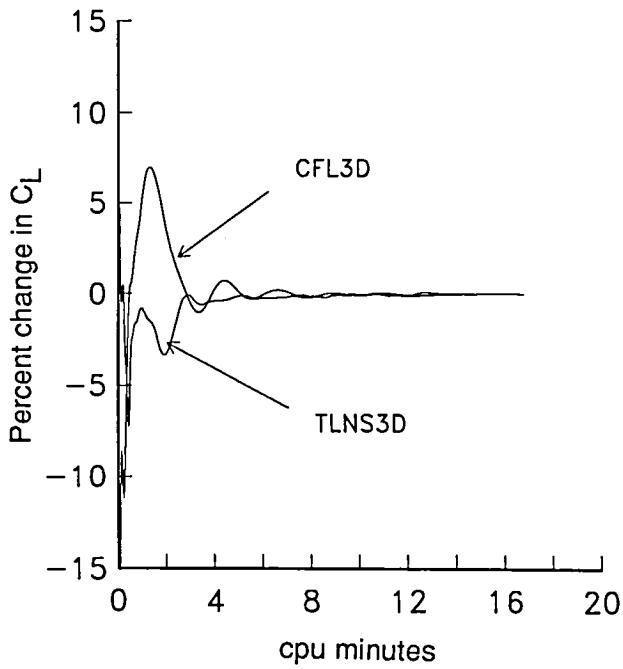

(d) Lift for Lockheed Wing B.

Figure 9. Convergence histories. $97 \times 25 \times 17$ grid.

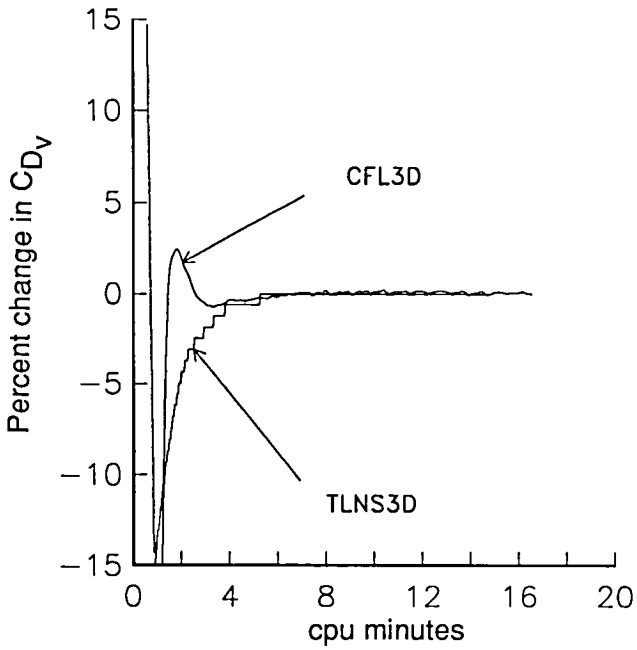

(e) Viscous drag for ONERA M6 wing.

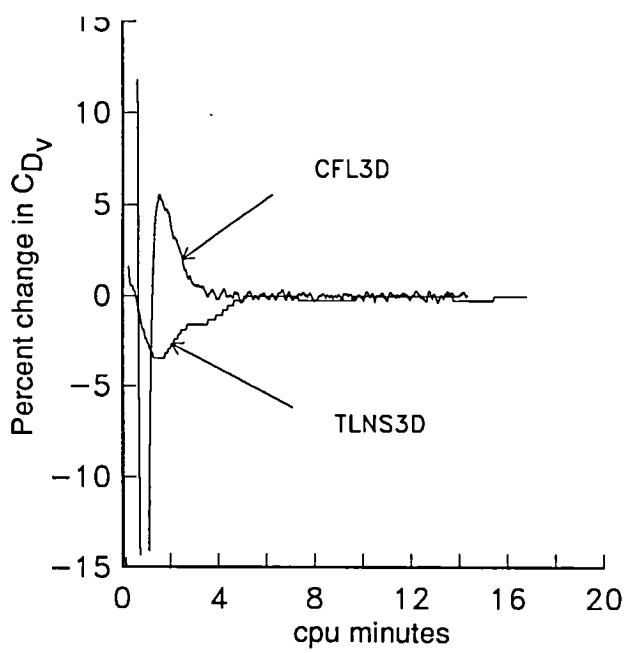

(f) Viscous drag for Lockheed Wing B.

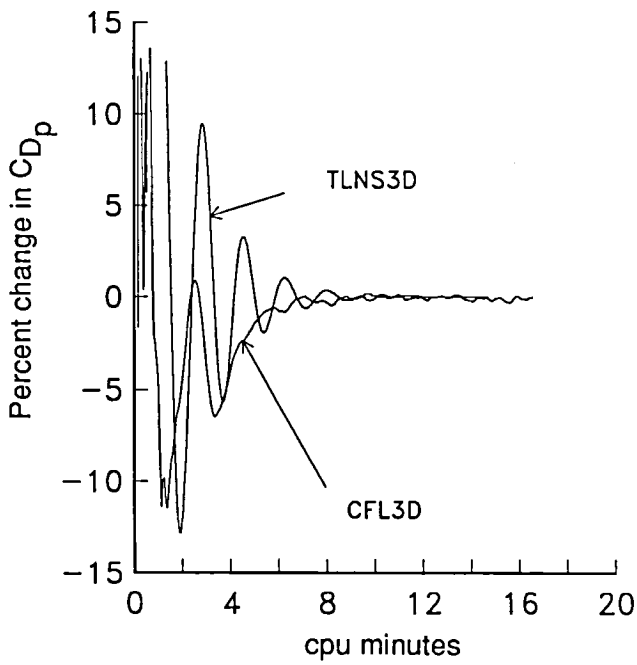

(g) Pressure drag for ONERA M6 wing.

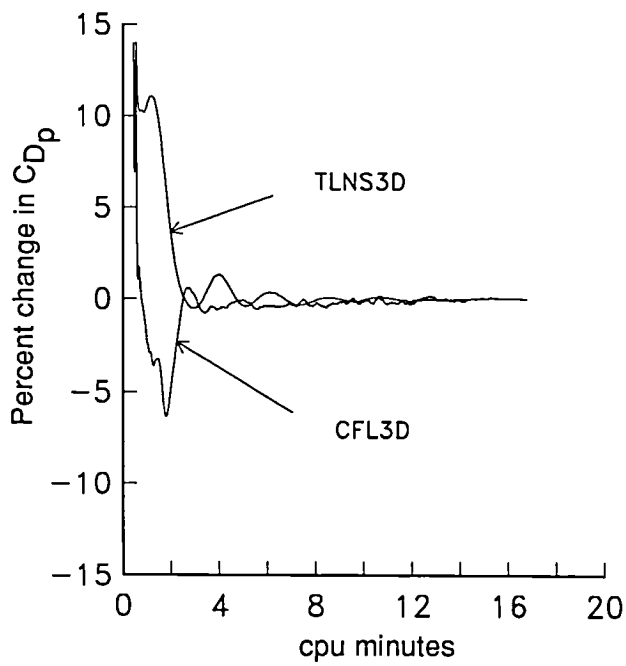

(h) Pressure drag for Lockheed Wing B.

Figure 9. Concluded.

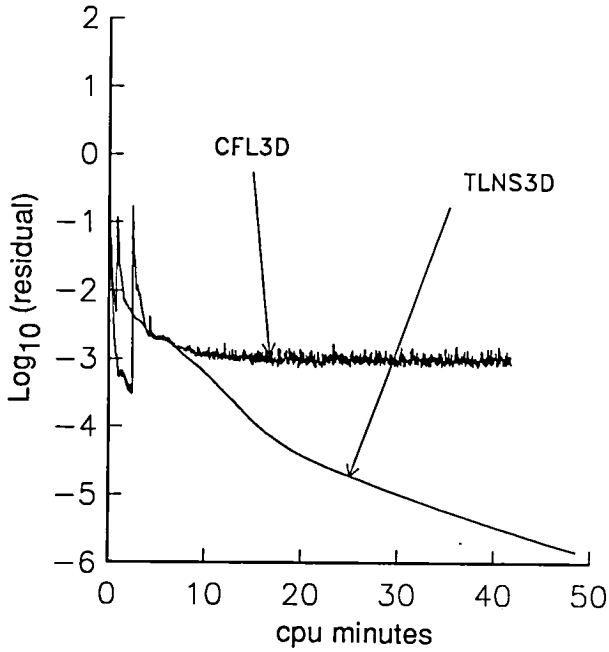

(a) Residual for ONERA M6 wing.

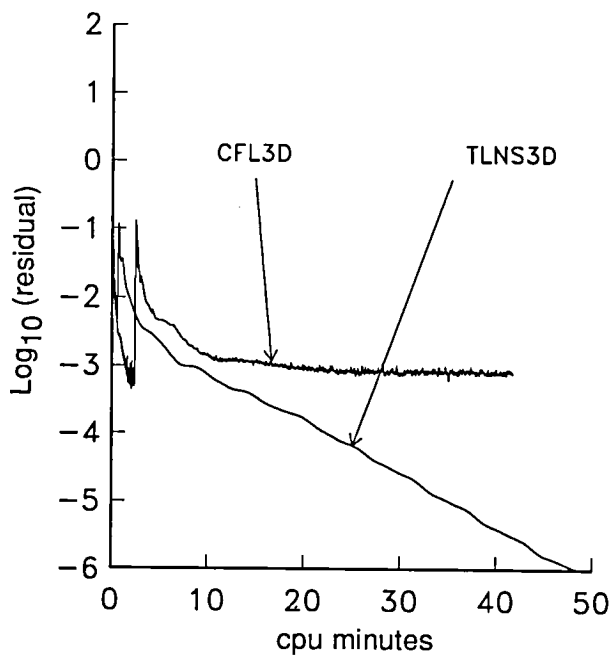

(b) Residual for Lockheed Wing B.

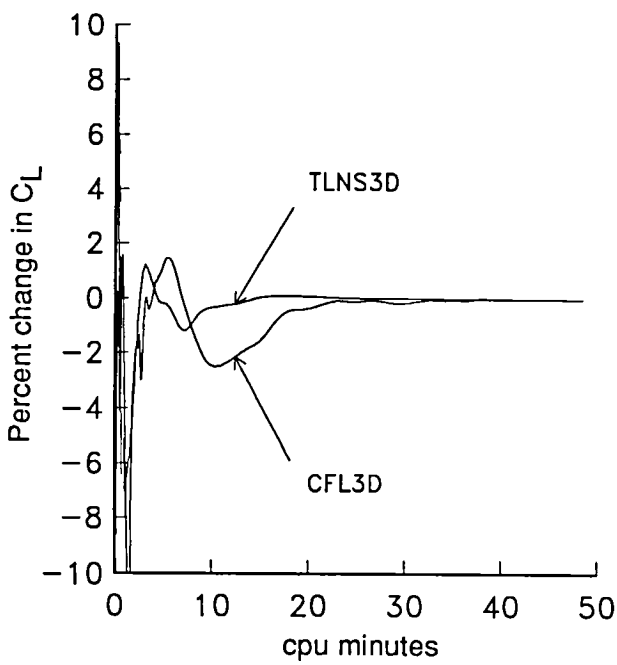

(c) Lift history for ONERA M6 wing.

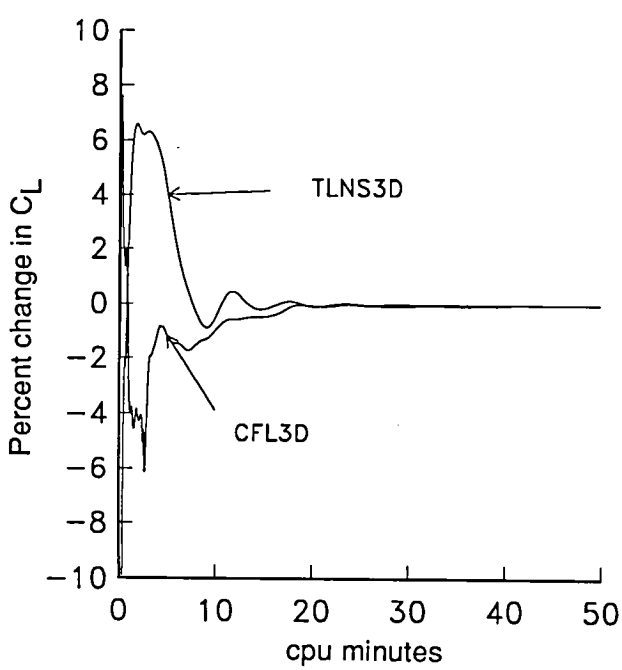

(d) Lift for Lockheed Wing B.

Figure 10. Convergence histories. $145 \times 33 \times 25$ grid.

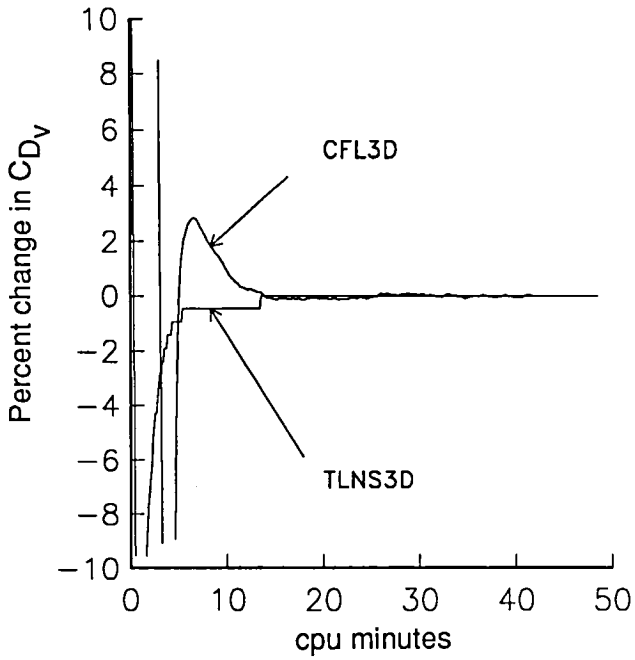

(e) Viscous drag for ONERA M6 wing.

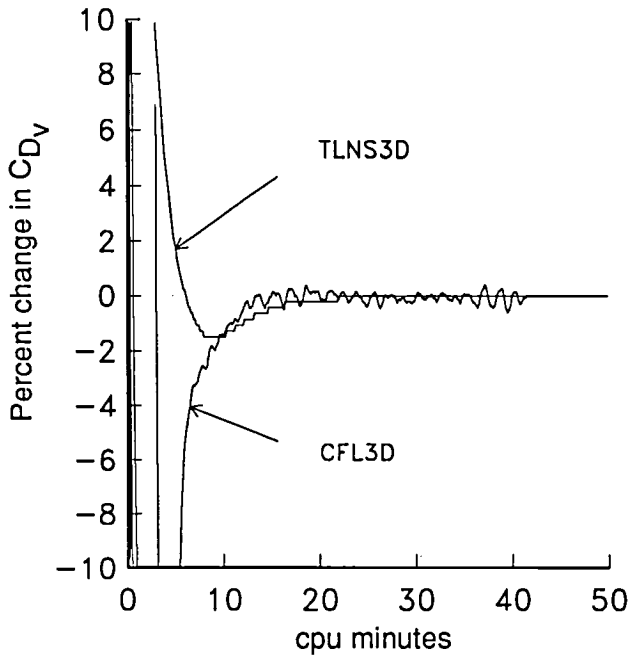

(f) Viscous drag for Lockheed Wing B.

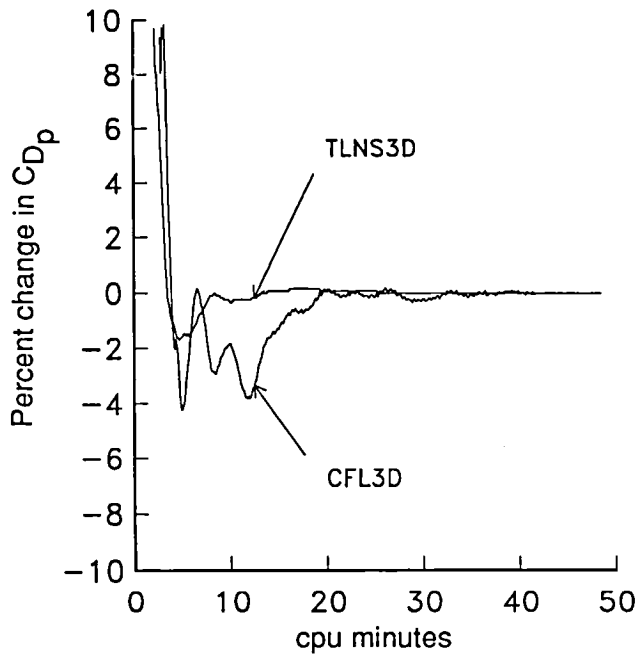

(g) Pressure drag for ONERA M6 wing.

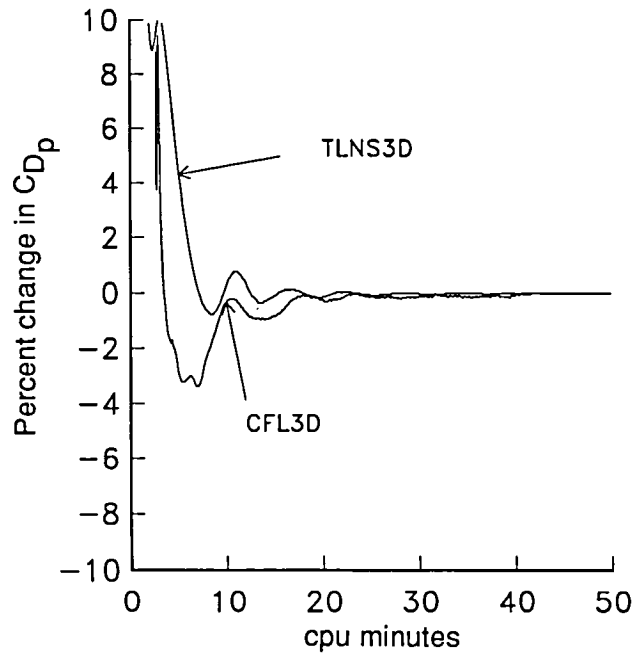

(h) Pressure drag for Lockheed Wing B.

Figure 10. Concluded.

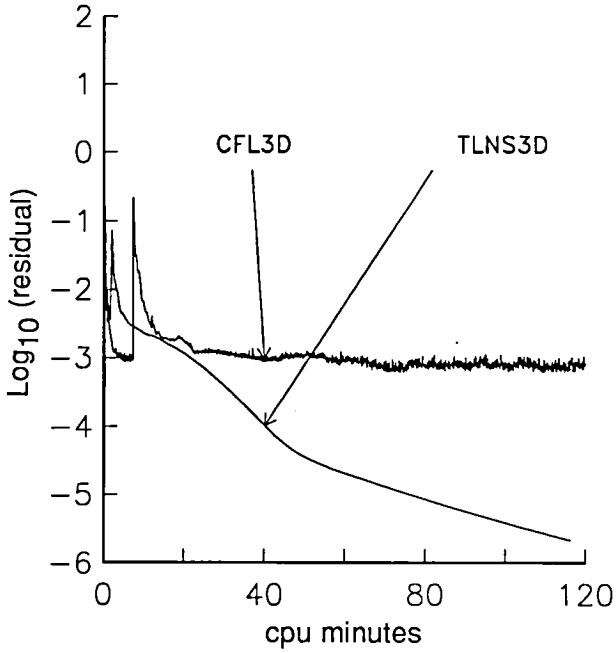

(a) Residual for ONERA M6 wing.

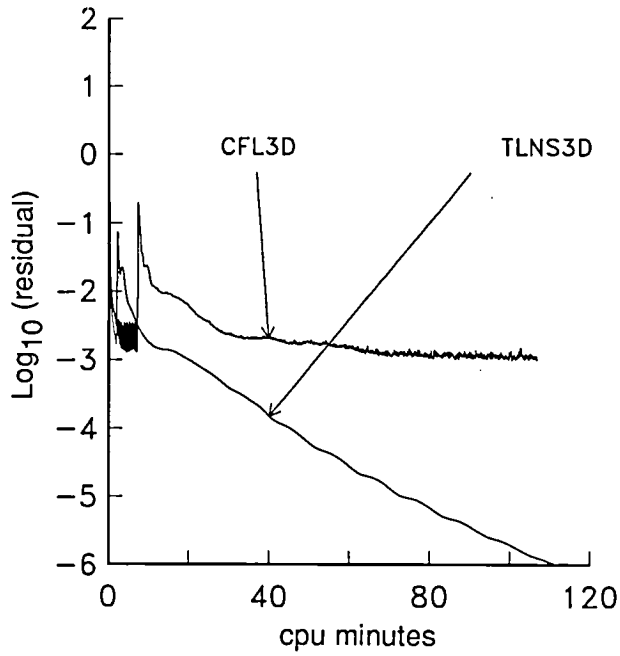

(b) Residual for Lockheed Wing B.

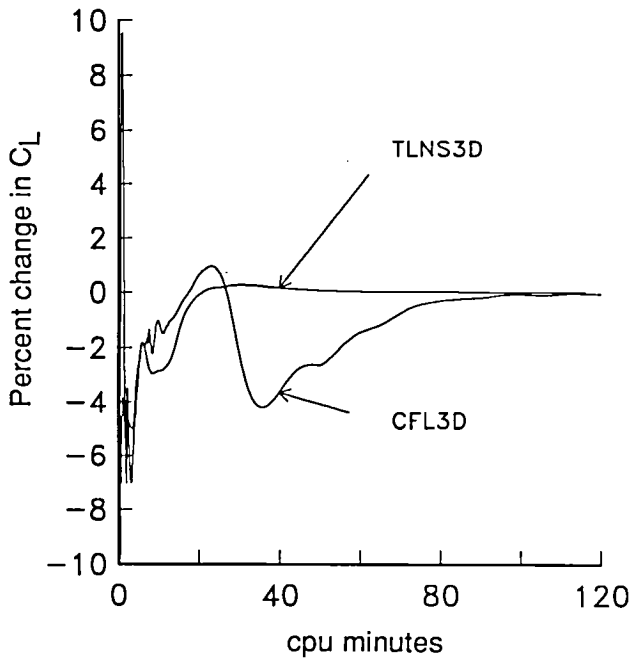

(c) Lift history for ONERA M6 wing.

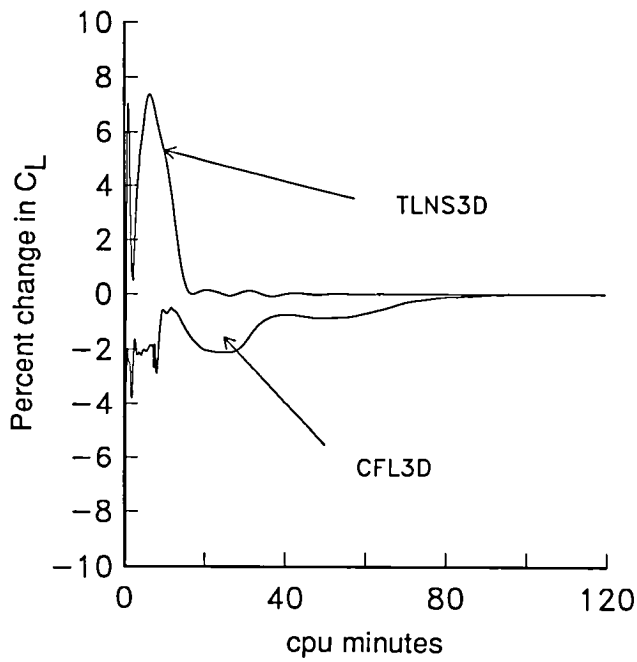

(d) Lift for Lockheed Wing B.

Figure 11. Convergence histories. $193 \times 49 \times 33$ grid.

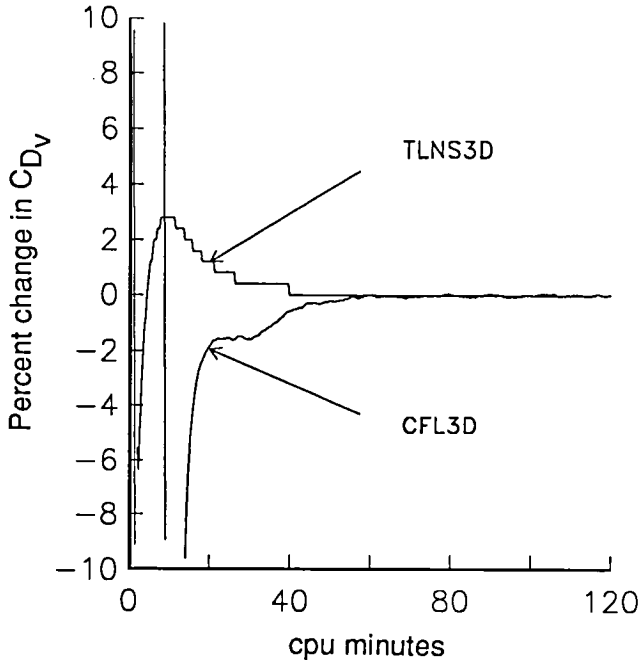

(e) Viscous drag for ONERA M6 wing.

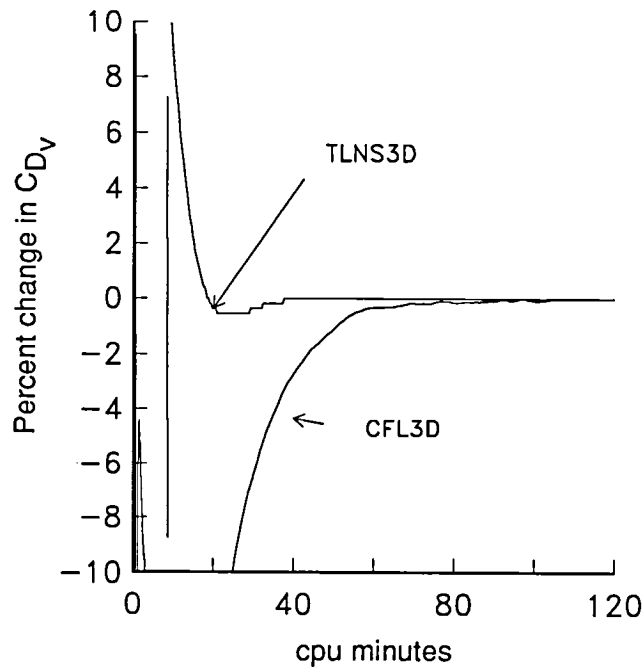

(f) Viscous drag for Lockheed Wing B.

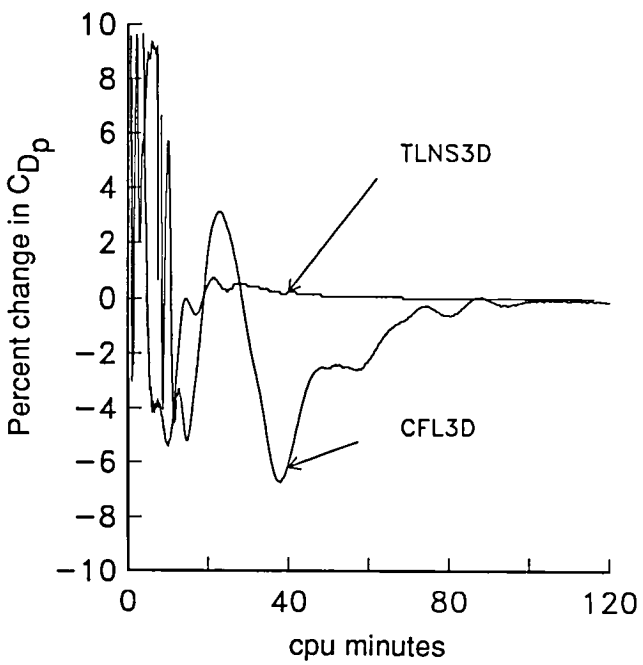

(g) Pressure drag for ONERA M6 wing.

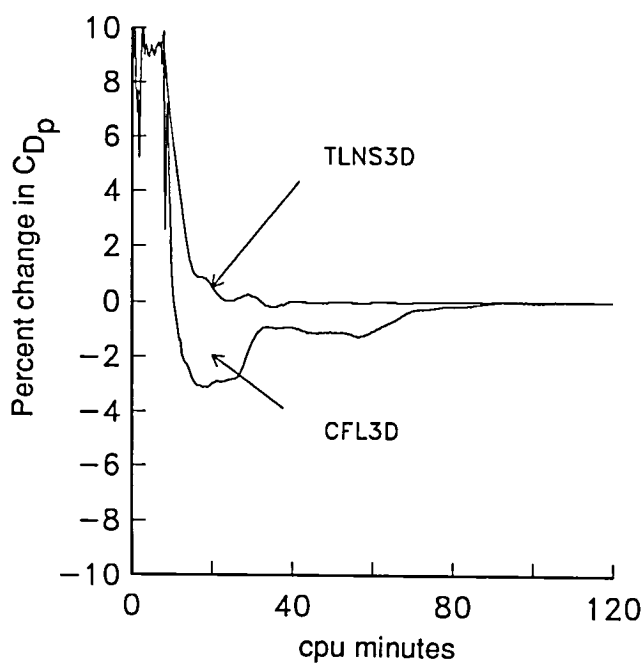

(h) Pressure drag for Lockheed Wing B.

Figure 11. Concluded.

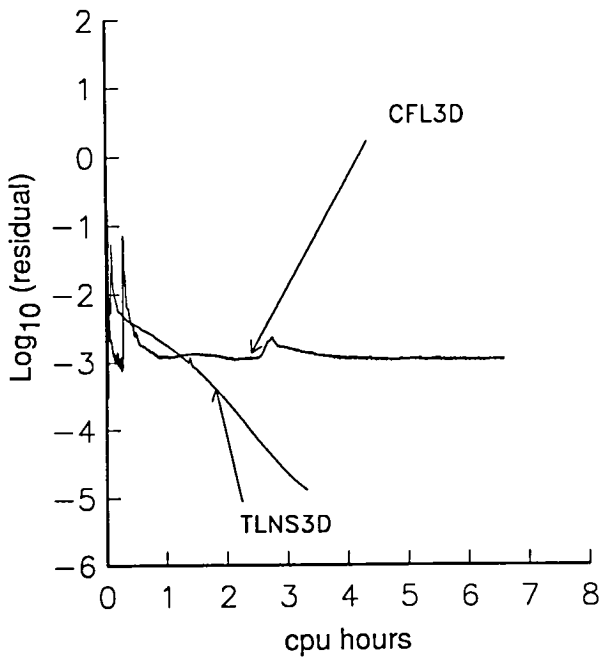

(a) Residual for ONERA M6 wing.

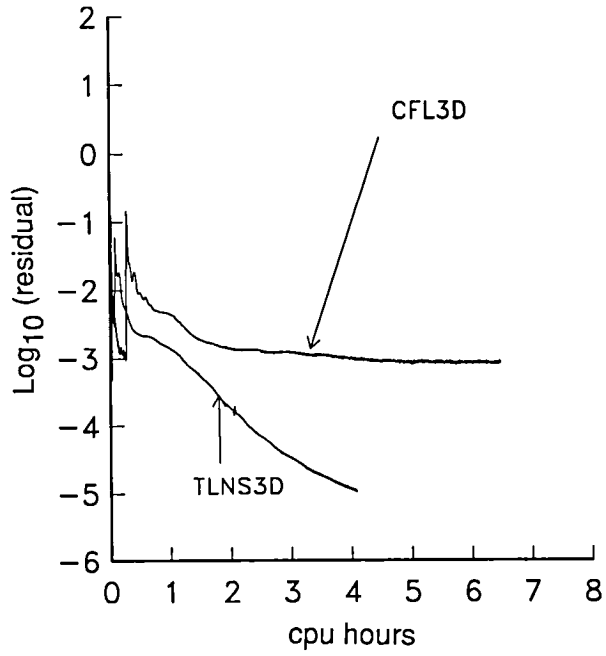

(b) Residual for Lockheed Wing B.

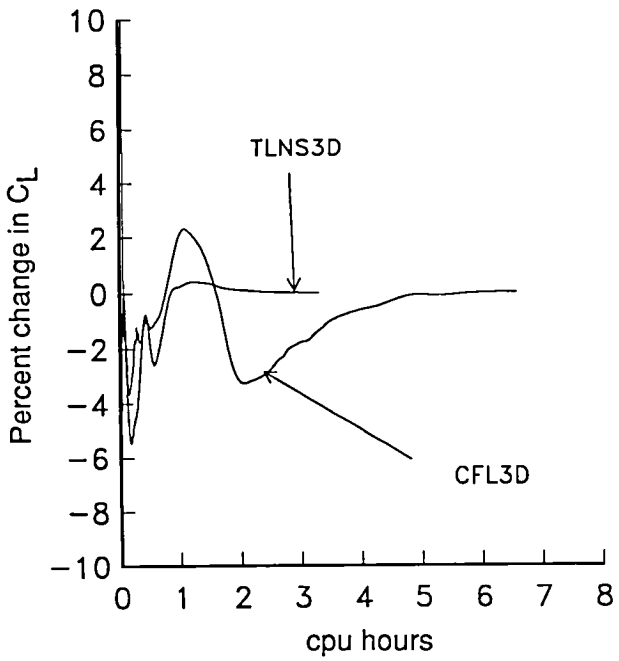

(c) Lift history for ONERA M6 wing.

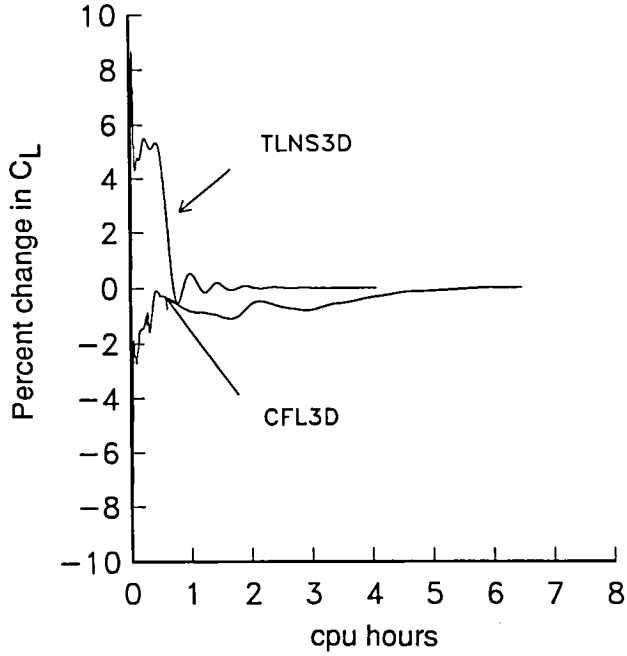

(d) Lift for Lockheed Wing B.

Figure 12. Convergence histories. $289 \times 65 \times 49$ grid.

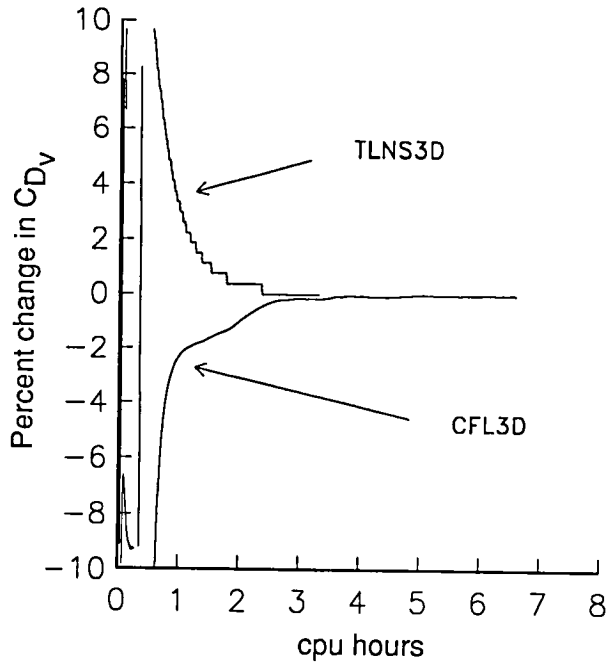

(e) Viscous drag for ONERA M6 wing.

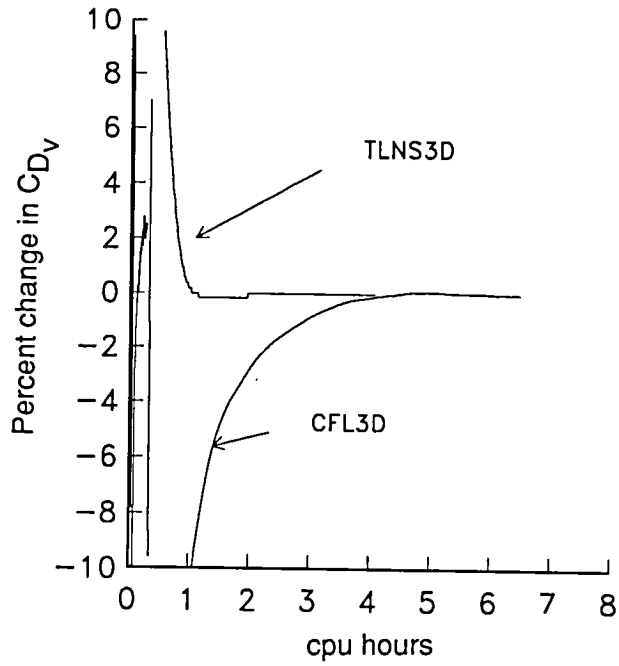

(f) Viscous drag for Lockheed Wing B.

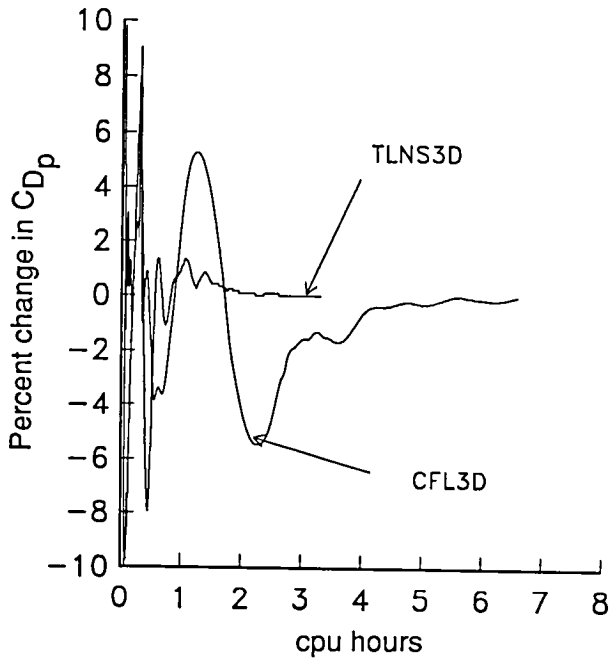

(g) Pressure drag for ONERA M6 wing.

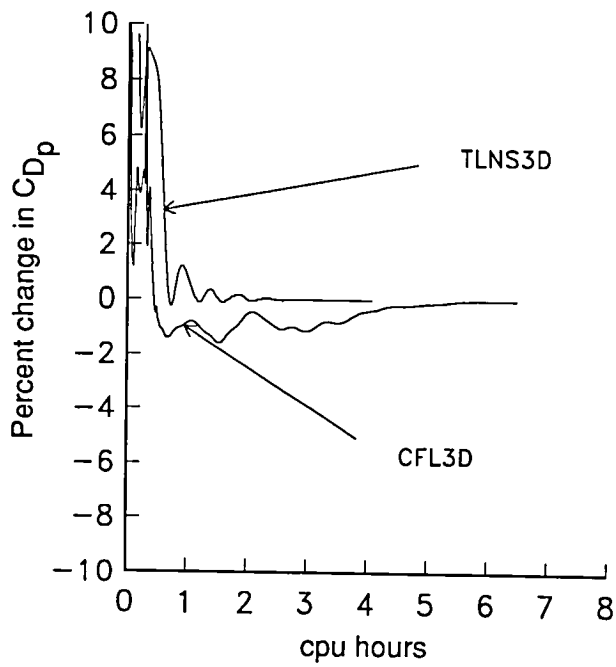

(h) Pressure drag for Lockheed Wing B.

Figure 12. Concluded.

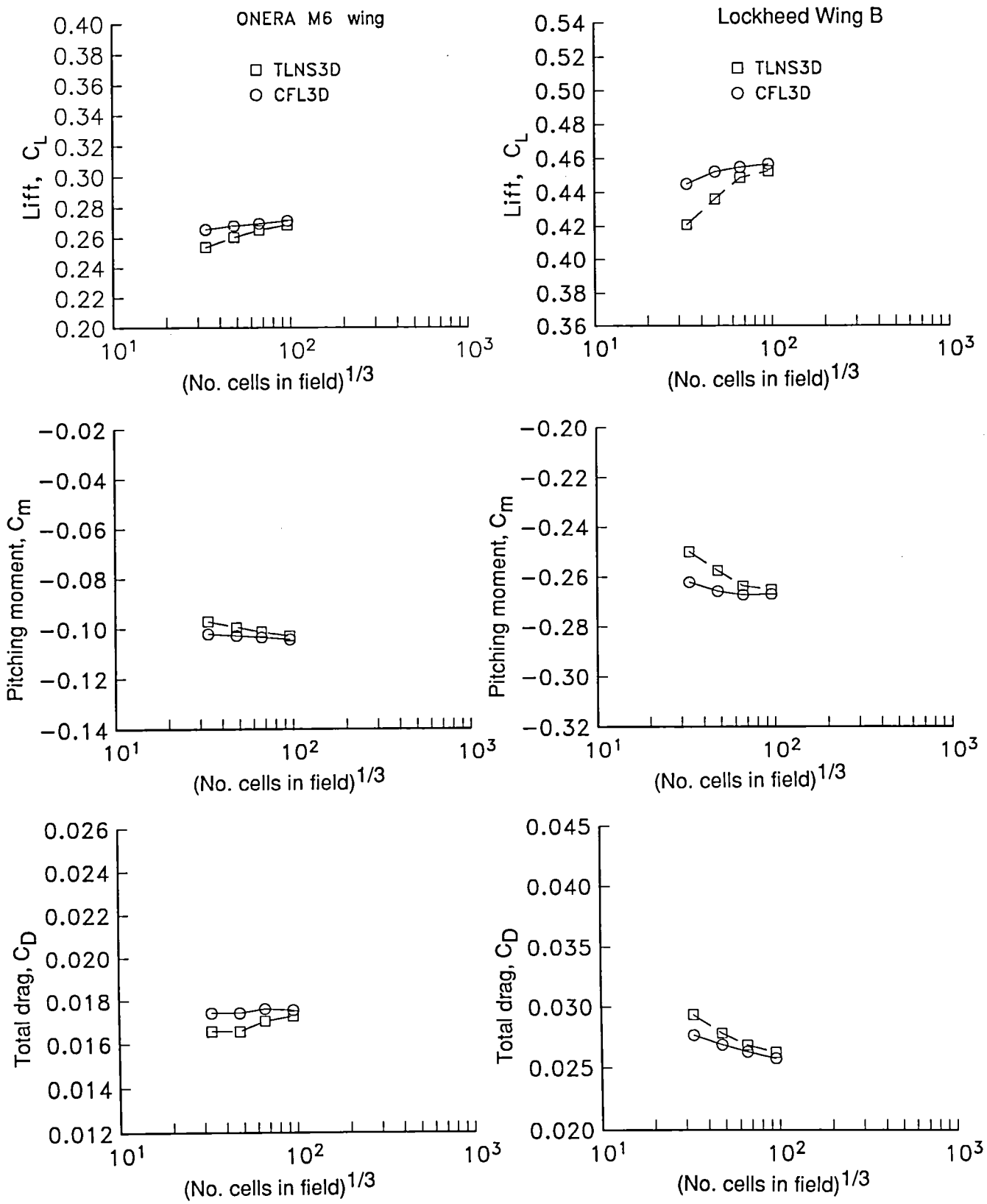

Figure 13. Values of force coefficients. .

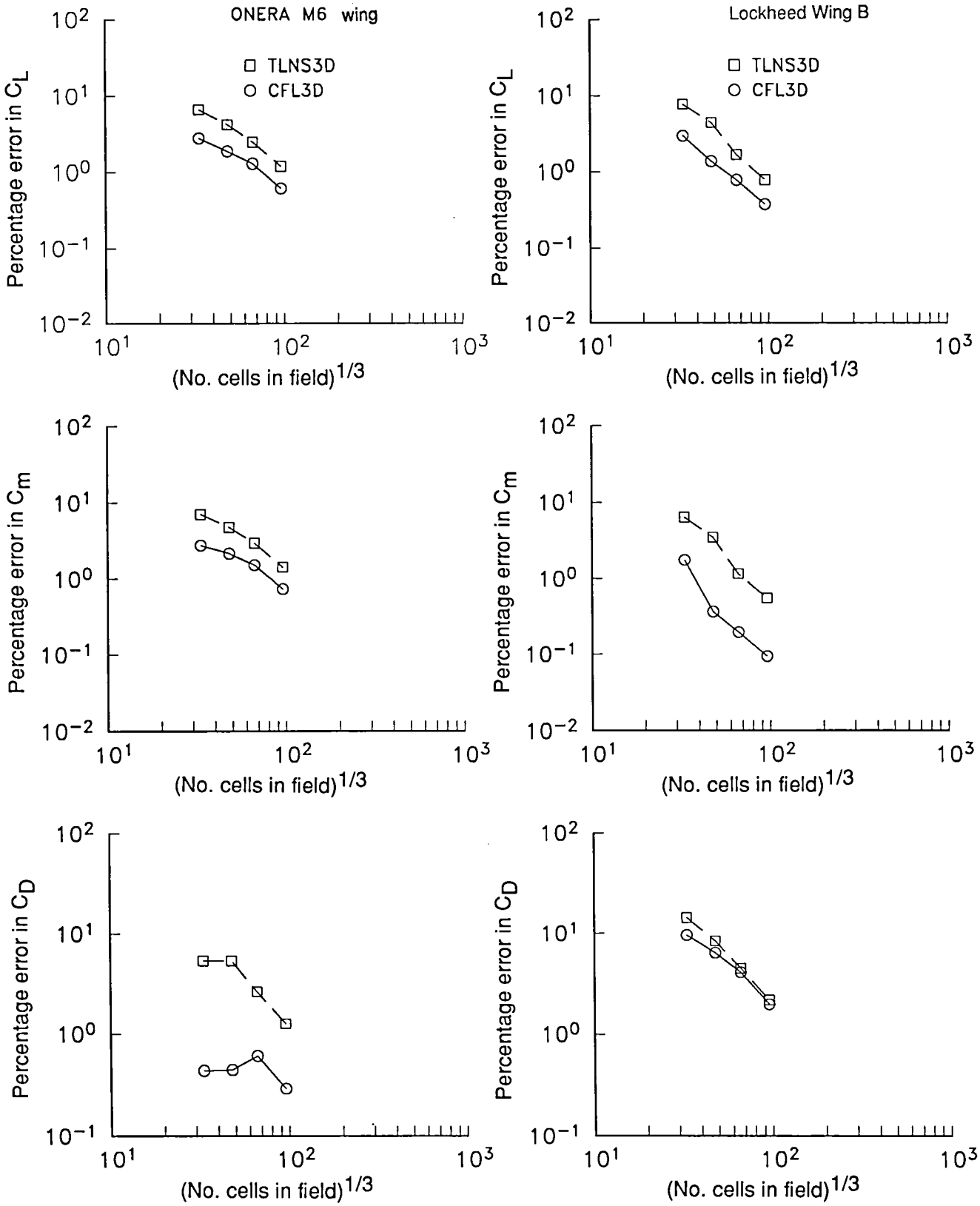

Figure 14. Percentage error in force coefficients.

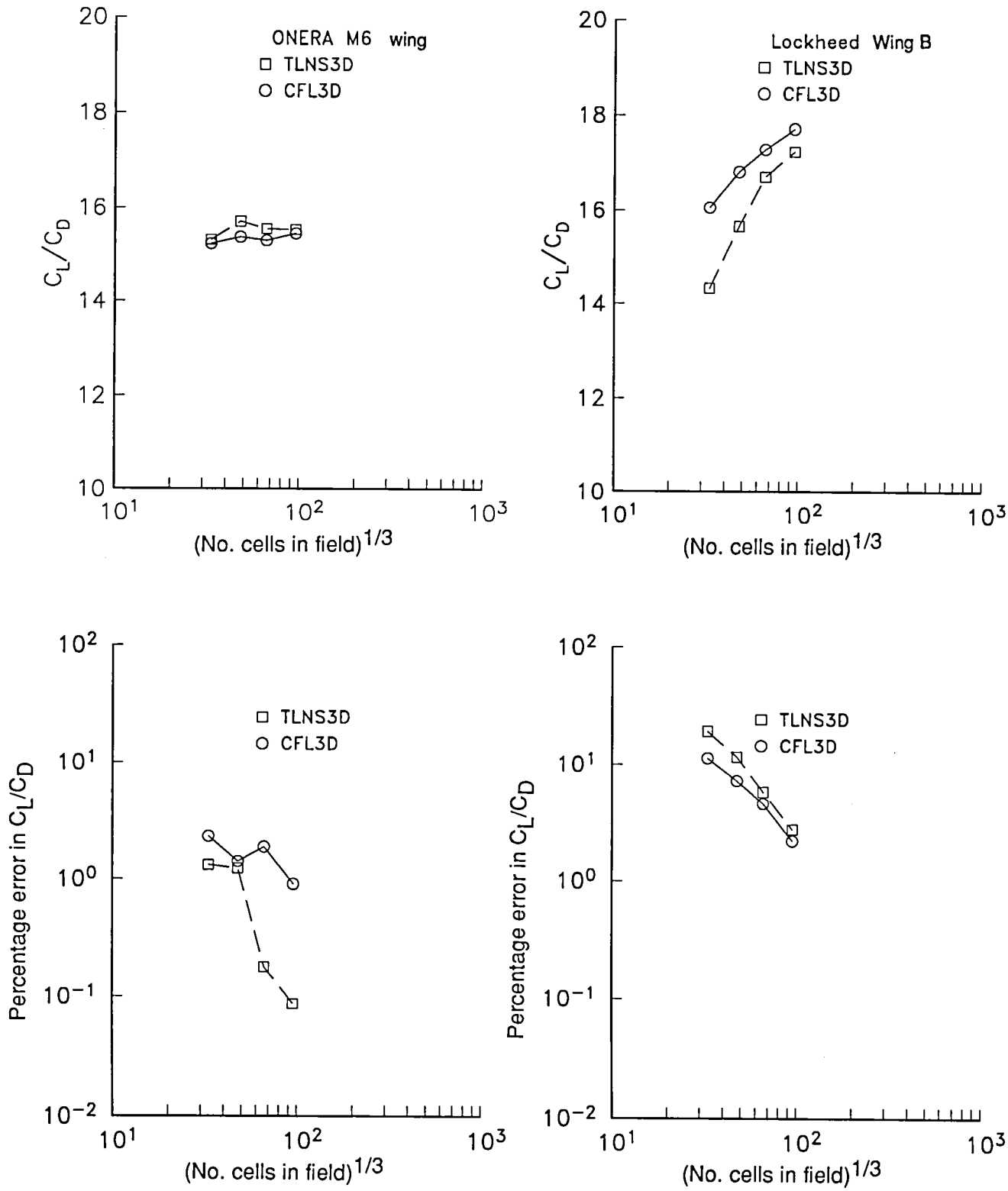

Figure 15. Lift-to-drag ratio.

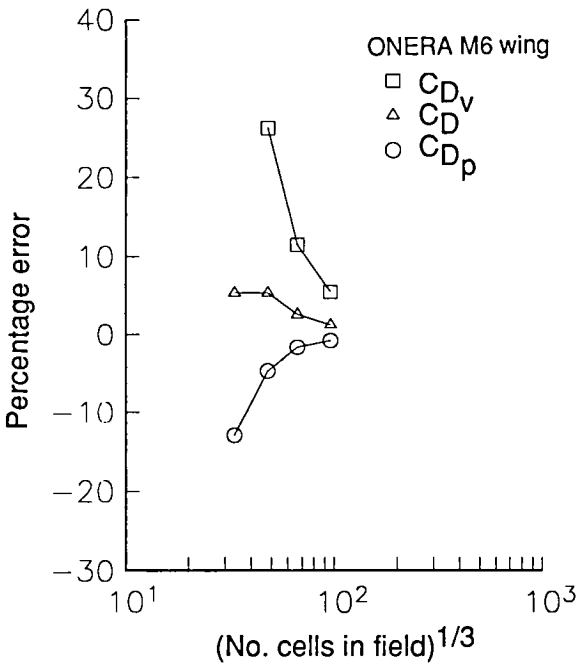

(a) TLNS3D.

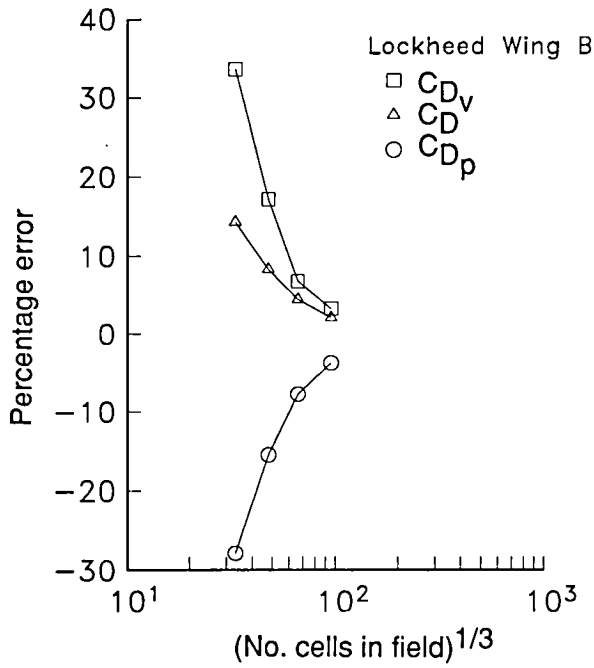

(b) TLNS3D.

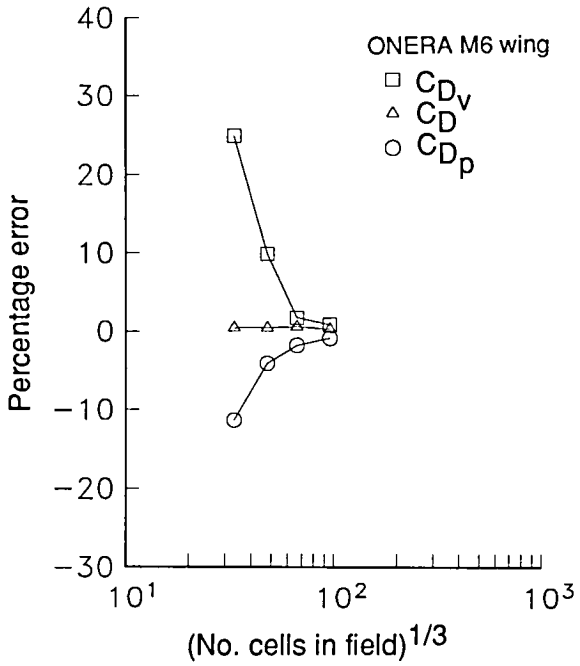

(c) CFL3D.

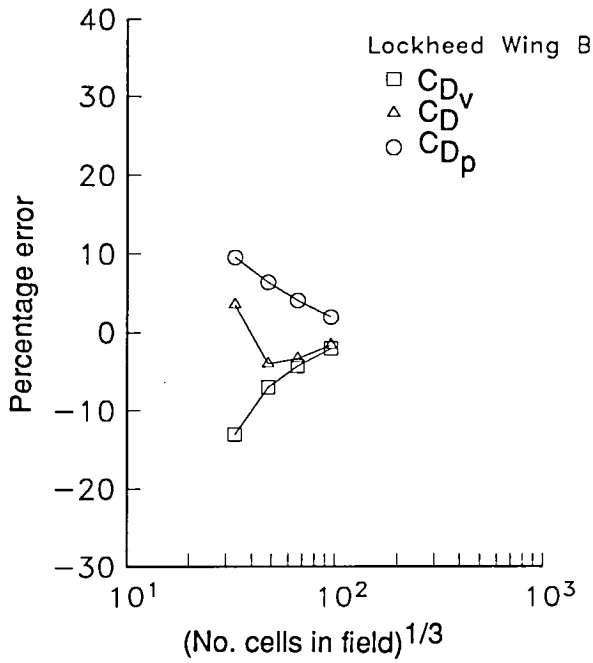

(d) CFL3D.

Figure 16. Errors in drag coefficients.

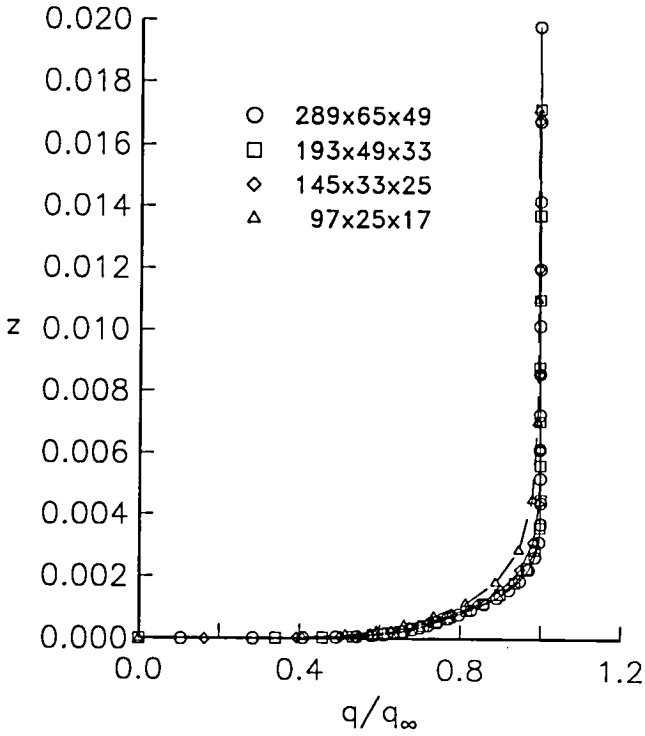

(a) TLNS3D—standard.

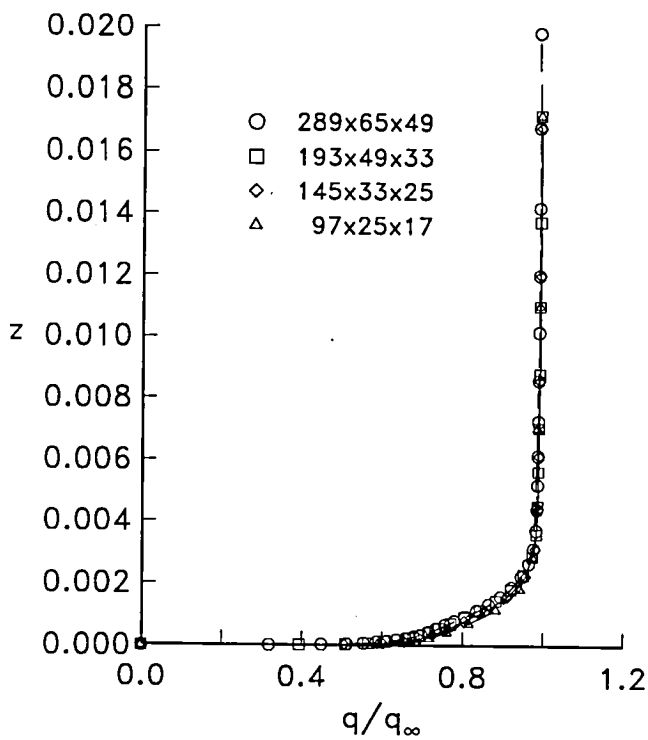

(b) CFL3D—standard.

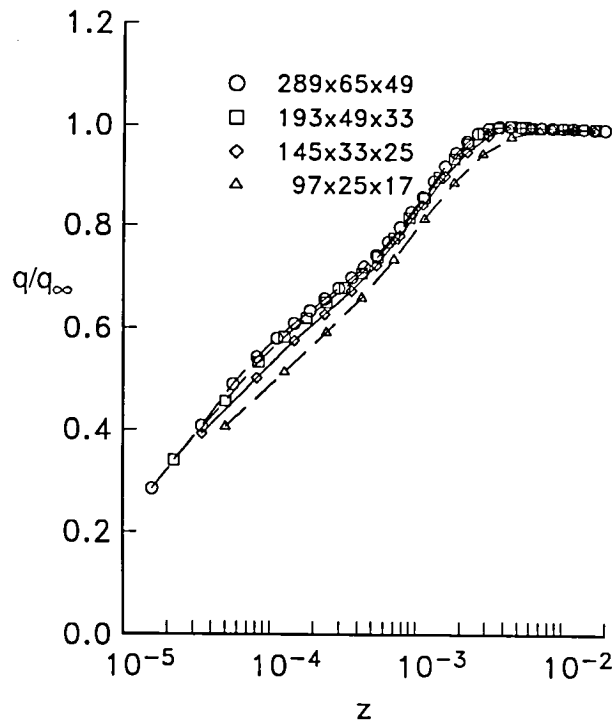

(c) TLNS3D—semilog.

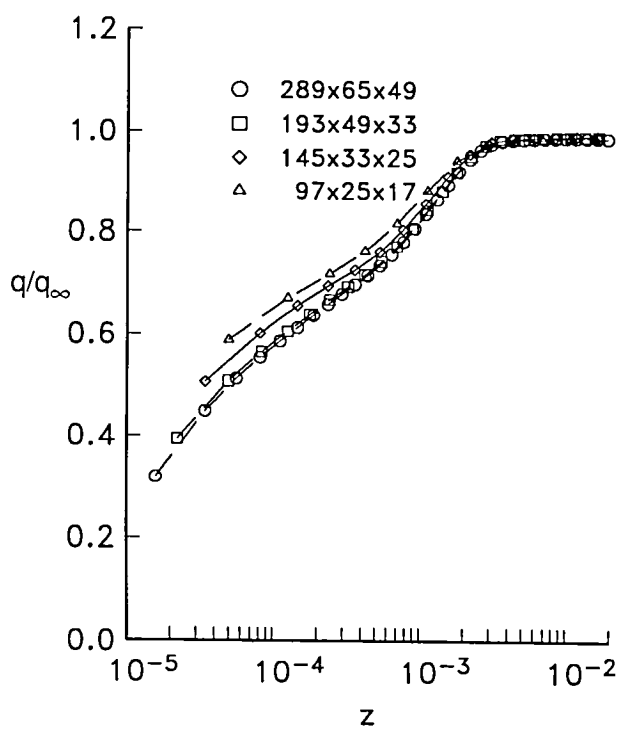

(d) CFL3D—semilog.

Figure 17. Effect of grid refinement on the upper-surface boundary-layer profiles for the ONERA M6 wing. $\eta = 0; \xi = 0.25$.

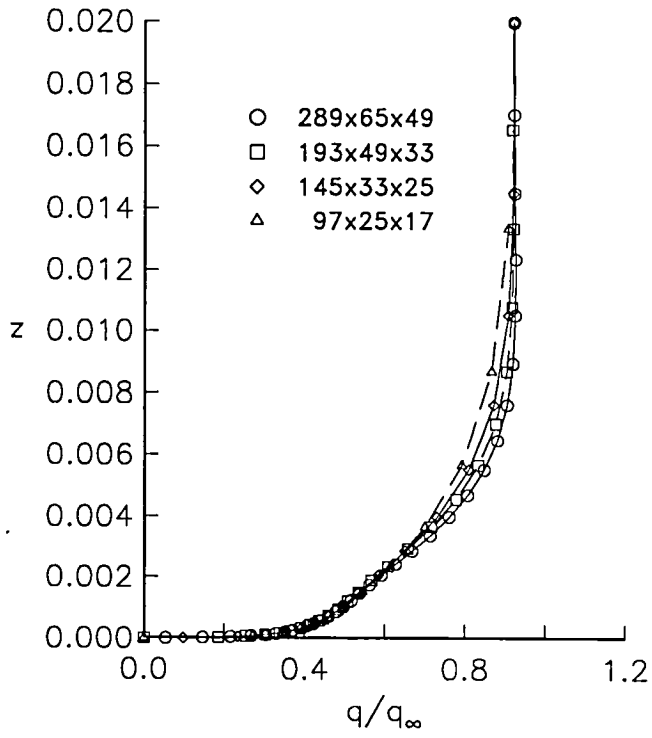

(a) TLNS3D—standard.

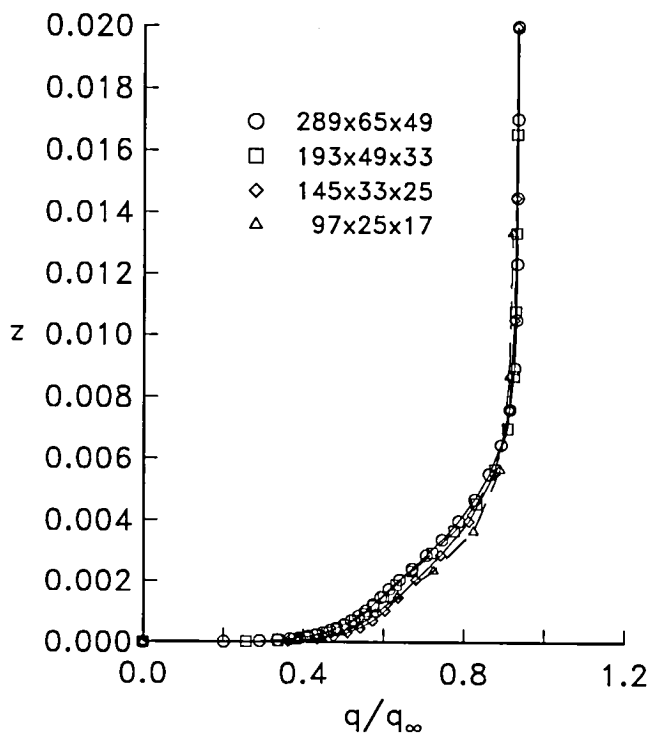

(b) CFL3D—standard.

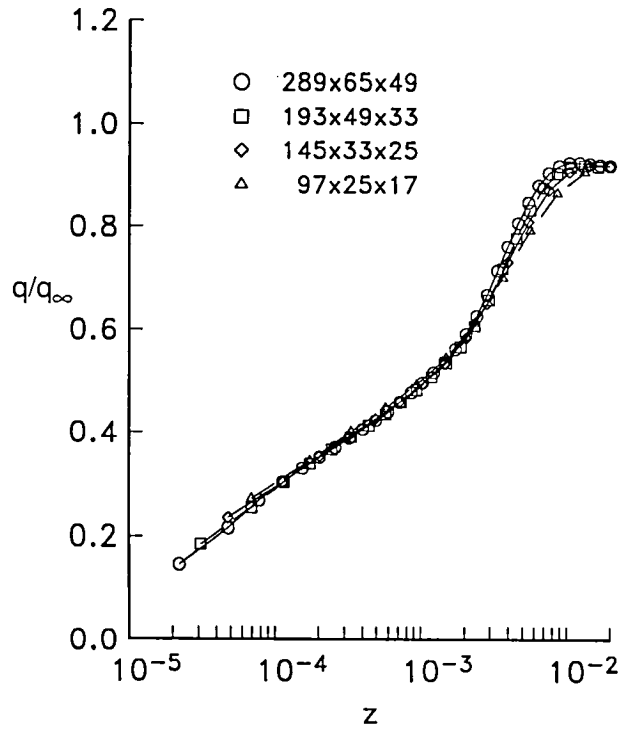

(c) TLNS3D—semilog.

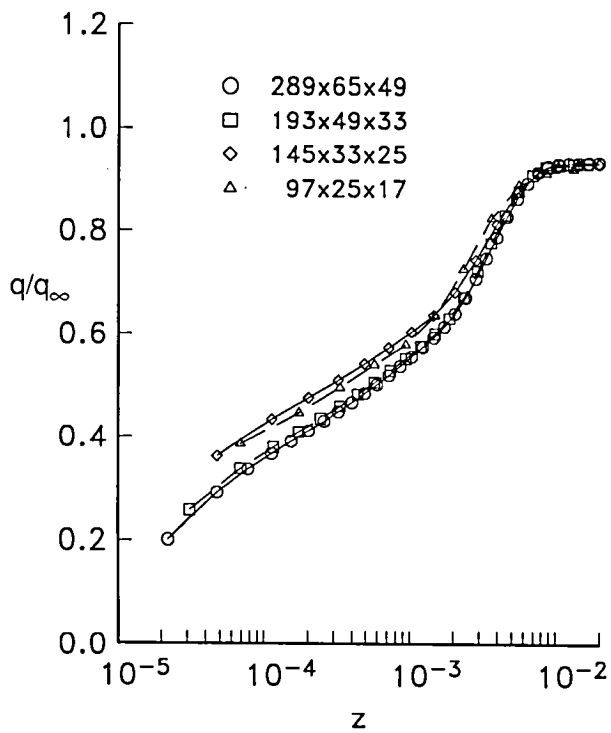

(d) CFL3D—semilog.

Figure 18. Effect of grid refinement on the upper-surface boundary-layer profiles for the ONERA M6 wing. $\eta = 0; \xi = 0.75$.

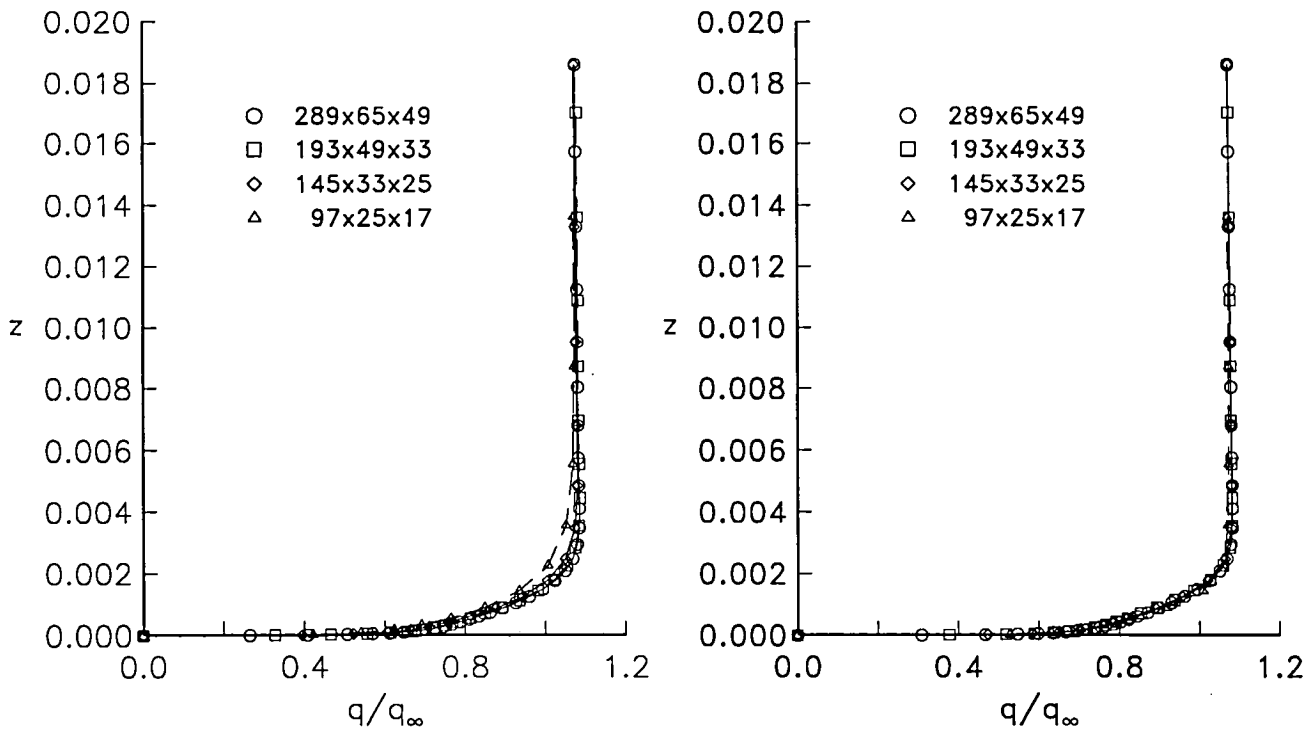

(a) TLNS3D—standard.

(b) CFL3D—standard.

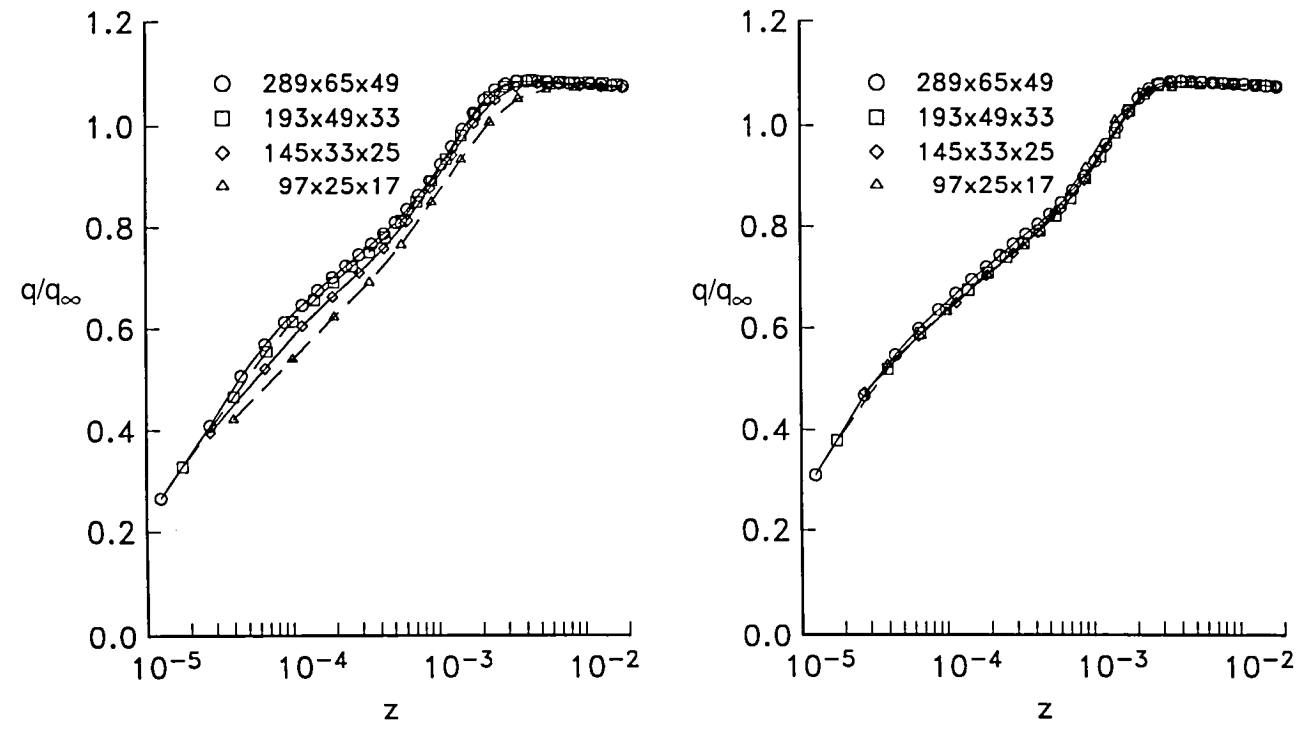

(c) TLNS3D—semilog.

(d) CFL3D—semilog.

Figure 19. Effect of grid refinement on the upper-surface boundary-layer profiles for the ONERA M6 wing. $\eta = 0.5; \xi = 0.25$.

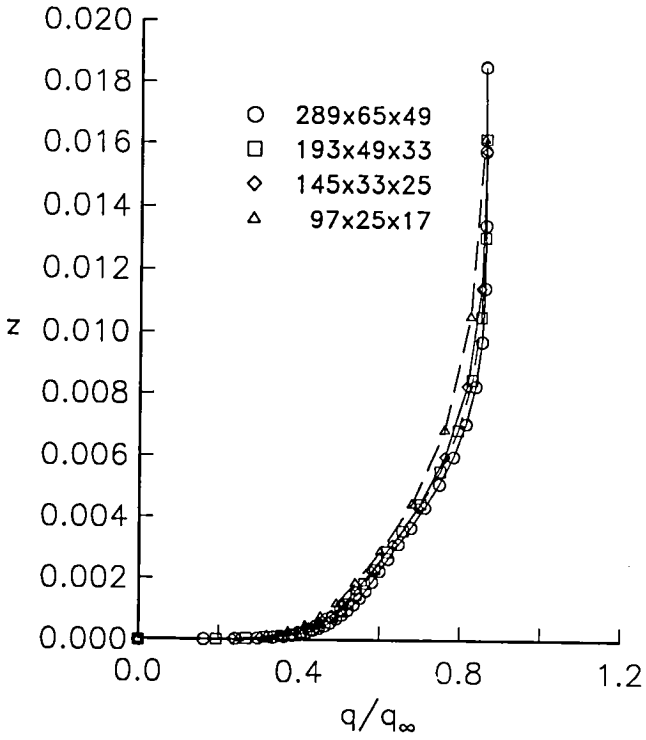

(a) TLNS3D—standard.

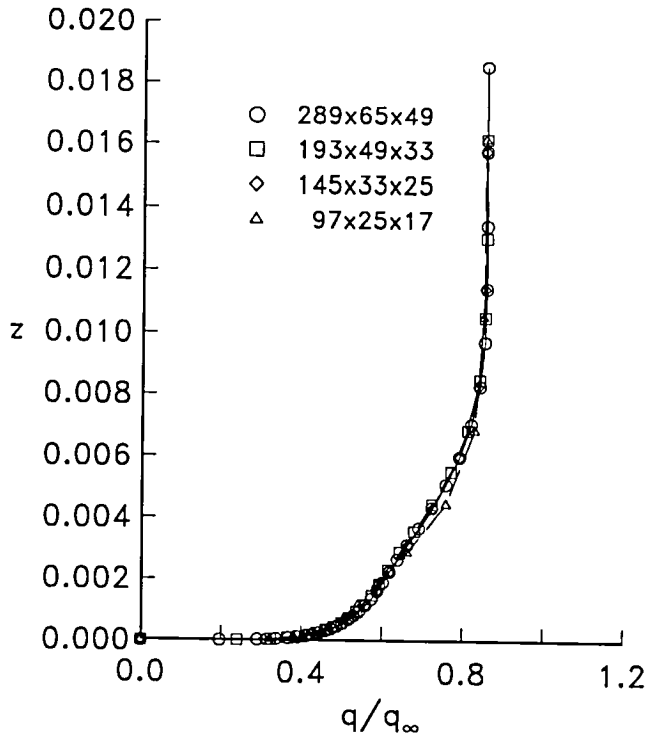

(b) CFL3D—standard.

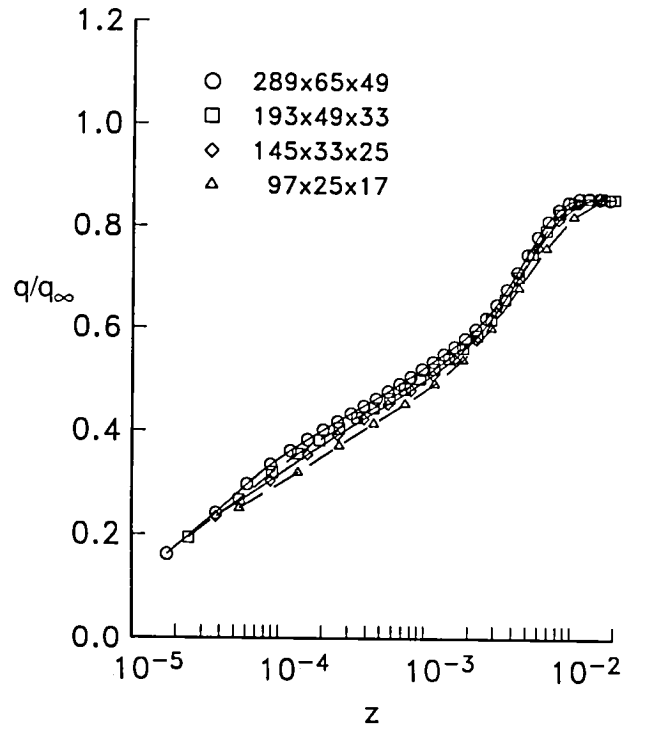

(c) TLNS3D—semilog.

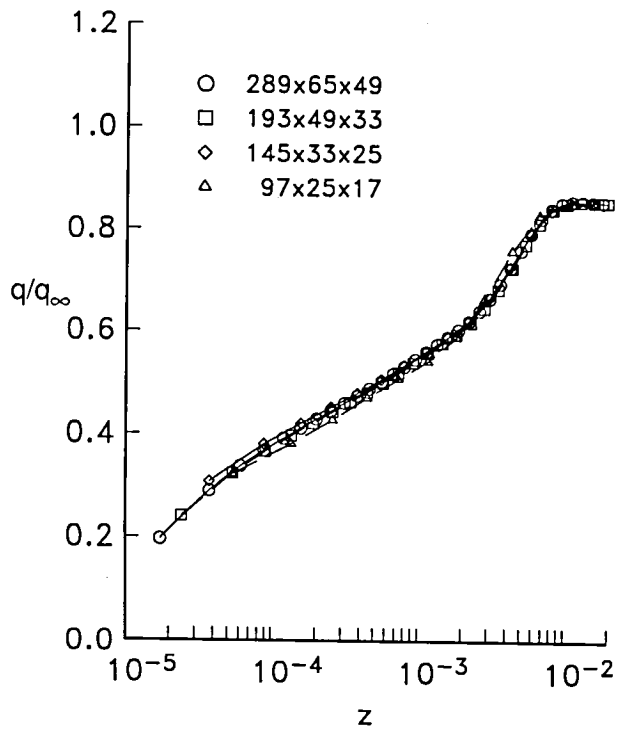

(d) CFL3D—semilog.

Figure 20. Effect of grid refinement on the upper-surface boundary-layer profiles for the ONERA M6 wing. $\eta = 0.5; \xi = 0.75$.

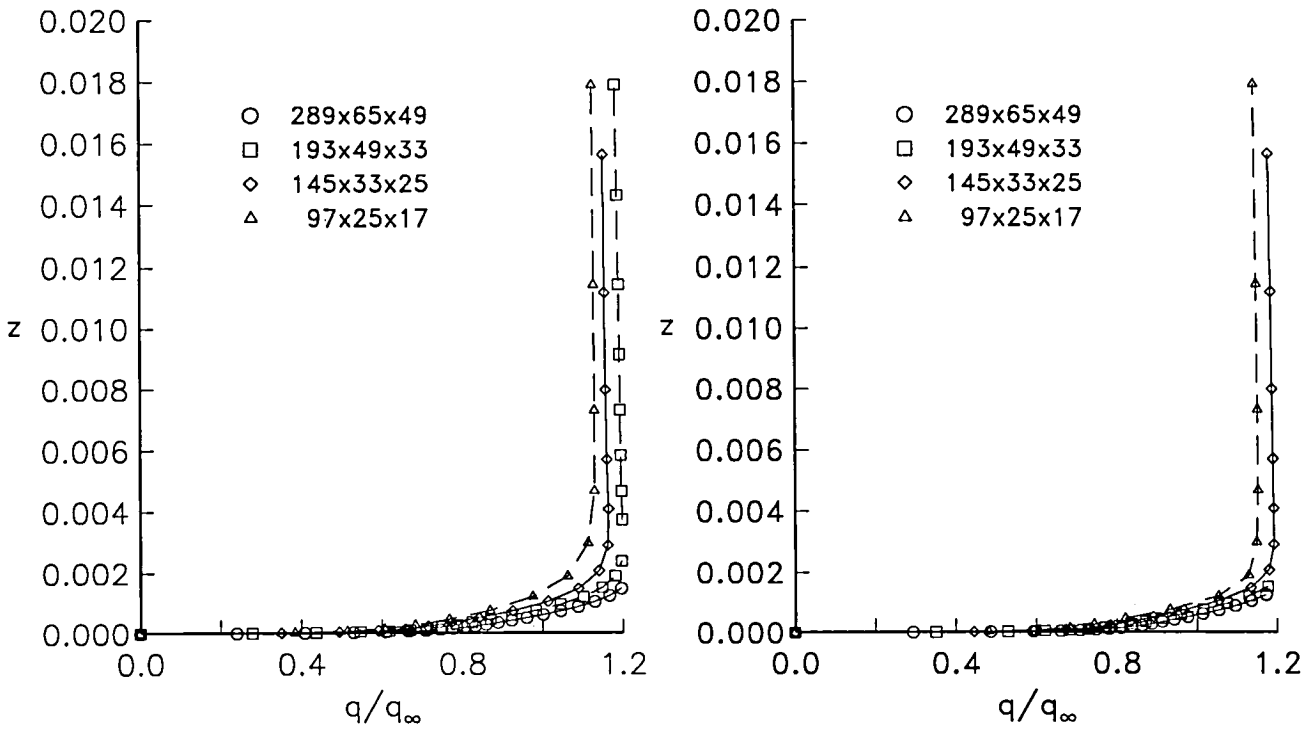

(a) TLNS3D—standard.

(b) CFL3D—standard.

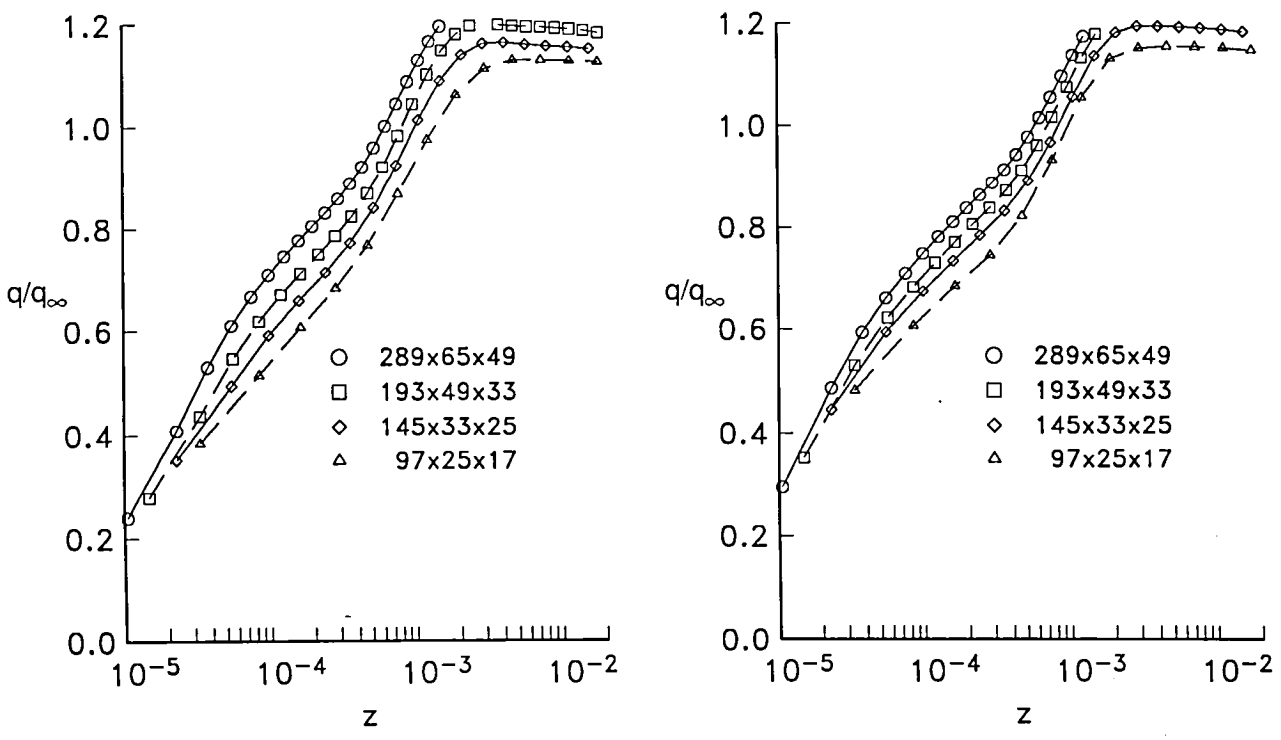

(c) TLNS3D—semilog.

(d) CFL3D—semilog.

Figure 21. Effect of grid refinement on the upper-surface boundary-layer profiles for the ONERA M6 wing. $\eta = 0.8; \xi = 0.25$.

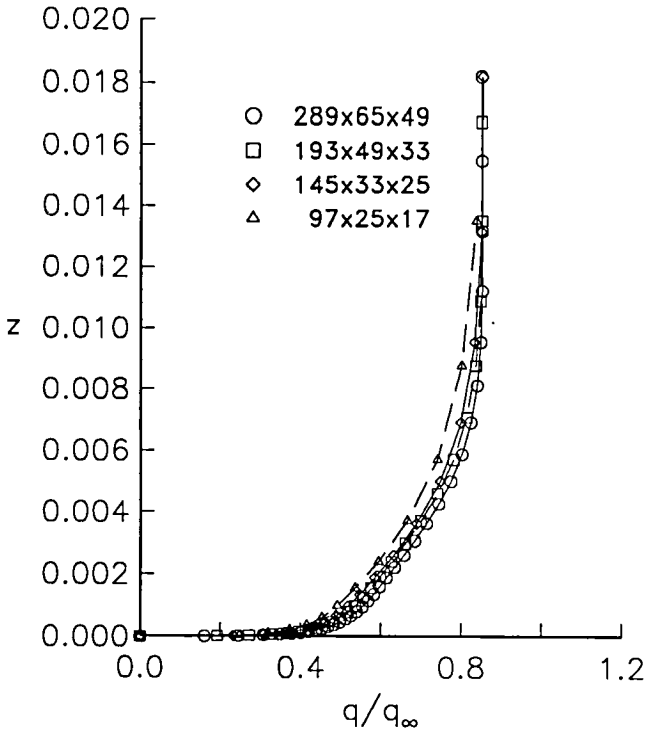

(a) TLNS3D—standard.

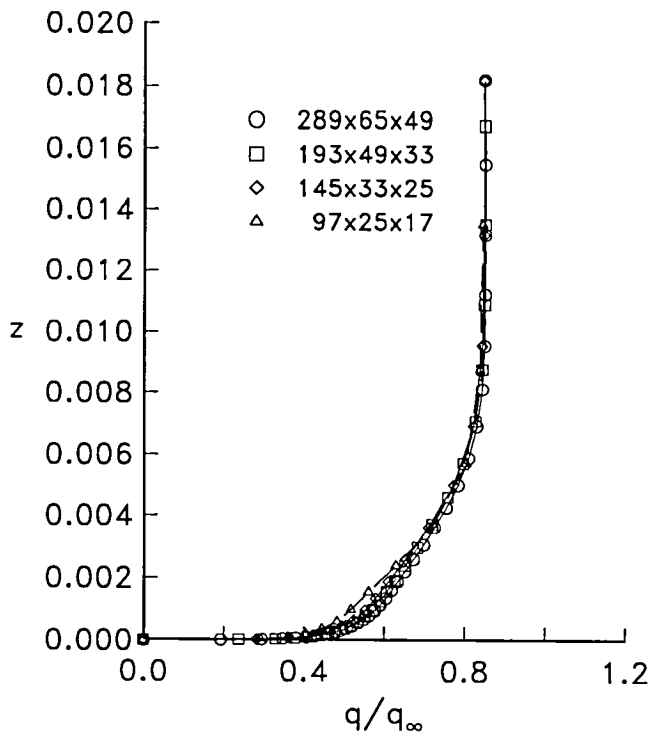

(b) CFL3D—standard.

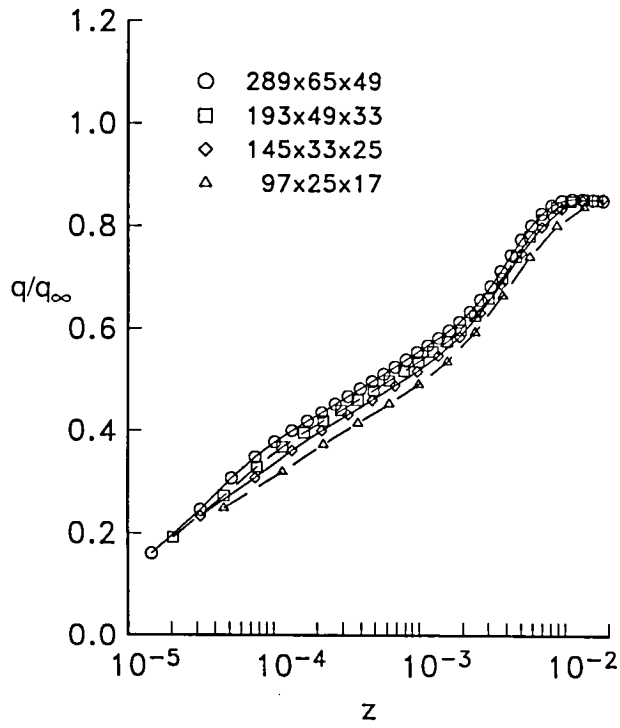

(c) TLNS3D—semilog.

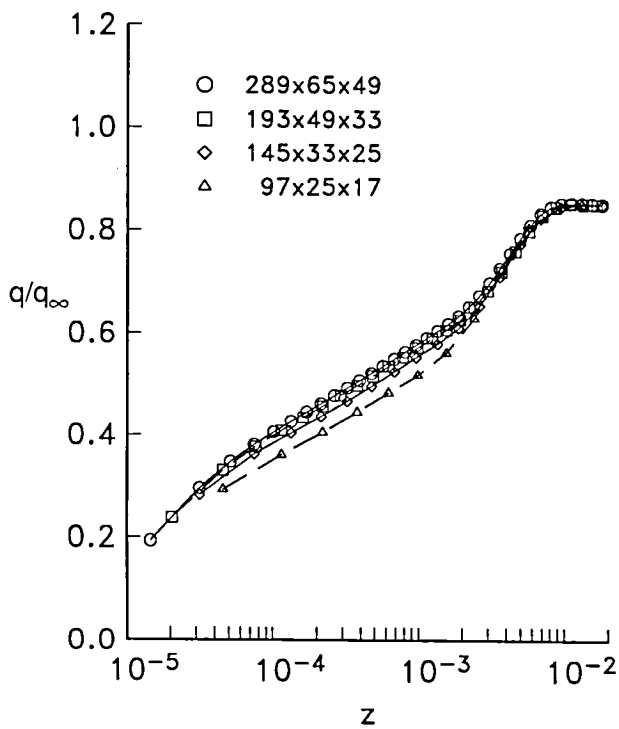

(d) CFL3D—semilog.

Figure 22. Effect of grid refinement on the upper-surface boundary-layer profiles for the ONERA M6 wing. $\eta = 0.8; \xi = 0.75$.

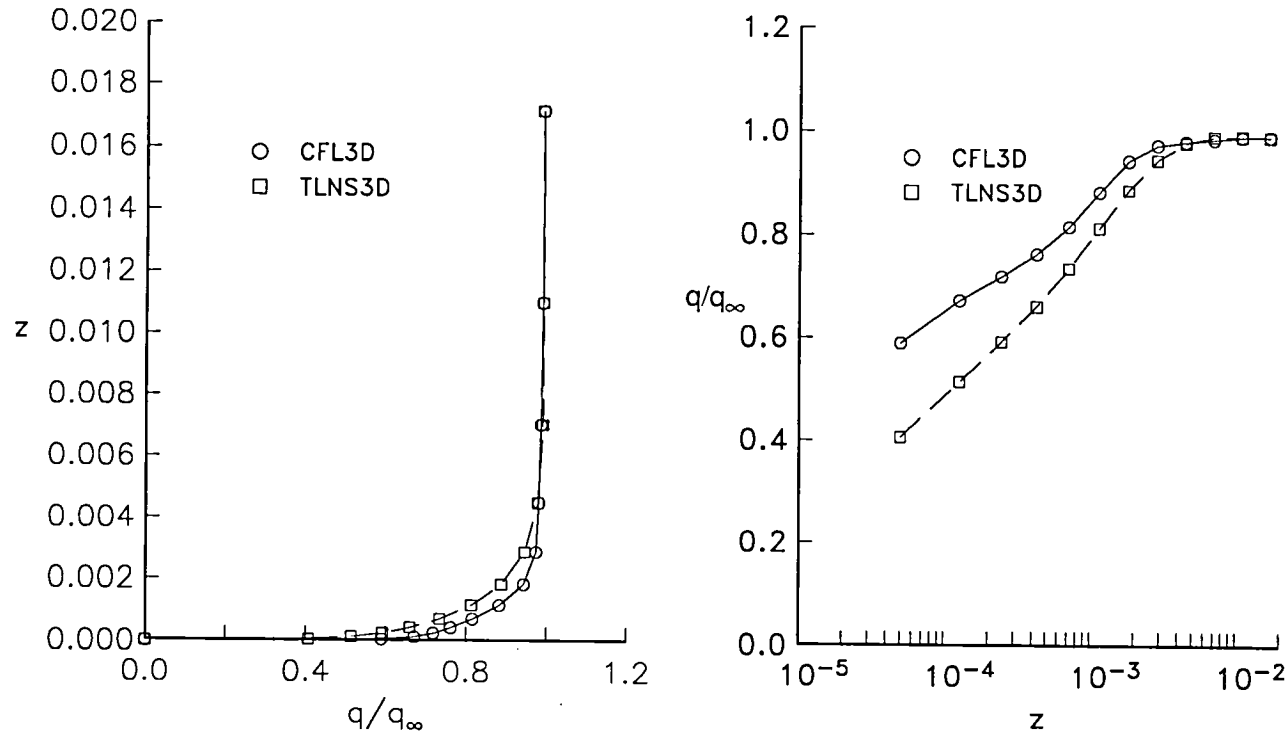

(a) $\eta = 0, \xi = 0.25$.

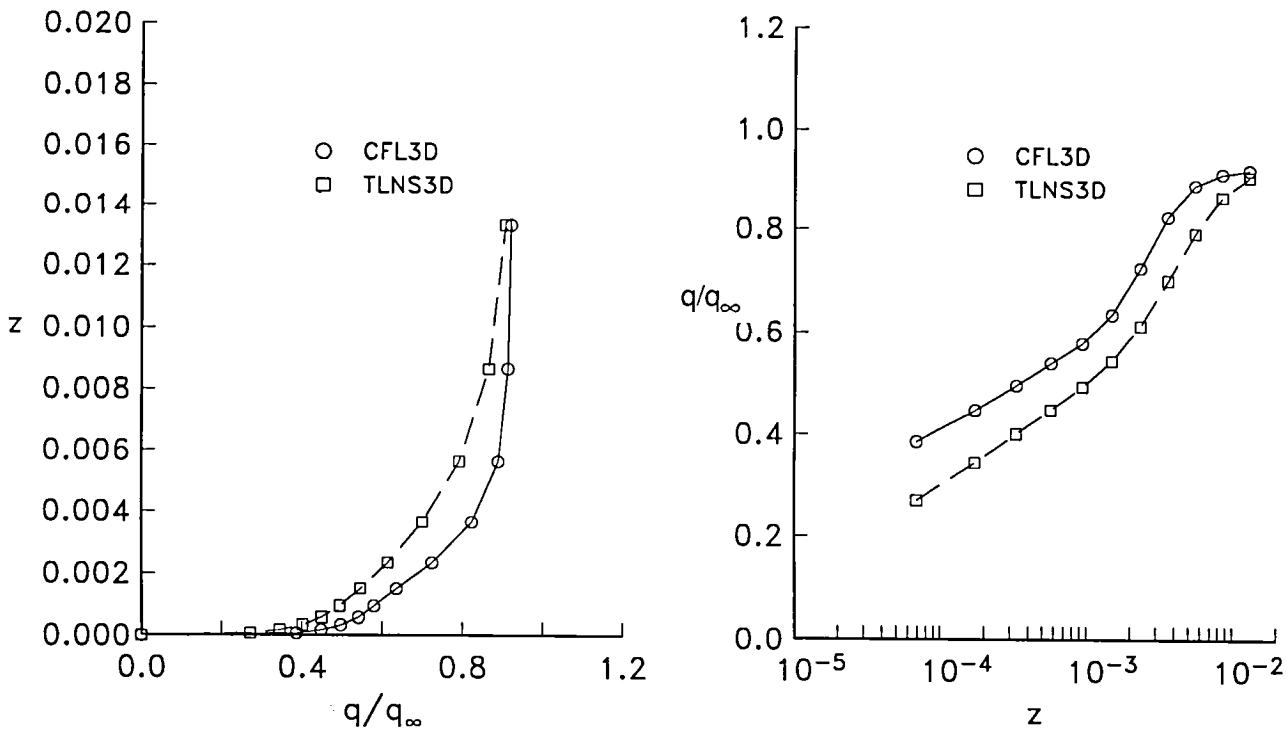

(b) $\eta = 0, \xi = 0.75$.

Figure 23. Upper-surface boundary-layer profiles for the ONERA M6 wing. $97 \times 25 \times 17$ grid.

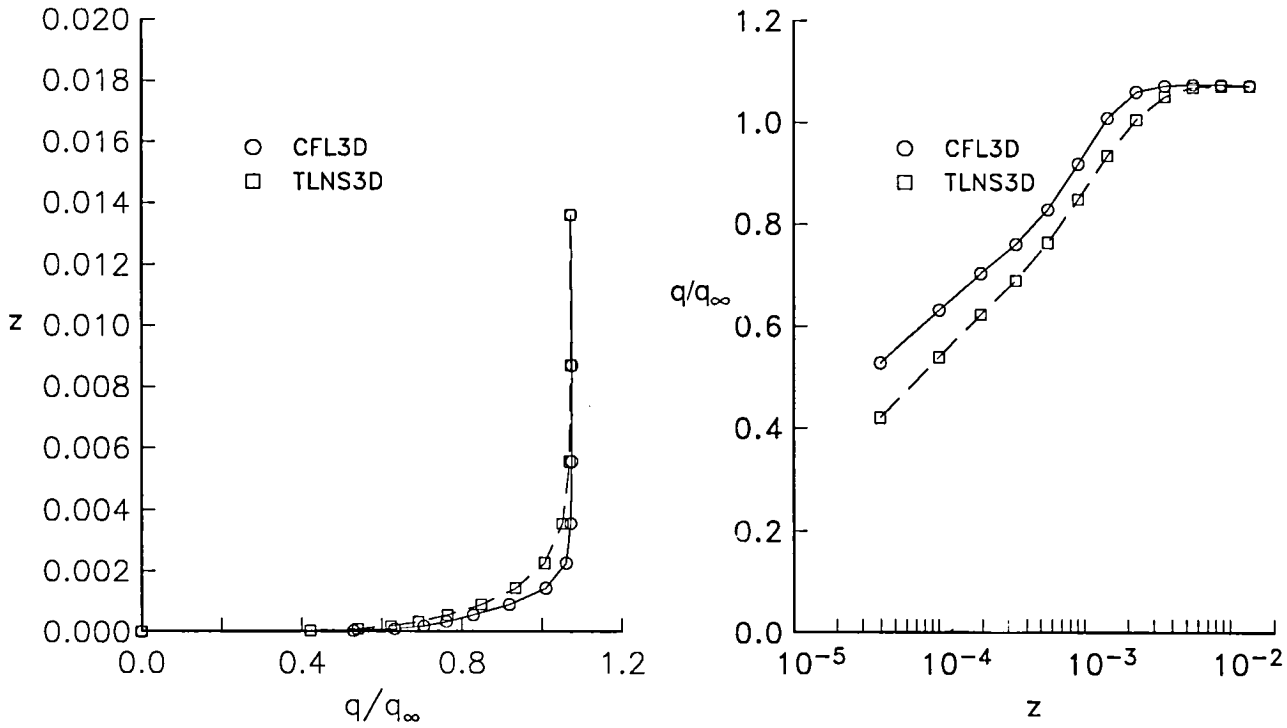

(c) $\eta = 0, \xi = 0.25$.

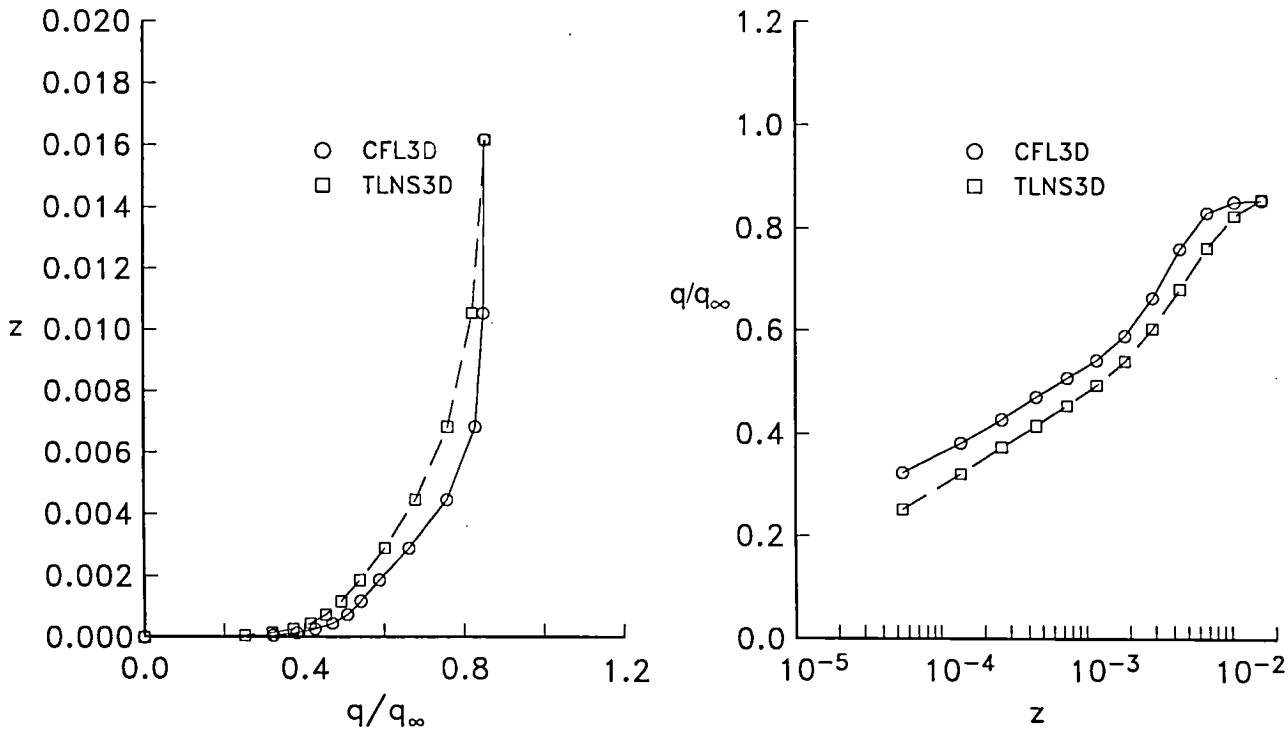

(d) $\eta = 0.5, \xi = 0.75$.

Figure 23. Continued.

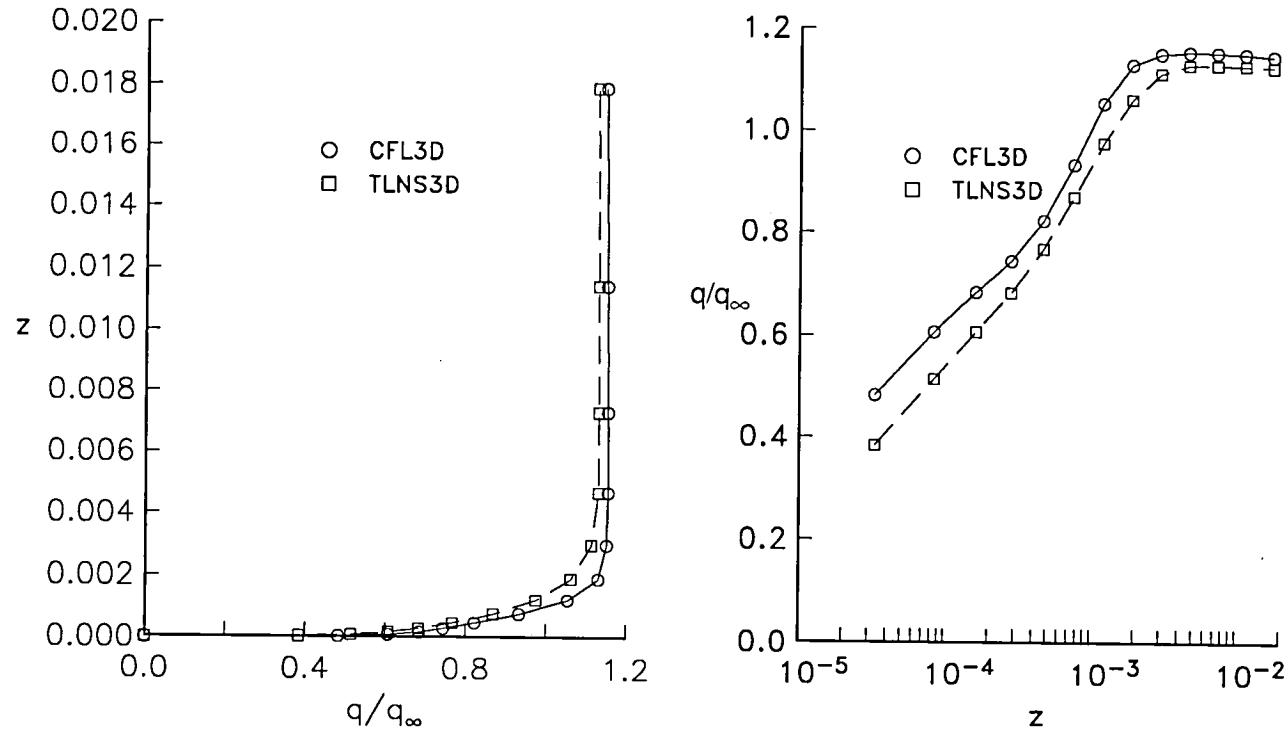

(e) $\eta = 0.8, \xi = 0.25$.

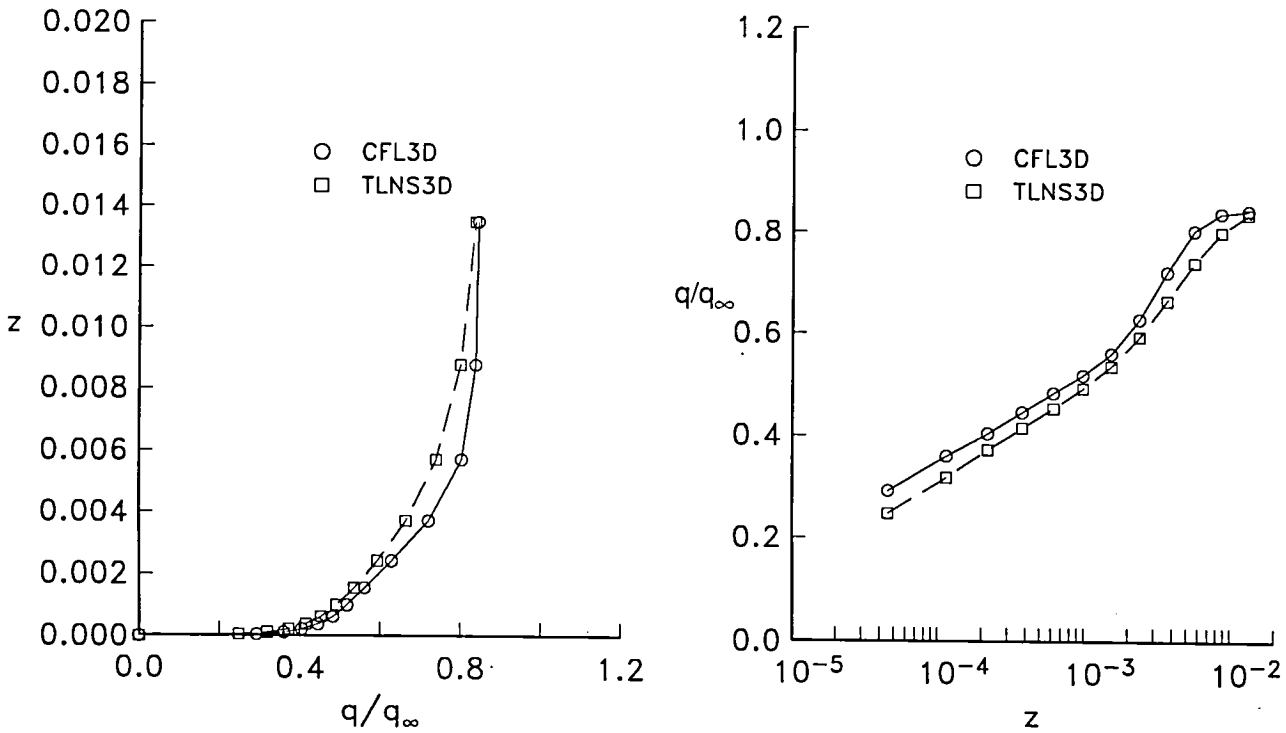

(f) $\eta = 0.8, \xi = 0.75$.

Figure 23. Concluded.

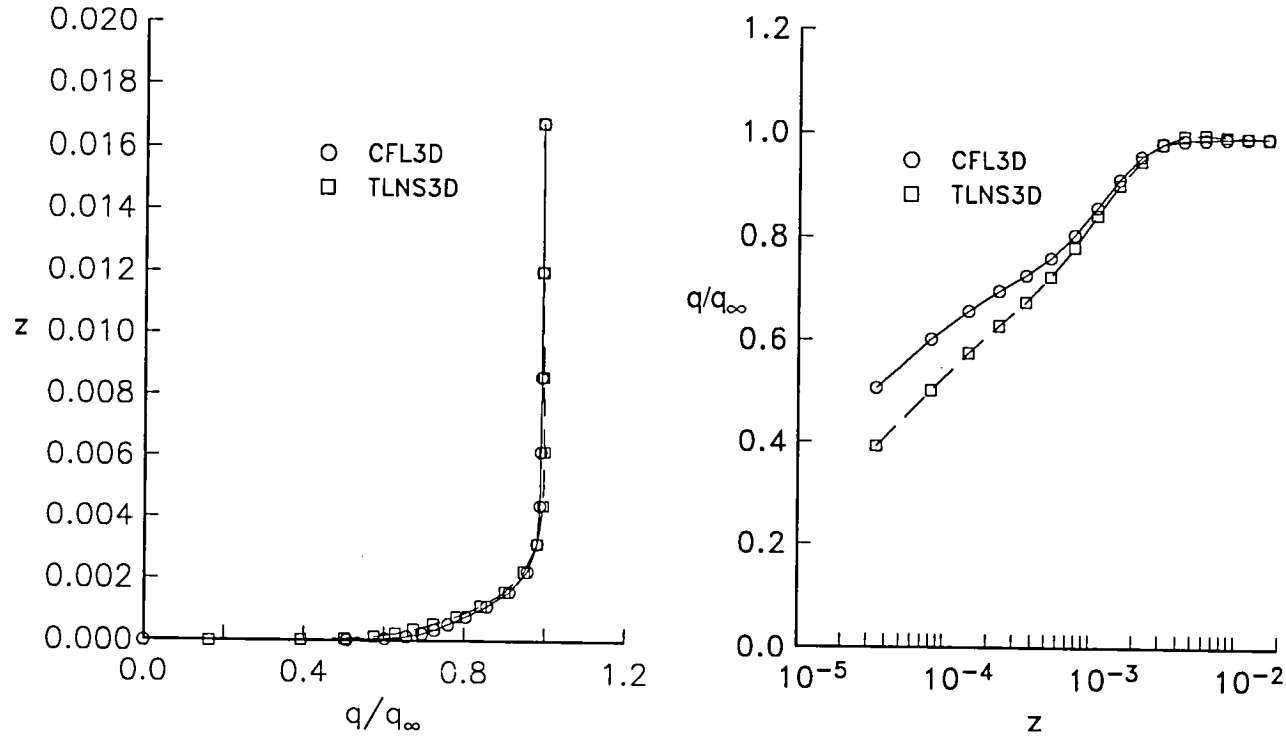

(a) $\eta = 0, \xi = 0.25$.

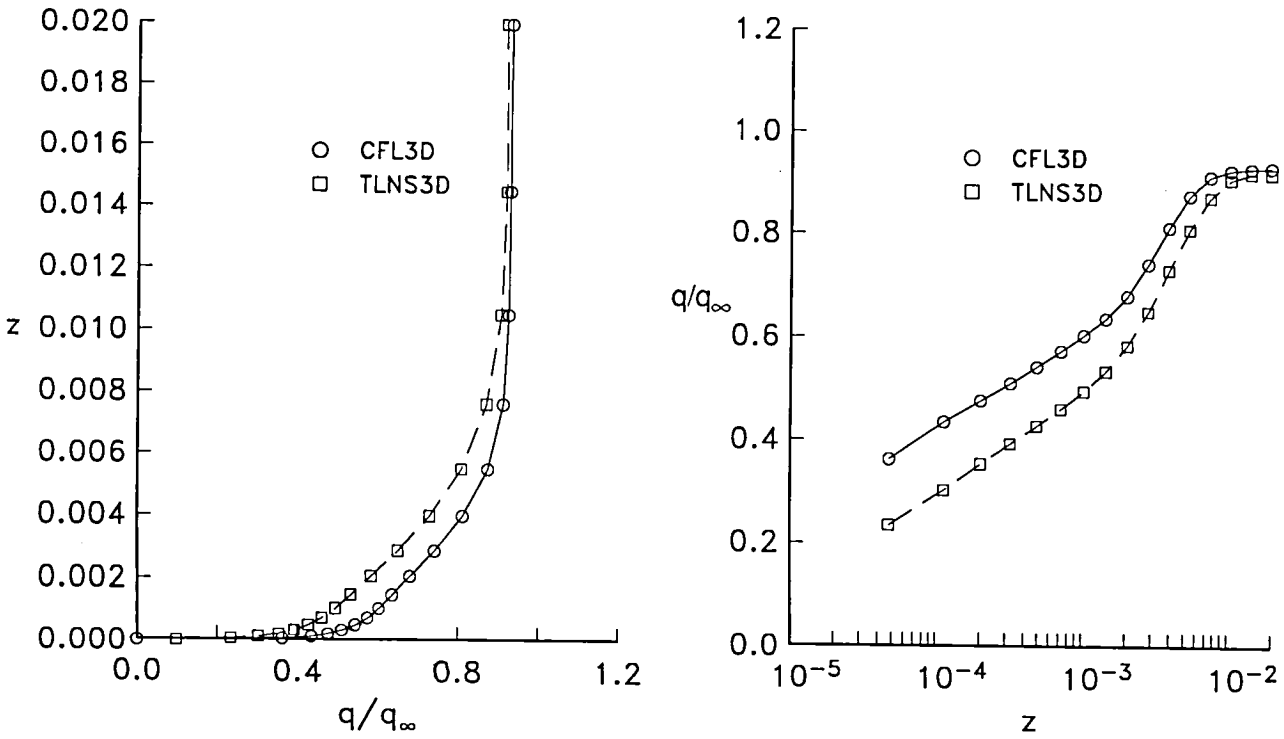

(b) $\eta = 0, \xi = 0.75$.

Figure 24. Upper-surface boundary-layer profiles for the ONERA M6 wing. $145 \times 33 \times 25$ grid.

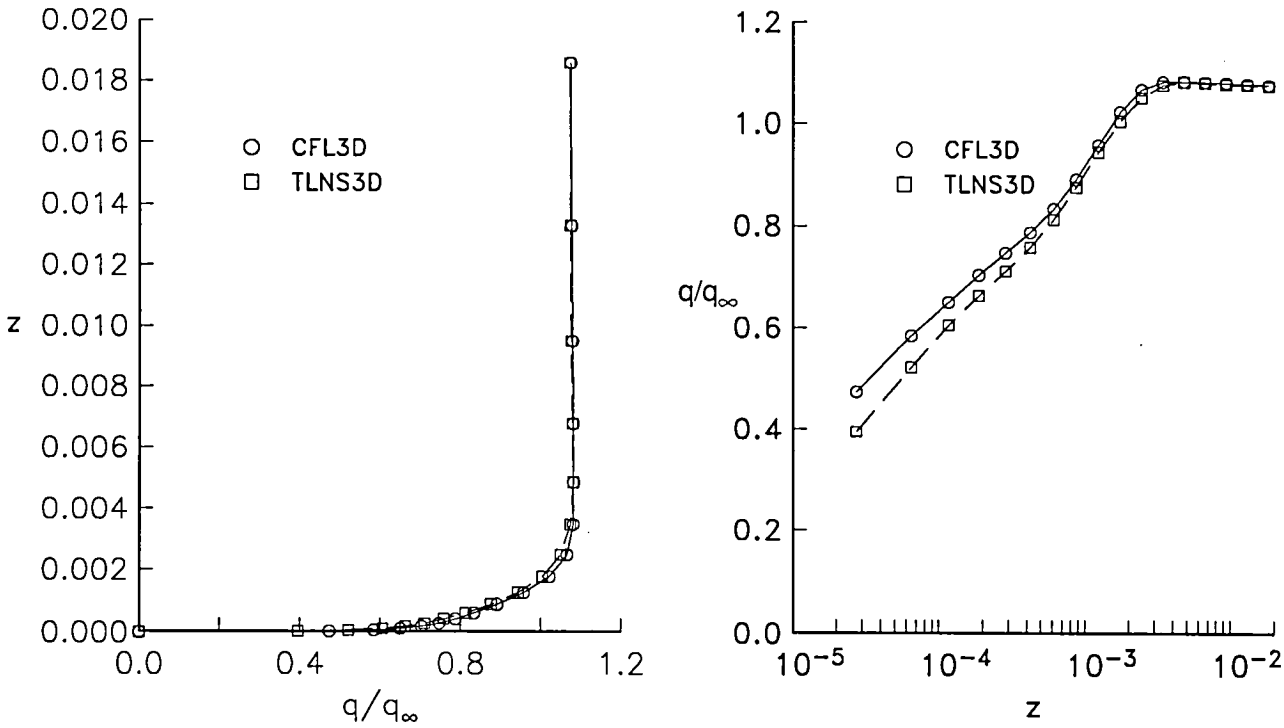

(c) $\eta = 0.5, \xi = 0.25$.

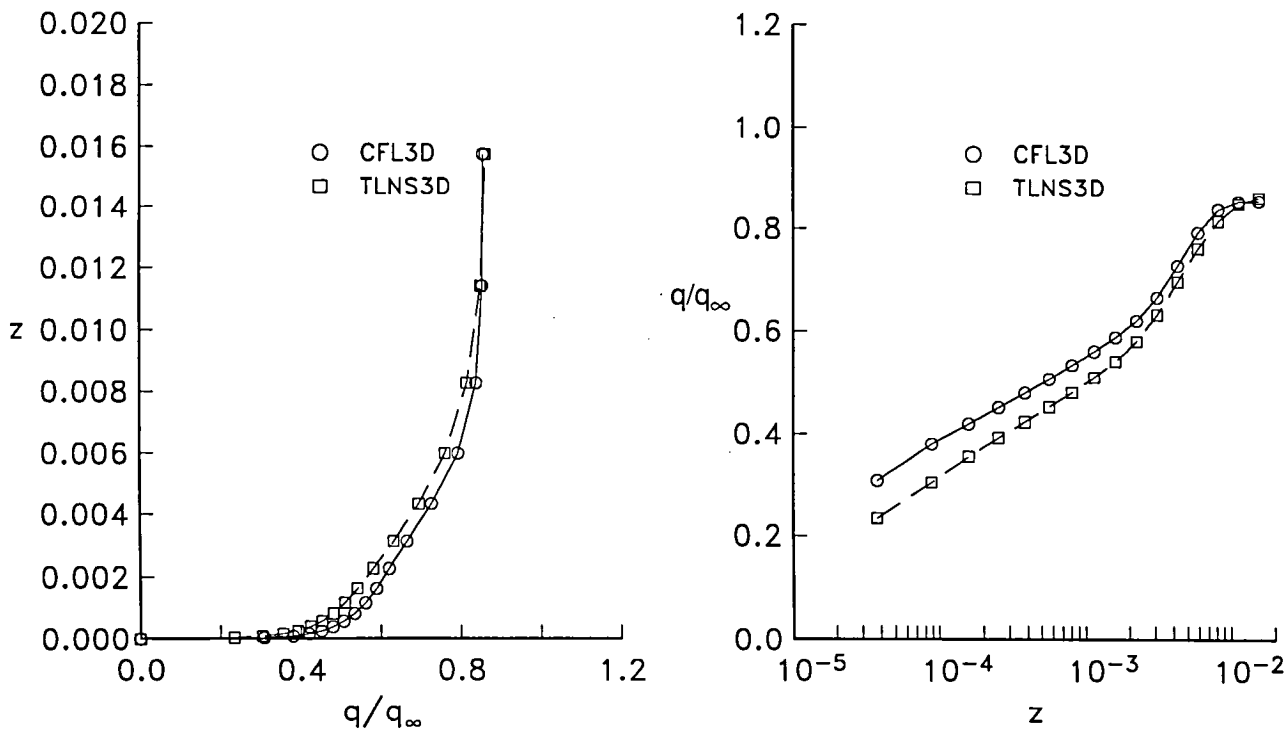

(d) $\eta = 0.5, \xi = 0.75$.

Figure 24. Continued.

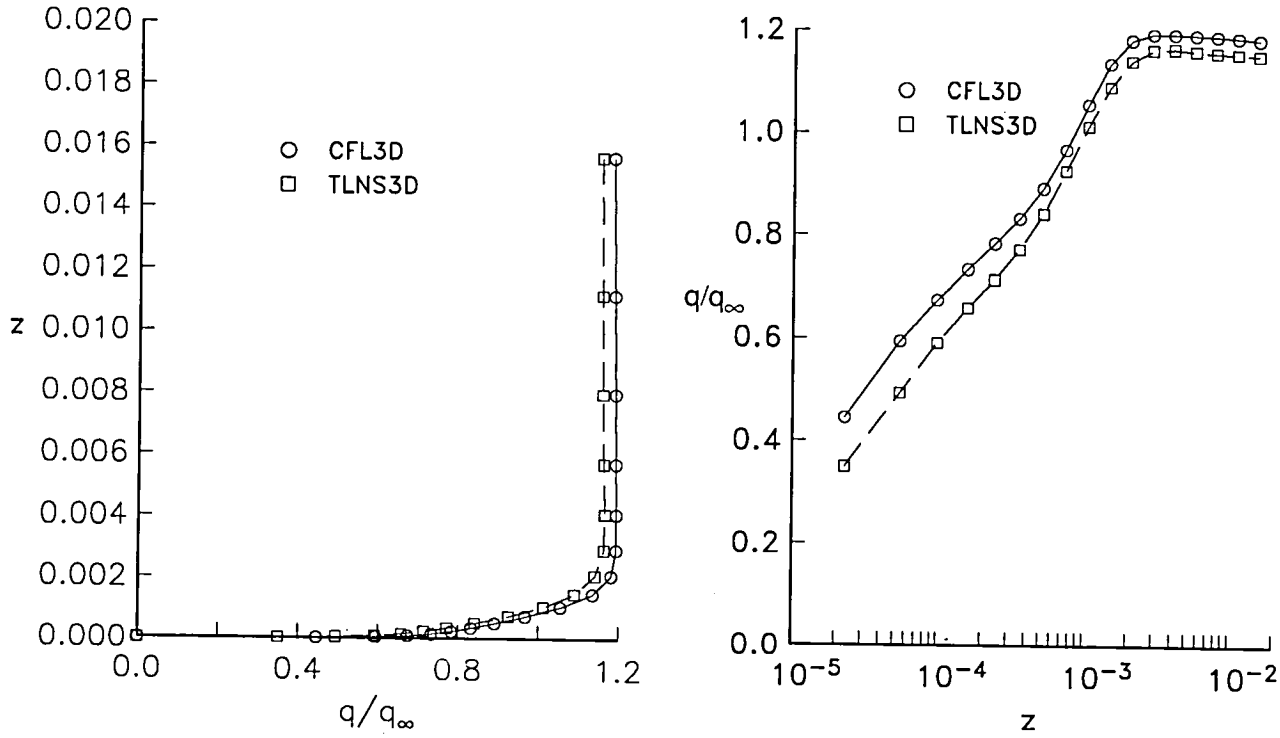

(e) $\eta = 0.8, \xi = 0.25$.

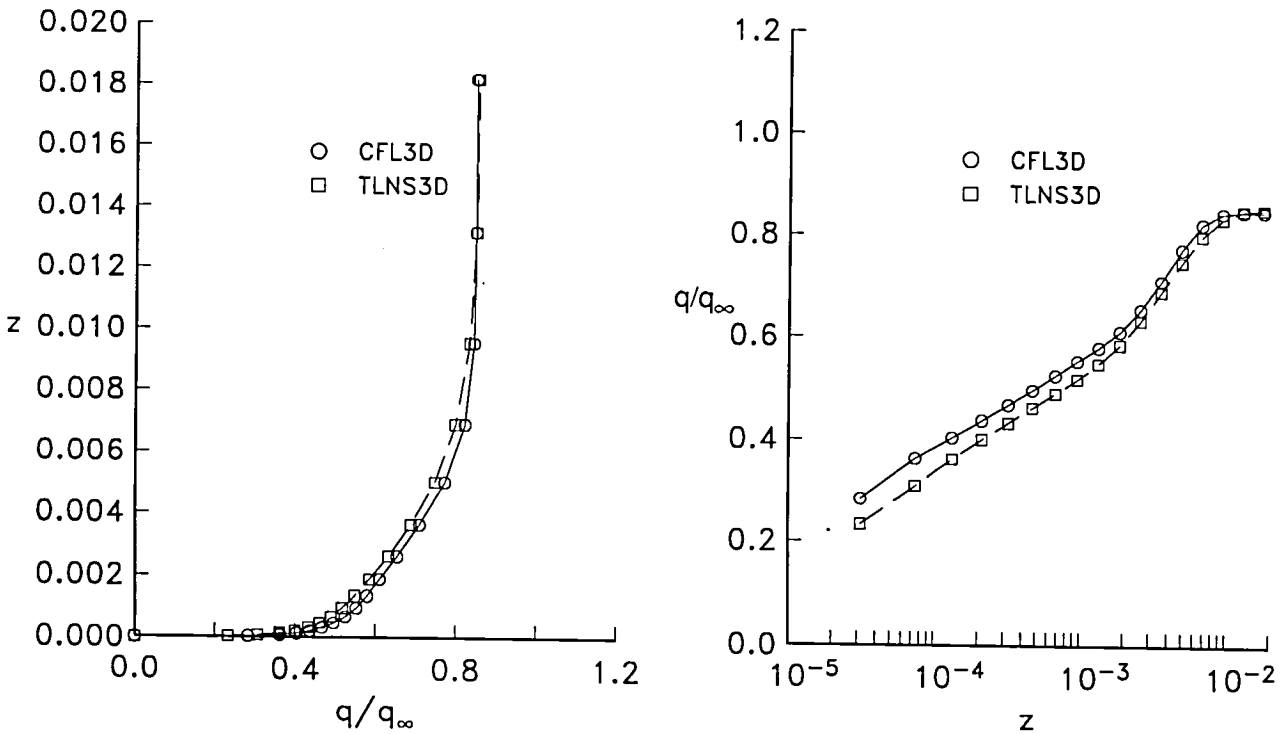

(f) $\eta = 0.8, \xi = 0.75$.

Figure 24. Concluded.

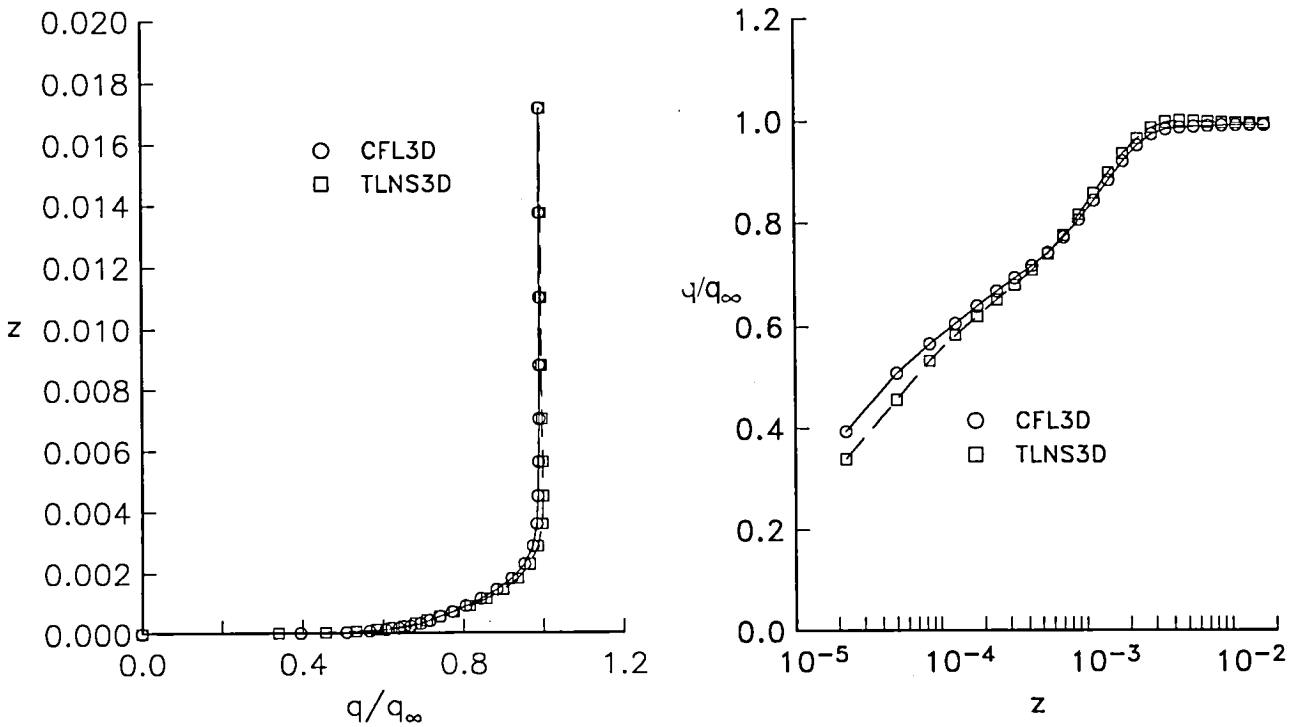

(a) $\eta = 0, \xi = 0.25$.

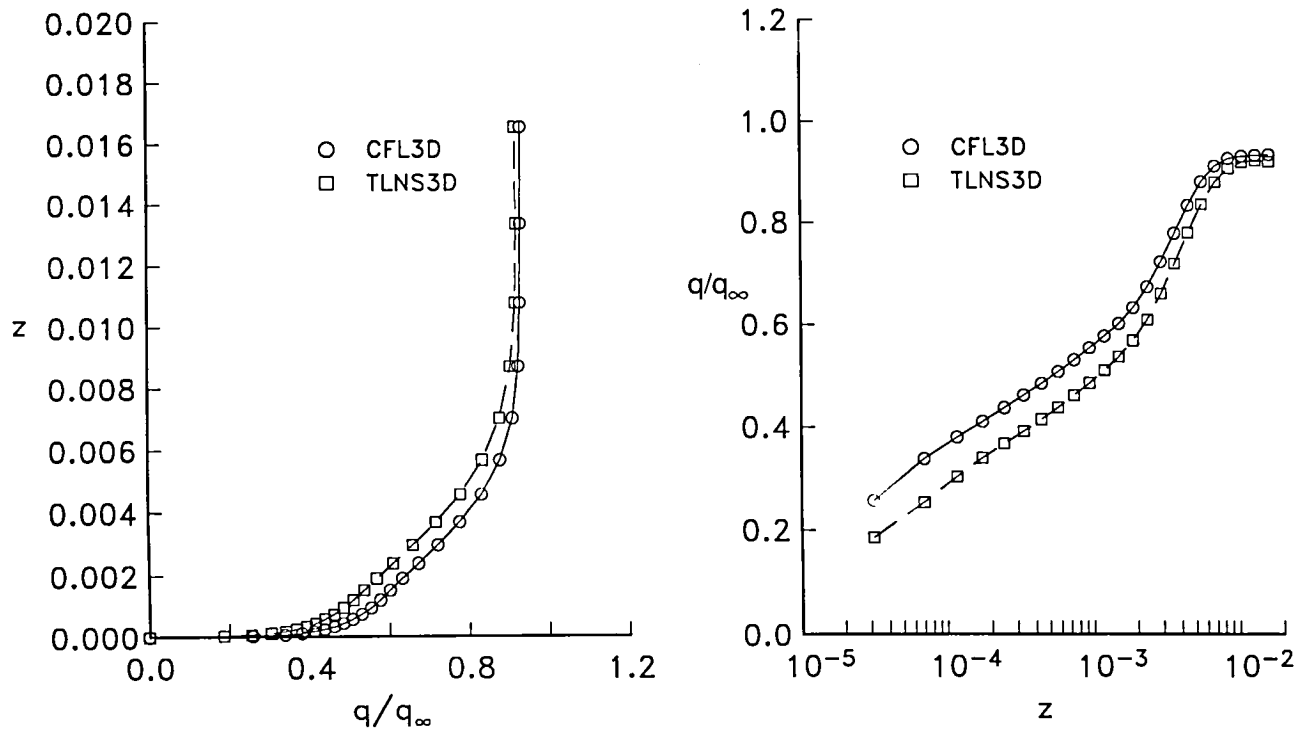

(b) $\eta = 0, \xi = 0.75$.

Figure 25. Upper-surface boundary-layer profiles for the ONERA M6 wing. $193 \times 49 \times 33$ grid.

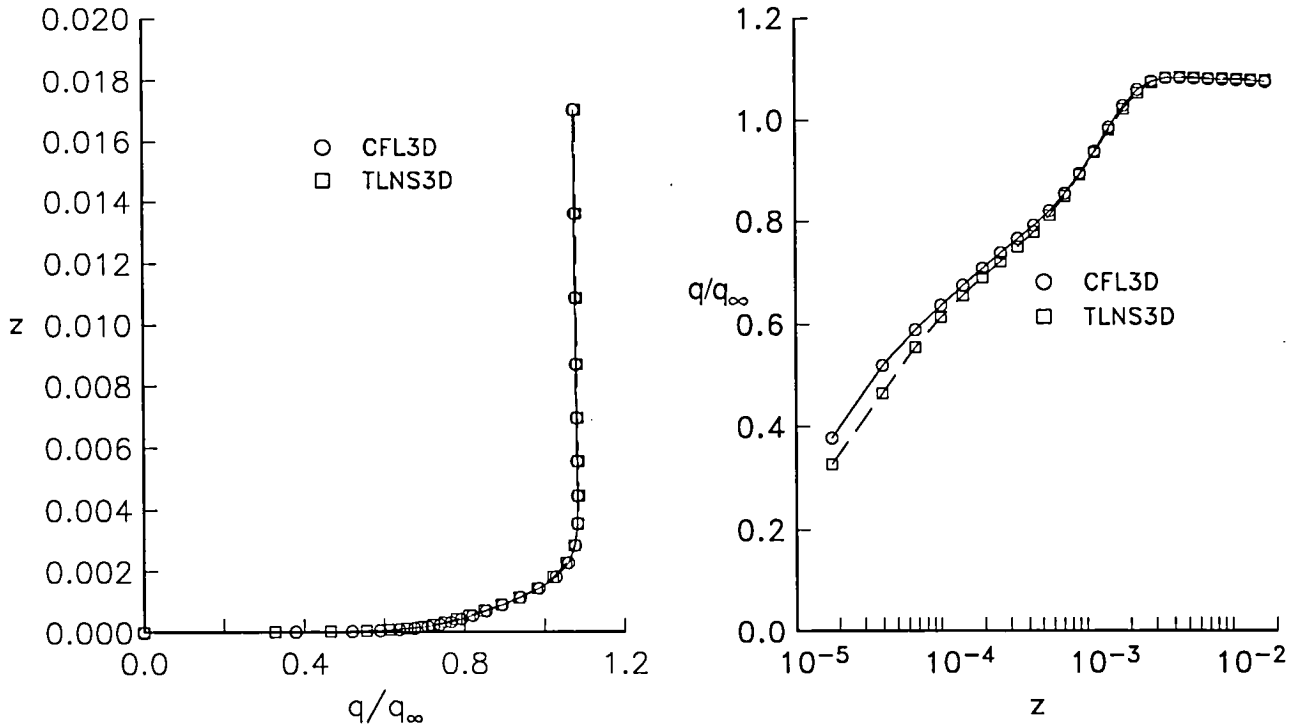

(c) $\eta = 0.5, \xi = 0.25$.

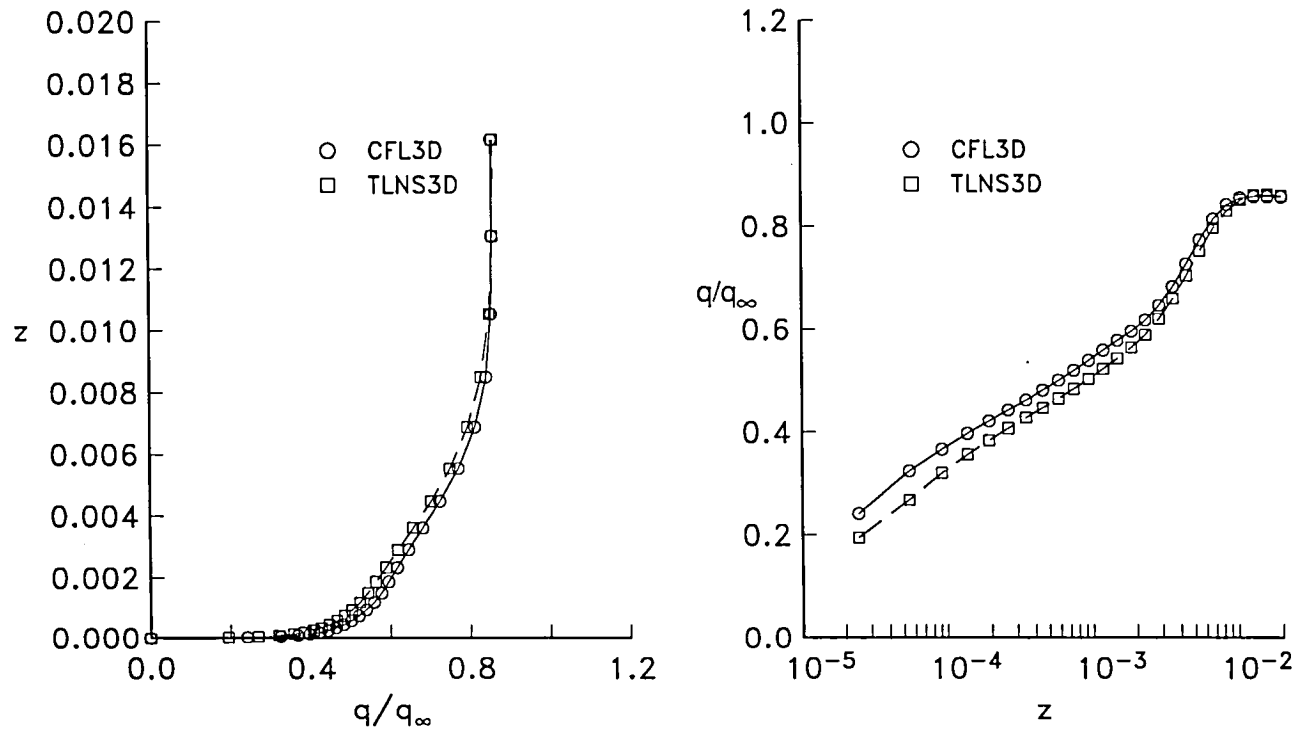

(d) $\eta = 0.5, \xi = 0.75$.

Figure 25. Continued.

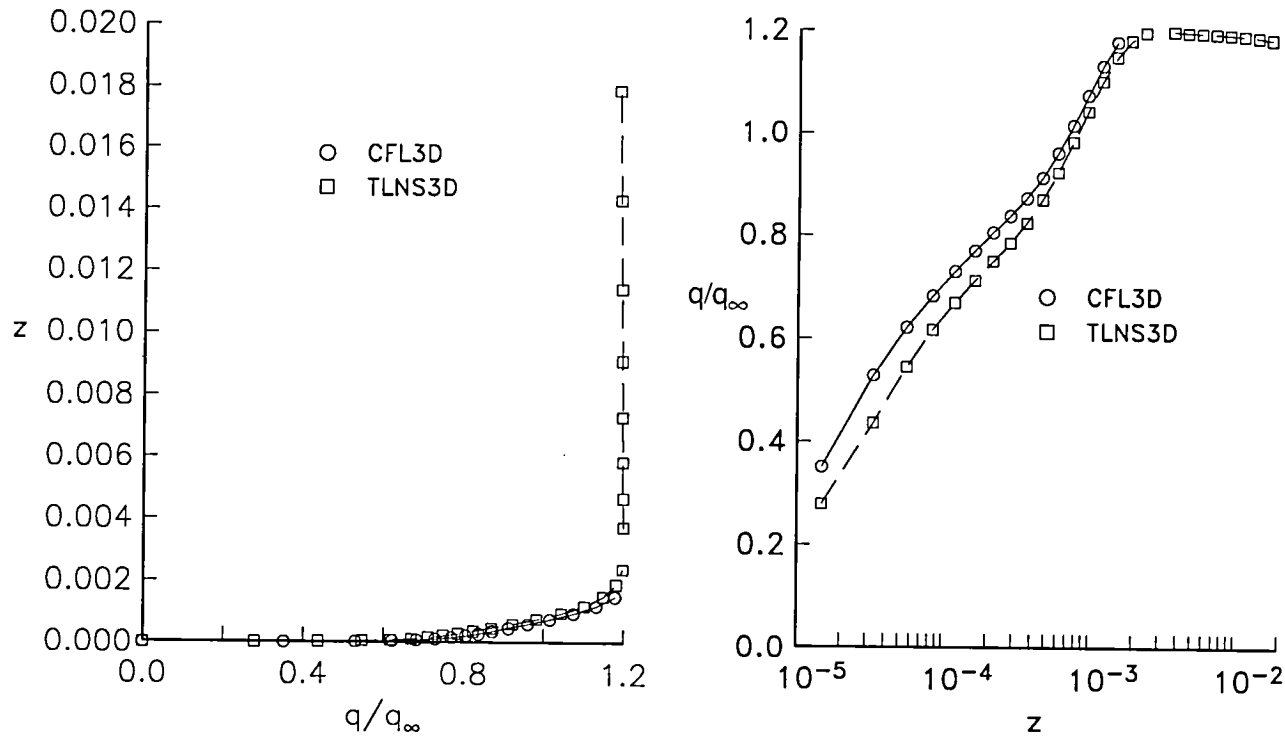

(e) $\eta = 0.8, \xi = 0.25$.

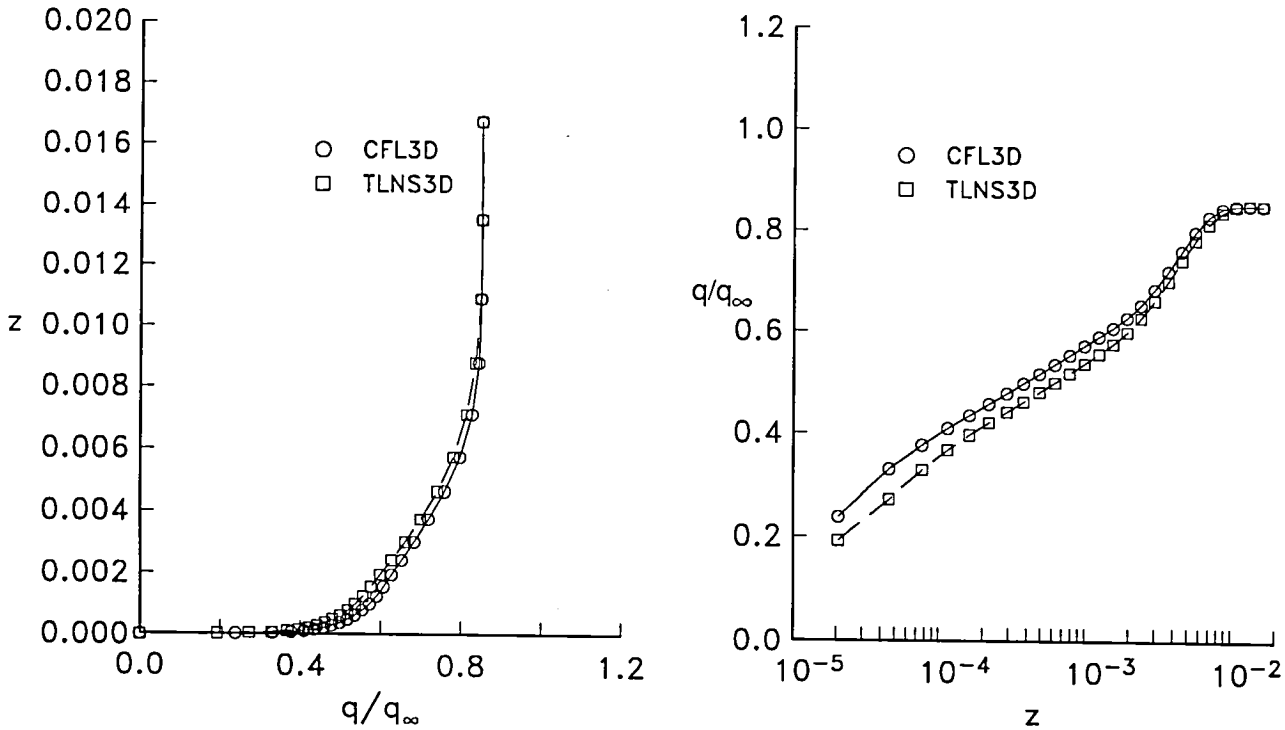

(f) $\eta = 0.8, \xi = 0.75$.

Figure 25. Concluded.

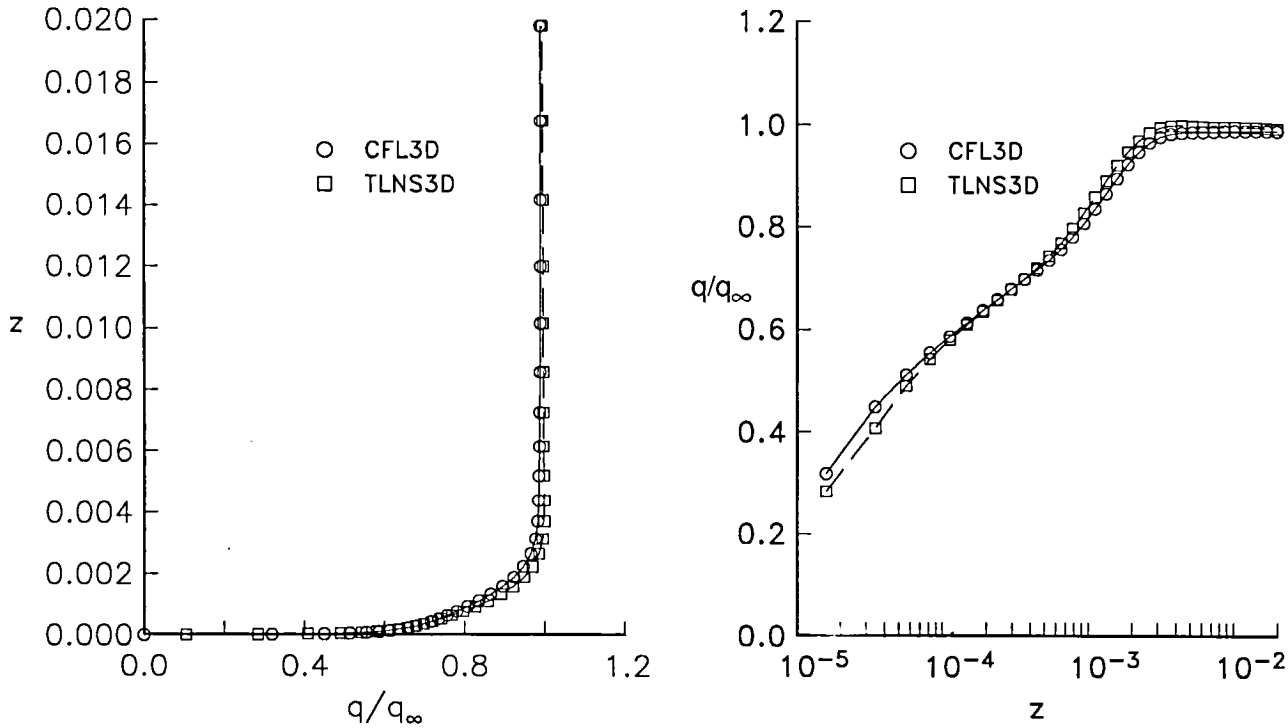

(a) $\eta = 0, \xi = 0.25$.

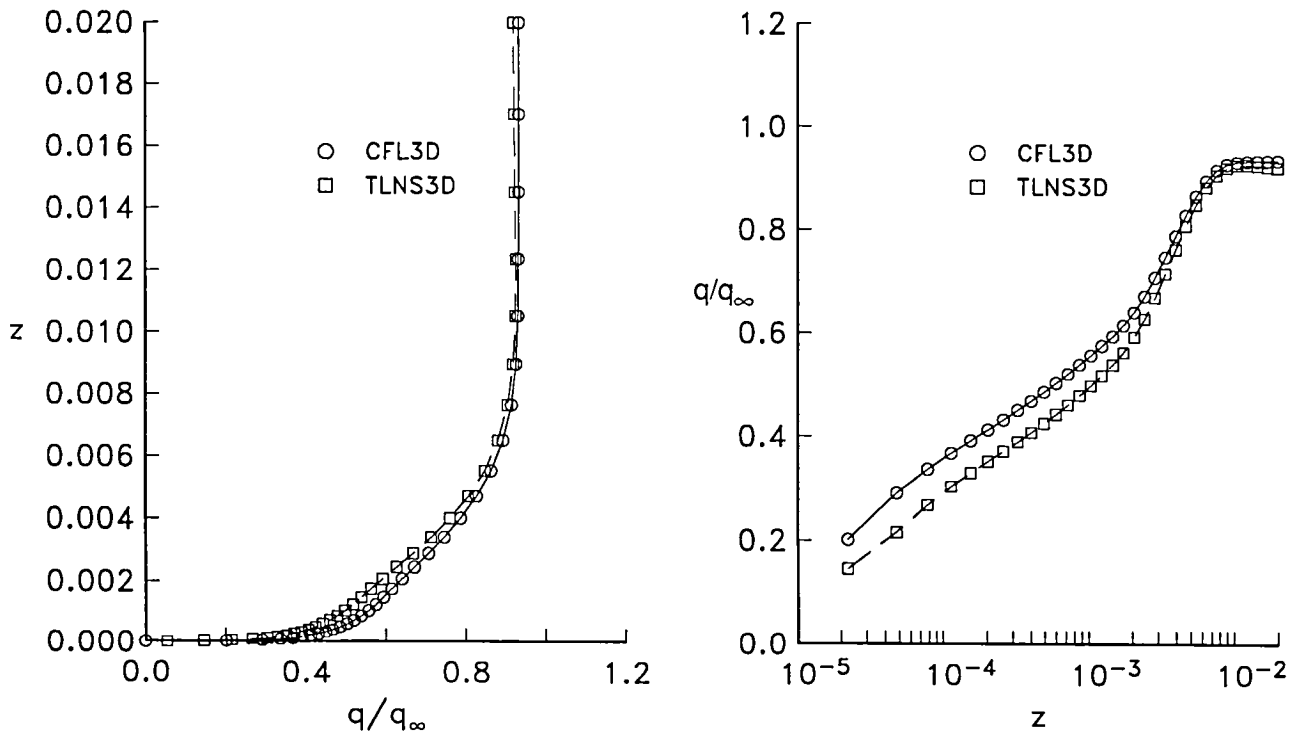

(b) $\eta = 0, \xi = 0.75$.

Figure 26. Upper-surface boundary-layer profiles for the ONERA M6 wing. $289 \times 65 \times 49$ grid.

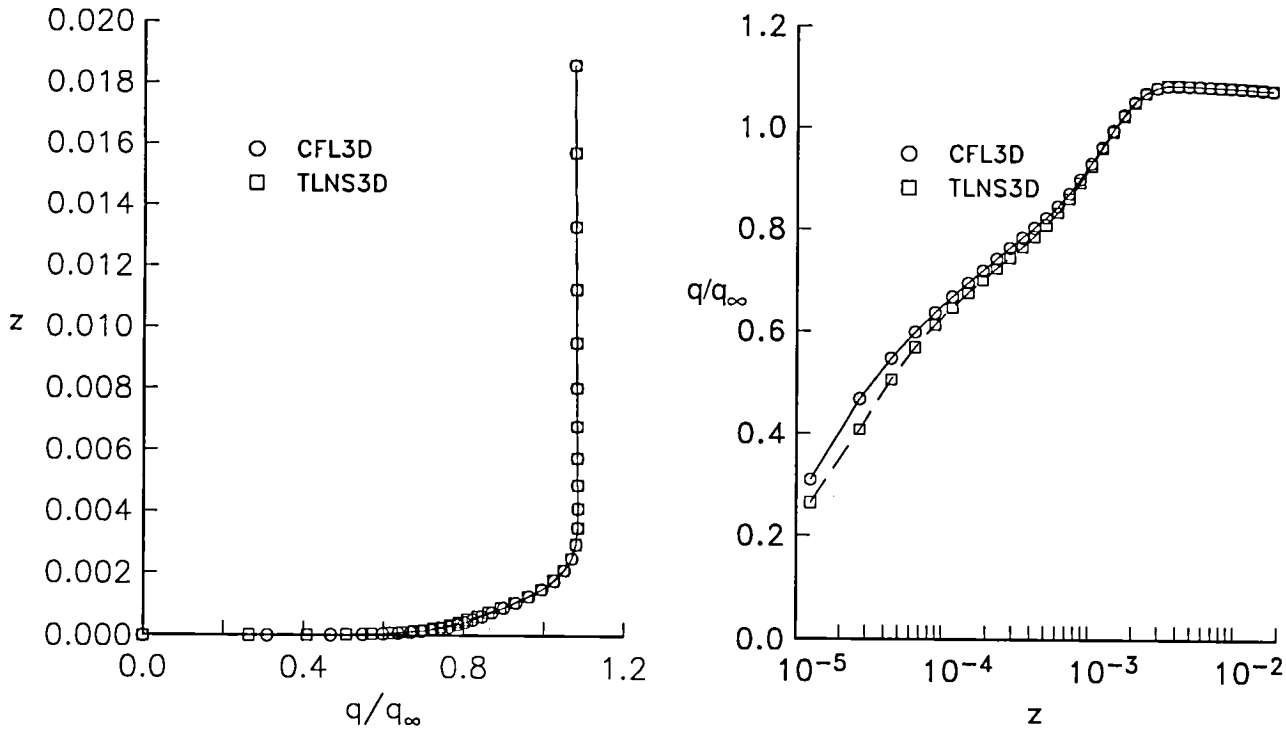

(c) $\eta = 0.5, \xi = 0.25$.

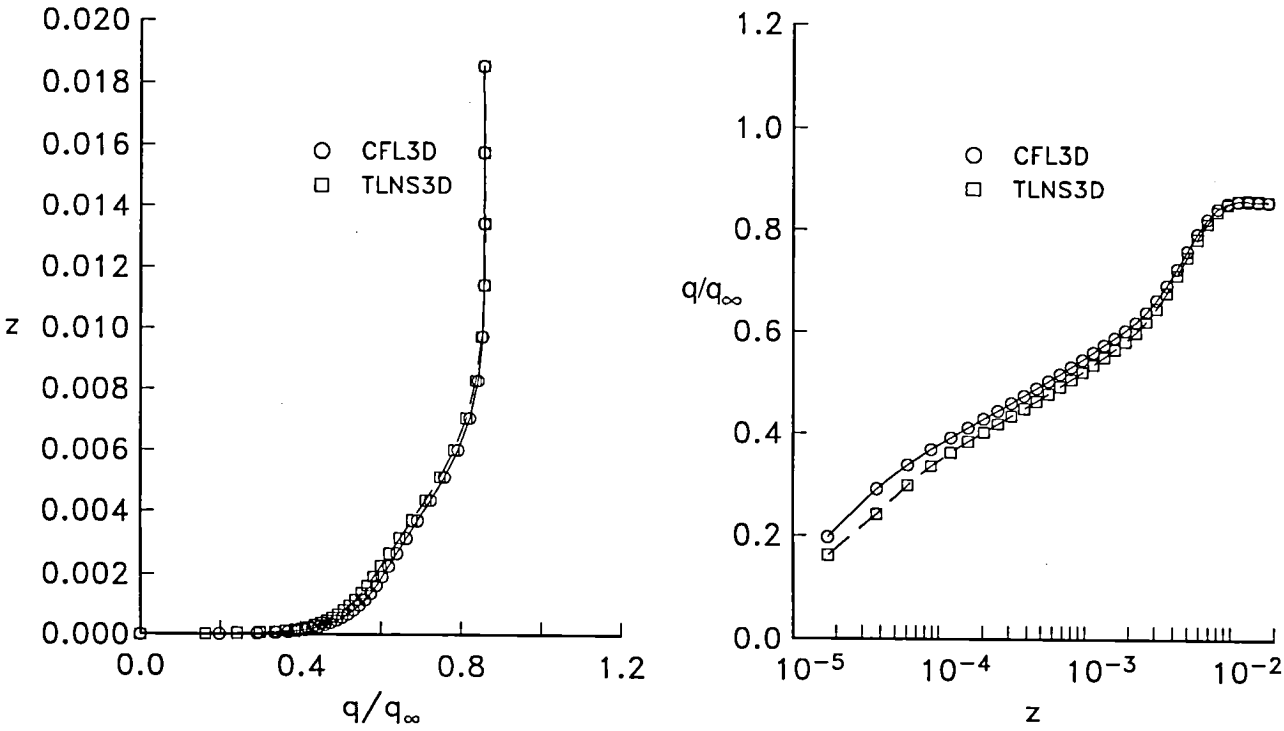

(d) $\eta = 0.5, \xi = 0.75$.

Figure 26. Continued.

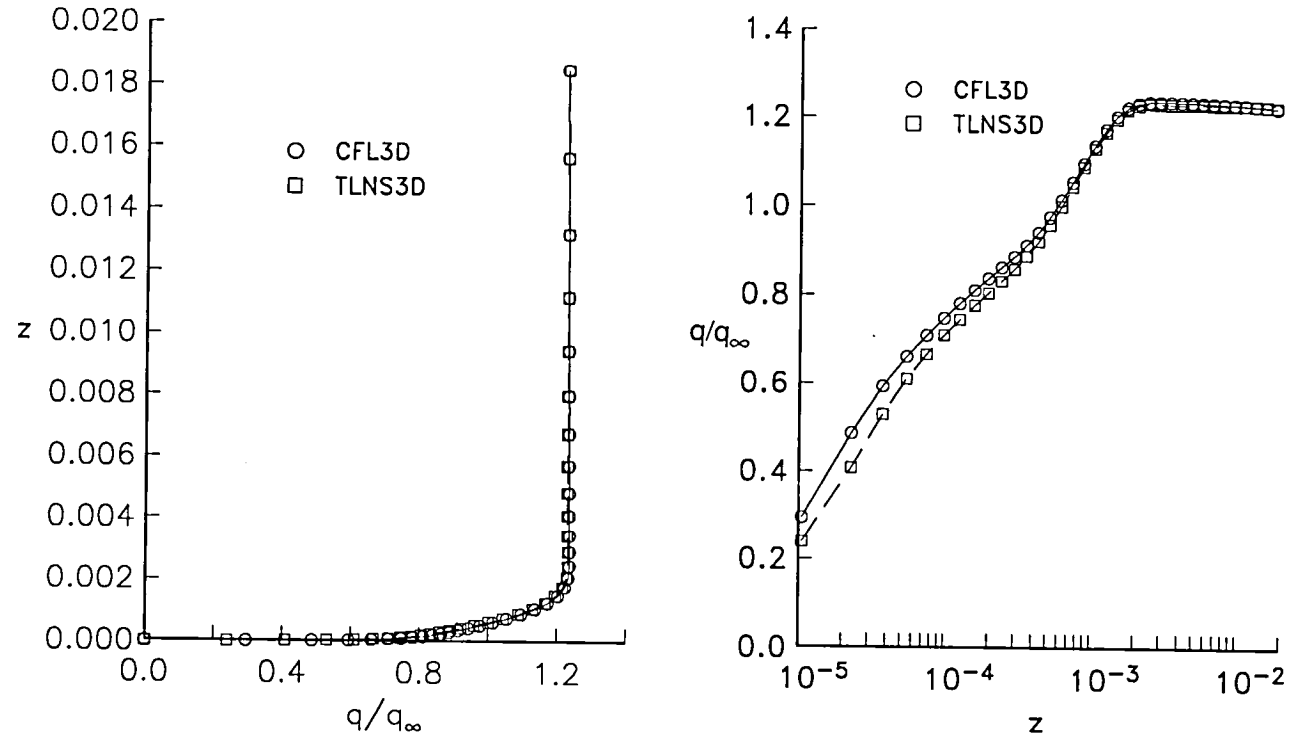

(e) $\eta = 0.8, \xi = 0.25$.

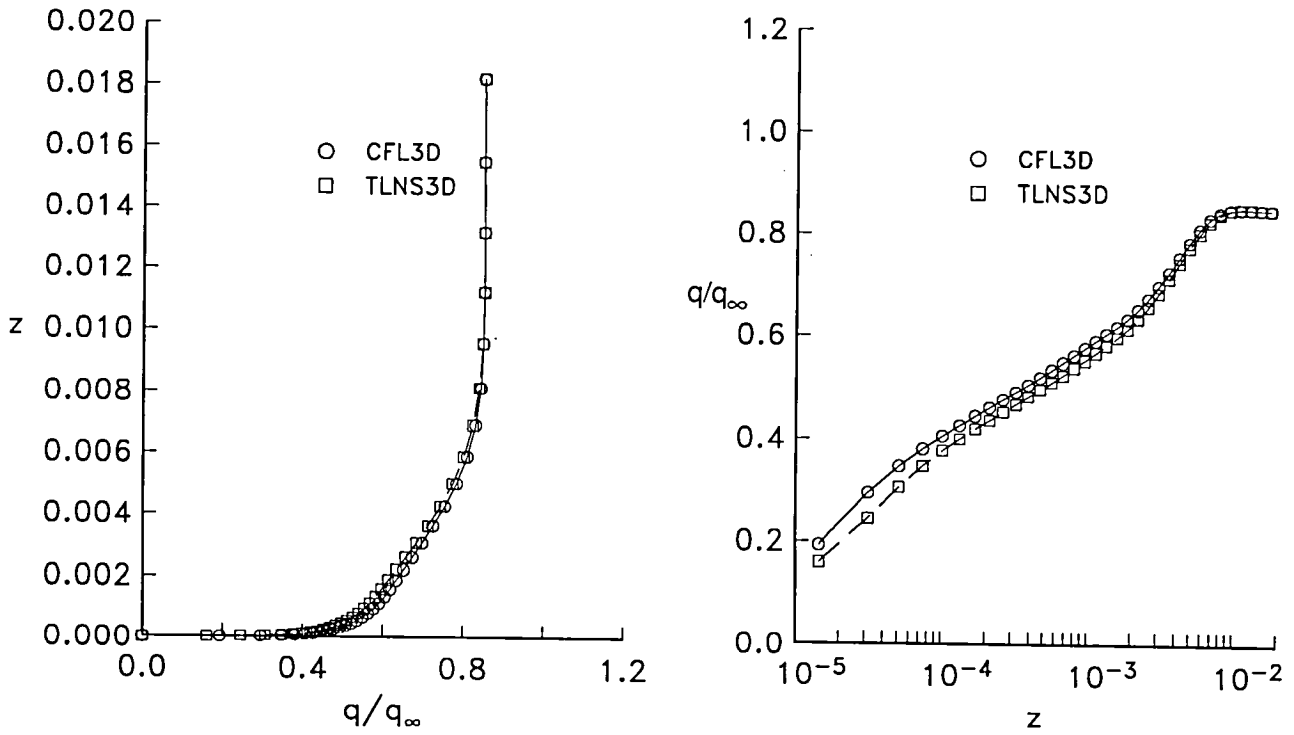

(f) $\eta = 0.8, \xi = 0.75$.

Figure 26. Concluded.

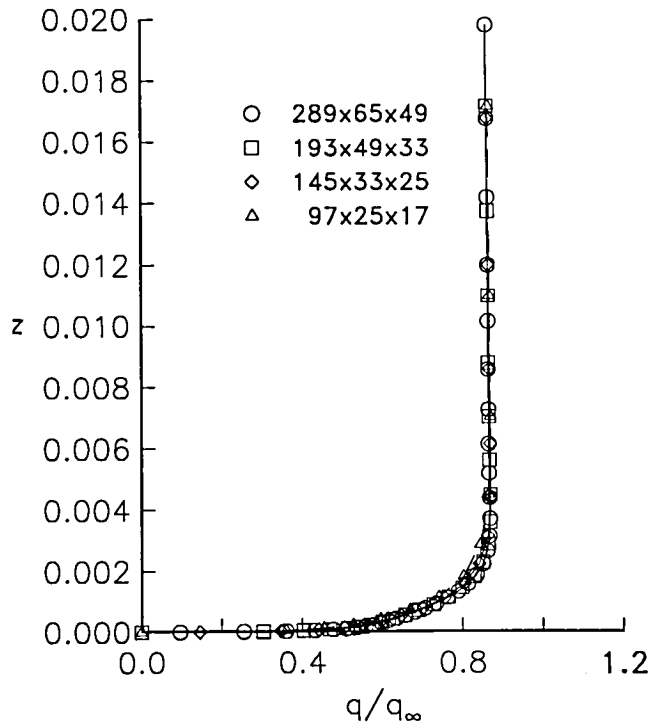

(a) TLNS3D—standard.

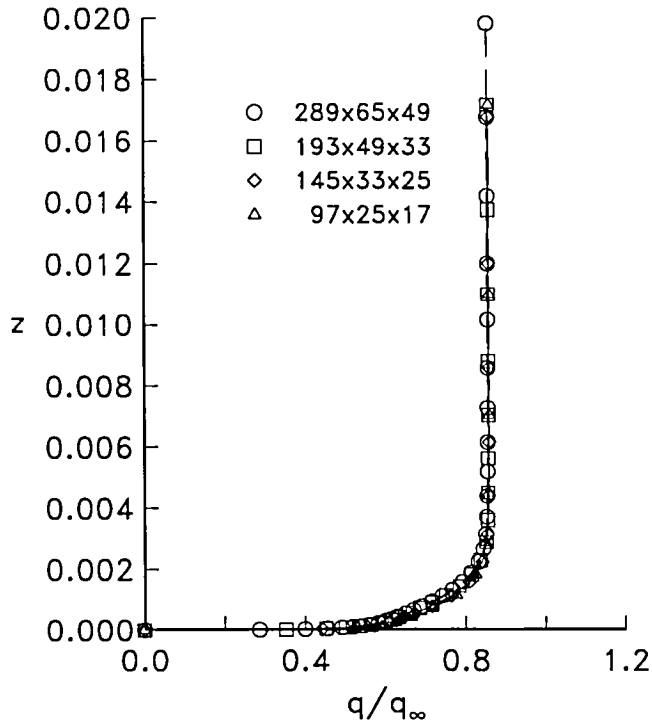

(b) CFL3D—standard.

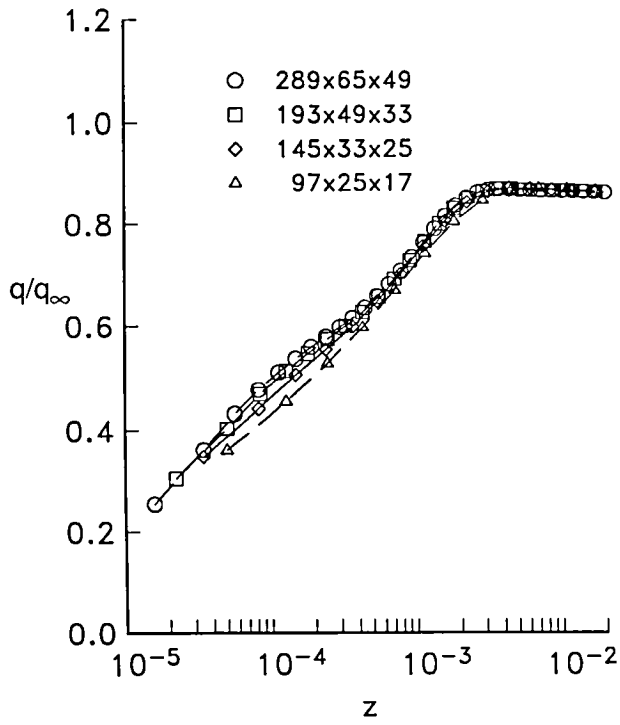

(c) TLNS3D—semilog.

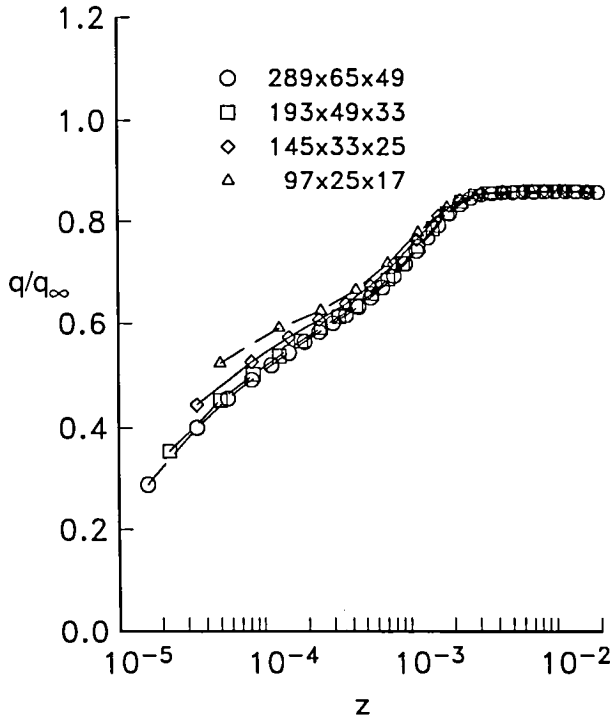

(d) CFL3D—semilog.

Figure 27. Effect of grid refinement on the lower-surface boundary-layer profiles for the ONERA M6 wing. $\eta = 0; \xi = 0.25$.

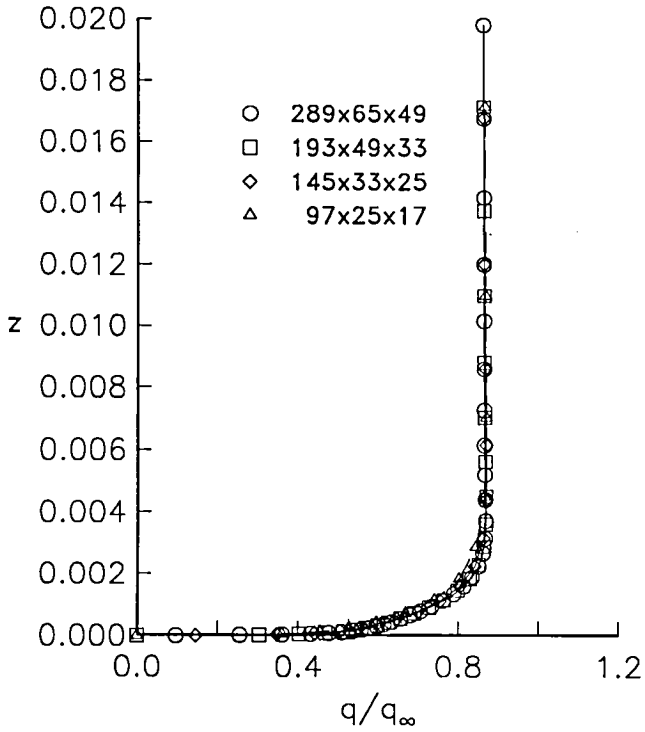

(a) TLNS3D—standard.

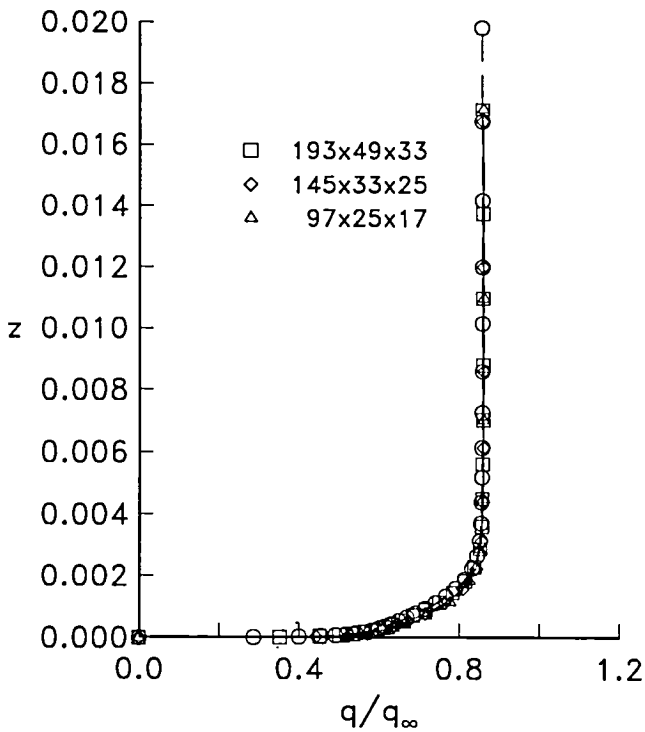

(b) CFL3D—standard.

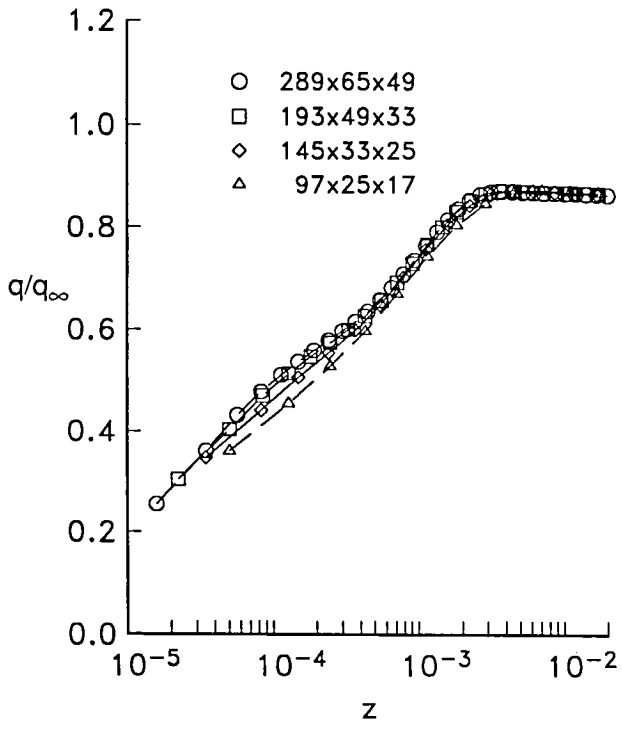

(c) TLNS3D—semilog.

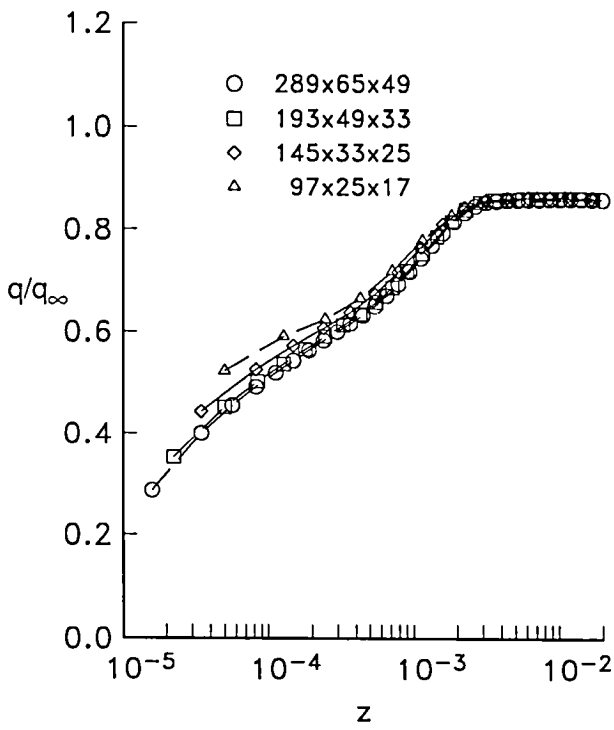

(d) CFL3D—semilog.

Figure 28. Effect of grid refinement on the lower-surface boundary-layer profiles for the ONERA M6 wing. $\eta = 0; \xi = 0.75$.

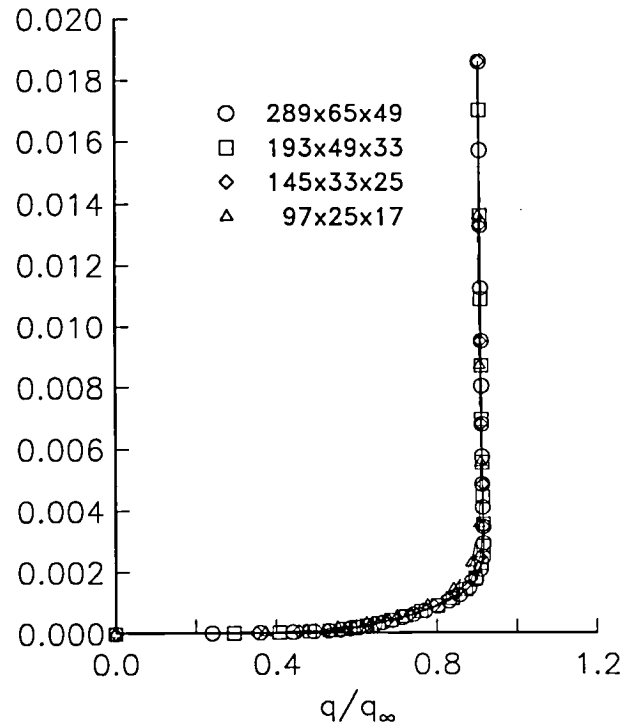

(a) TLNS3D—standard.

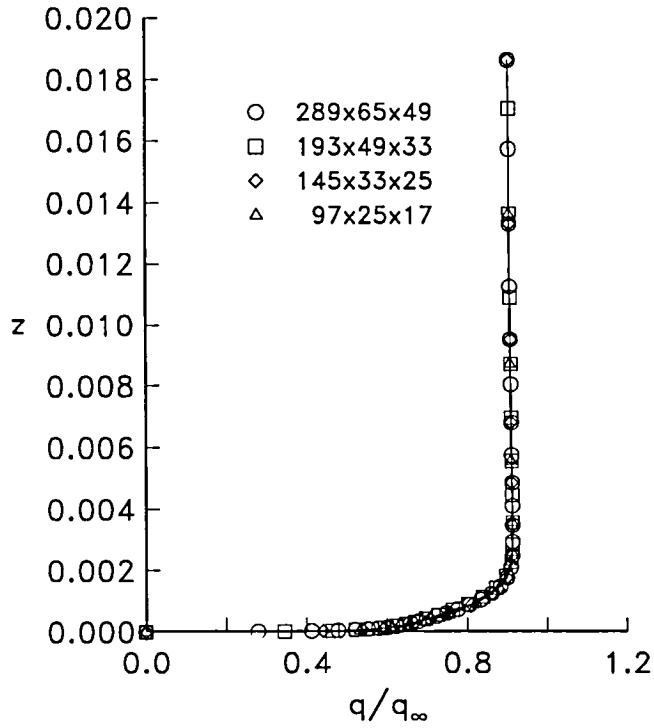

(b) CFL3D—standard.

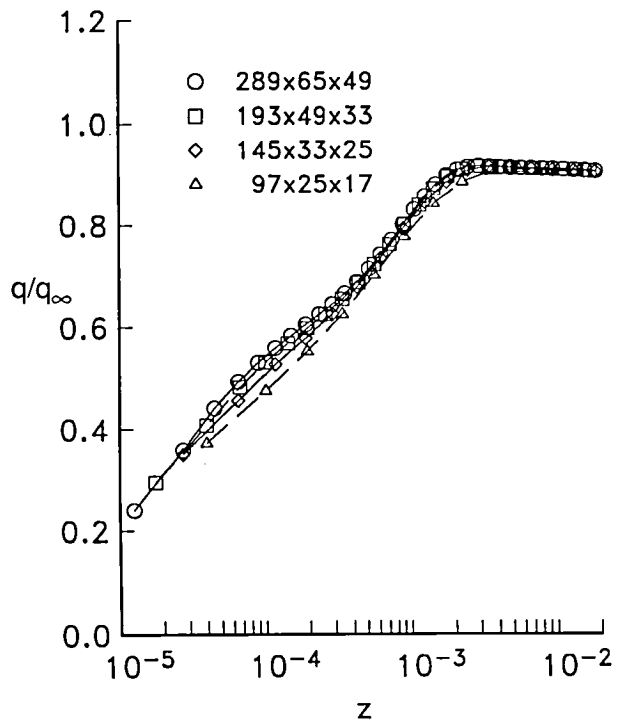

(c) TLNS3D—semilog.

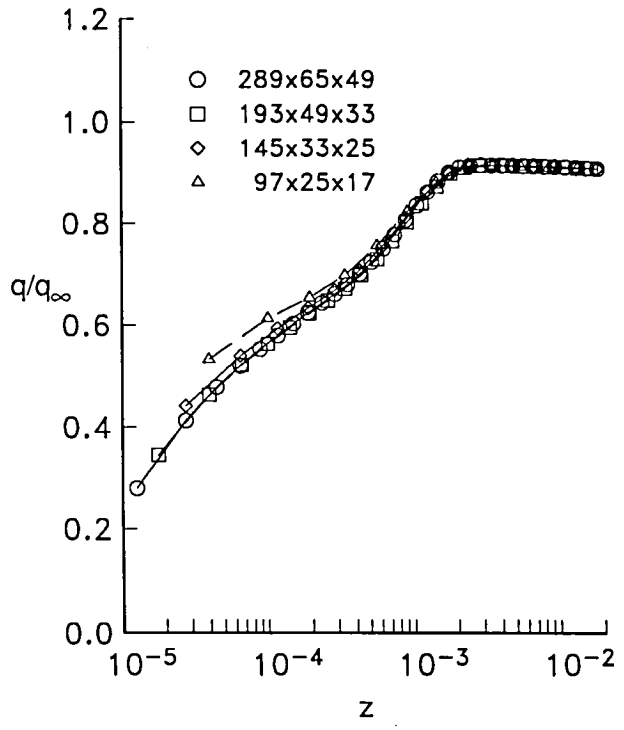

(d) CFL3D—semilog.

Figure 29. Effect of grid refinement on the lower-surface boundary-layer profiles for the ONERA M6 wing. $\eta = 0.5; \xi = 0.25$.

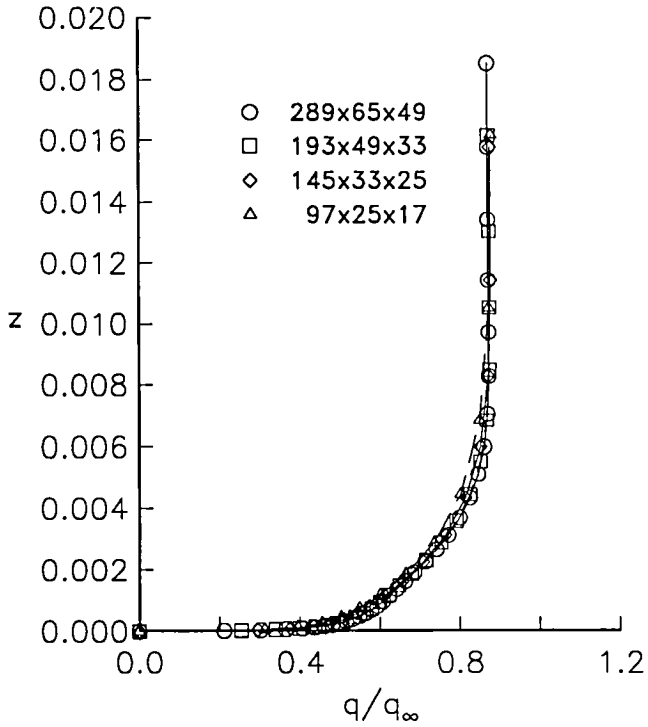

(a) TLNS3D—standard.

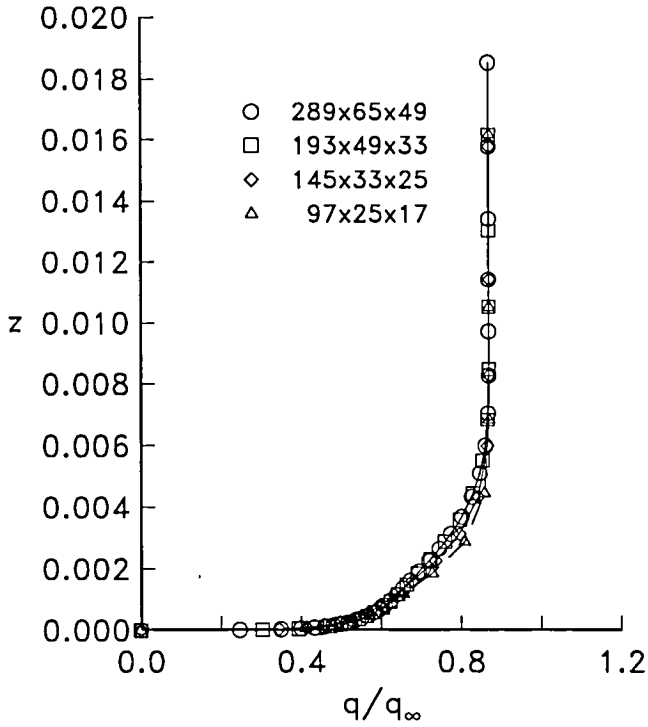

(b) CFL3D—standard.

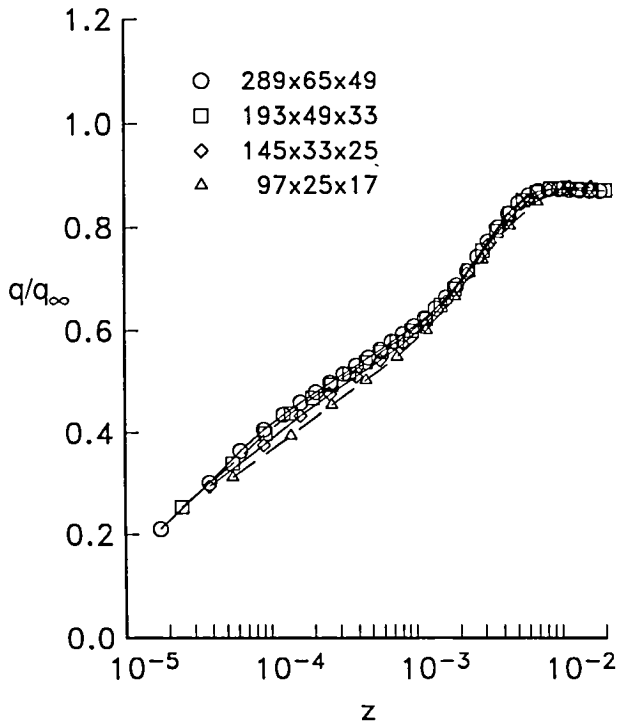

(c) TLNS3D—semilog.

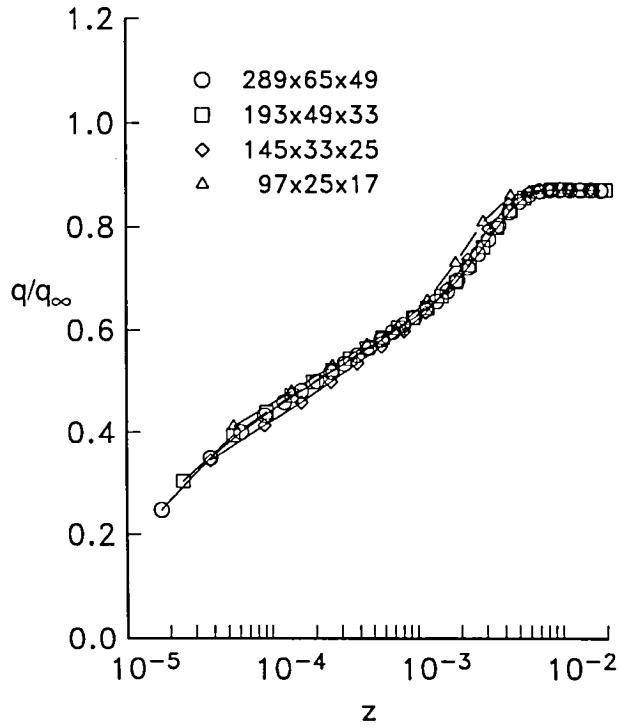

(d) CFL3D—semilog.

Figure 30. Effect of grid refinement on the lower-surface boundary-layer profiles for the ONERA M6 wing. $\eta = 0.5; \xi = 0.75$.

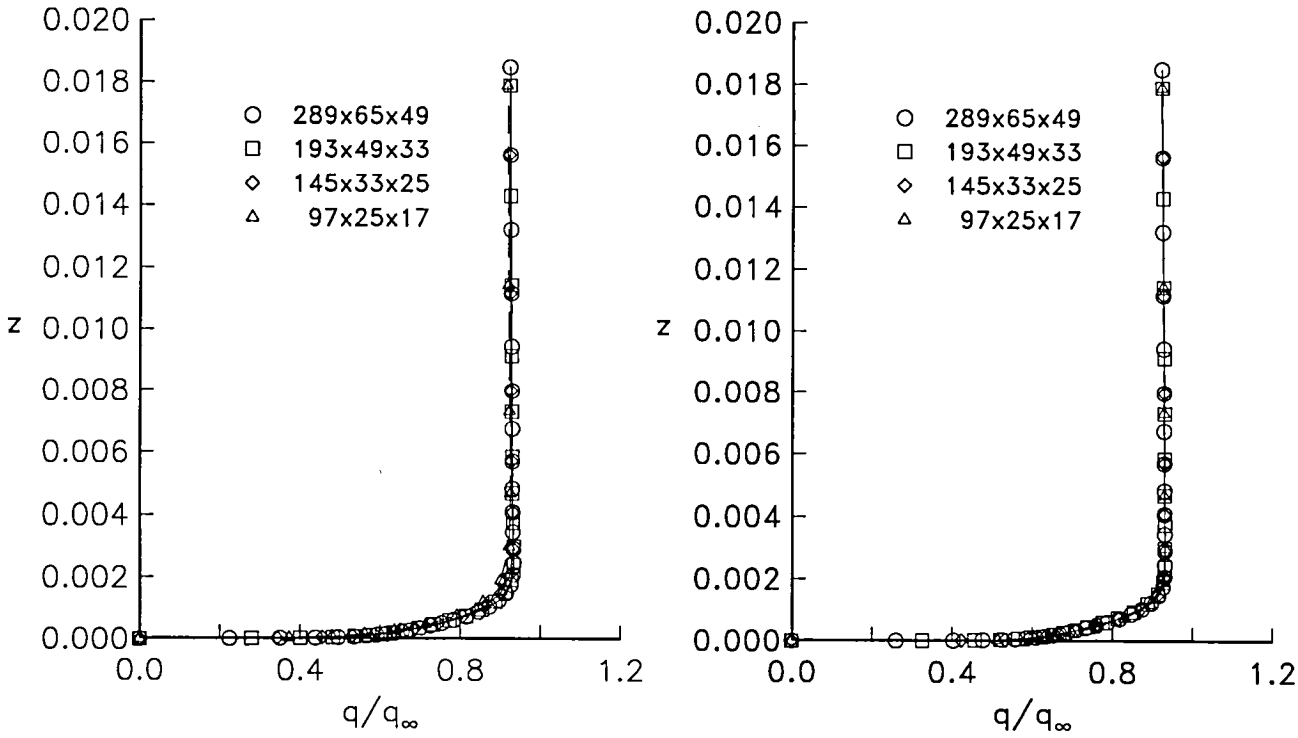

(a) TLNS3D—standard.

(b) CFL3D—standard.

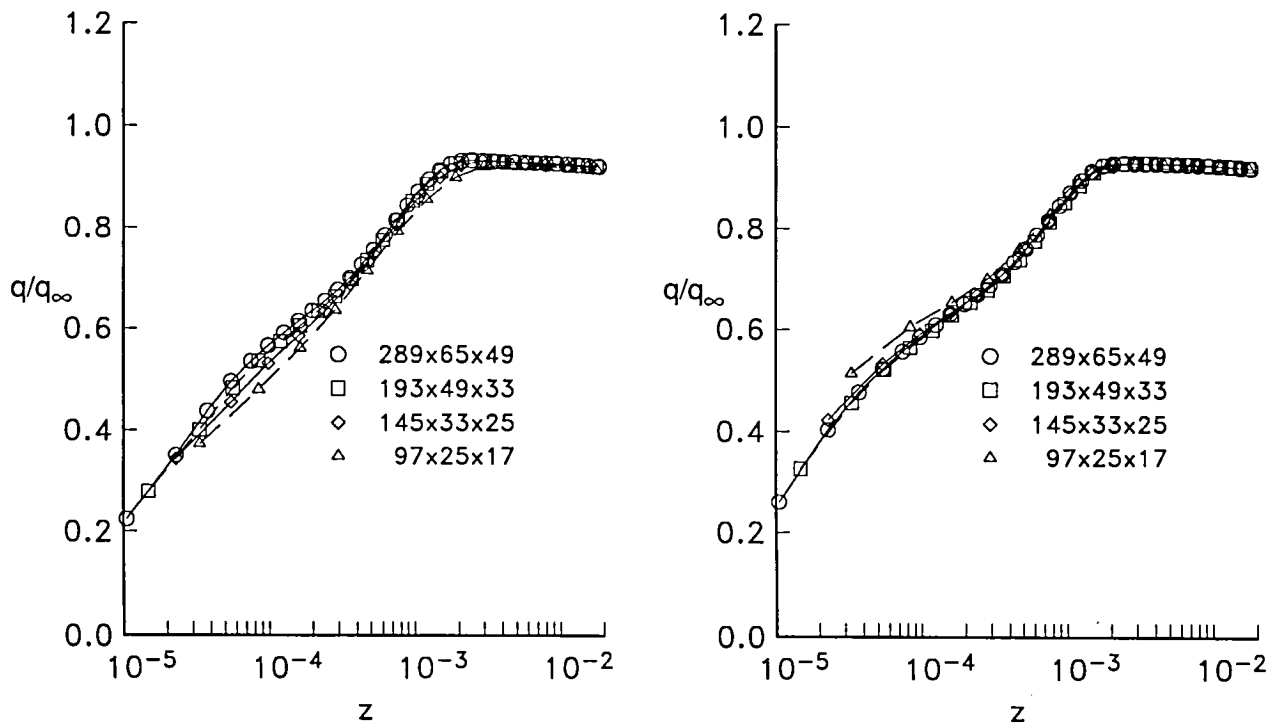

(c) TLNS3D—semilog.

(d) CFL3D—semilog.

Figure 31. Effect of grid refinement on the lower-surface boundary-layer profiles for the ONERA M6 wing. $\eta = 0.8; \xi = 0.25$.

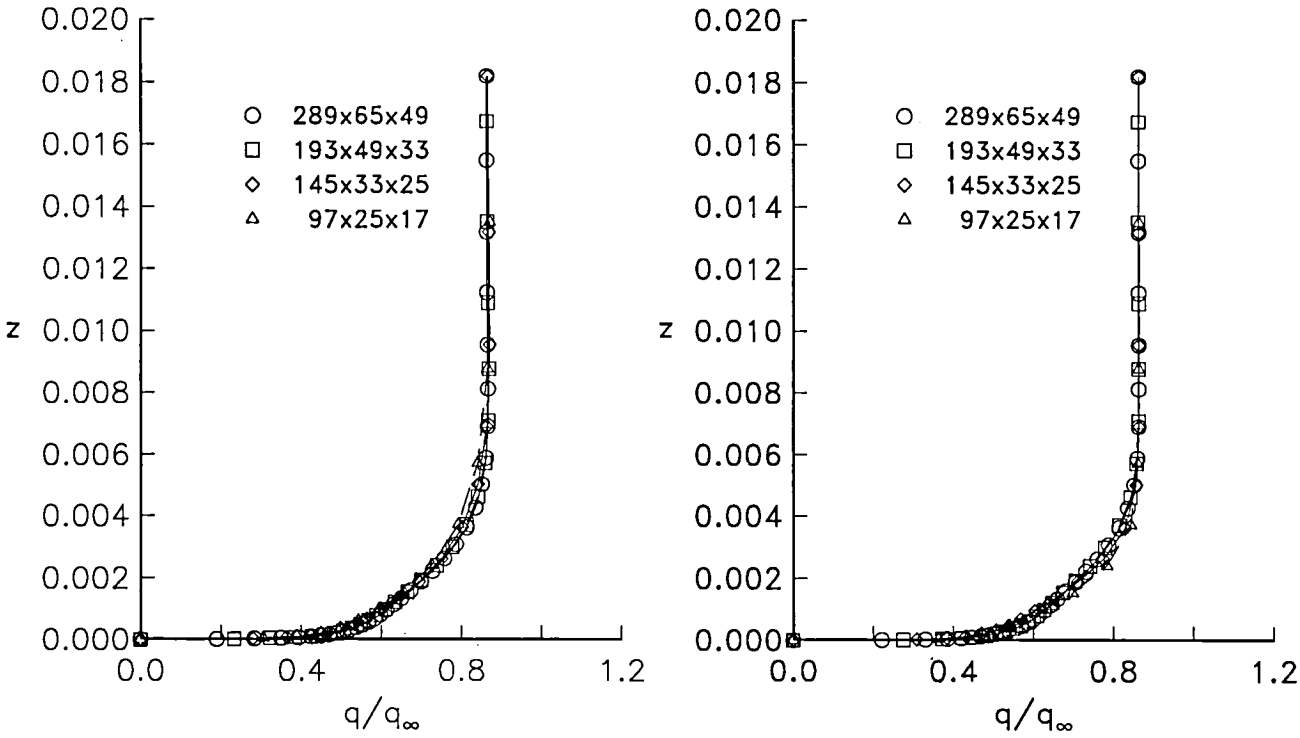

(a) TLNS3D—standard.

(b) CFL3D—standard.

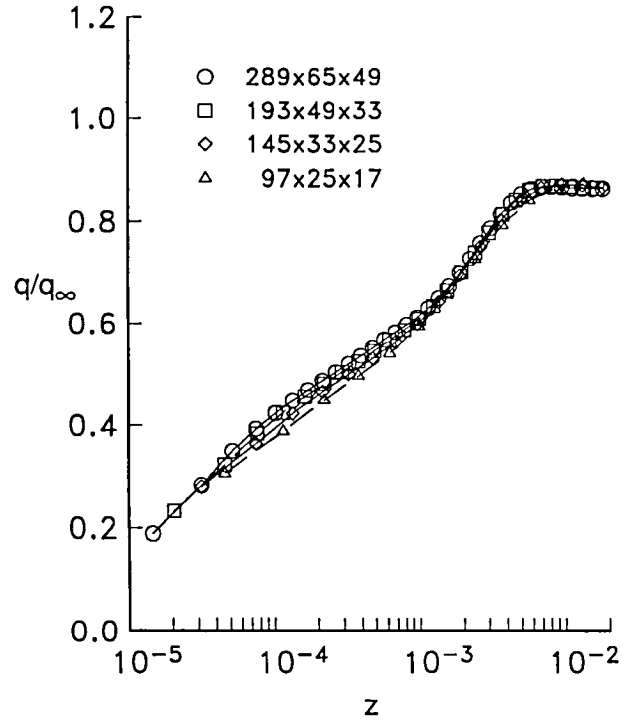

(c) TLNS3D—semilog.

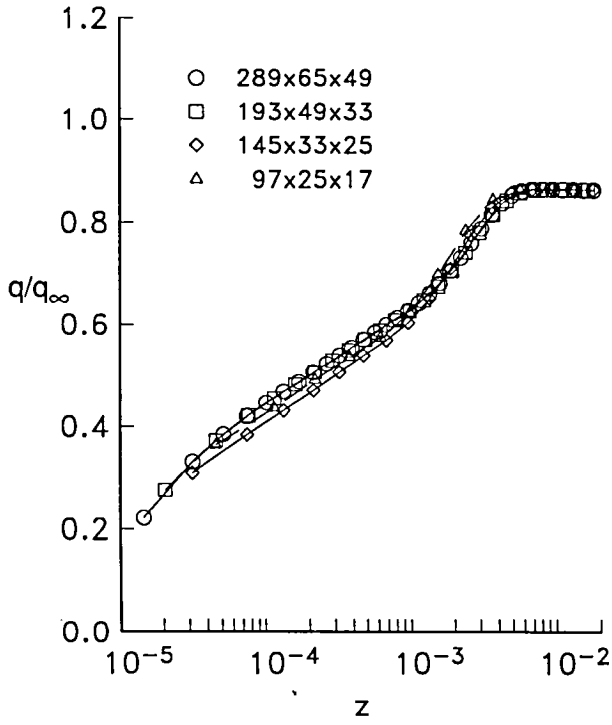

(d) CFL3D—semilog.

Figure 32. Effect of grid refinement on the lower-surface boundary-layer profiles for the ONERA M6 wing. $\eta = 0.8; \xi = 0.75$.

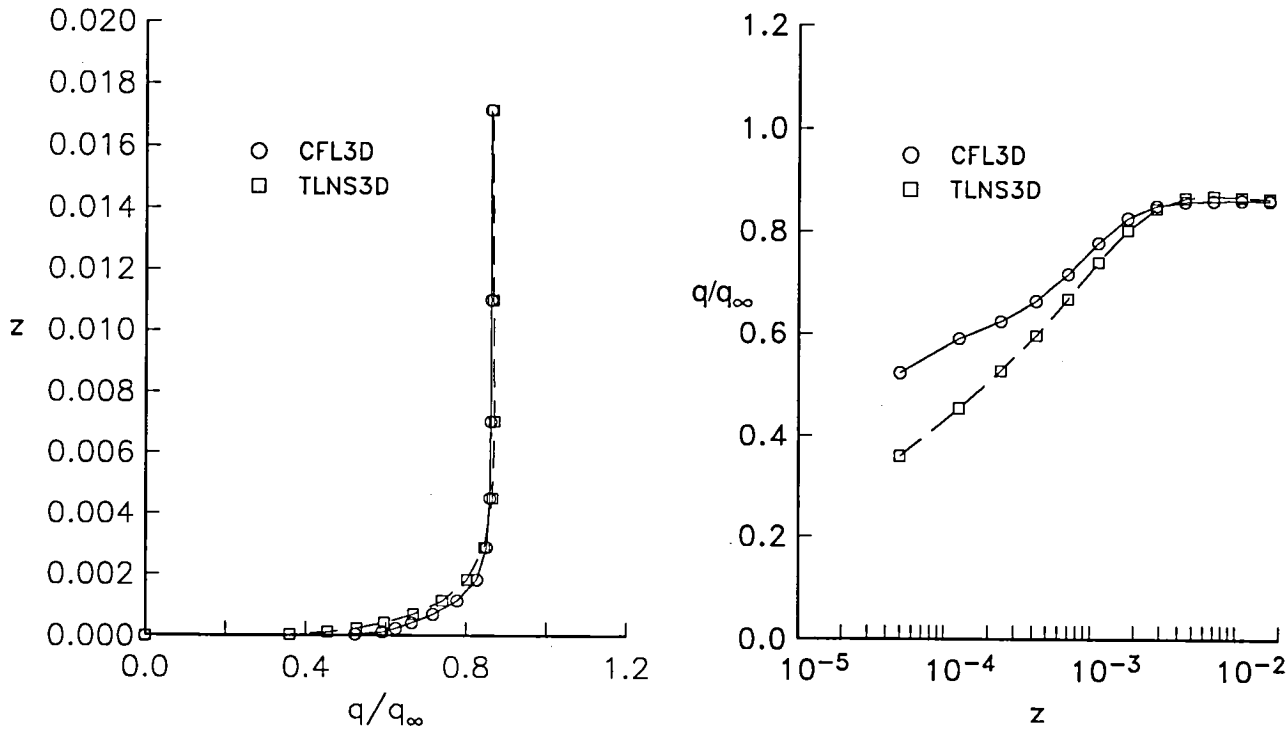

(a) $\eta = 0, \xi = 0.25$.

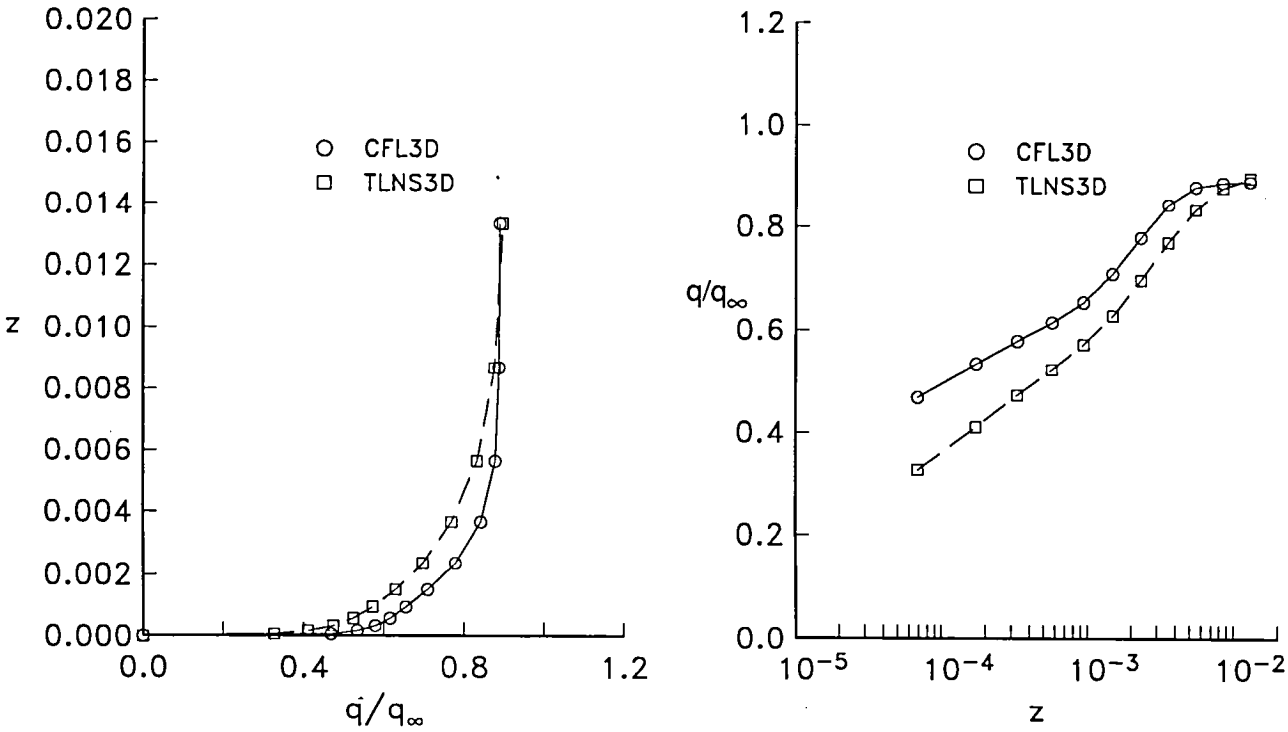

(b) $\eta = 0, \xi = 0.75$.

Figure 33. Lower-surface boundary-layer profiles for the ONERA M6 wing. $97 \times 25 \times 17$ grid.

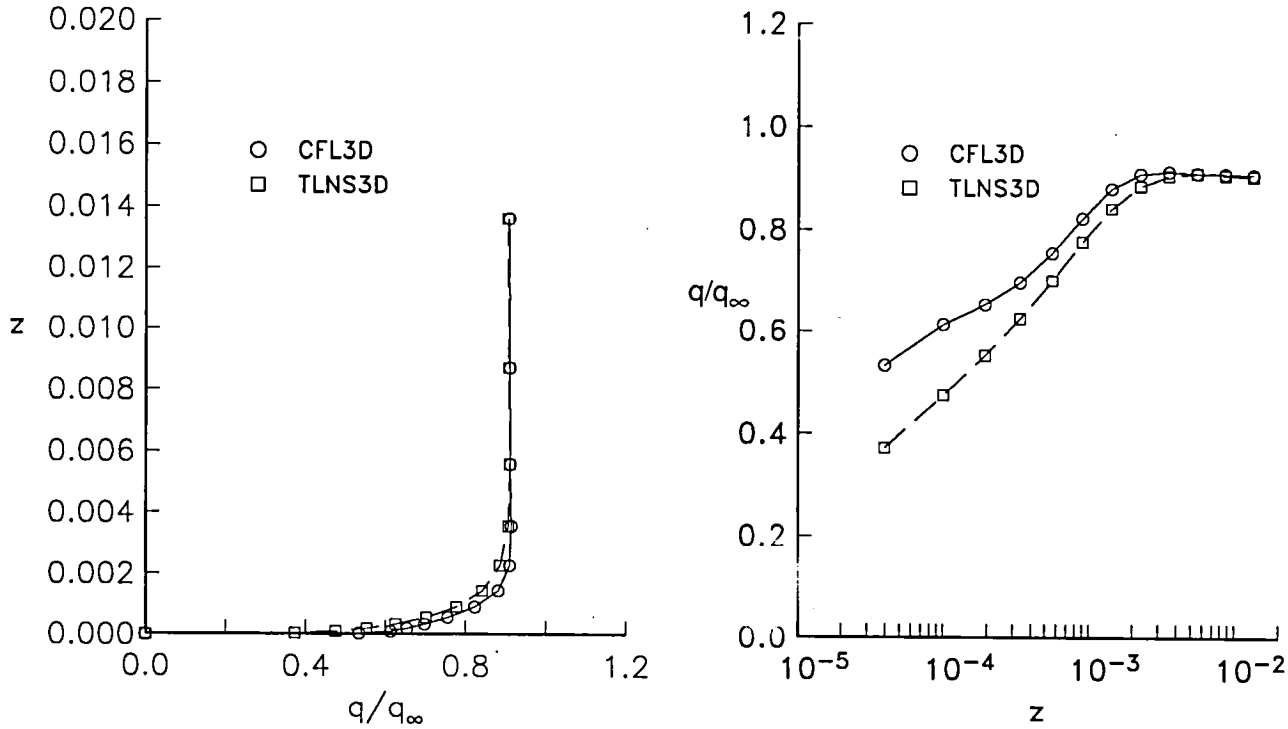

(c) $\eta = 0.5, \xi = 0.25$.

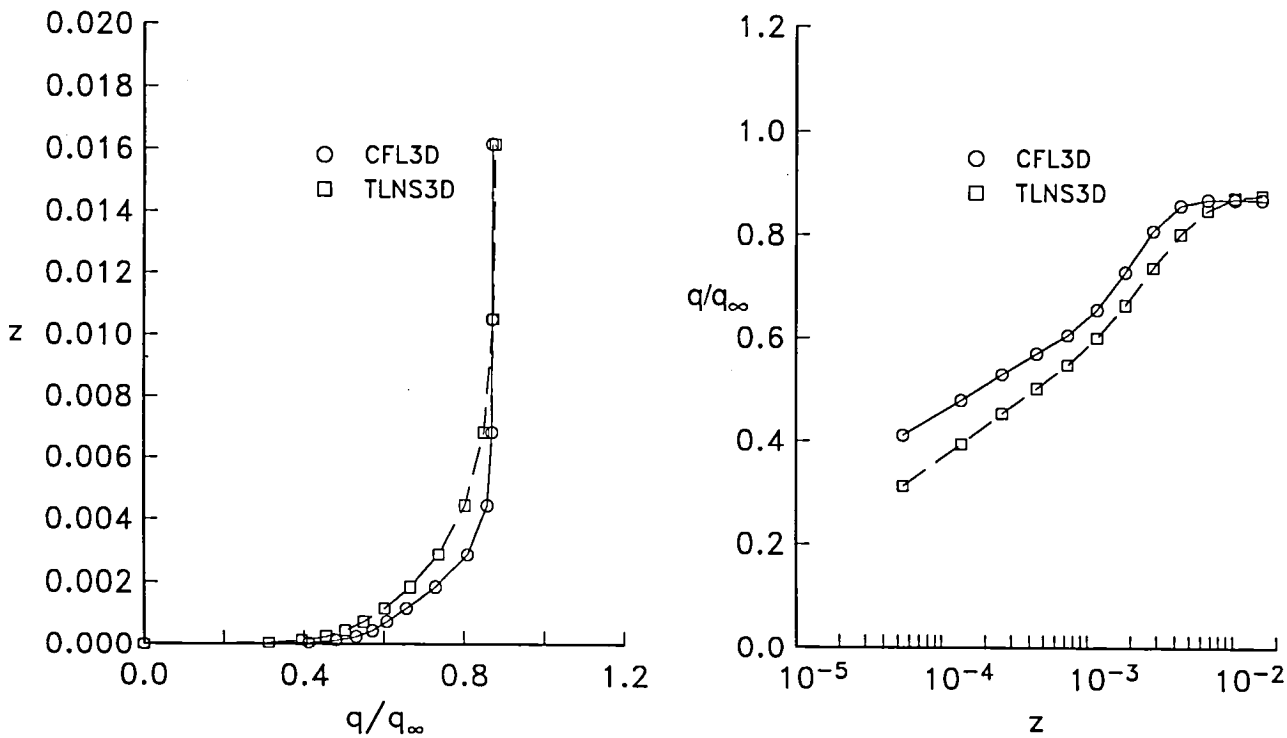

(d) $\eta = 0.5, \xi = 0.75$.

Figure 33. Continued.

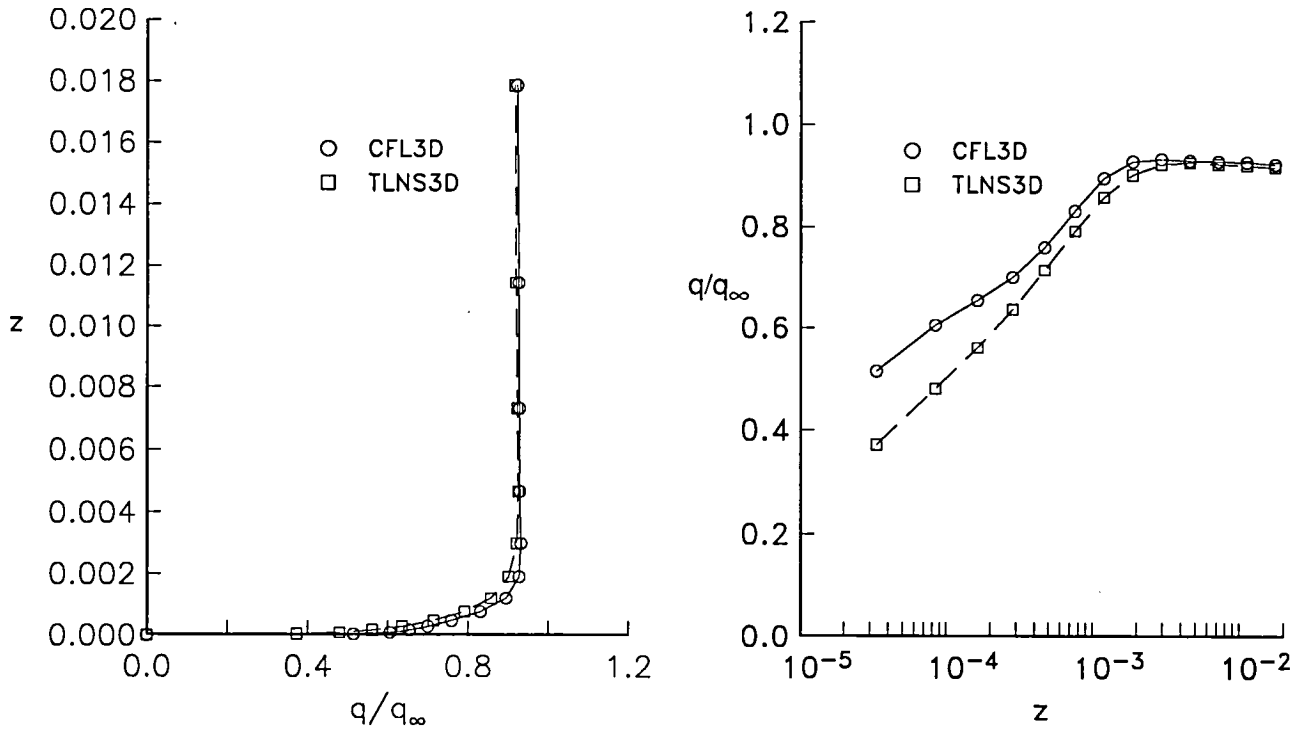

(e) $\eta = 0.8, \xi = 0.25$.

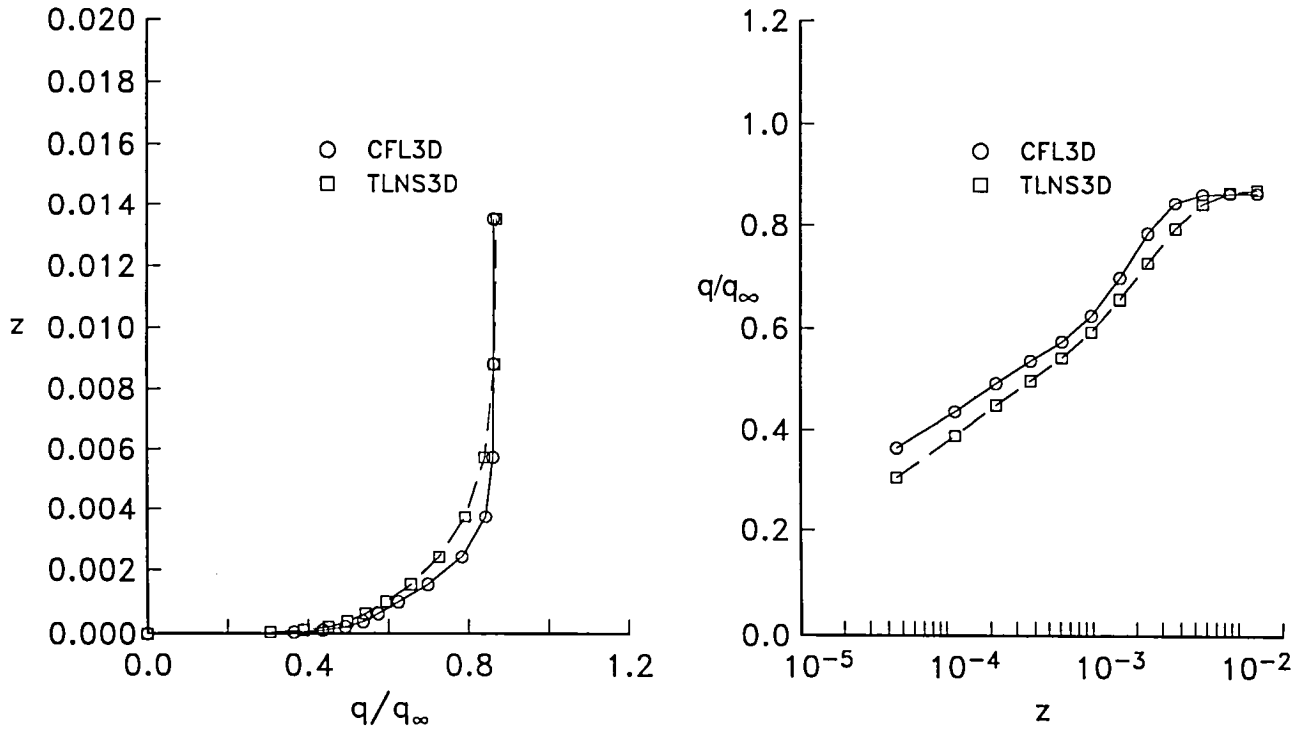

(f) $\eta = 0.8, \xi = 0.75$.

Figure 33. Concluded.

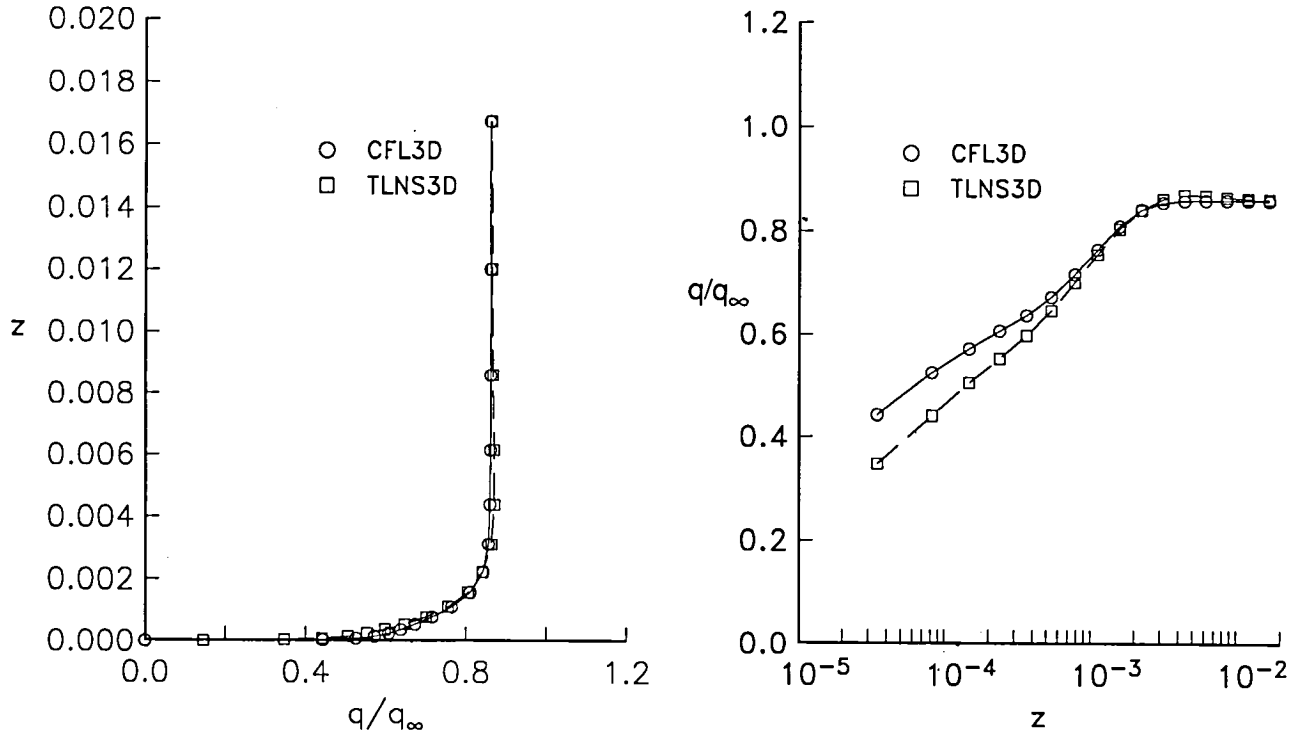

(a) $\eta = 0, \xi = 0.25$.

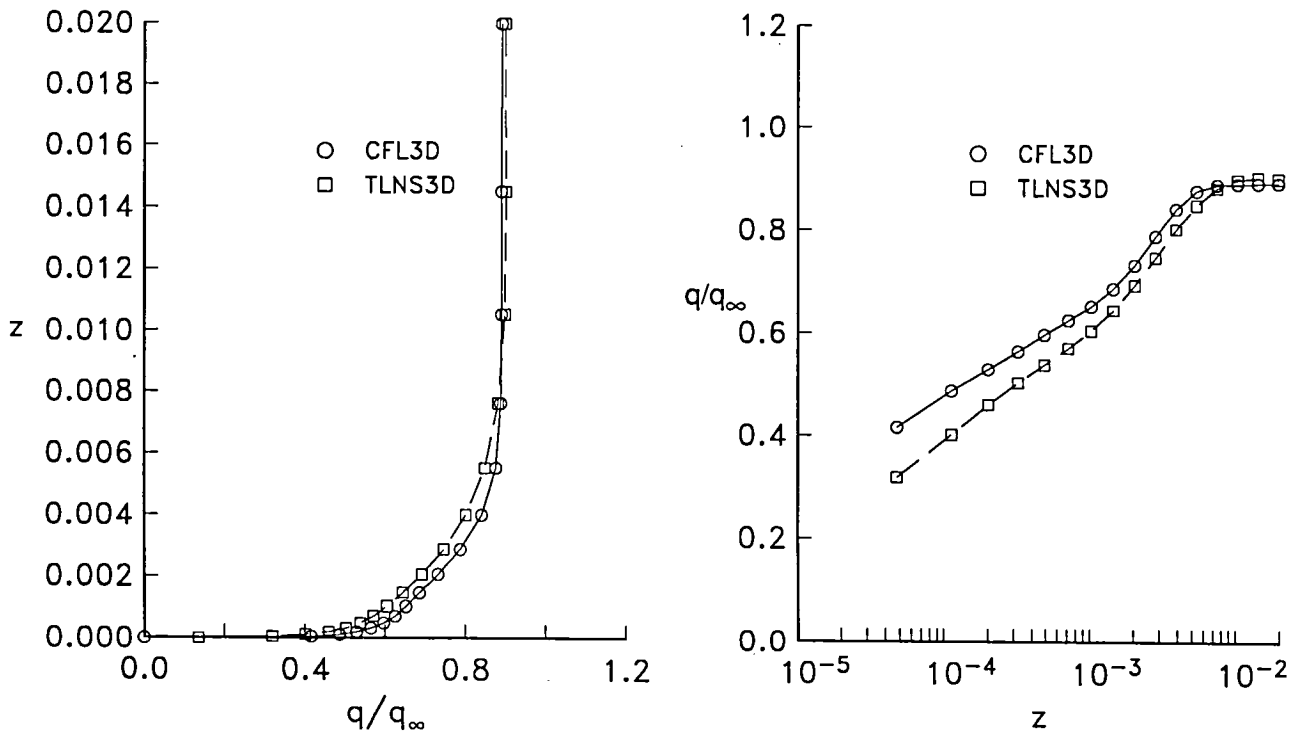

(b) $\eta = 0, \xi = 0.75$.

Figure 34. Lower-surface boundary-layer profiles for the ONERA M6 wing. $145 \times 33 \times 25$ grid.

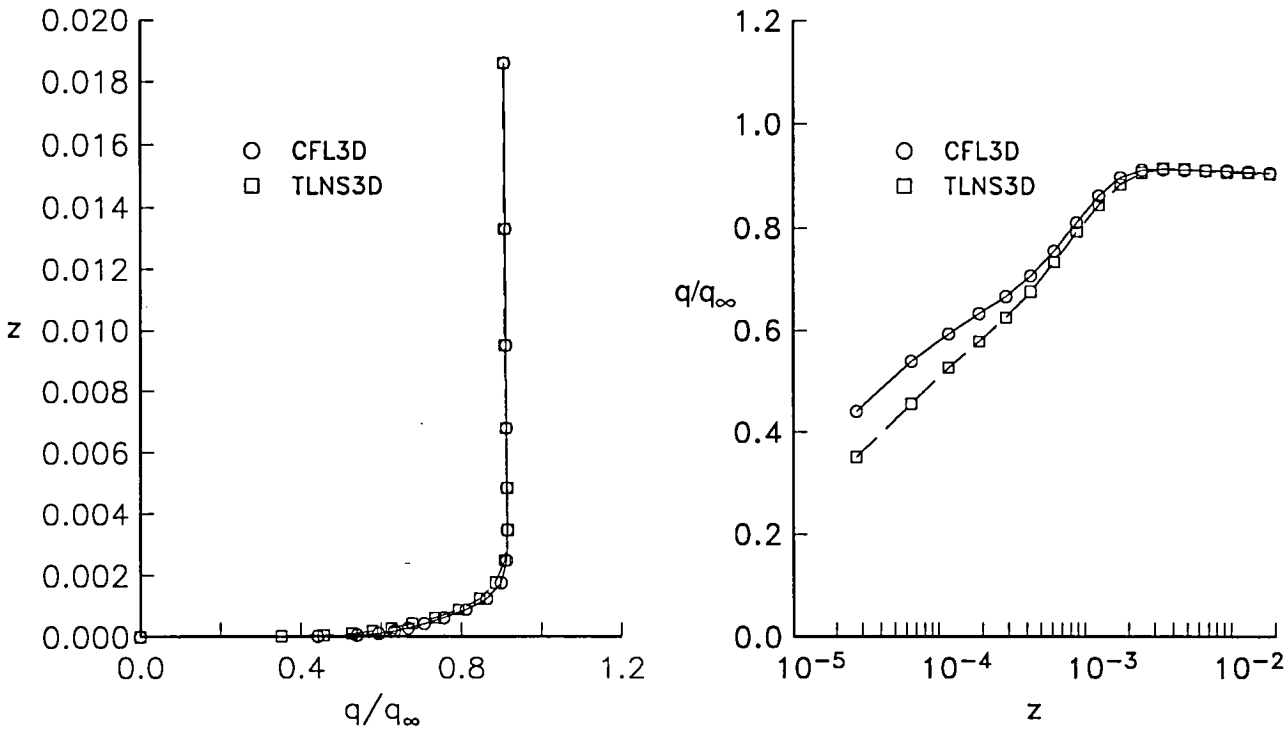

(c) $\eta = 0.5, \xi = 0.25$.

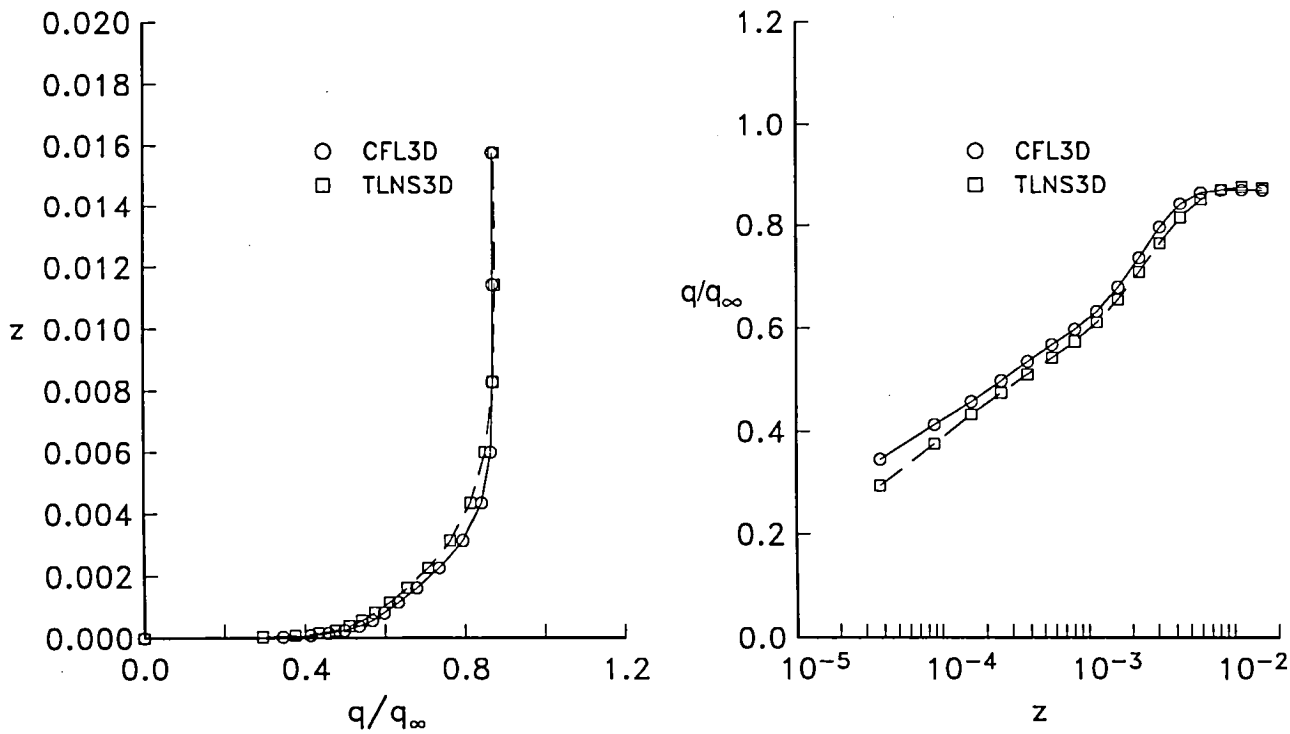

(d) $\eta = 0.5, \xi = 0.75$.

Figure 34. Continued.

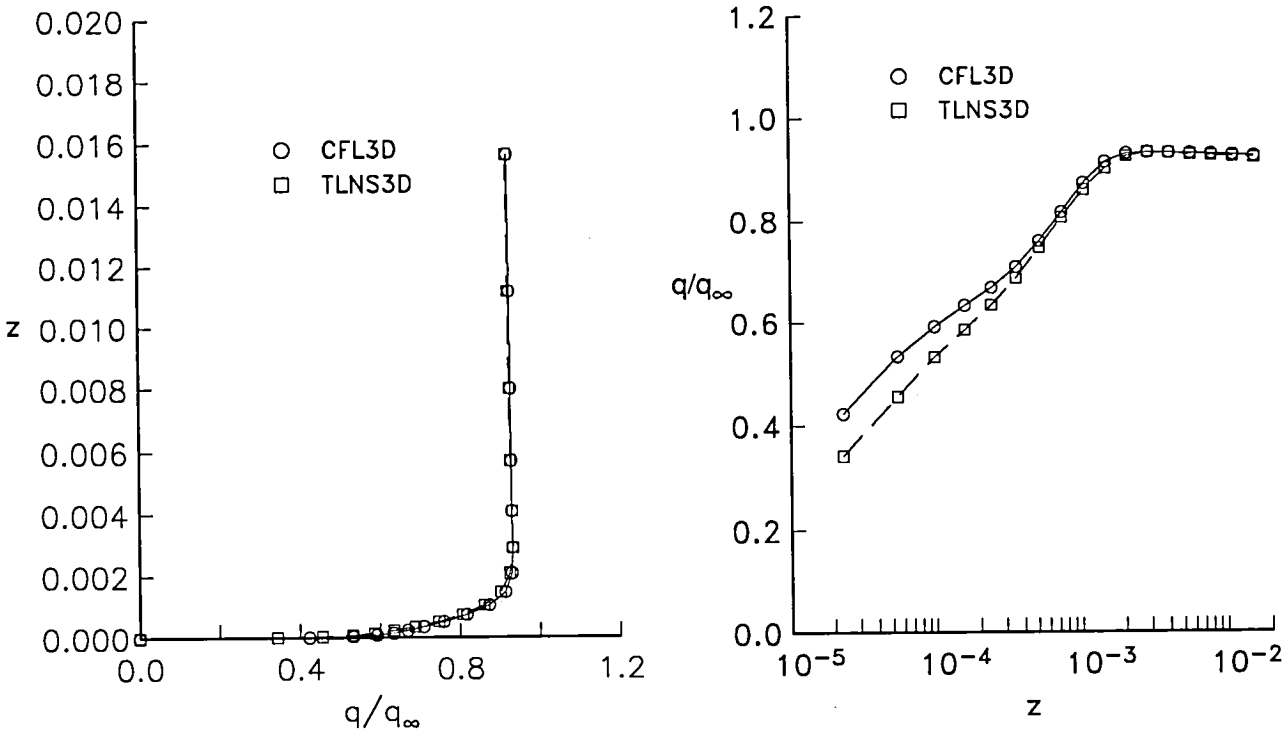

(e) $\eta = 0.8, \xi = 0.25$.

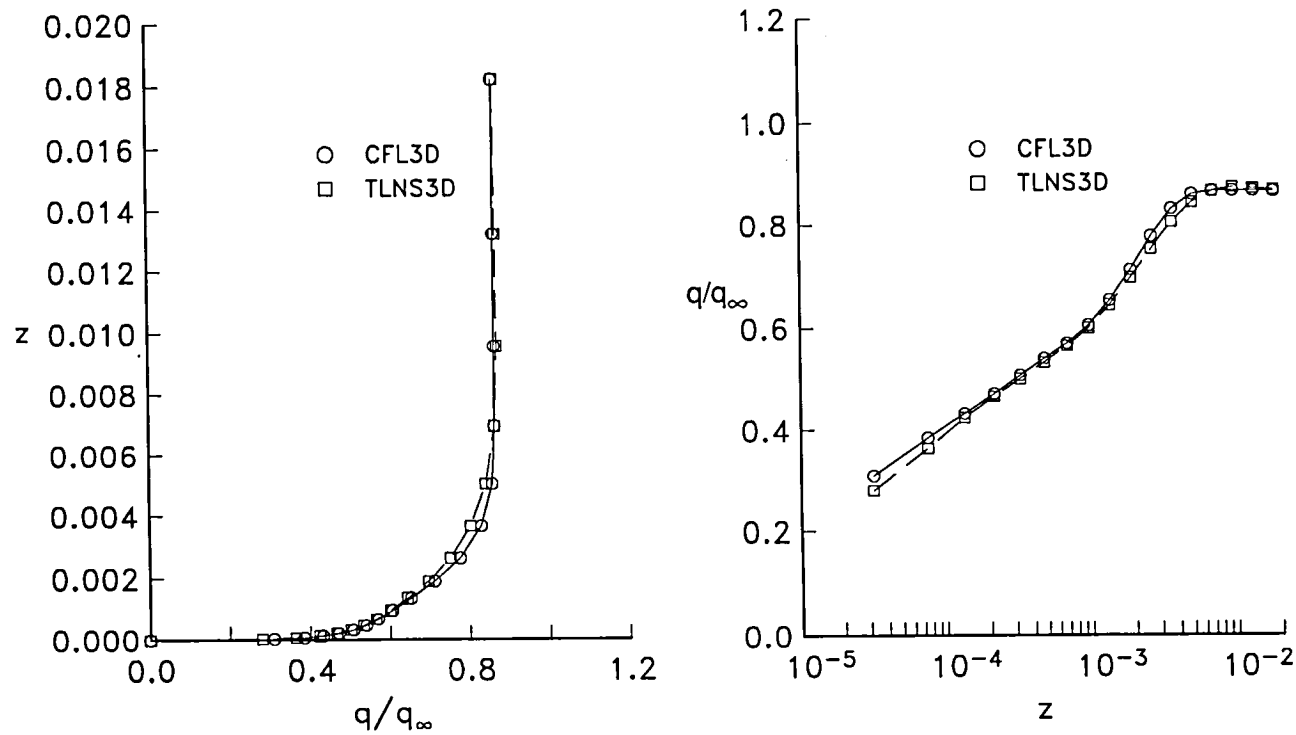

(f) $\eta = 0.8, \xi = 0.75$.

Figure 34. Concluded.

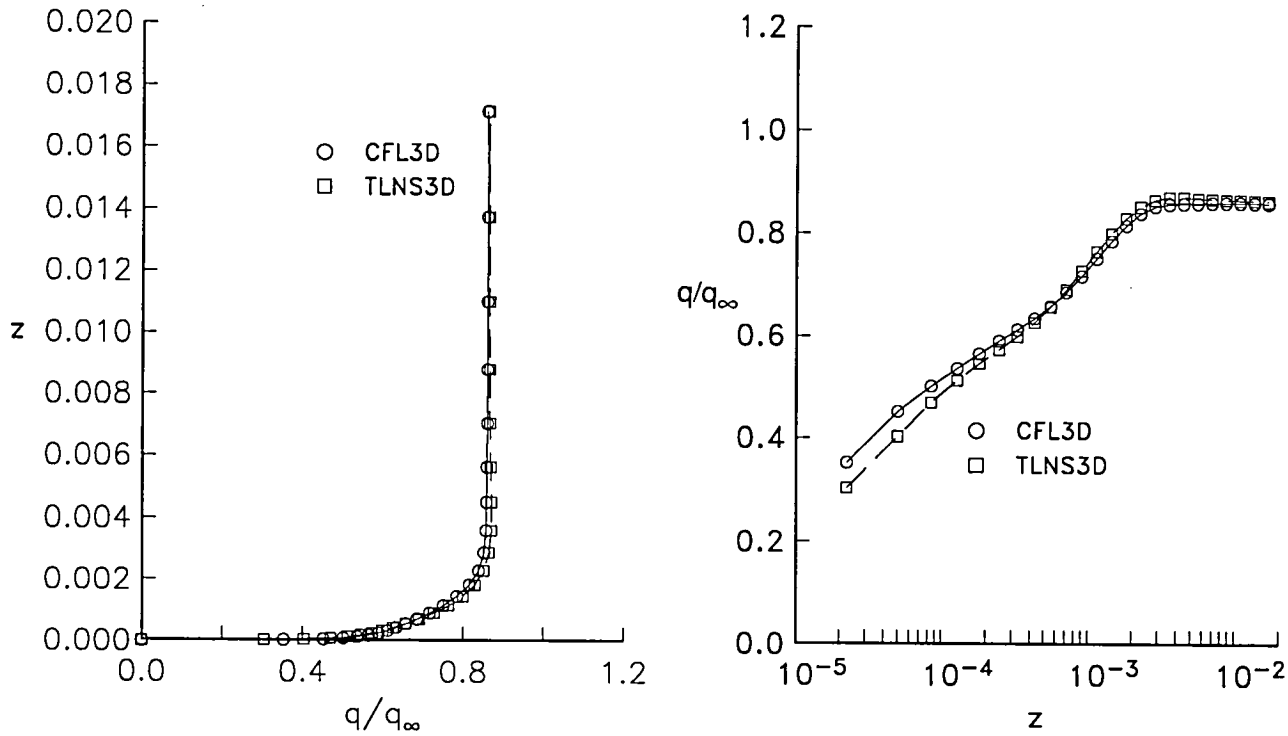

(a) $\eta = 0, \xi = 0.25$.

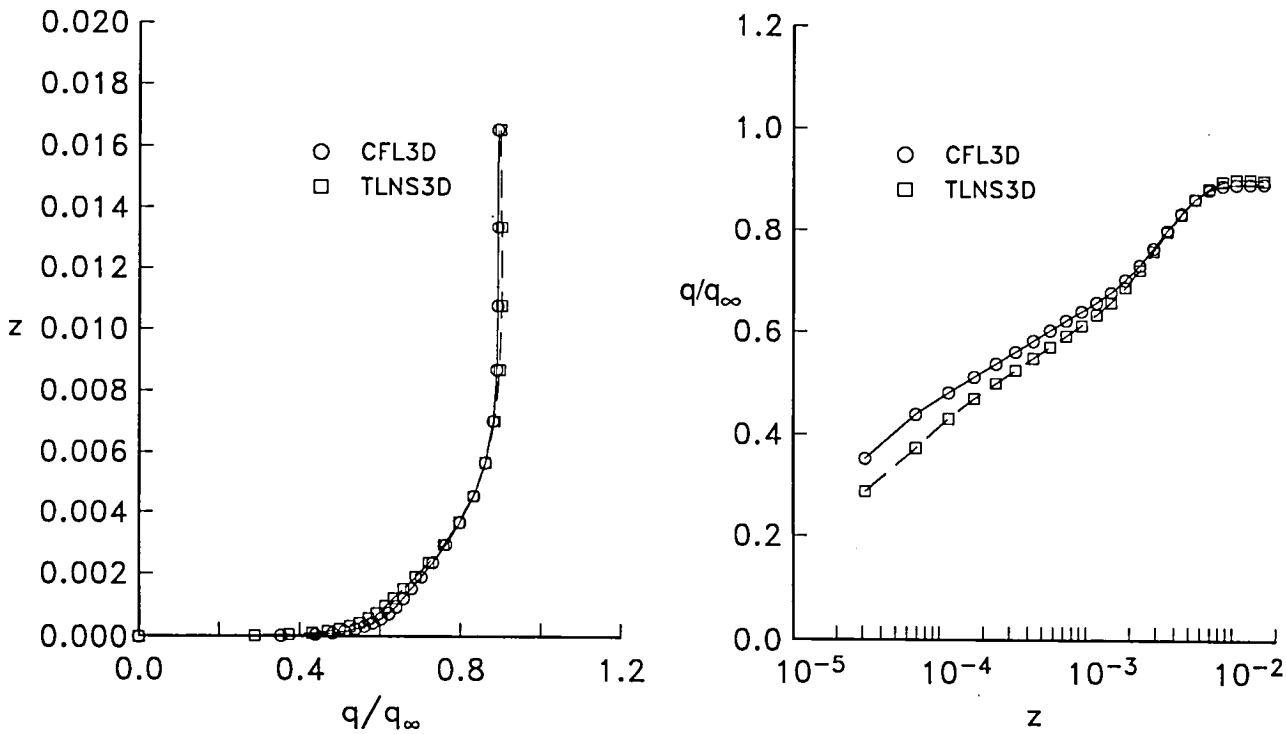

(b) $\eta = 0, \xi = 0.75$.

Figure 35. Lower-surface boundary-layer profiles for the ONERA M6 wing. $193 \times 49 \times 33$ grid.

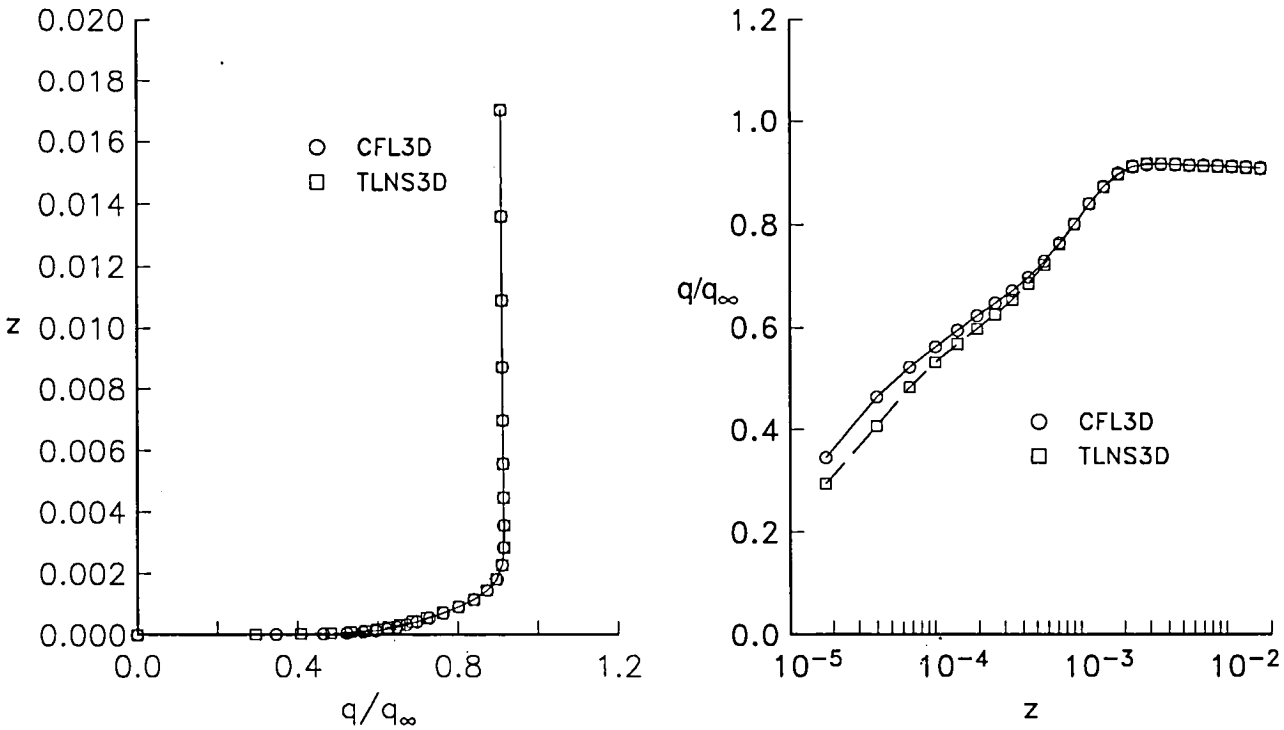

(c) $\eta = 0.5, \xi = 0.25$.

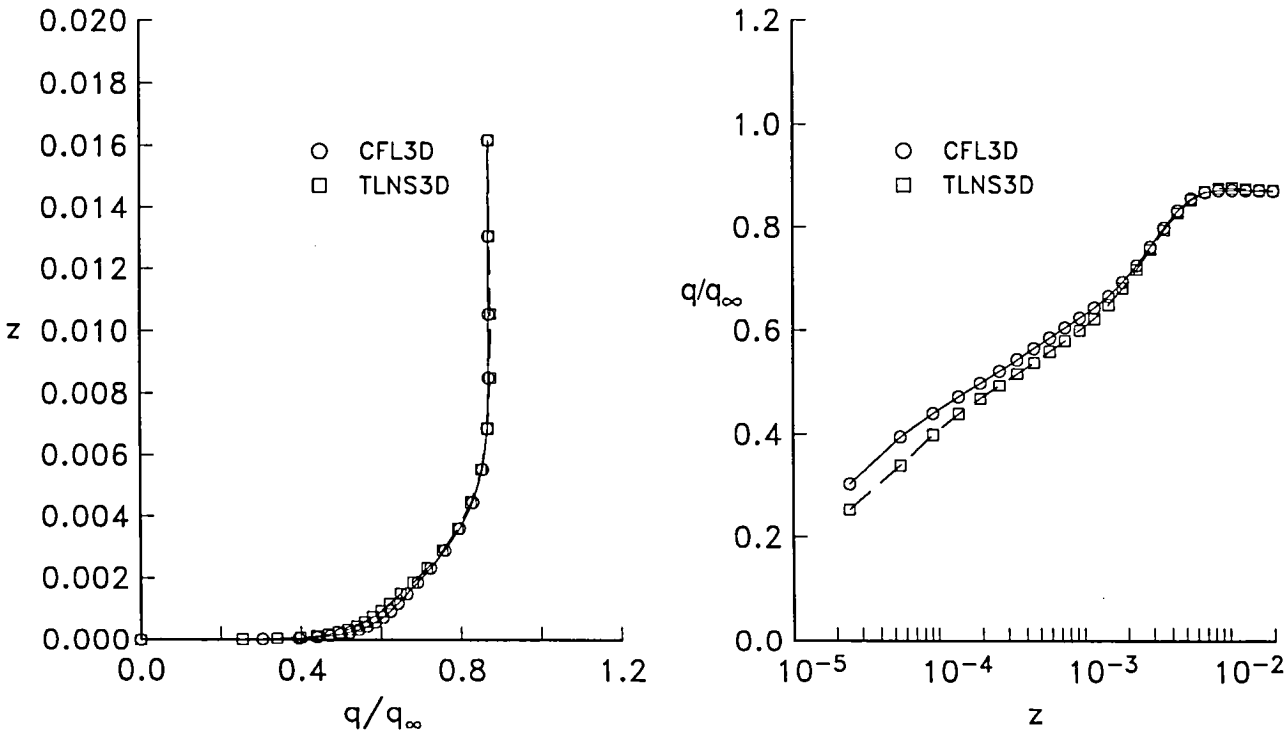

(d) $\eta = 0.5, \xi = 0.75$.

Figure 35. Continued.

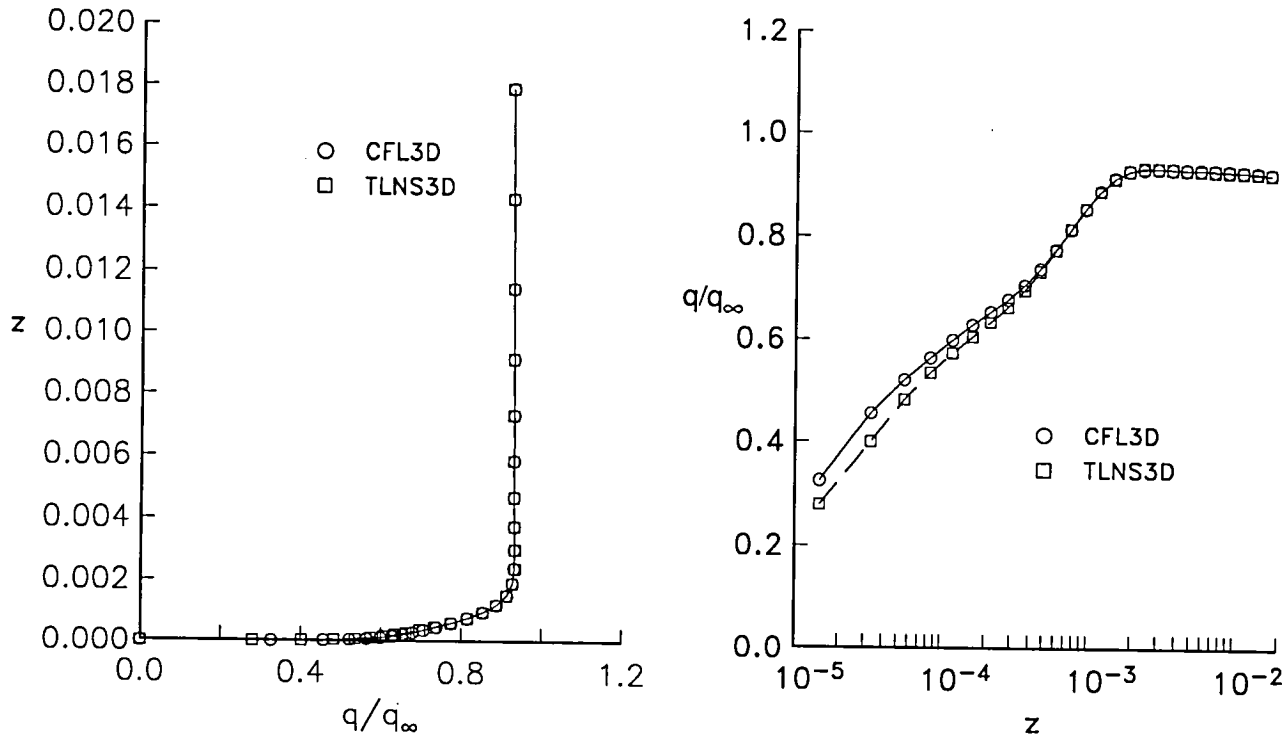

(e) $\eta = 0.8, \xi = 0.25$.

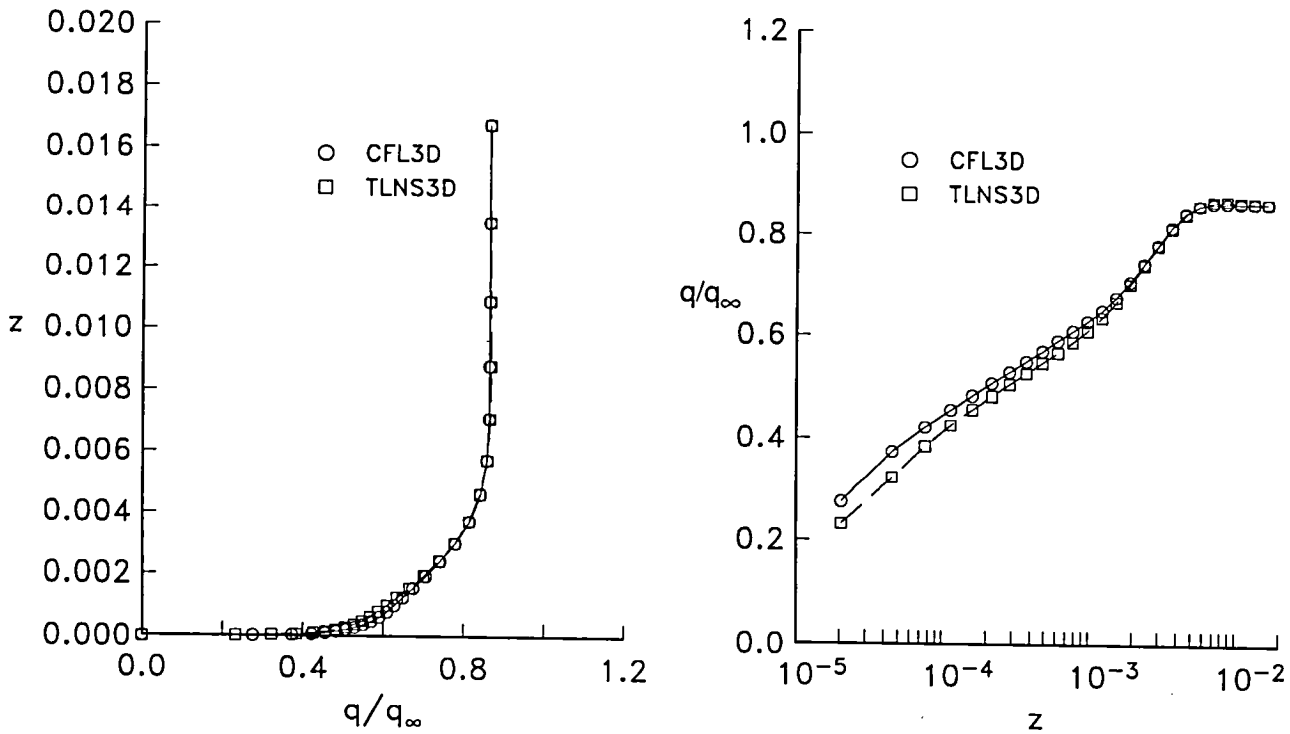

(f) $\eta = 0.8, \xi = 0.75$.

Figure 35. Concluded.

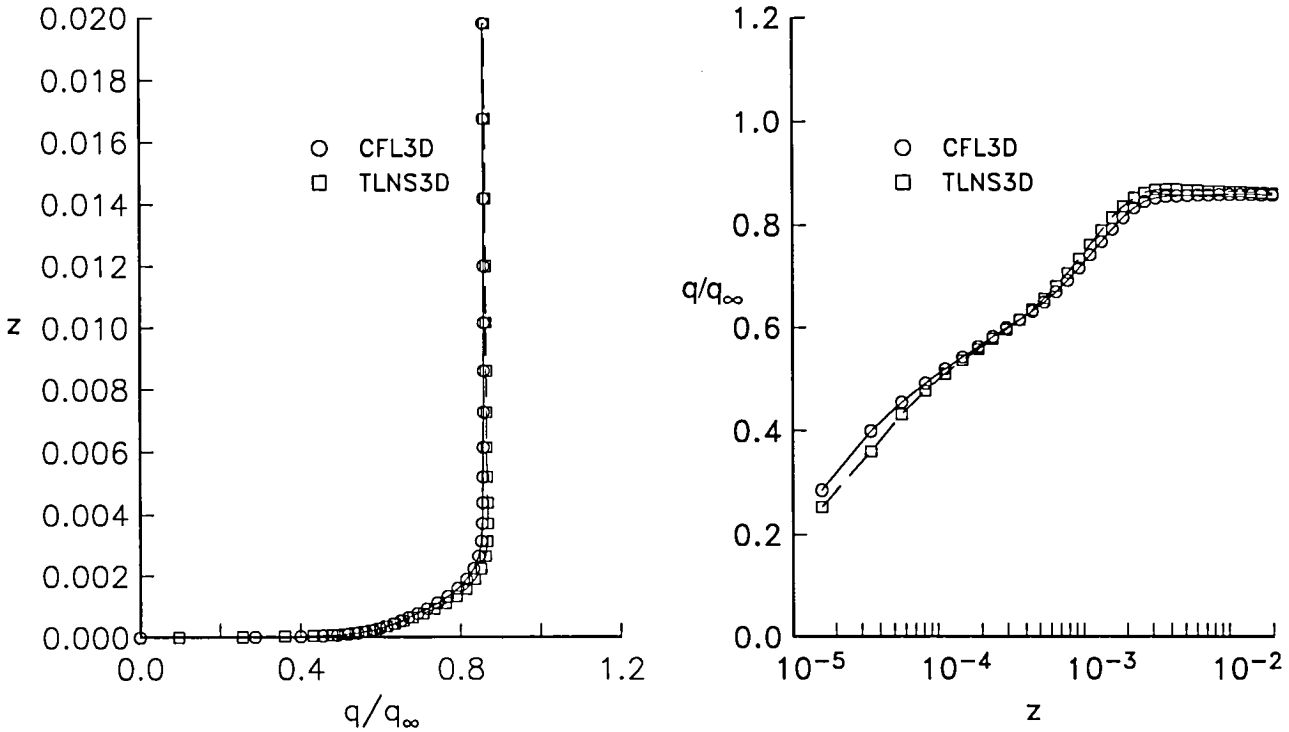

(a) $\eta = 0, \xi = 0.25$.

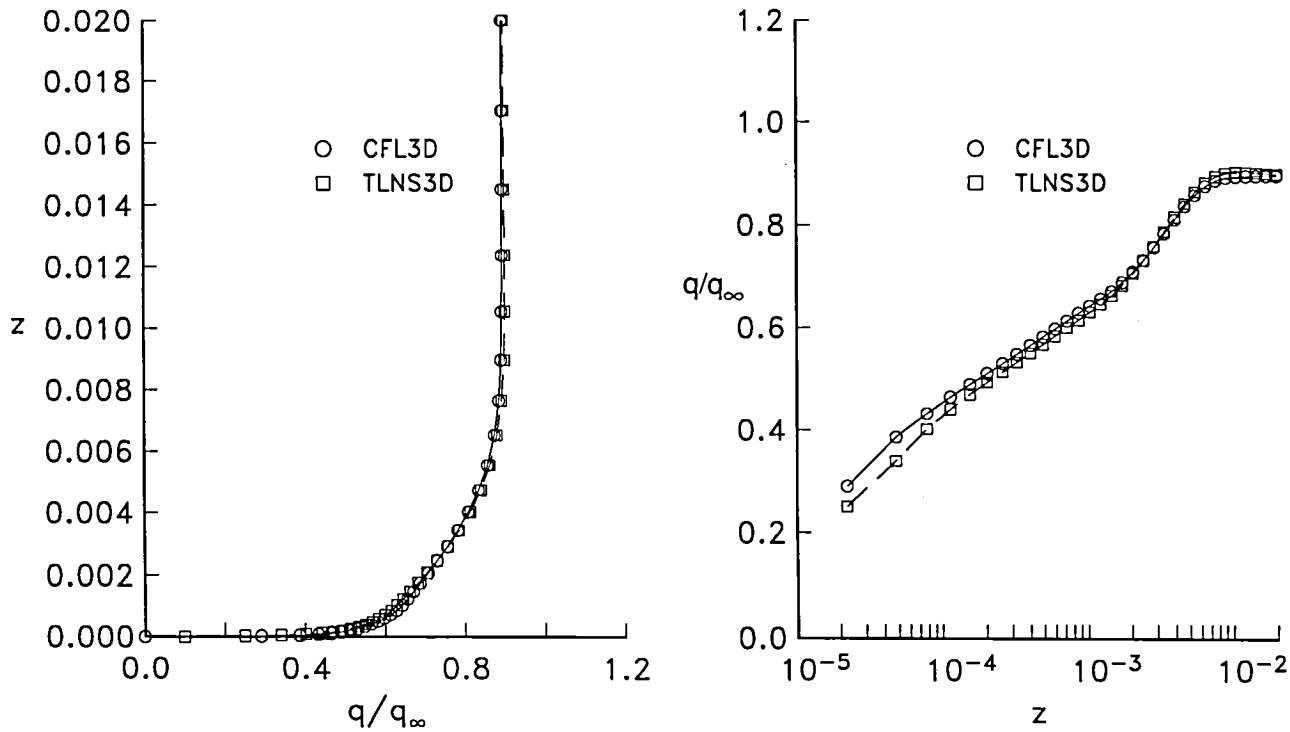

(b) $\eta = 0, \xi = 0.75$.

Figure 36. Lower-surface boundary-layer profiles for the ONERA M6 wing. $289 \times 65 \times 49$ grid.

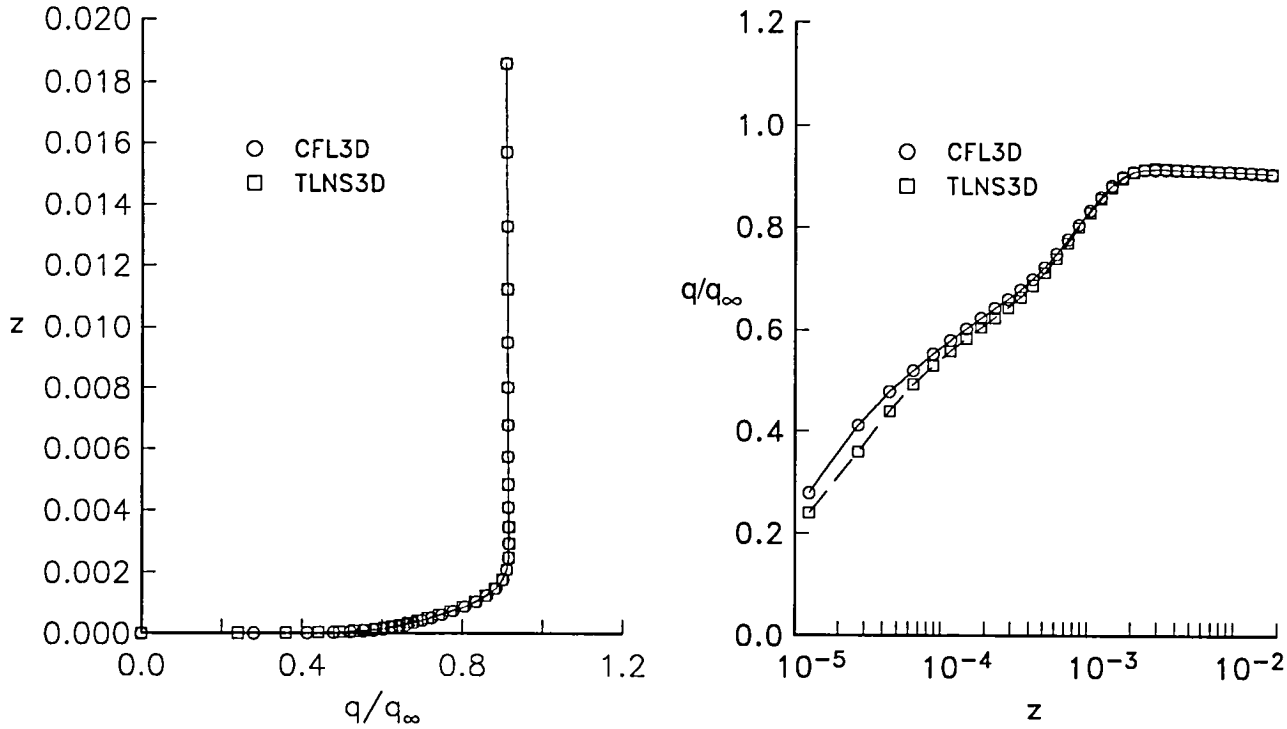

(c) $\eta = 0.5, \xi = 0.25$.

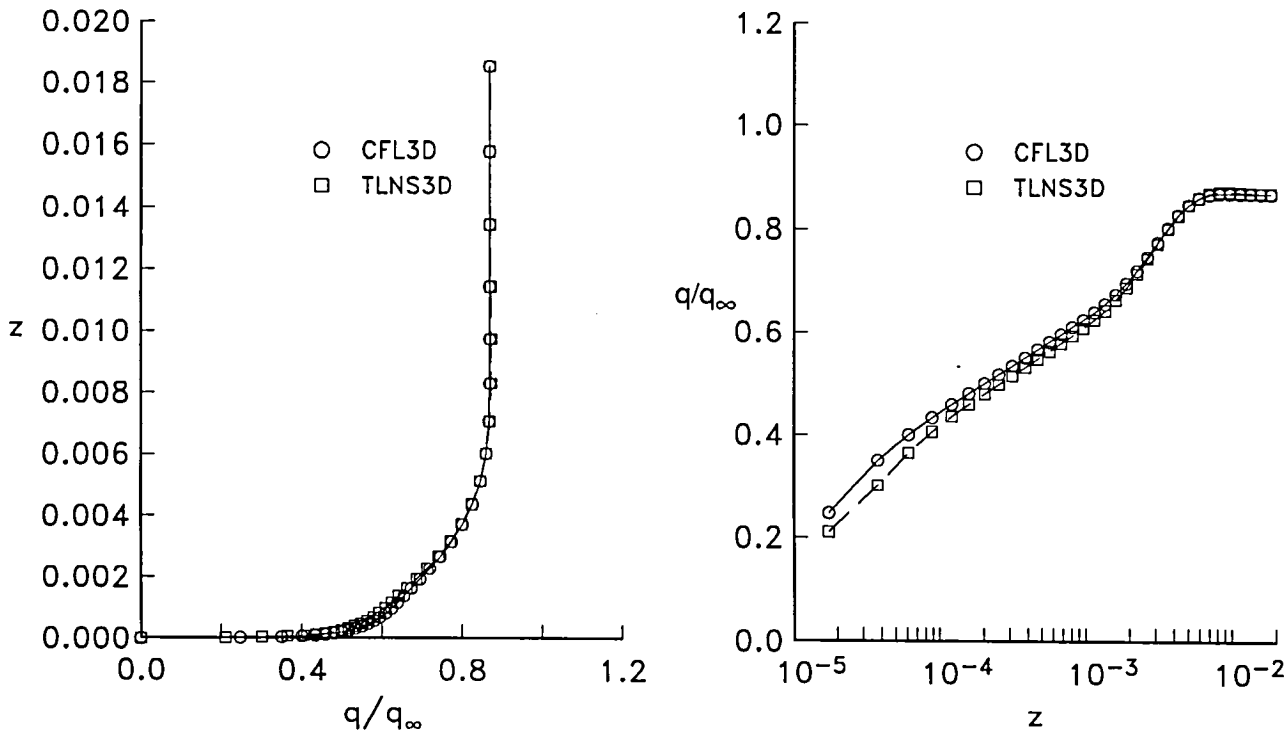

(d) $\eta = 0.5, \xi = 0.75$.

Figure 36. Continued.

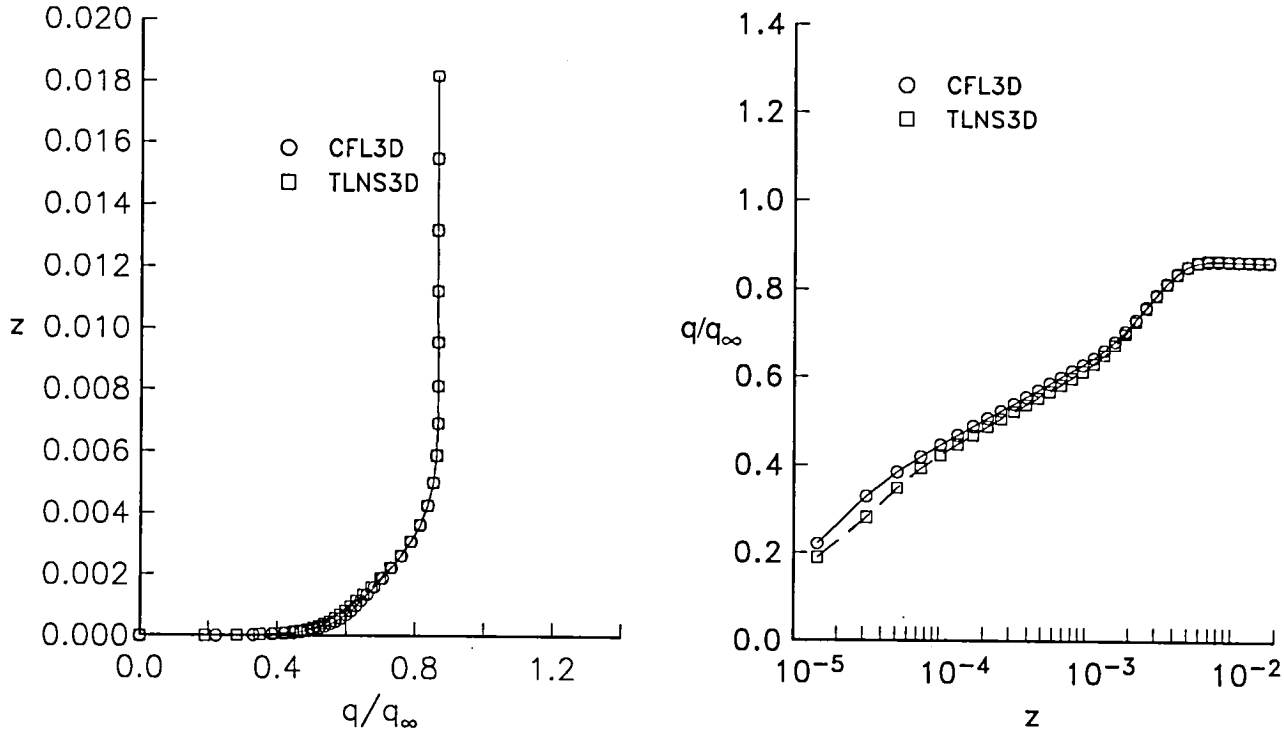

(e) $\eta = 0.8, \xi = 0.25$.

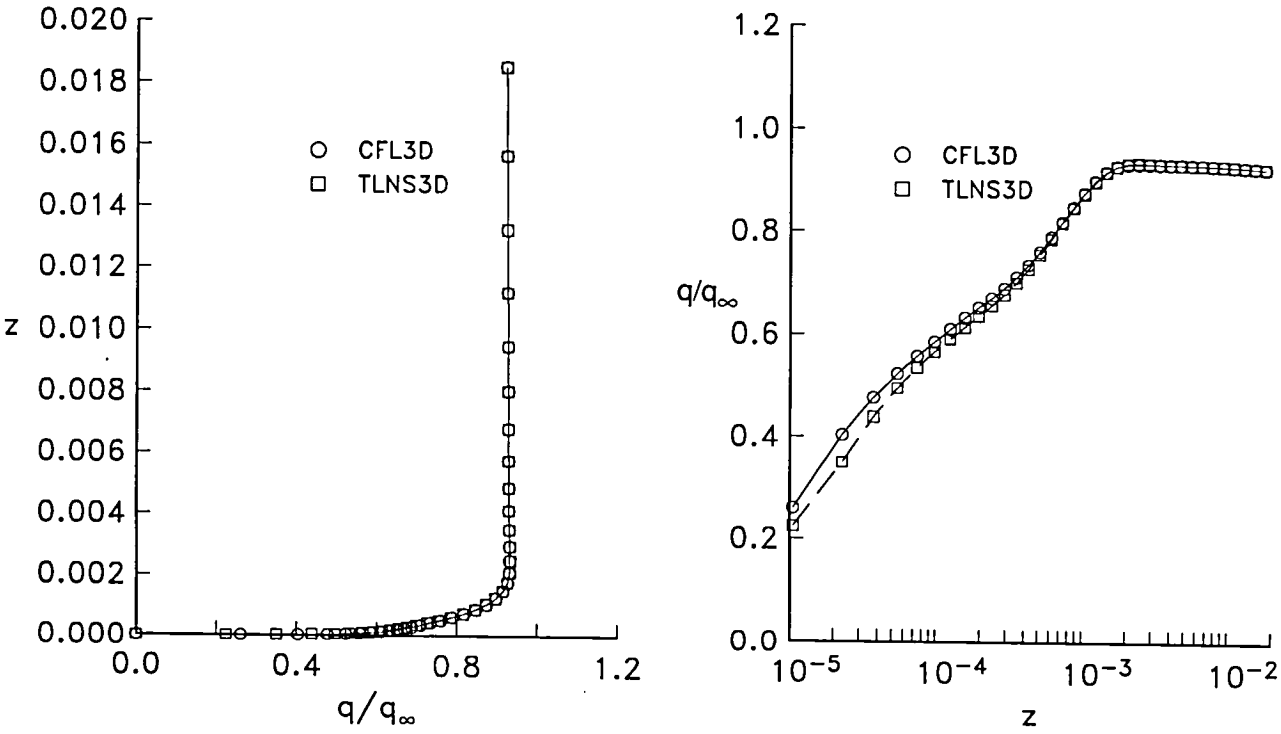

(f) $\eta = 0.8, \xi = 0.75$.

Figure 36. Concluded.

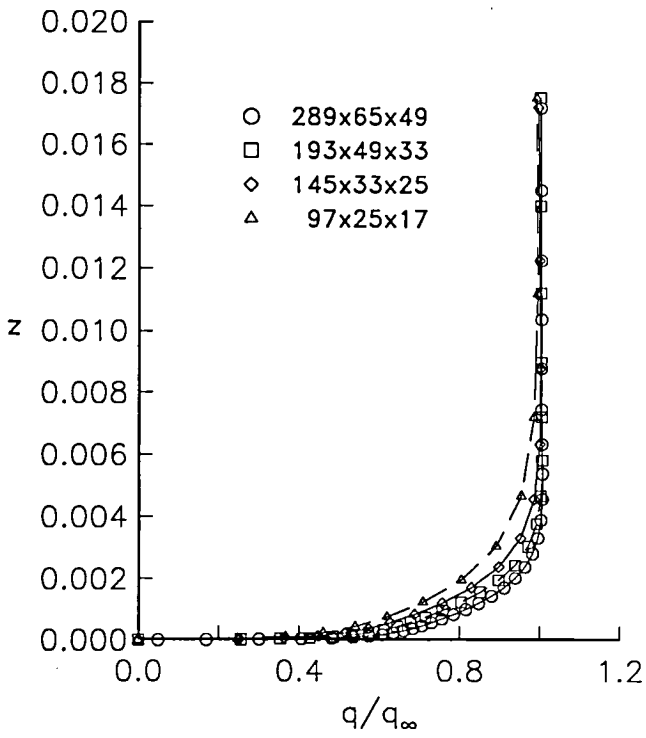

(a) TLNS3D—standard.

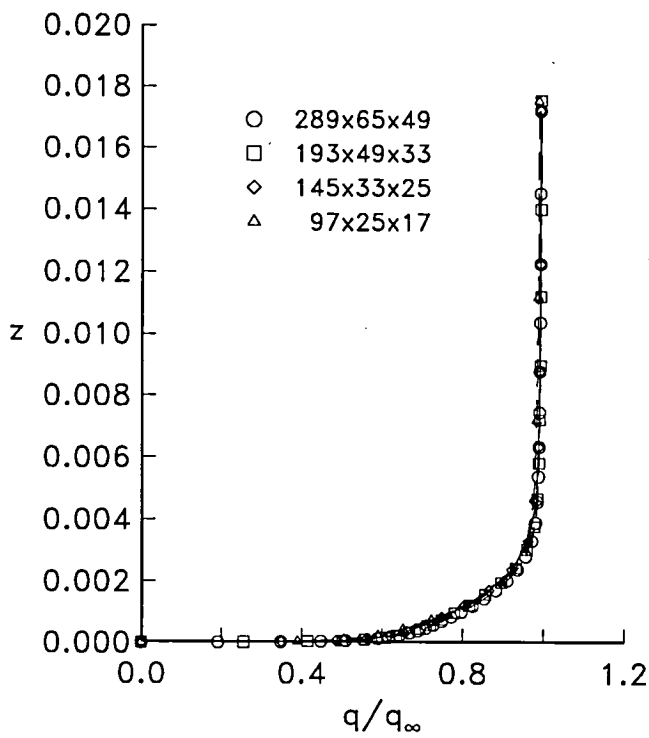

(b) CFL3D—standard.

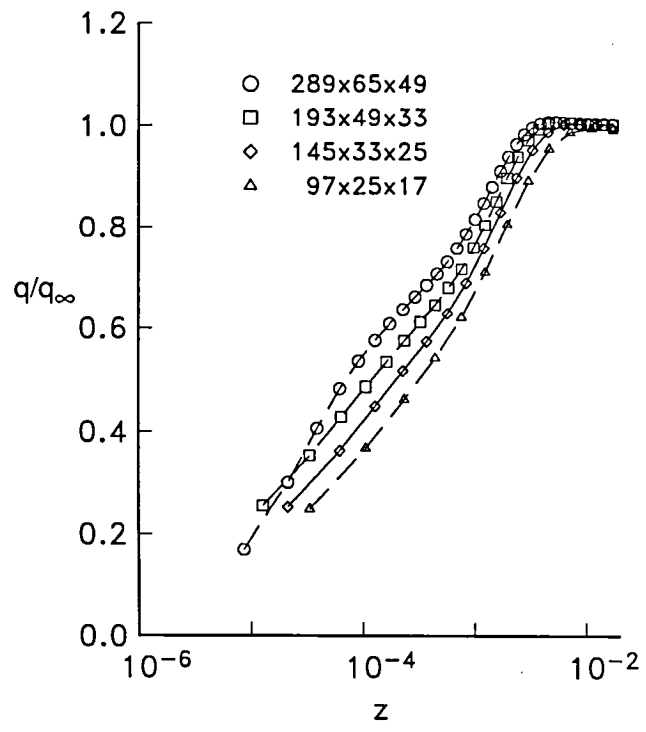

(c) TLNS3D—semilog.

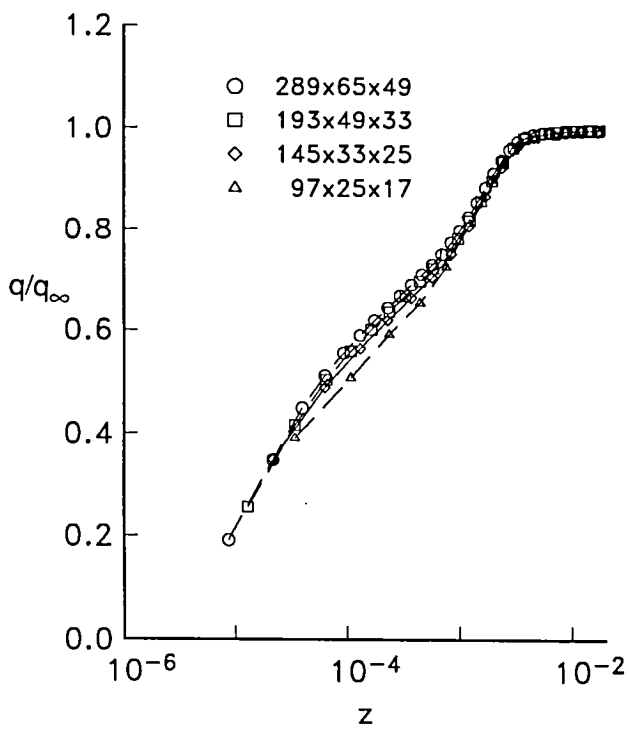

(d) CFL3D—semilog.

Figure 37. Effect of grid refinement on the upper-surface boundary-layer profiles for the Lockheed Wing B. $\eta = 0; \xi = 0.25$.

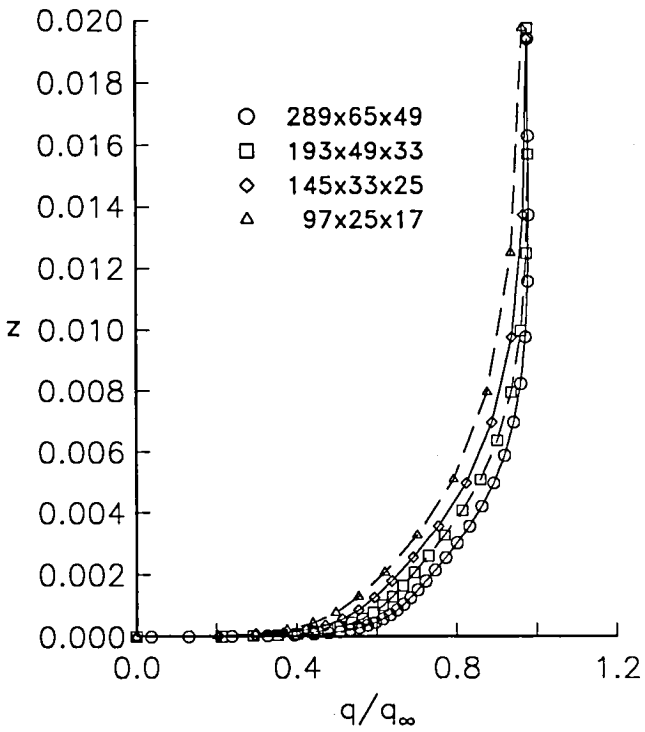

(a) TLNS3D—standard.

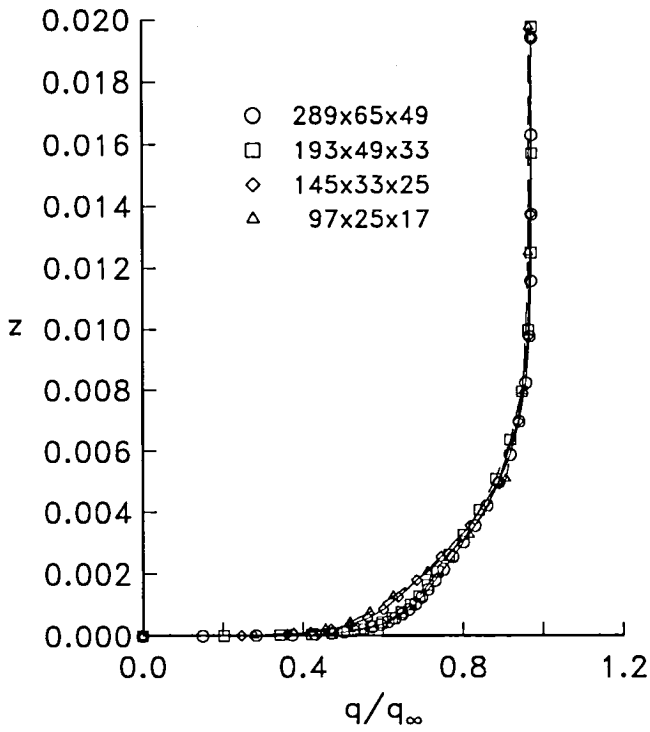

(b) CFL3D—standard.

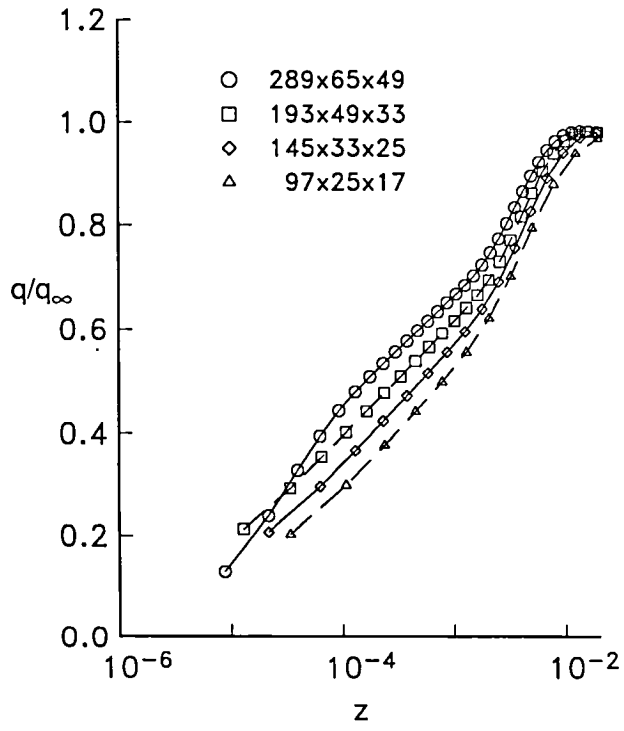

(c) TLNS3D—semilog.

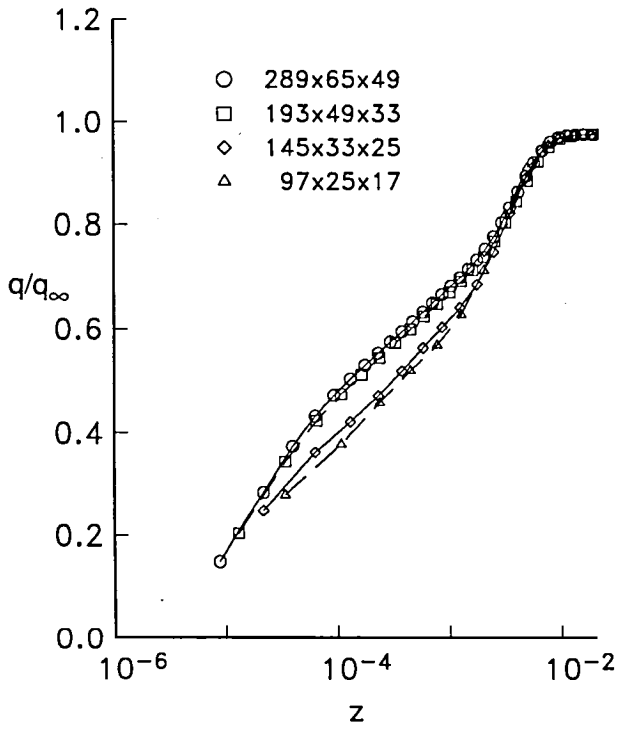

(d) CFL3D—semilog.

Figure 38. Effect of grid refinement on the upper-surface boundary-layer profiles for the Lockheed Wing B. $\eta = 0; \xi = 0.75$.

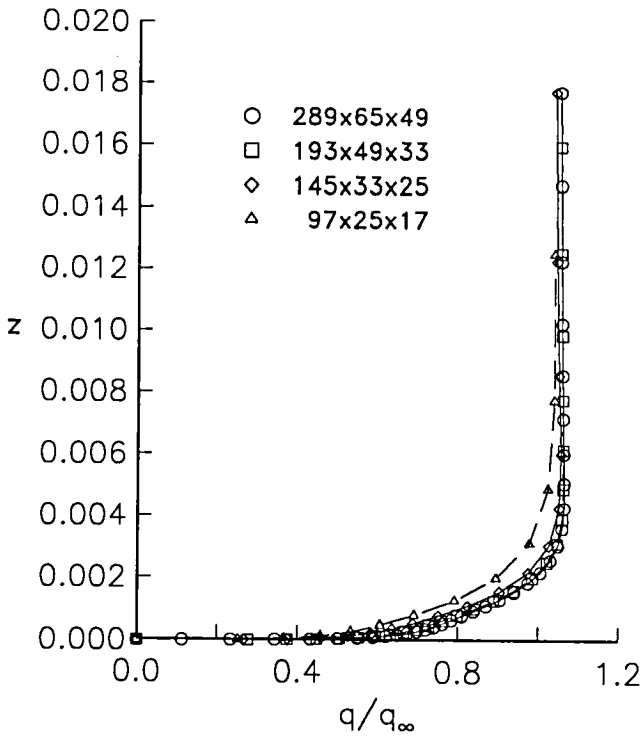

(a) TLNS3D—standard.

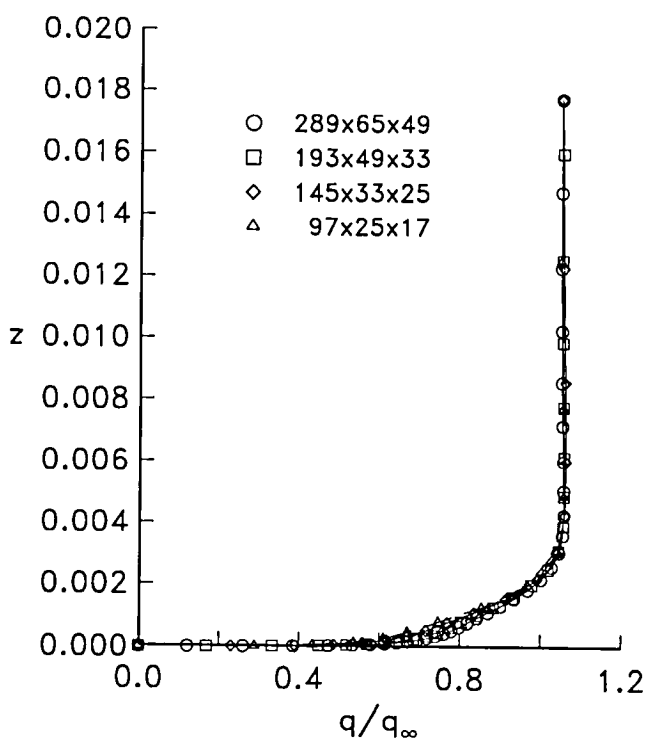

(b) CFL3D—standard.

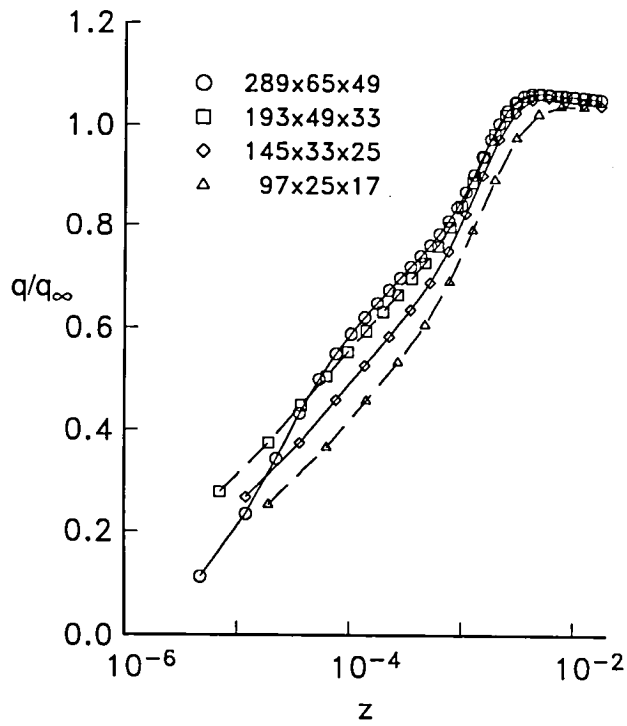

(c) TLNS3D—semilog.

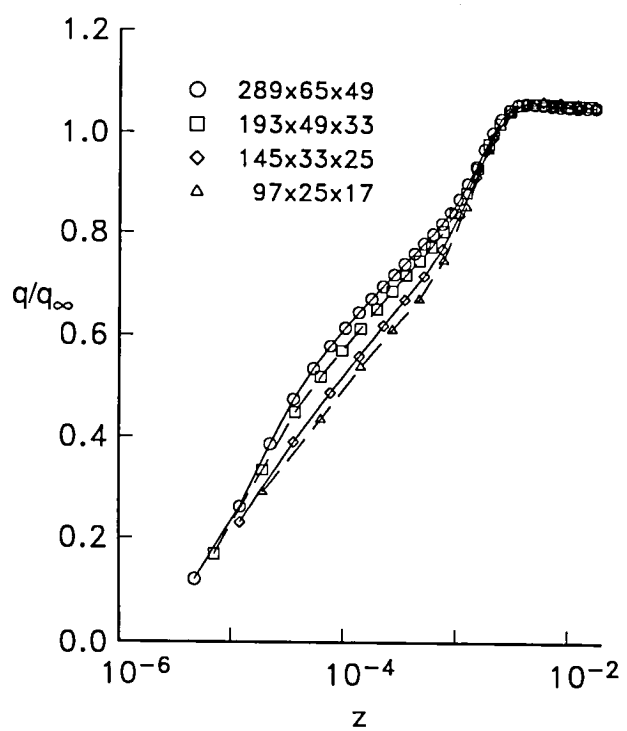

(d) CFL3D—semilog.

Figure 39. Effect of grid refinement on the upper-surface boundary-layer profiles for the Lockheed Wing B. $\eta = 0.5; \xi = 0.25$.

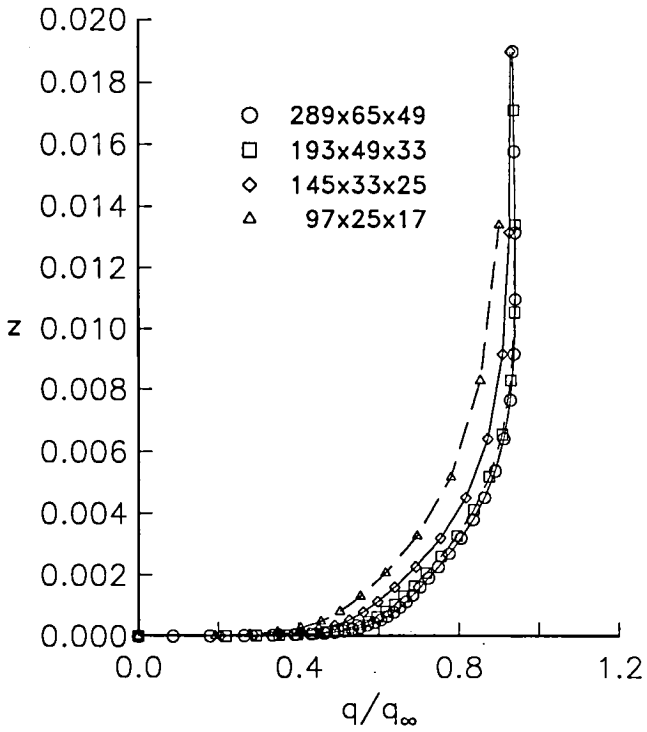

(a) TLNS3D—standard.

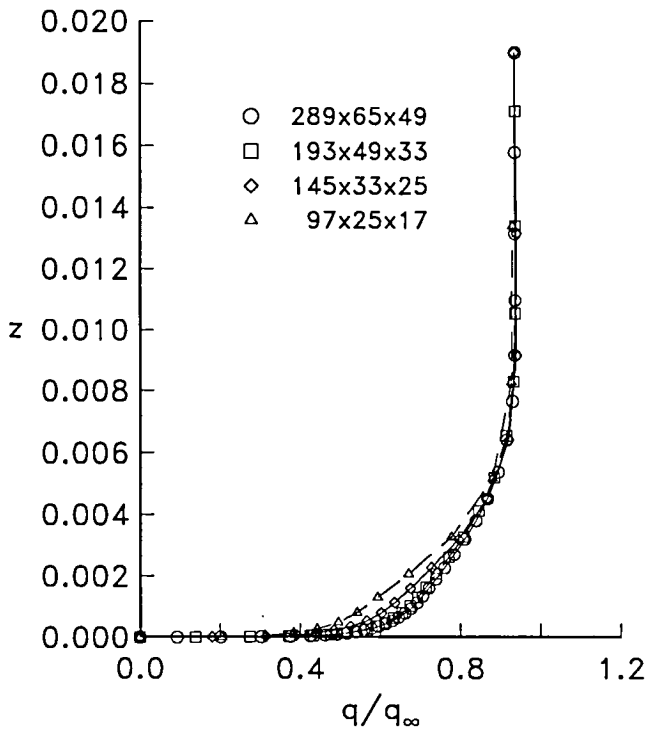

(b) CFL3D—standard.

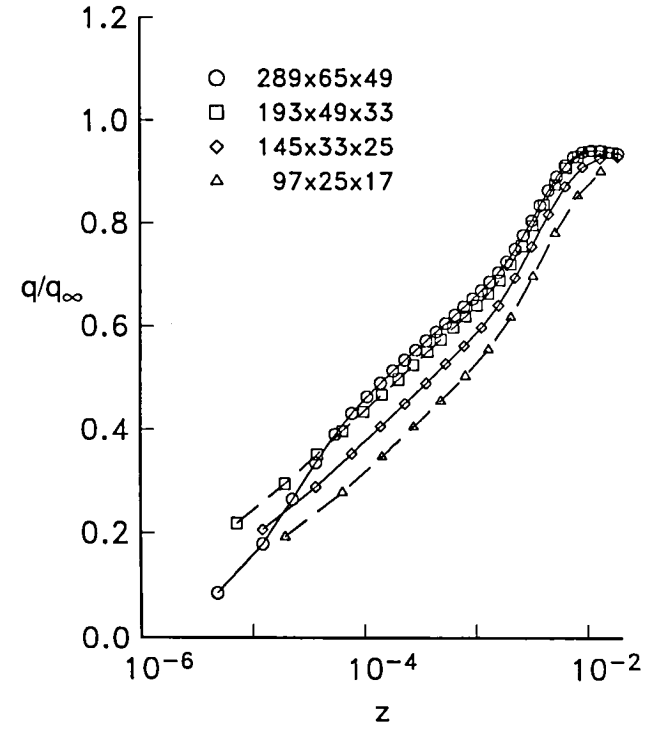

(c) TLNS3D—semilog.

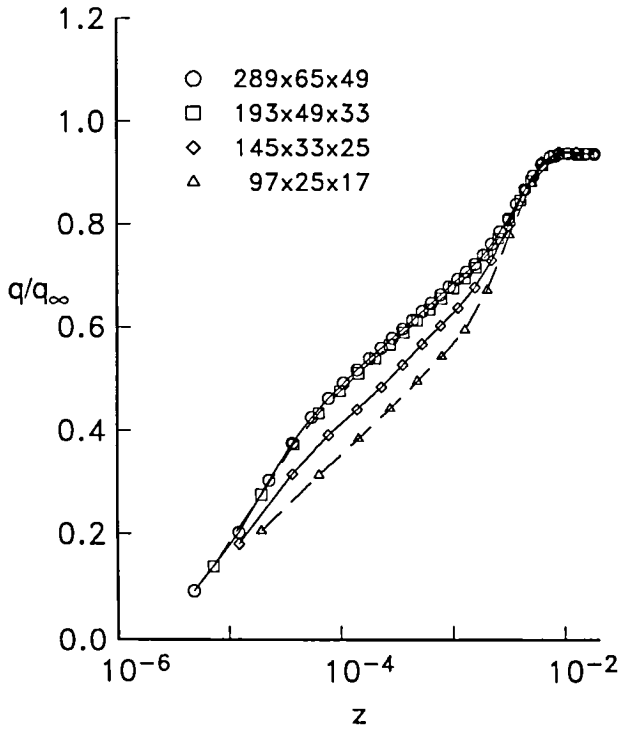

(d) CFL3D—semilog.

Figure 40. Effect of grid refinement on the upper-surface boundary-layer profiles for the Lockheed Wing B. $\eta = 0.5; \xi = 0.75$.

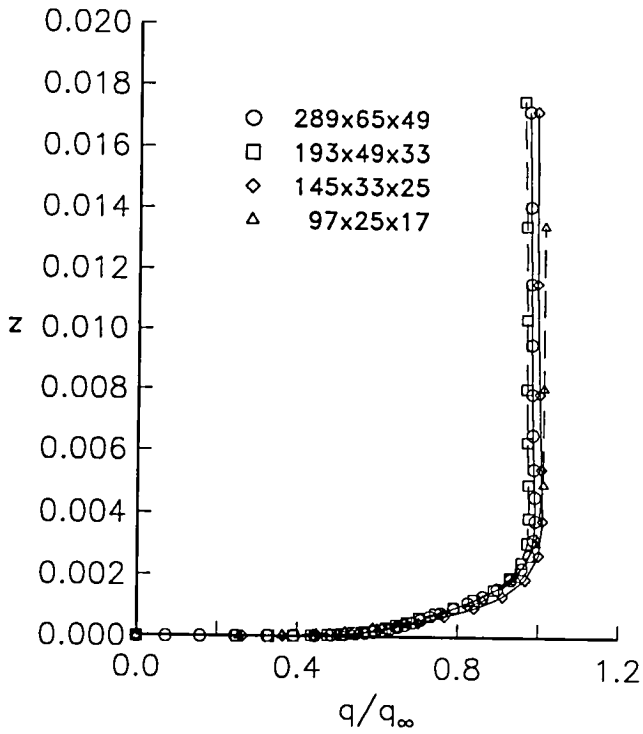

(a) TLNS3D—standard.

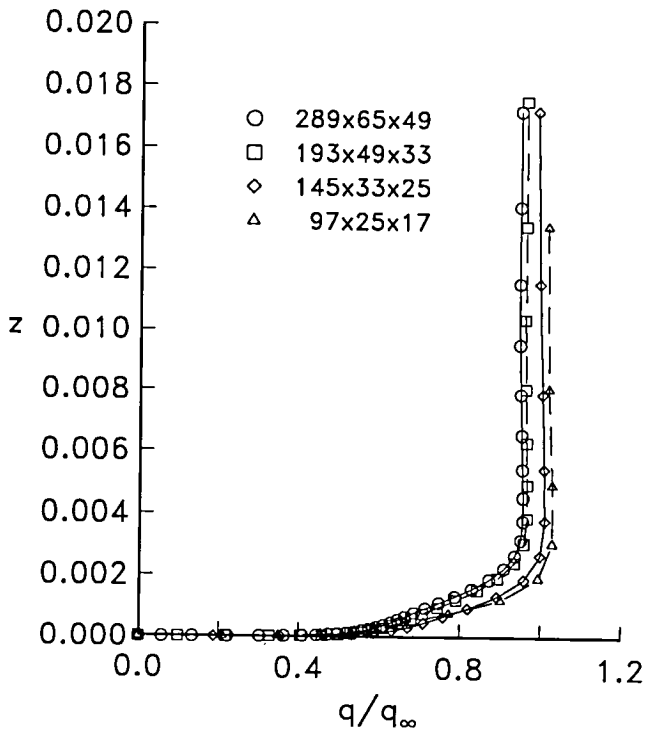

(b) CFL3D—standard.

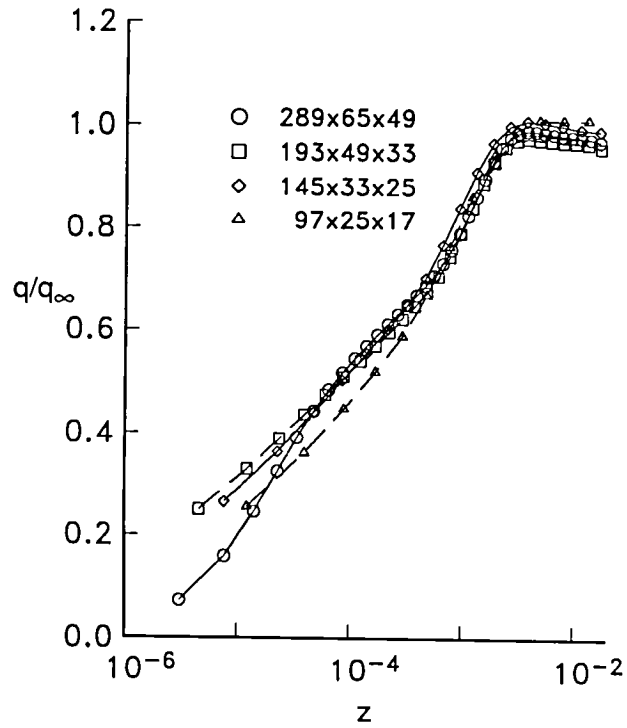

(c) TLNS3D—semilog.

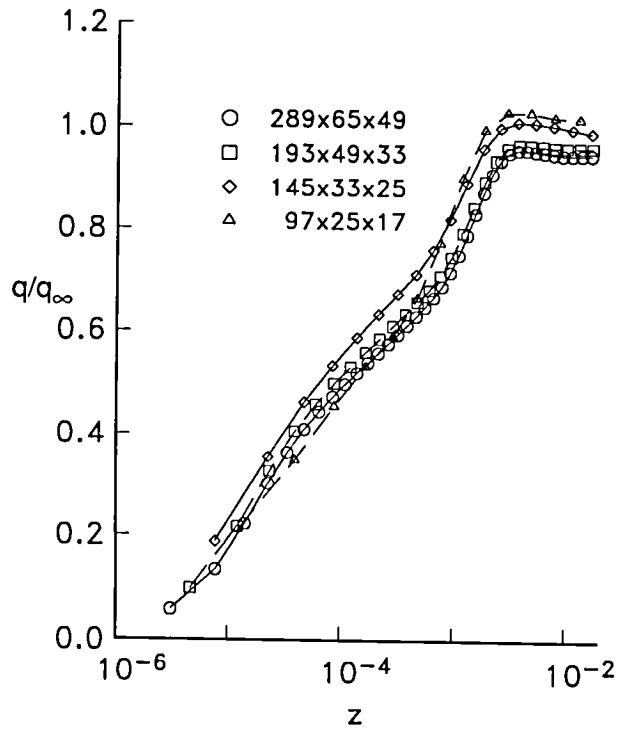

(d) CFL3D—semilog.

Figure 41. Effect of grid refinement on the upper-surface boundary-layer profiles for the Lockheed Wing B. $\eta = 0.8; \xi = 0.25$.

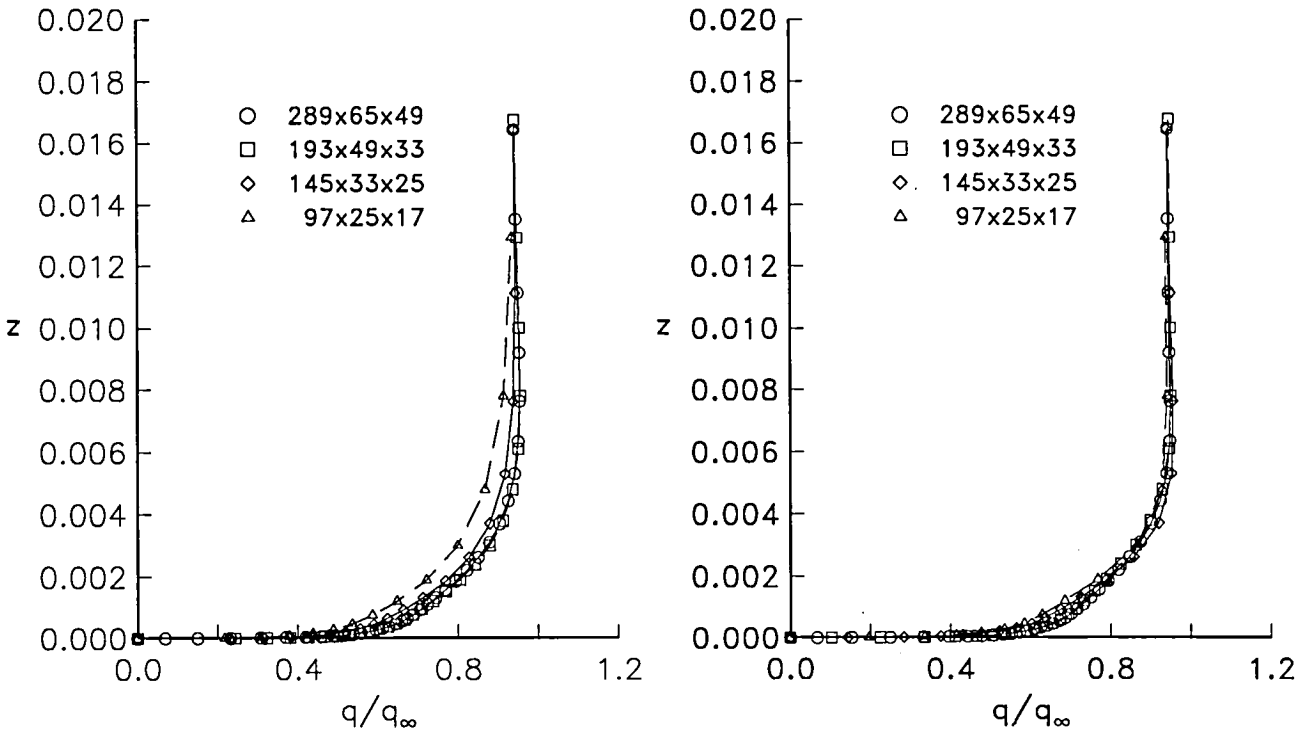

(a) TLNS3D—standard.

(b) CFL3D—standard.

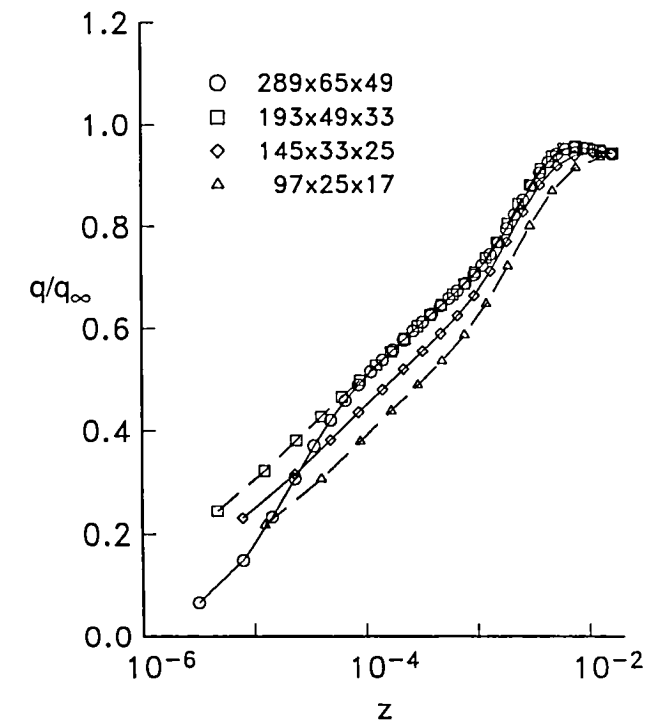

(c) TLNS3D—semilog.

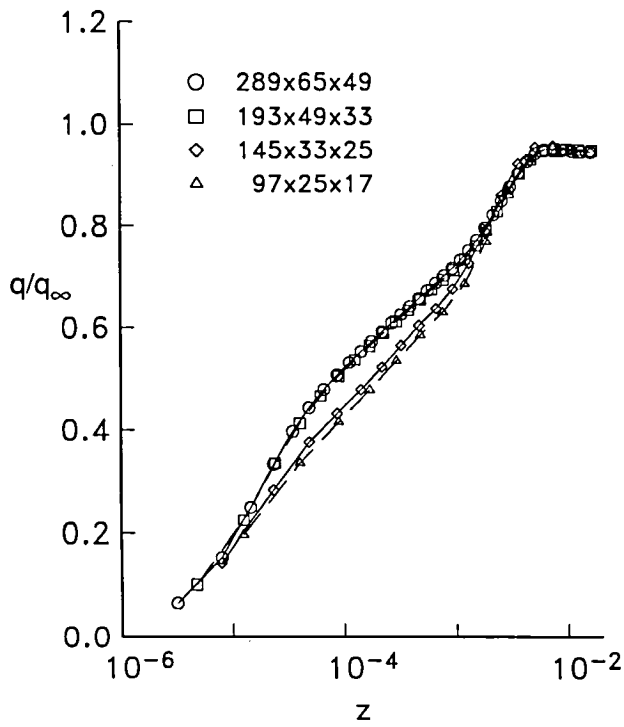

(d) CFL3D—semilog.

Figure 42. Effect of grid refinement on the upper-surface boundary-layer profiles for the Lockheed Wing B. $\eta = 0.8; \xi = 0.75$.

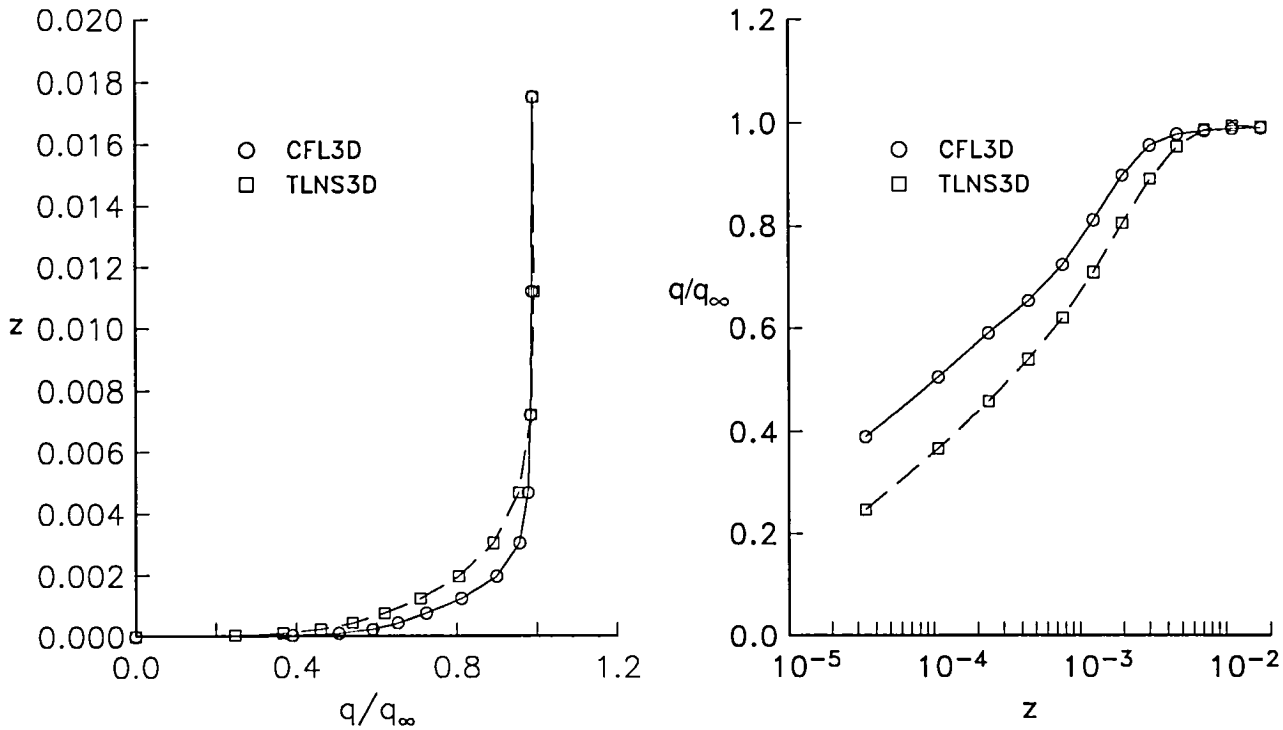

(a) $\eta = 0, \xi = 0.25$.

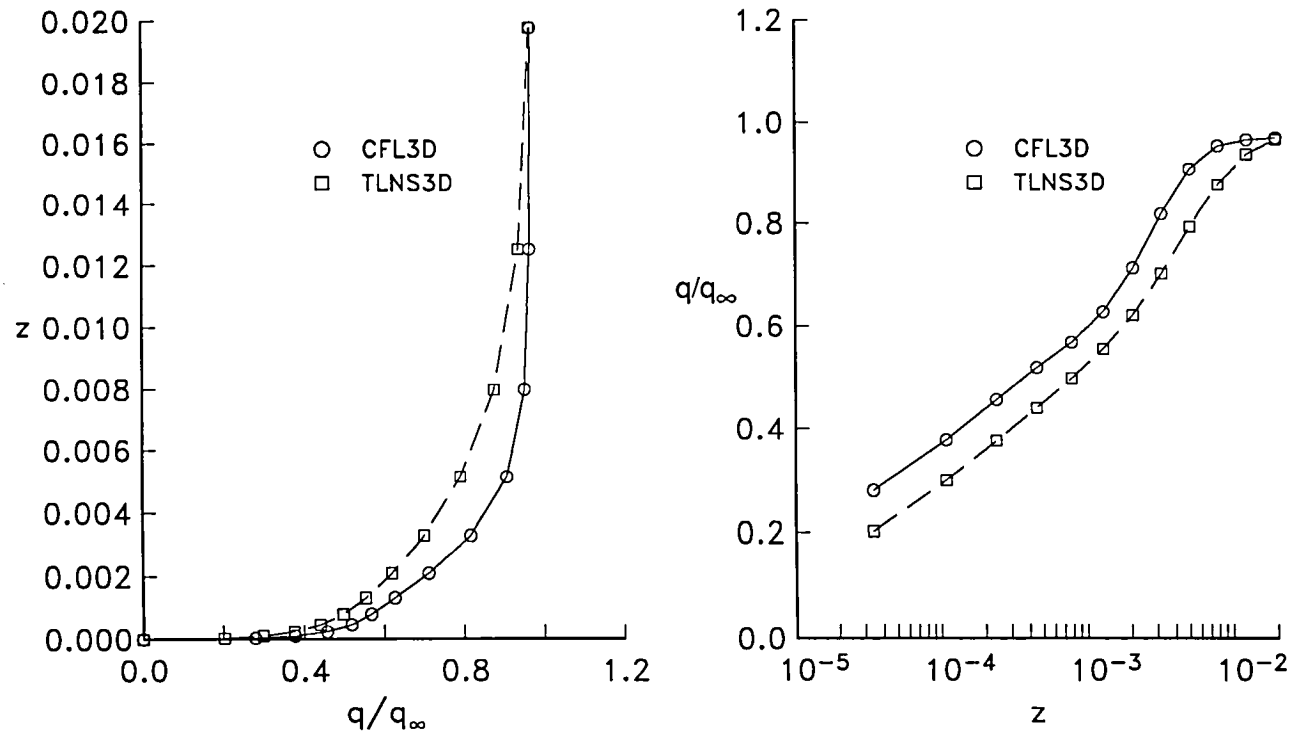

(b) $\eta = 0, \xi = 0.75$.

Figure 43. Upper-surface boundary-layer profiles for the Lockheed Wing B. 97 × 25 × 17 grid.

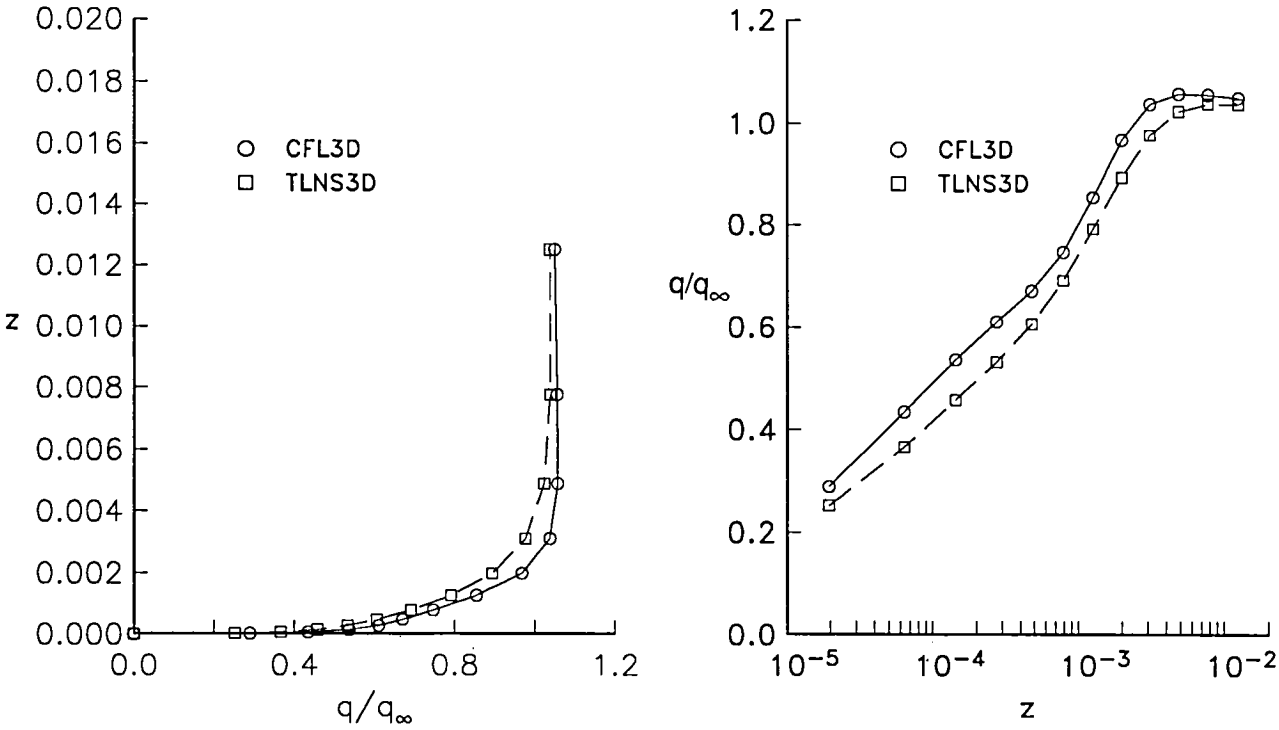

(c) $\eta = 0.5, \xi = 0.25$.

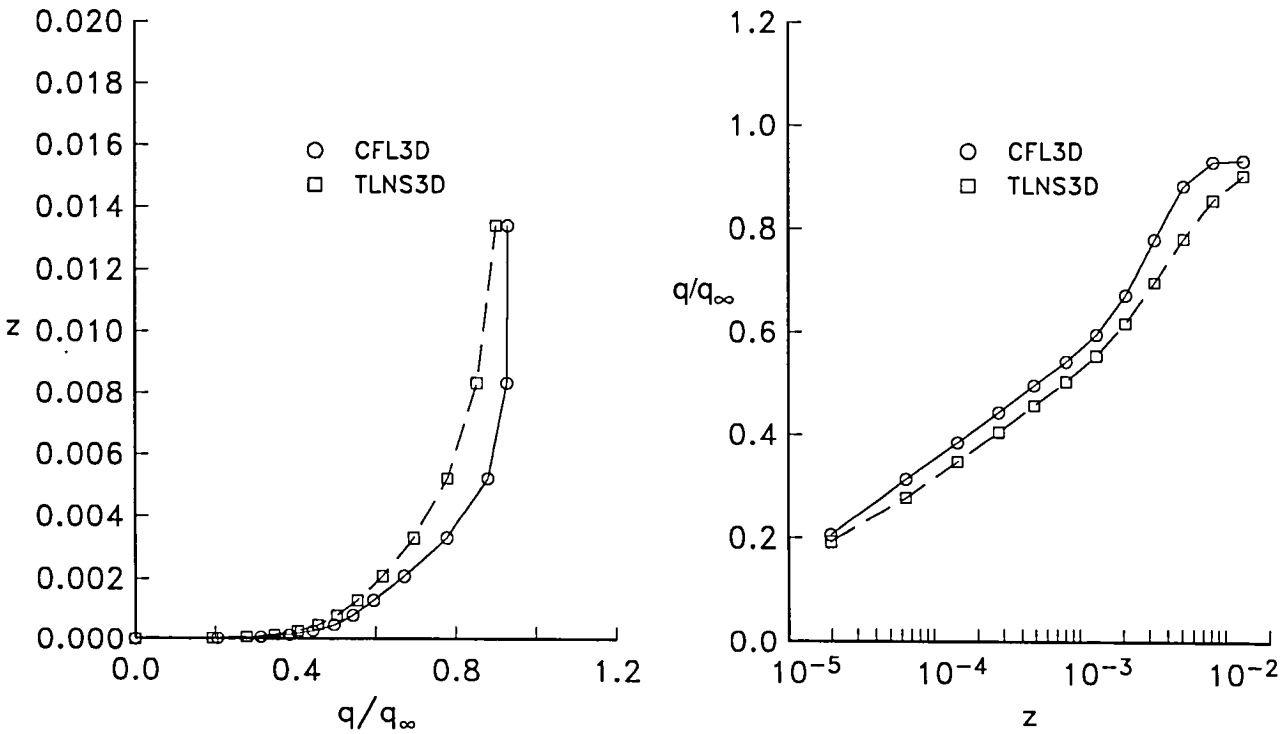

(d) $\eta = 0.5, \xi = 0.75$.

Figure 43. Continued.

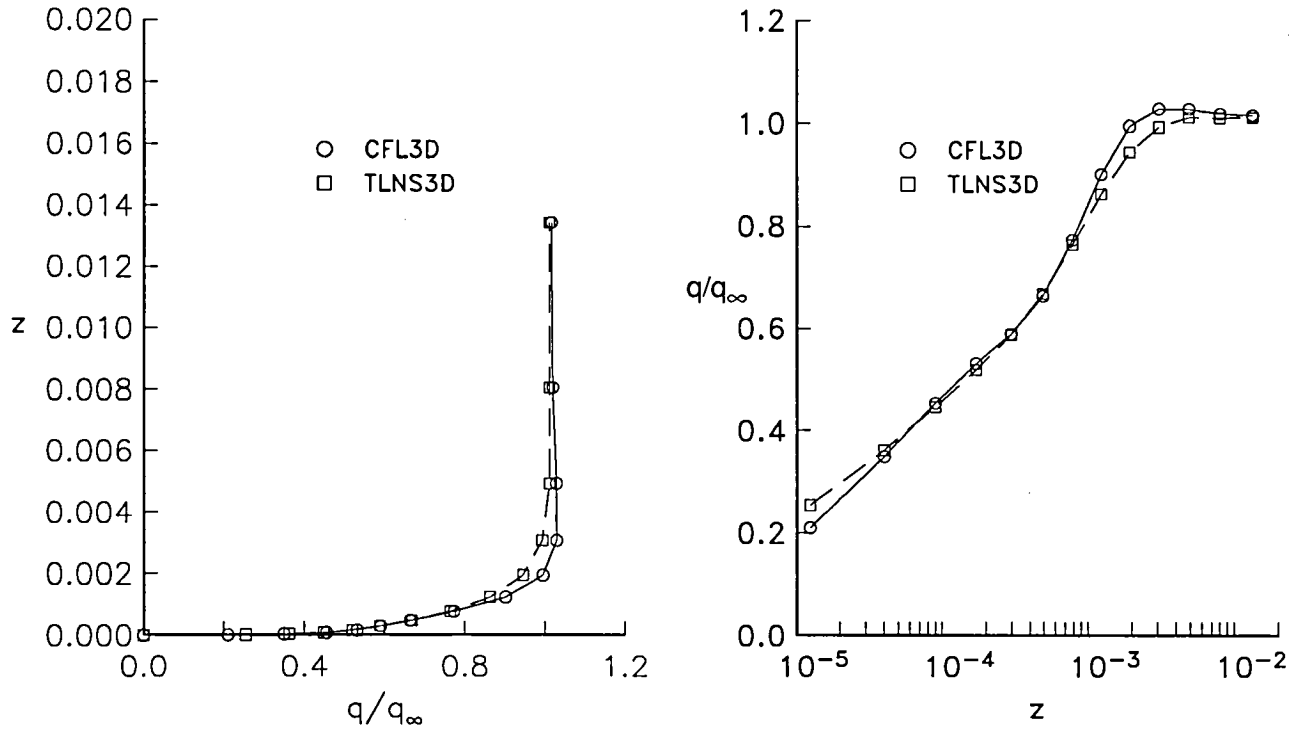

(e) $\eta = 0.8, \xi = 0.25$.

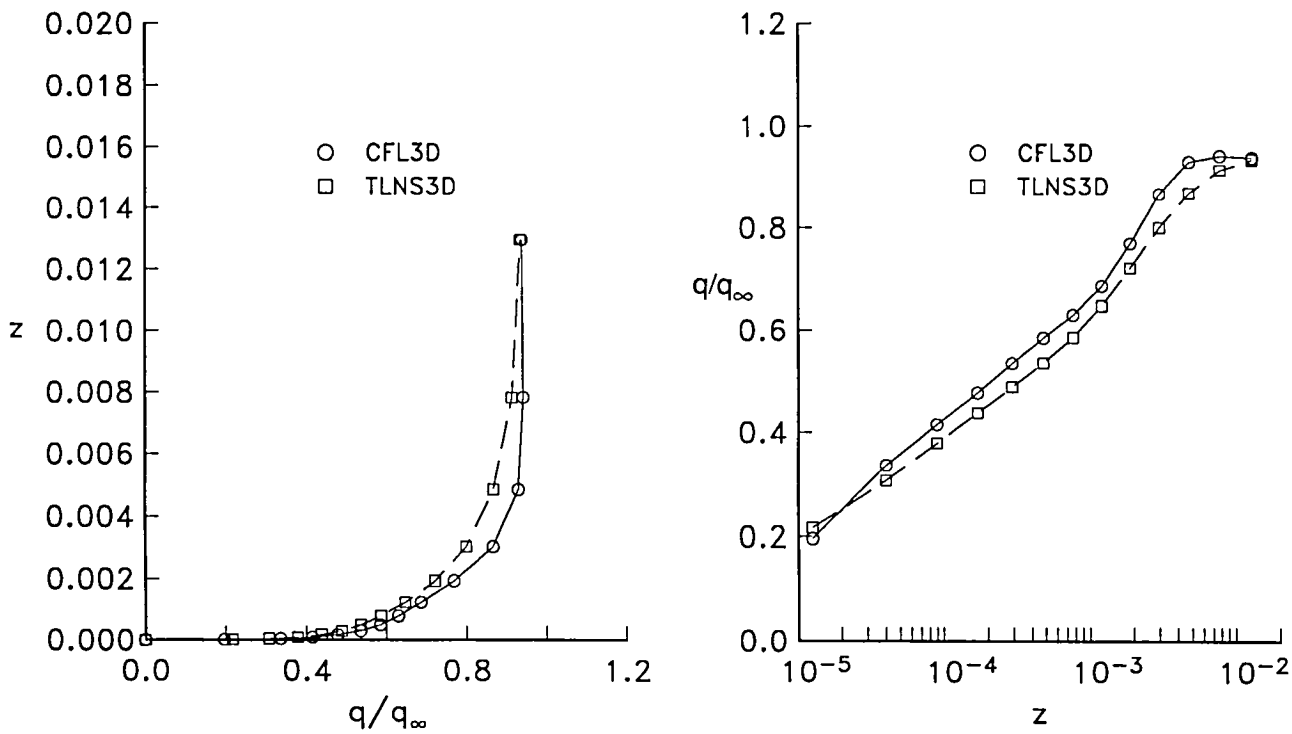

(f) $\eta = 0.8, \xi = 0.75$.

Figure 43. Concluded.

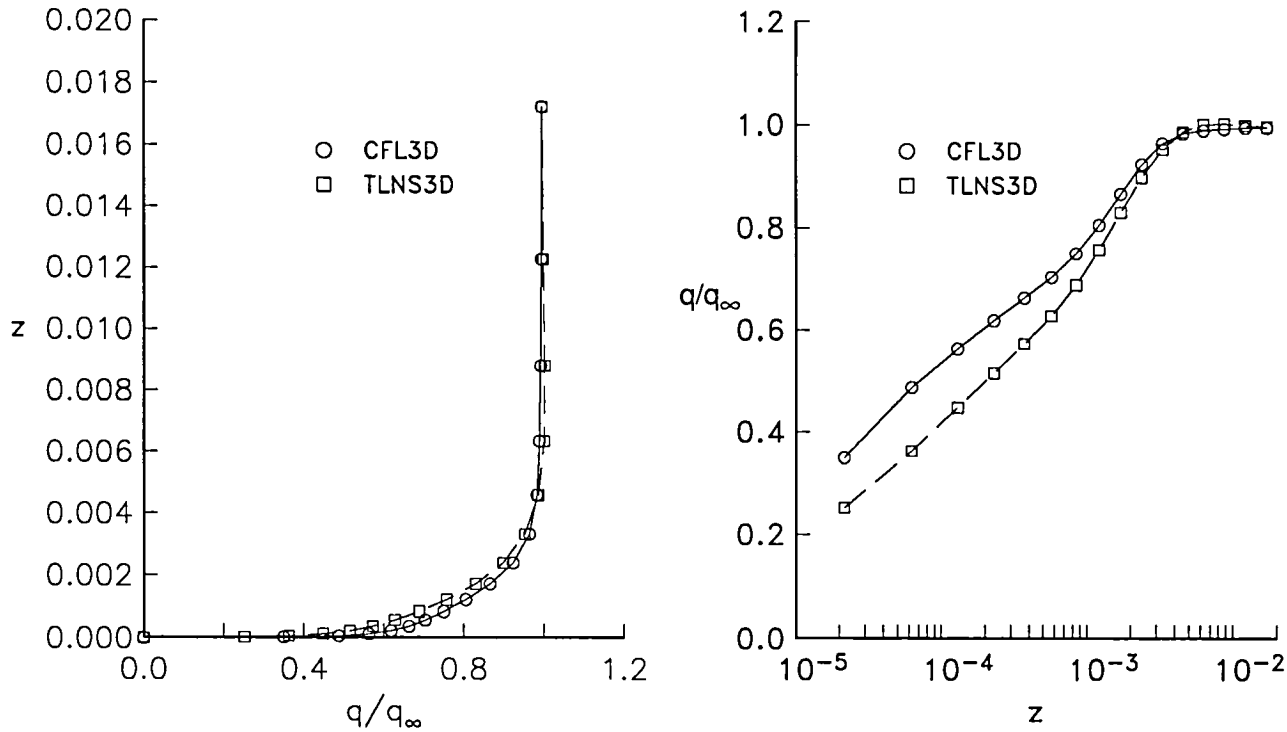

(a) $\eta = 0, \xi = 0.25$.

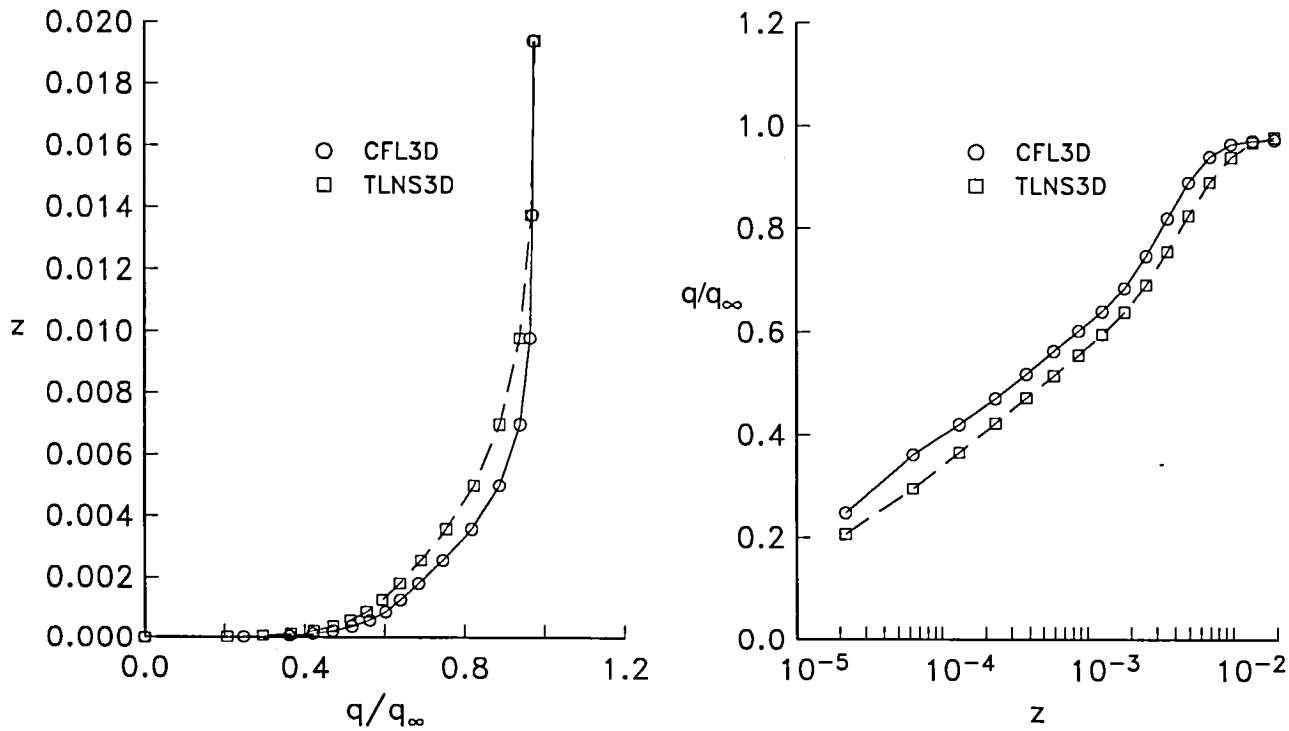

(b) $\eta = 0, \xi = 0.75$.

Figure 44. Upper-surface boundary-layer profiles for the Lockheed Wing B. 145 × 33 × 25 grid.

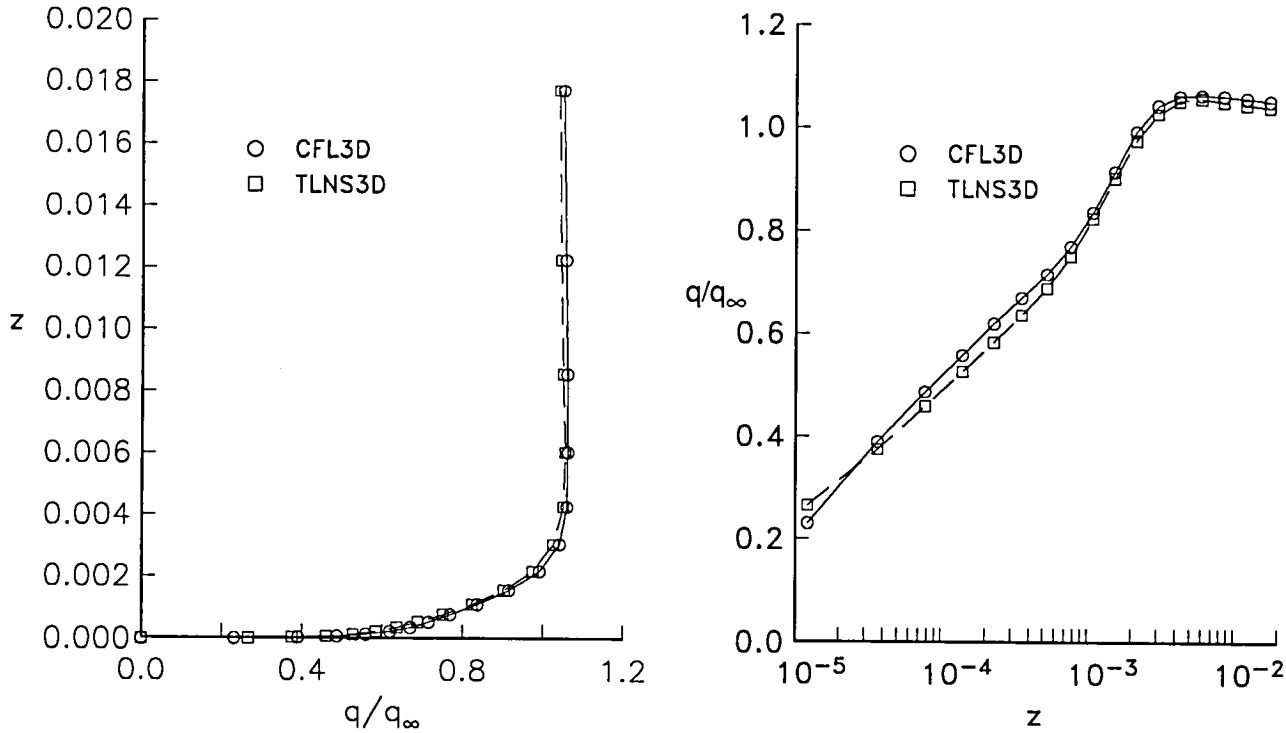

(c) $\eta = 0.5, \xi = 0.25$.

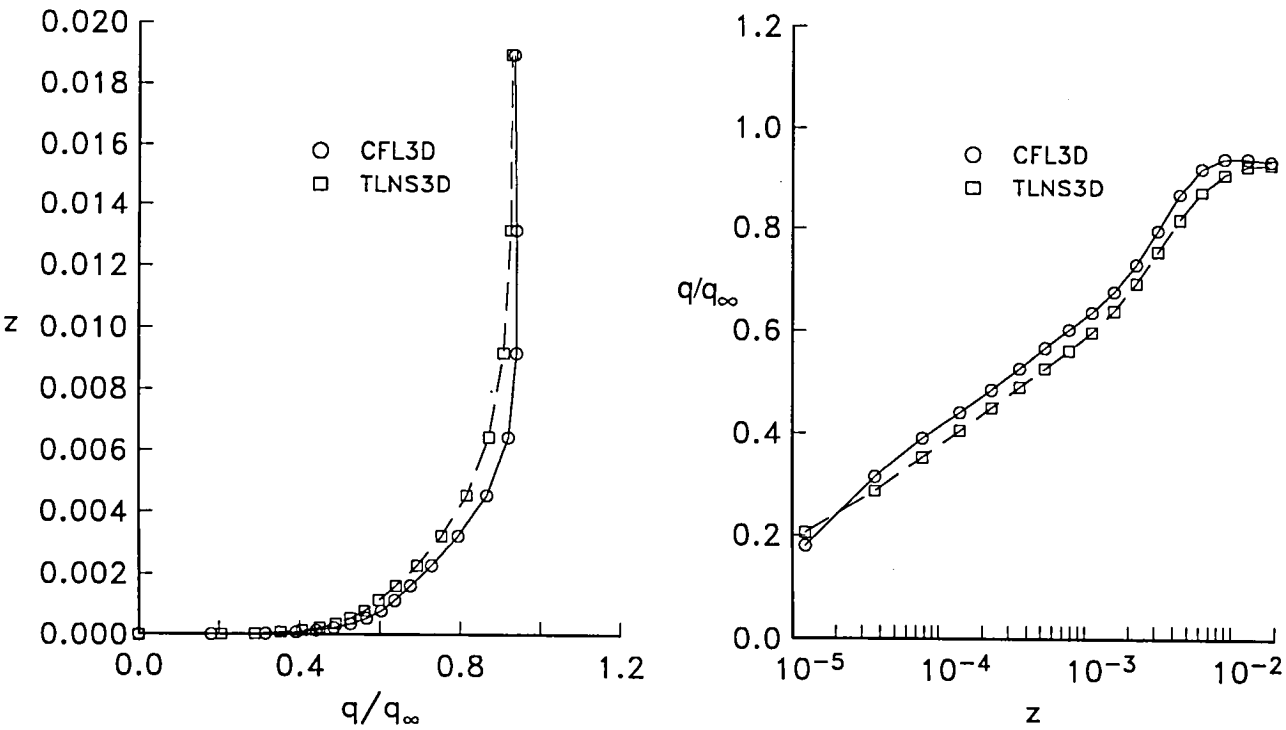

(d) $\eta = 0.5, \xi = 0.75$.

Figure 44. Continued.

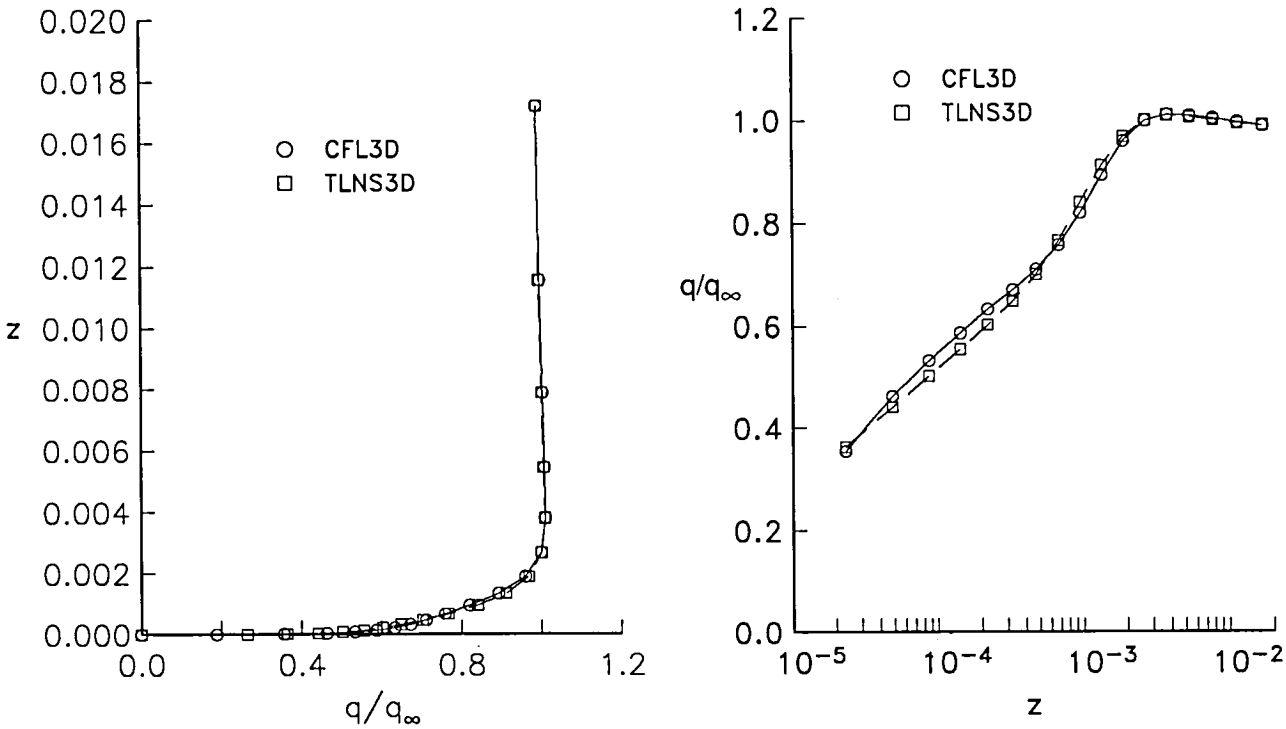

(e) $\eta = 0.8, \xi = 0.25$.

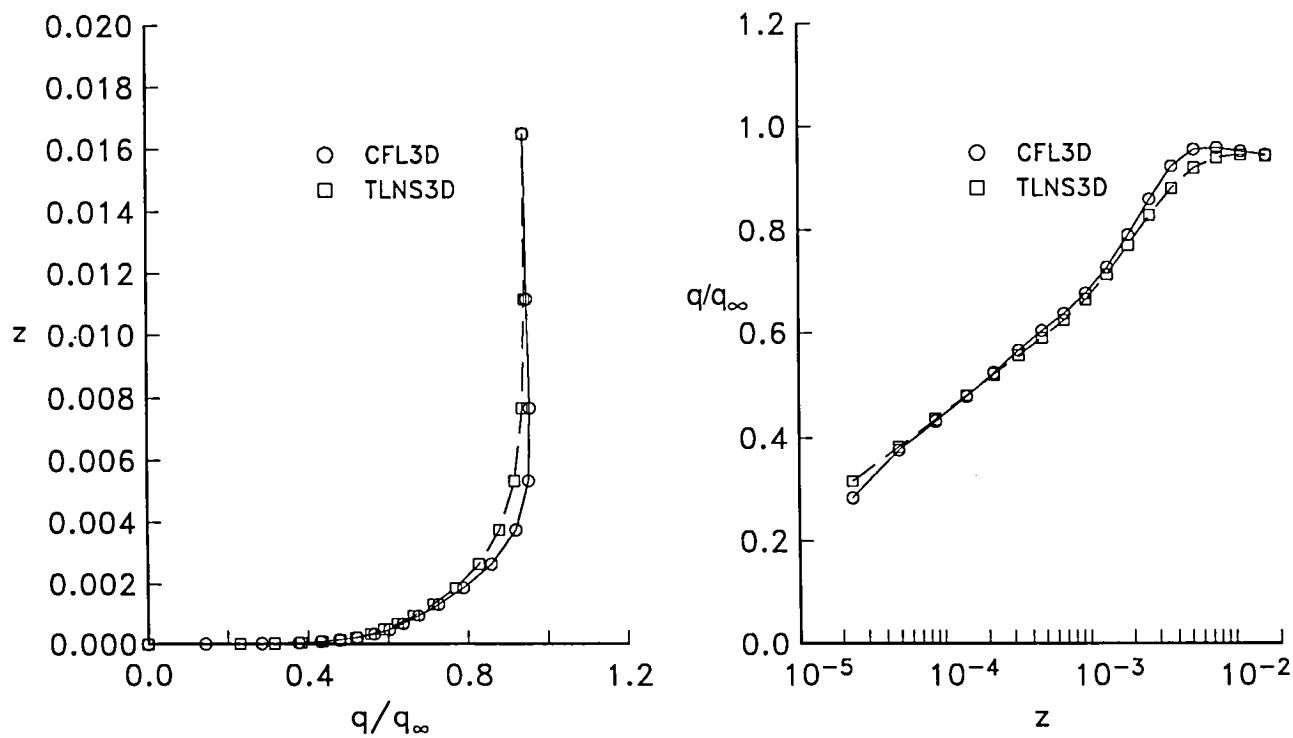

(f) $\eta = 0.8, \xi = 0.75$.

Figure 44. Concluded.

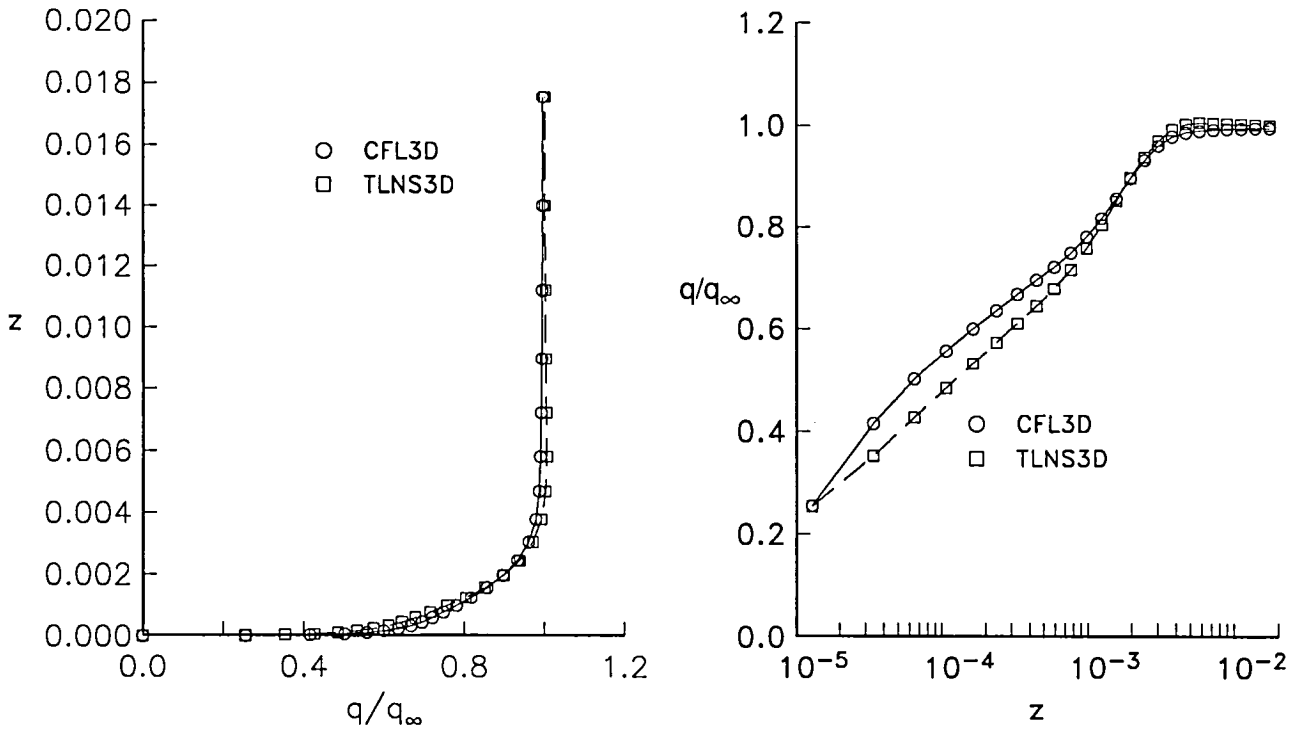

(a) $\eta = 0, \xi = 0.25$.

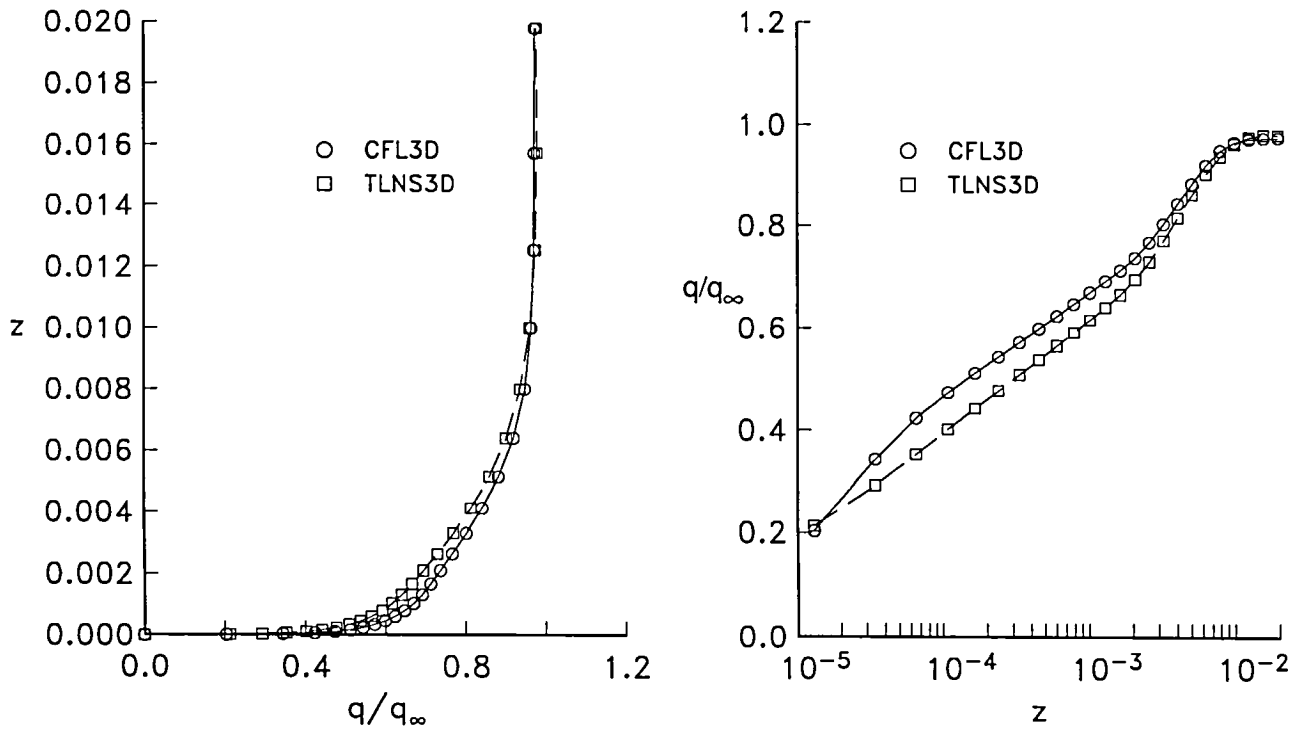

(b) $\eta = 0, \xi = 0.75$.

Figure 45. Upper-surface boundary-layer profiles for the Lockheed Wing B. 193 × 49 × 33 grid.

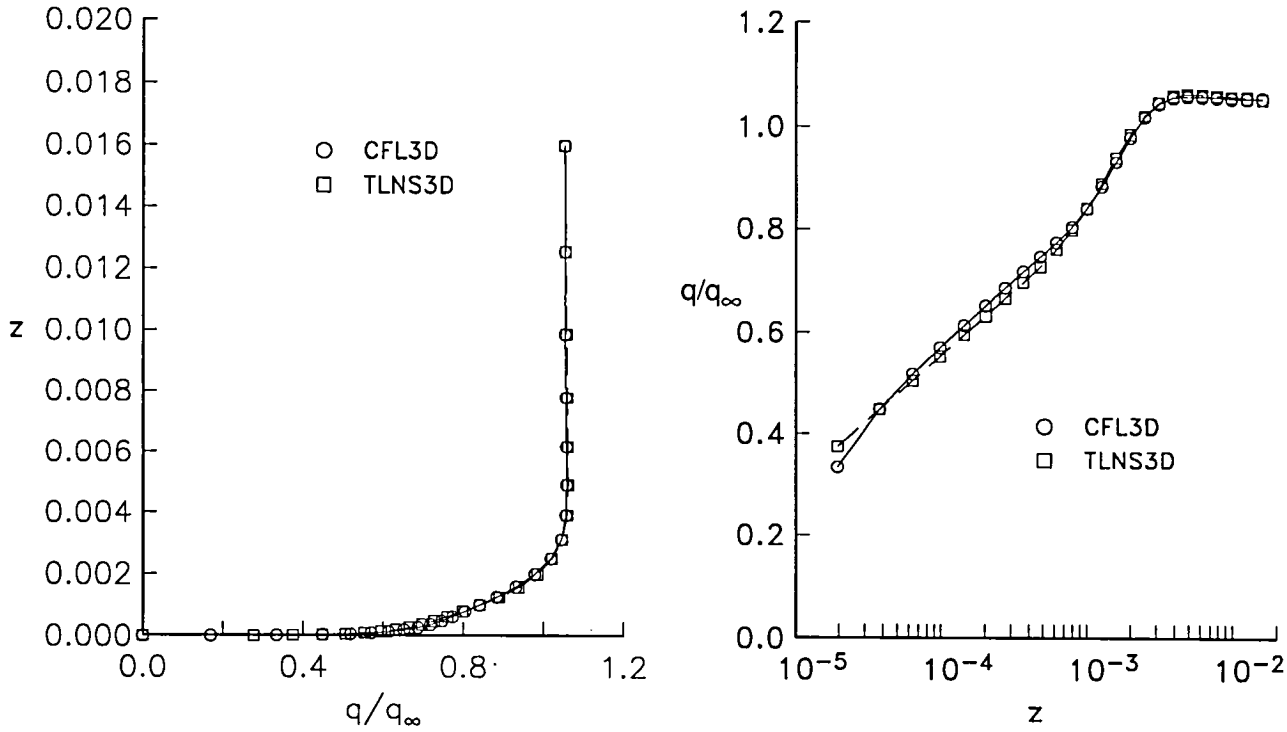

(c) $\eta = 0.5, \xi = 0.25$.

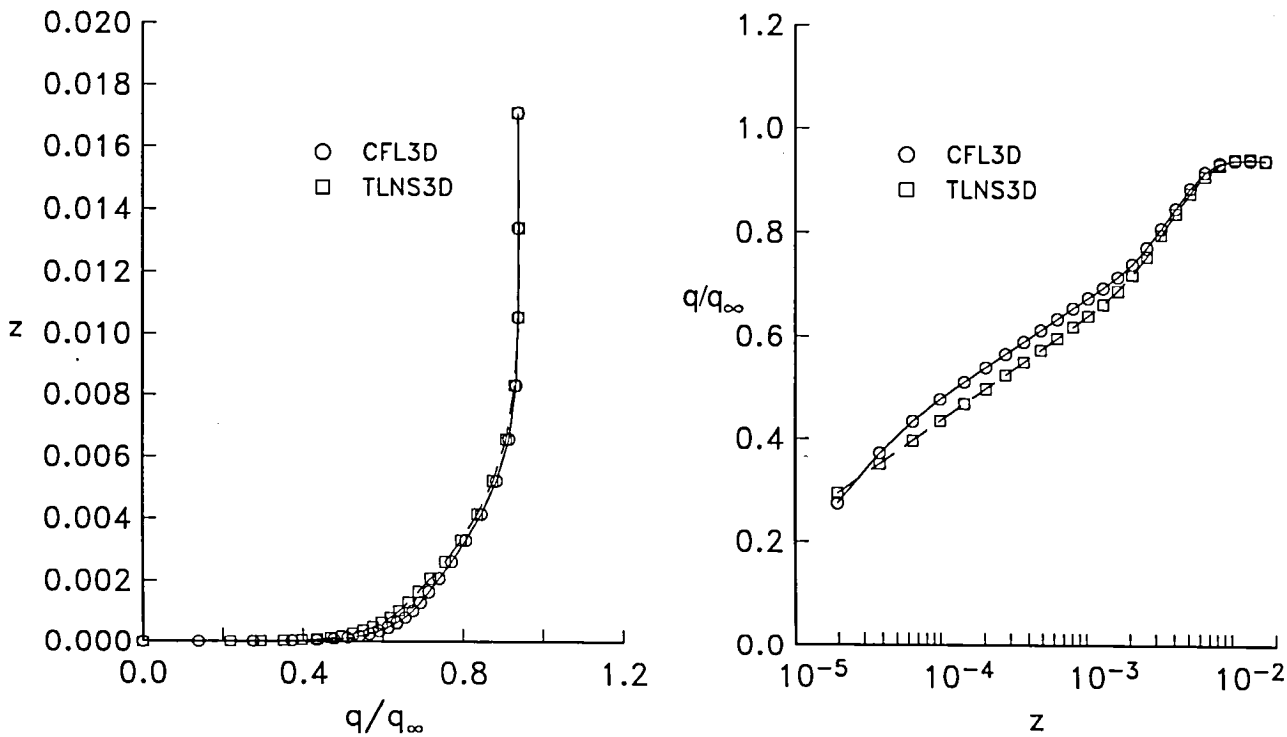

(d) $\eta = 0.5, \xi = 0.75$.

Figure 45. Continued.

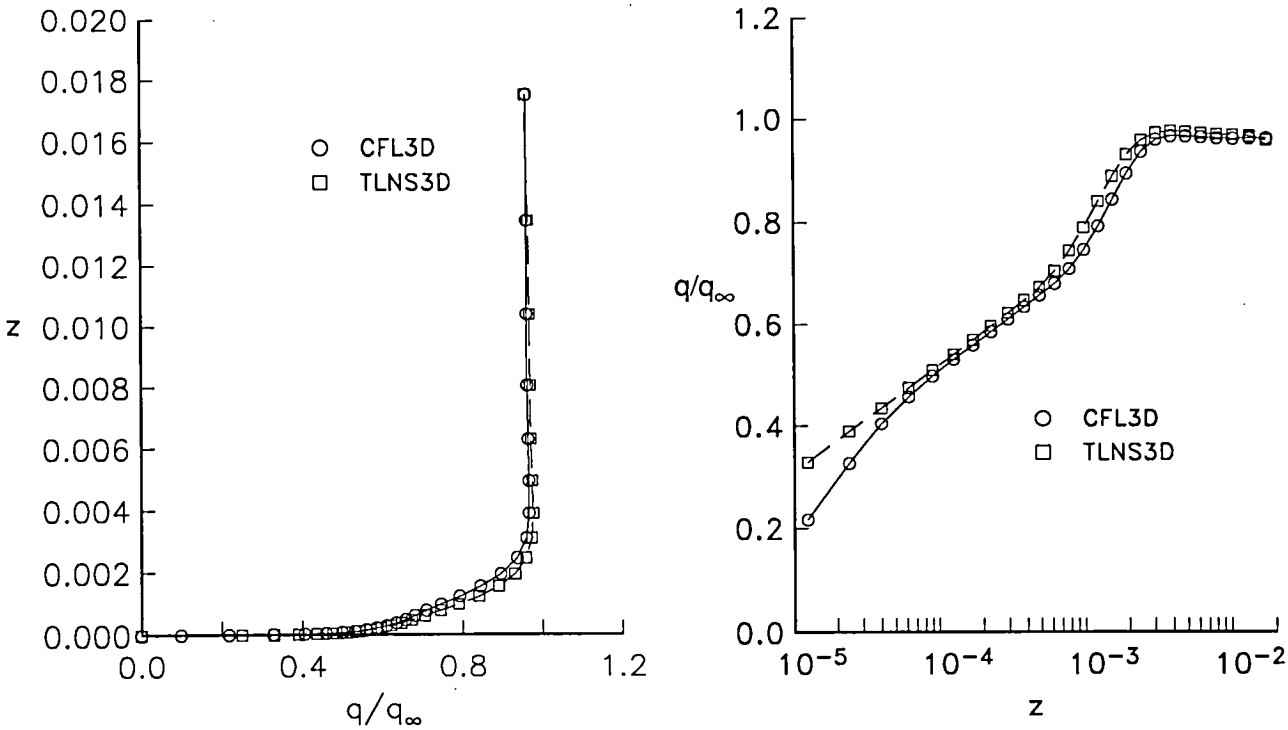

(e) $\eta = 0.8, \xi = 0.25$.

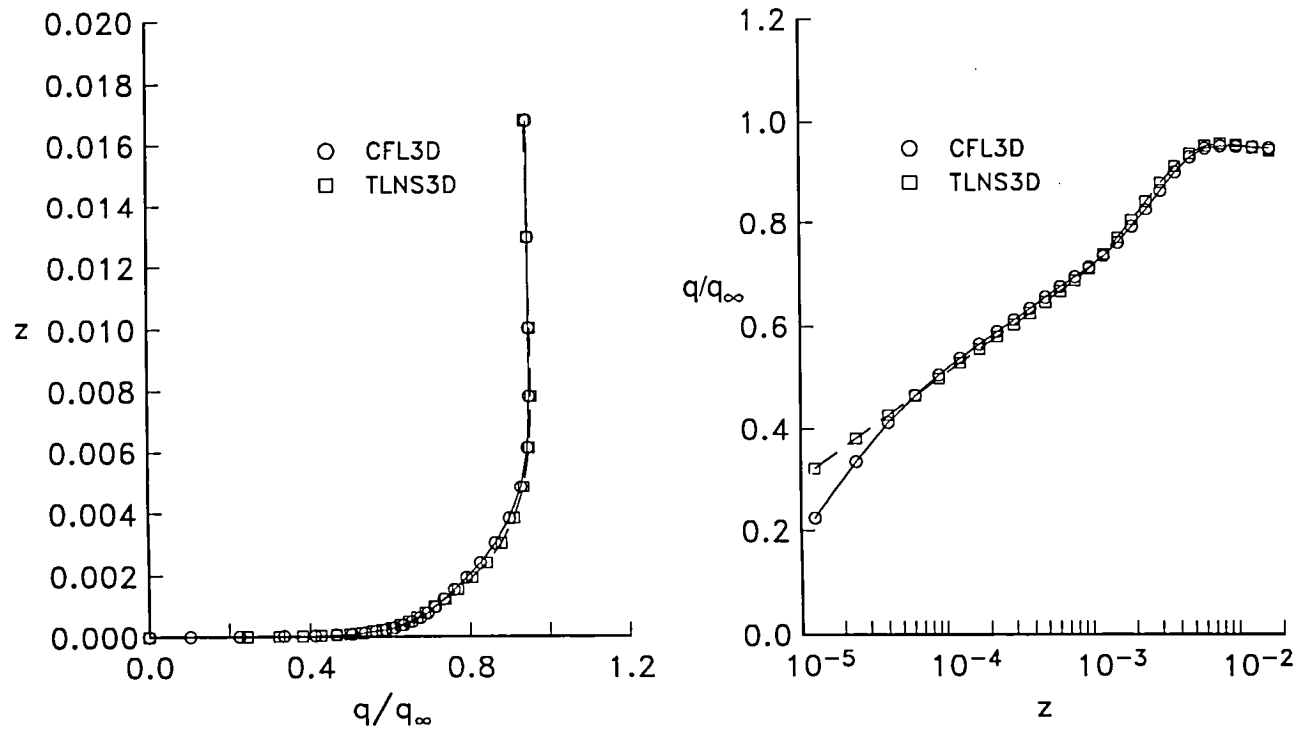

(f) $\eta = 0.8, \xi = 0.75$.

Figure 45. Concluded.

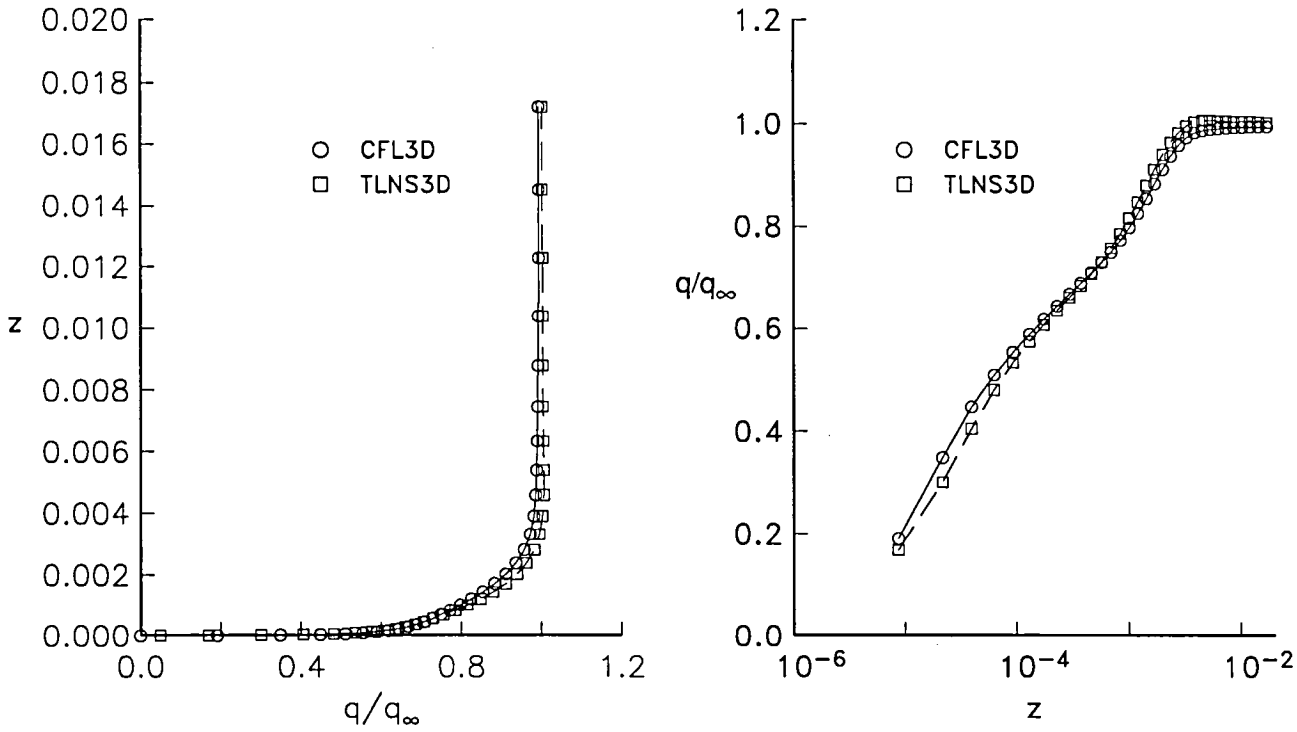

(a) $\eta = 0, \xi = 0.25$.

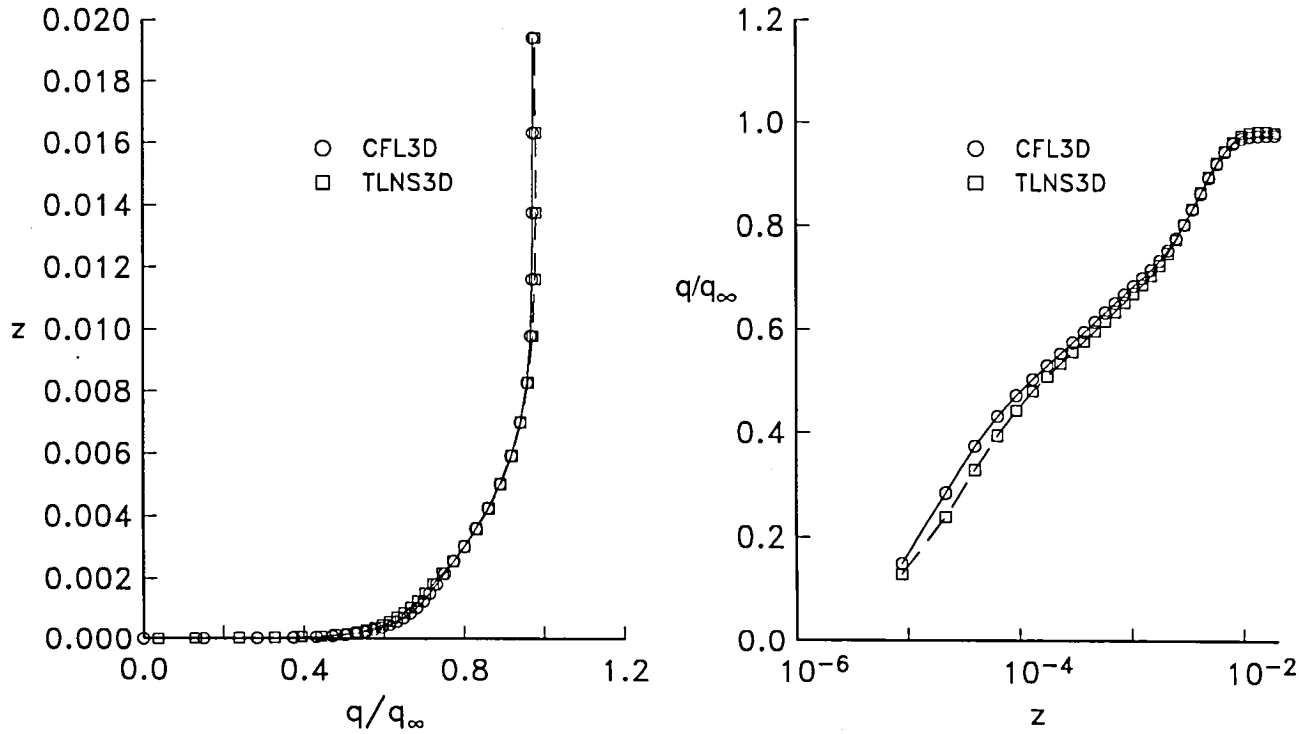

(b) $\eta = 0, \xi = 0.75$.

Figure 46. Upper-surface boundary-layer profiles for the Lockheed Wing B. $289 \times 65 \times 49$ grid.

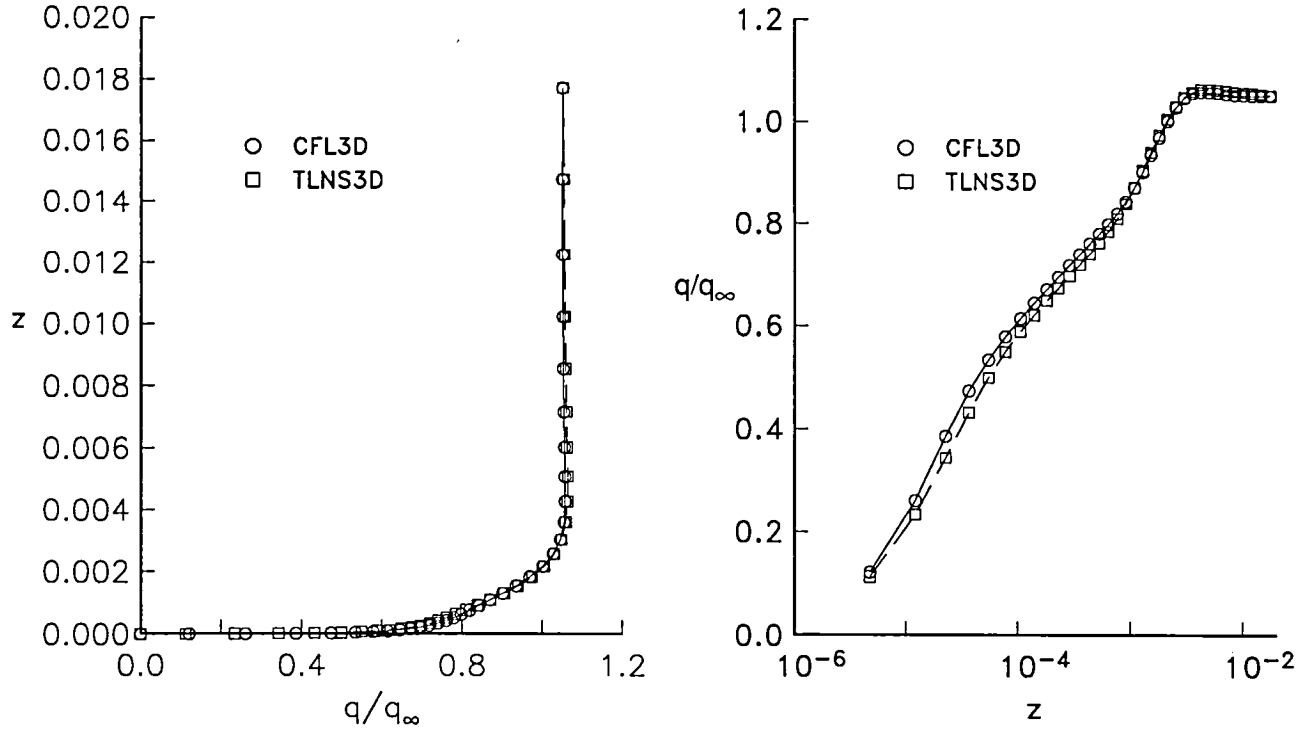

(c) $\eta = 0.5, \xi = 0.25$.

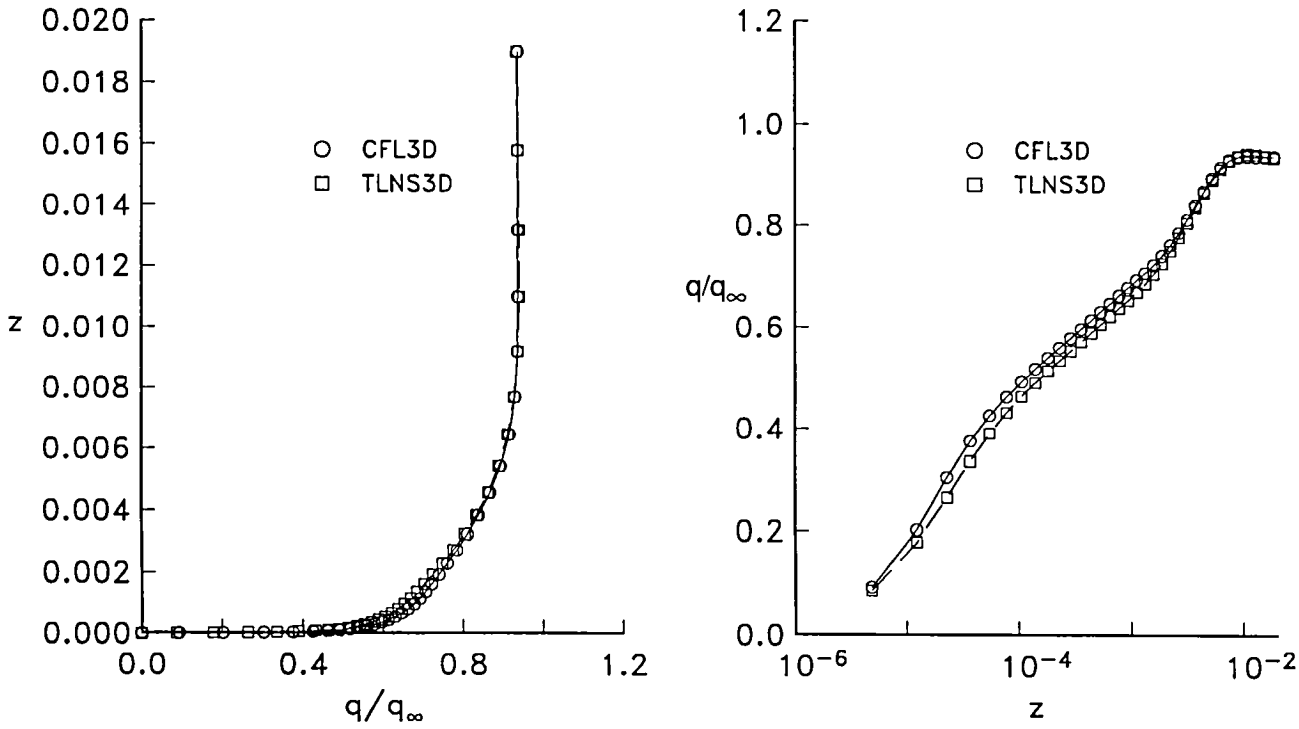

(d) $\eta = 0.5, \xi = 0.75$.

Figure 46. Continued.

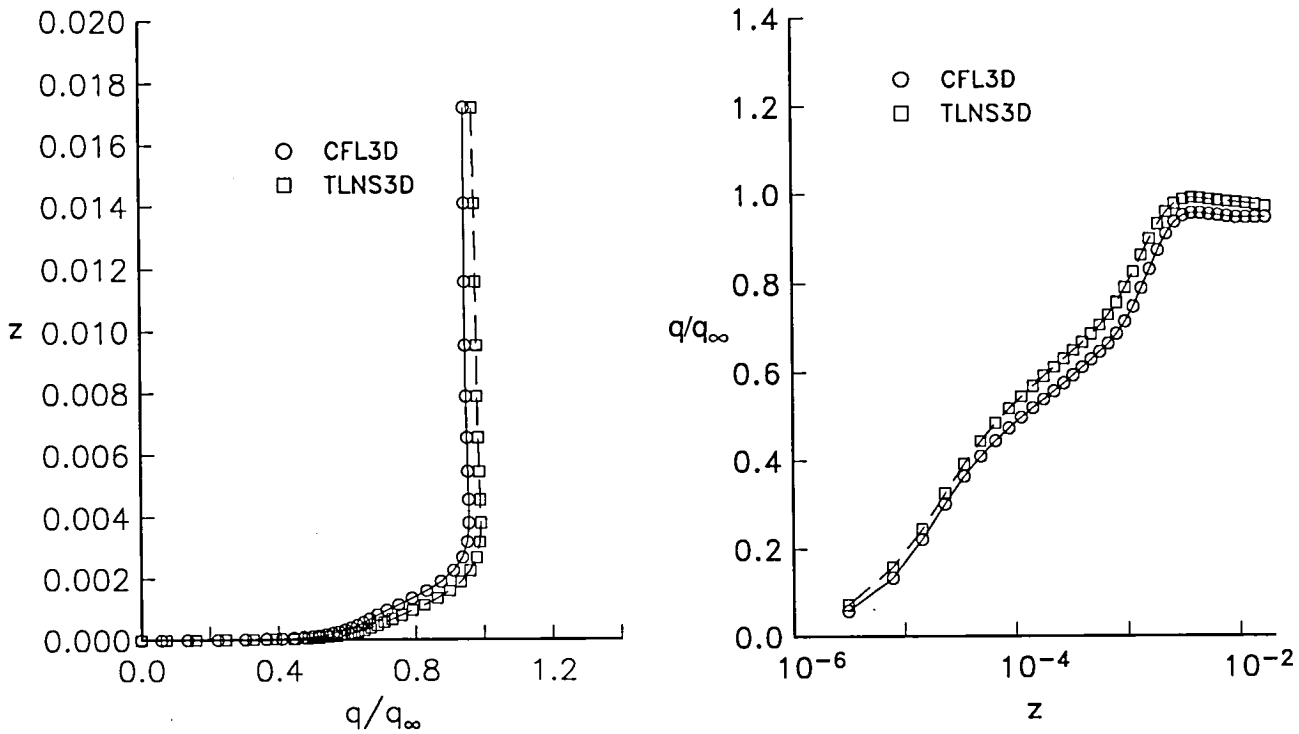

(e) $\eta = 0.8, \xi = 0.25$.

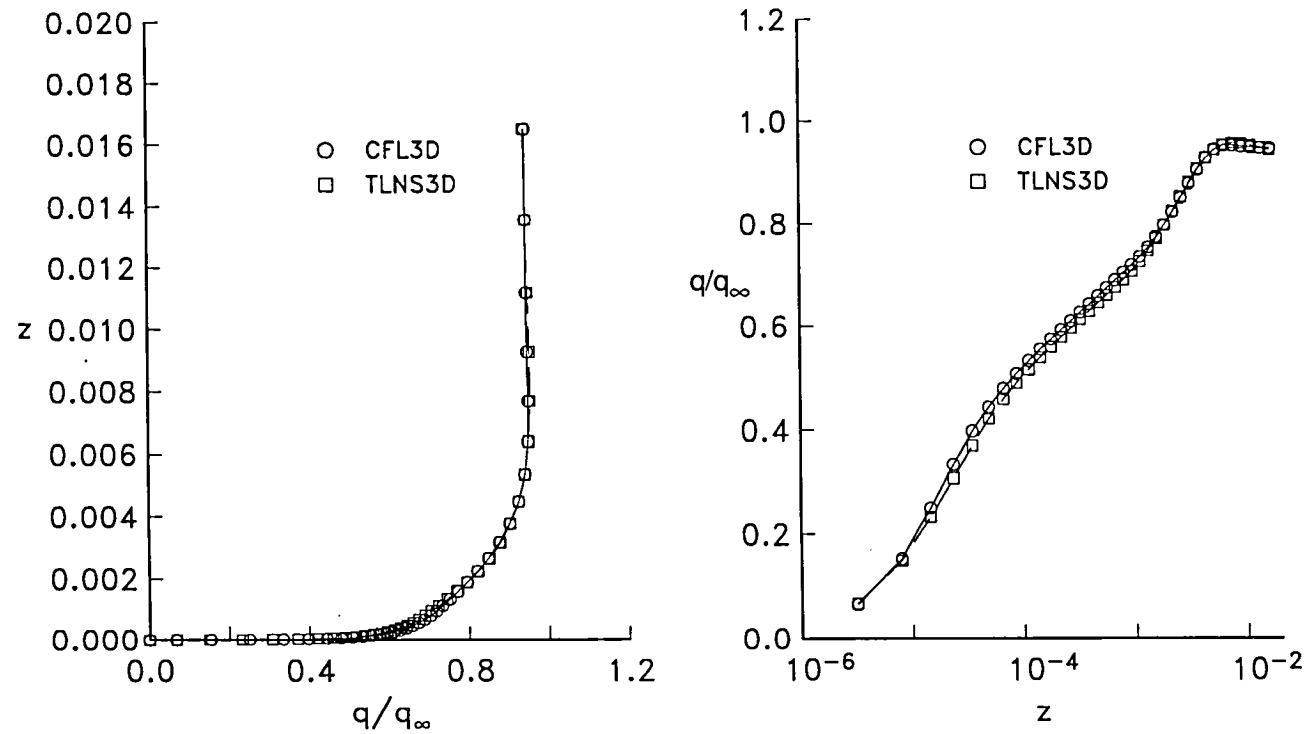

(f) $\eta = 0.8, \xi = 0.75$.

Figure 46. Concluded.

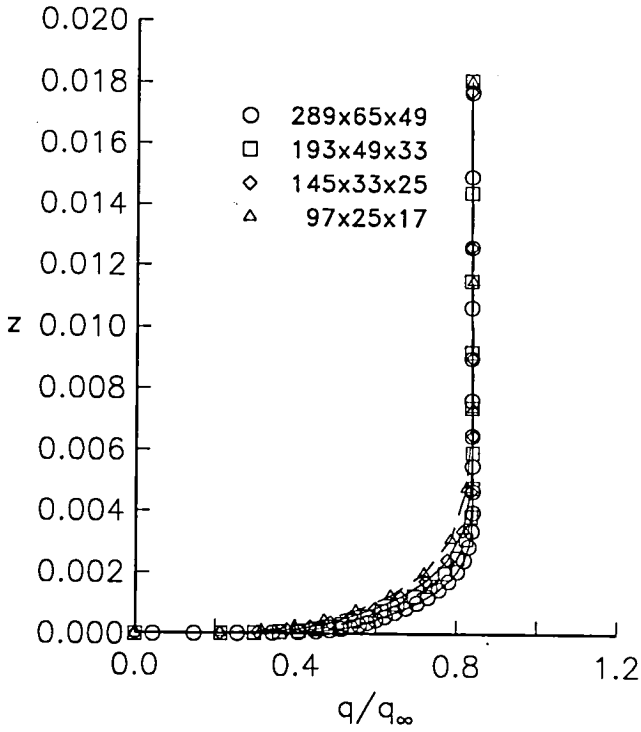

(a) TLNS3D—standard.

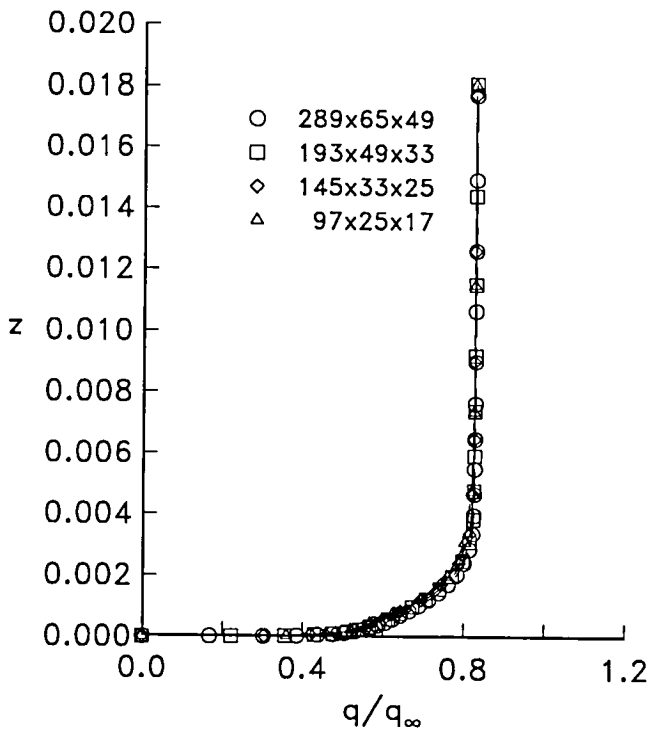

(b) CFL3D—standard.

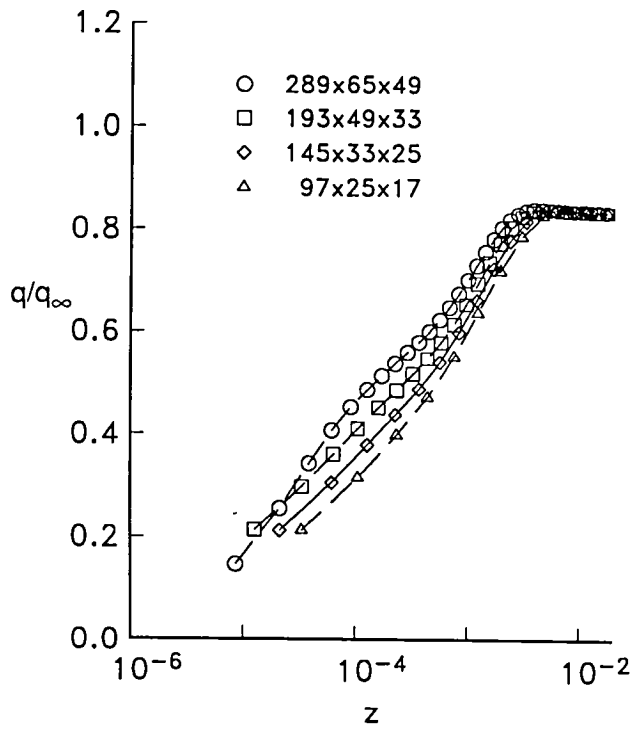

(c) TLNS3D—semilog.

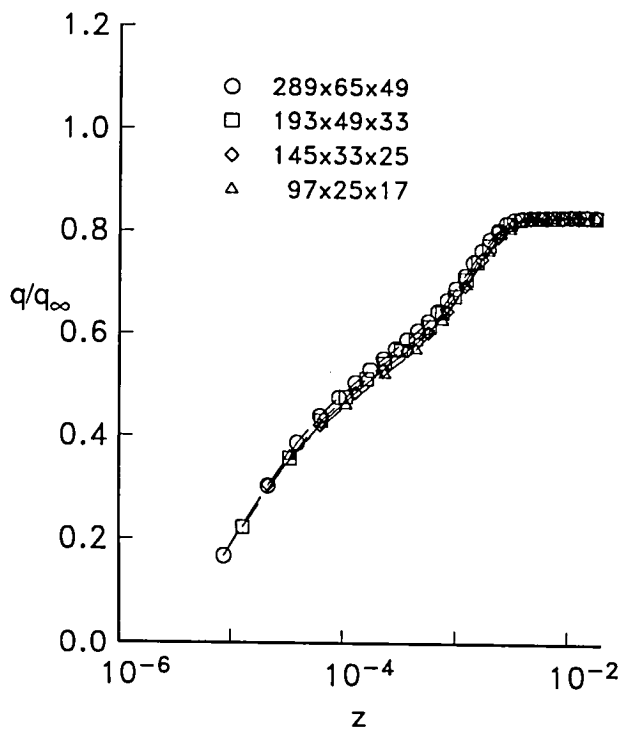

(d) CFL3D—semilog.

Figure 47. Effect of grid refinement on the lower-surface boundary-layer profiles for the Lockheed Wing B. $\eta = 0; \xi = 0.25$.

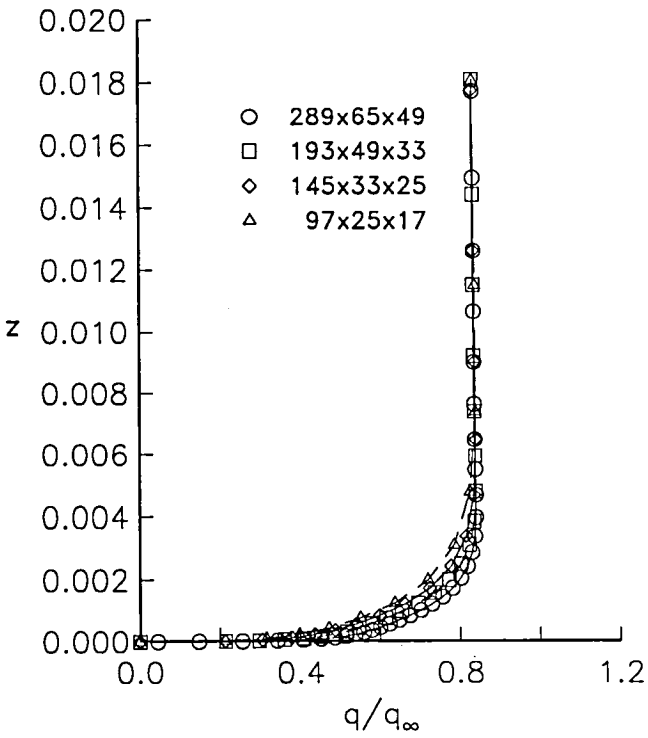

(a) TLNS3D—standard.

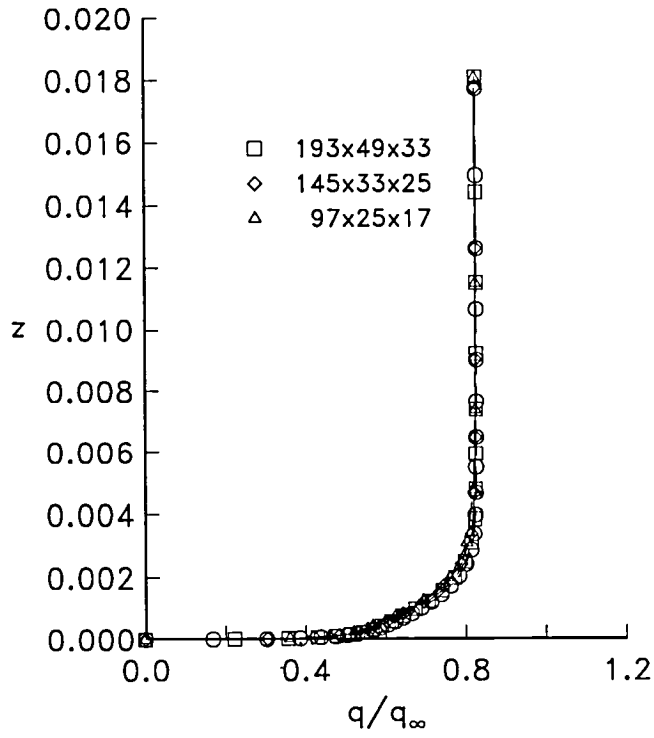

(b) CFL3D—standard.

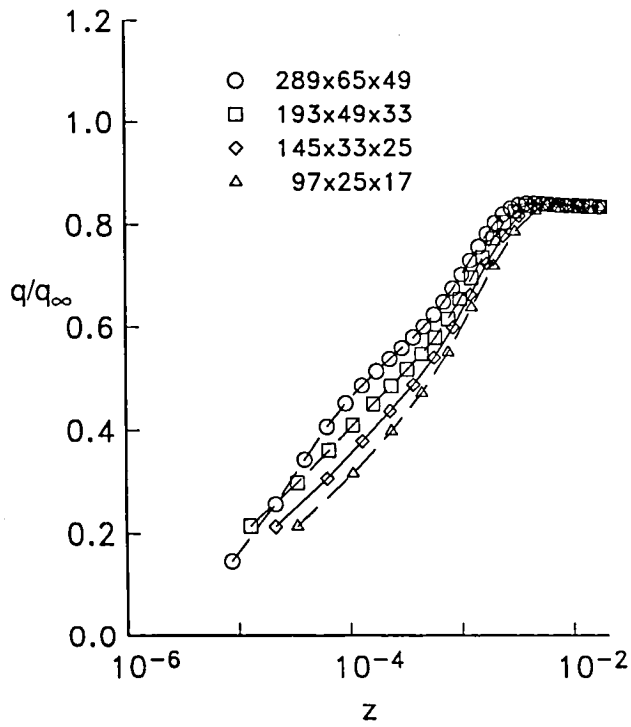

(c) TLNS3D—semilog.

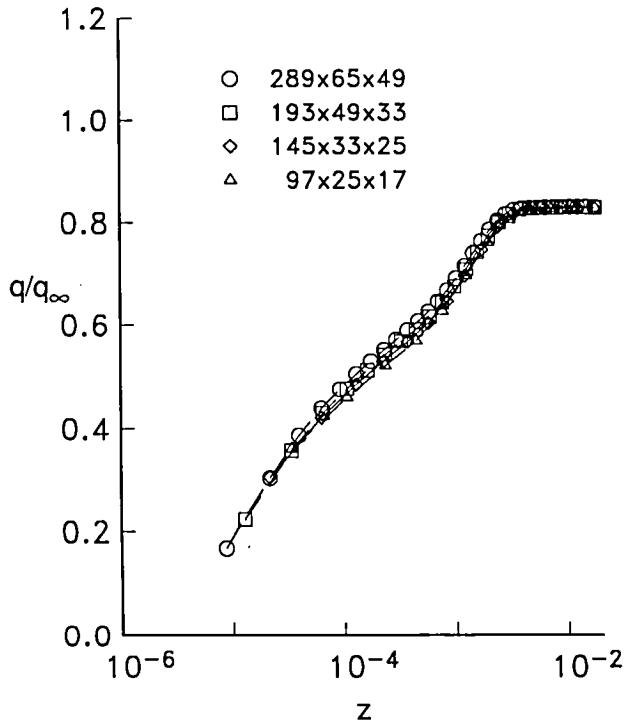

(d) CFL3D—semilog.

Figure 48. Effect of grid refinement on the lower-surface boundary-layer profiles for the Lockheed Wing B. $\eta = 0; \xi = 0.75$.

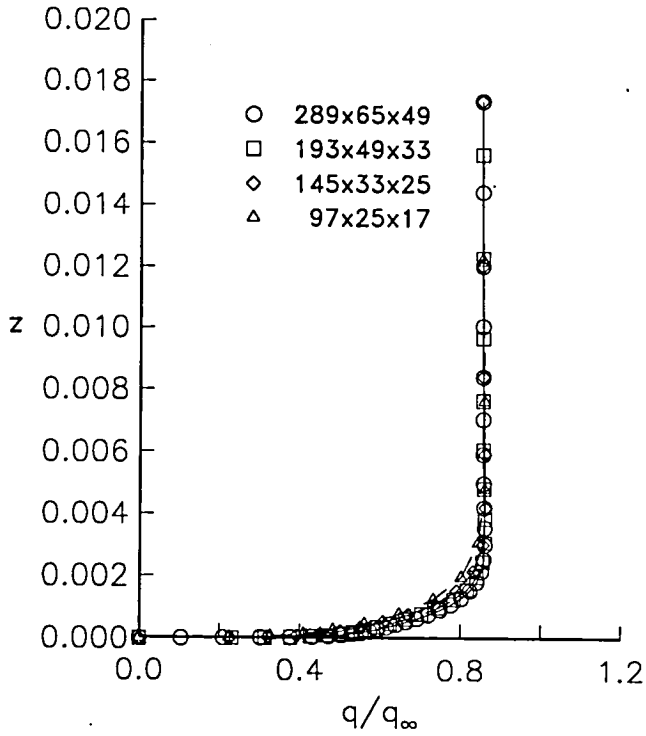

(a) TLNS3D—standard.

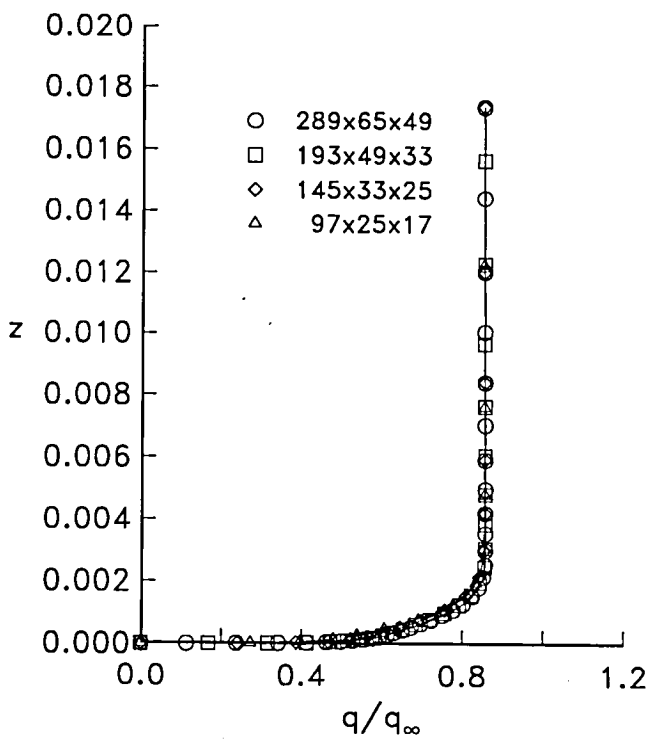

(b) CFL3D—standard.

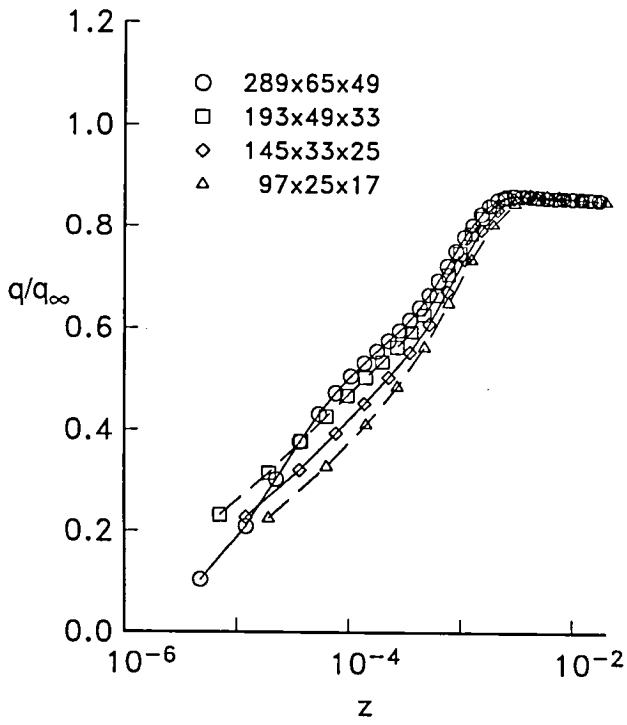

(c) TLNS3D—semilog.

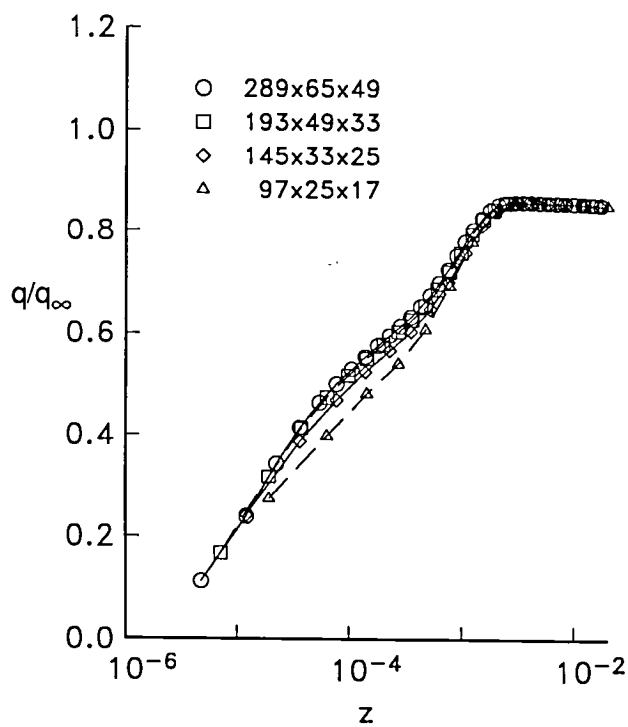

(d) CFL3D—semilog.

Figure 49. Effect of grid refinement on the lower-surface boundary-layer profiles for the Lockheed Wing B. $\eta = 0.5; \xi = 0.25$.

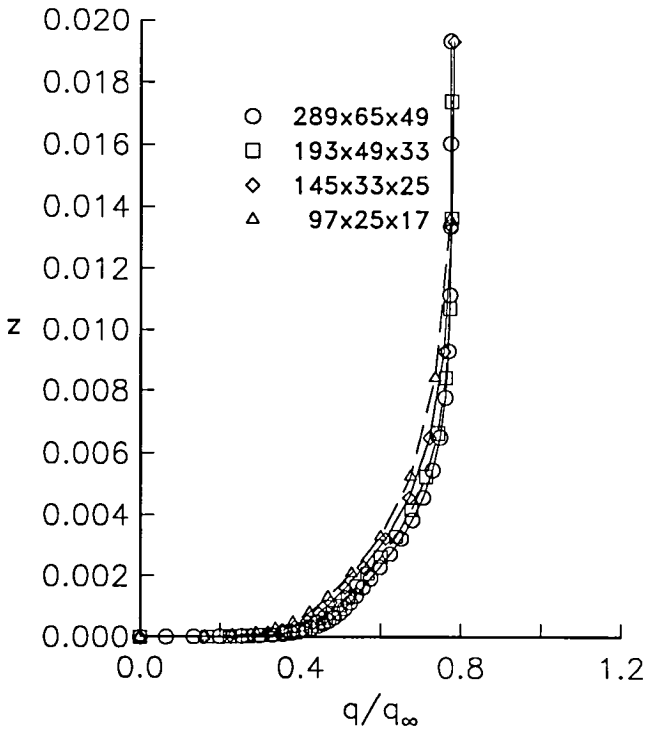

(a) TLNS3D—standard.

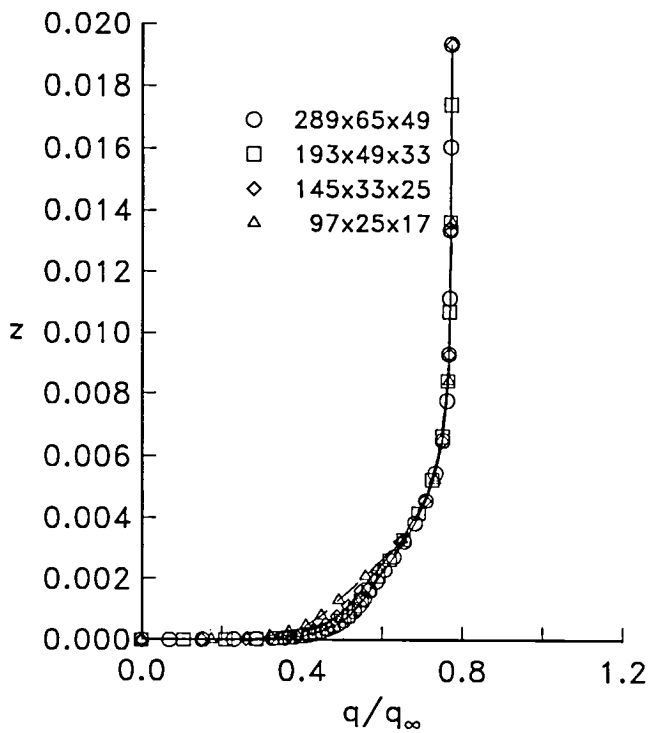

(b) CFL3D—standard.

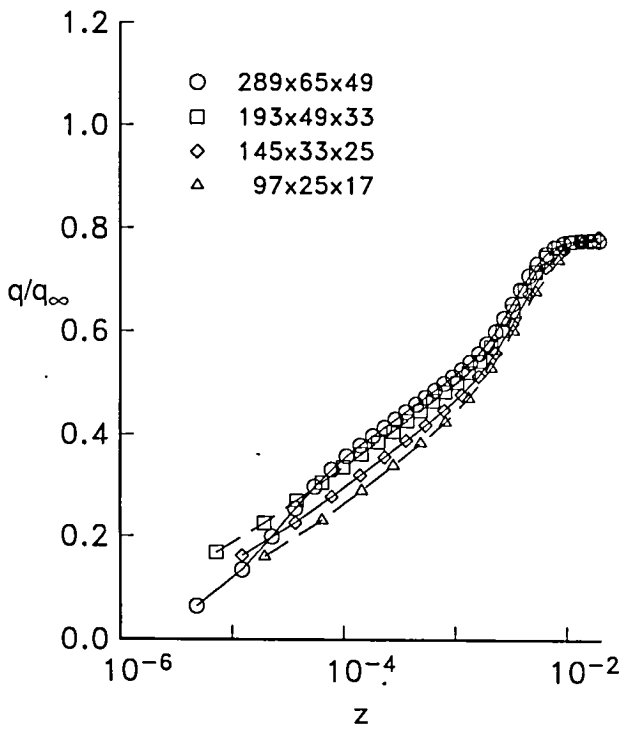

(c) TLNS3D—semilog.

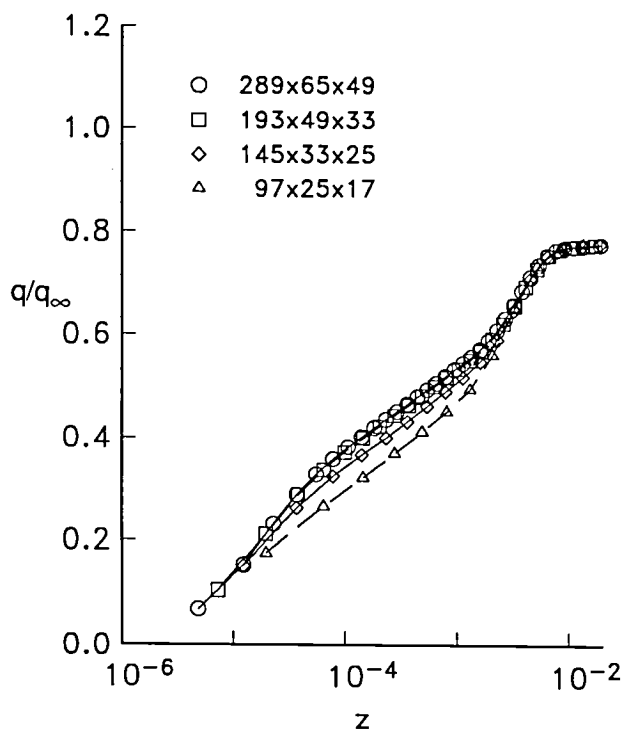

(d) CFL3D—semilog.

Figure 50. Effect of grid refinement on the lower-surface boundary-layer profiles for the Lockheed Wing B. $\eta = 0.5; \xi = 0.75$.

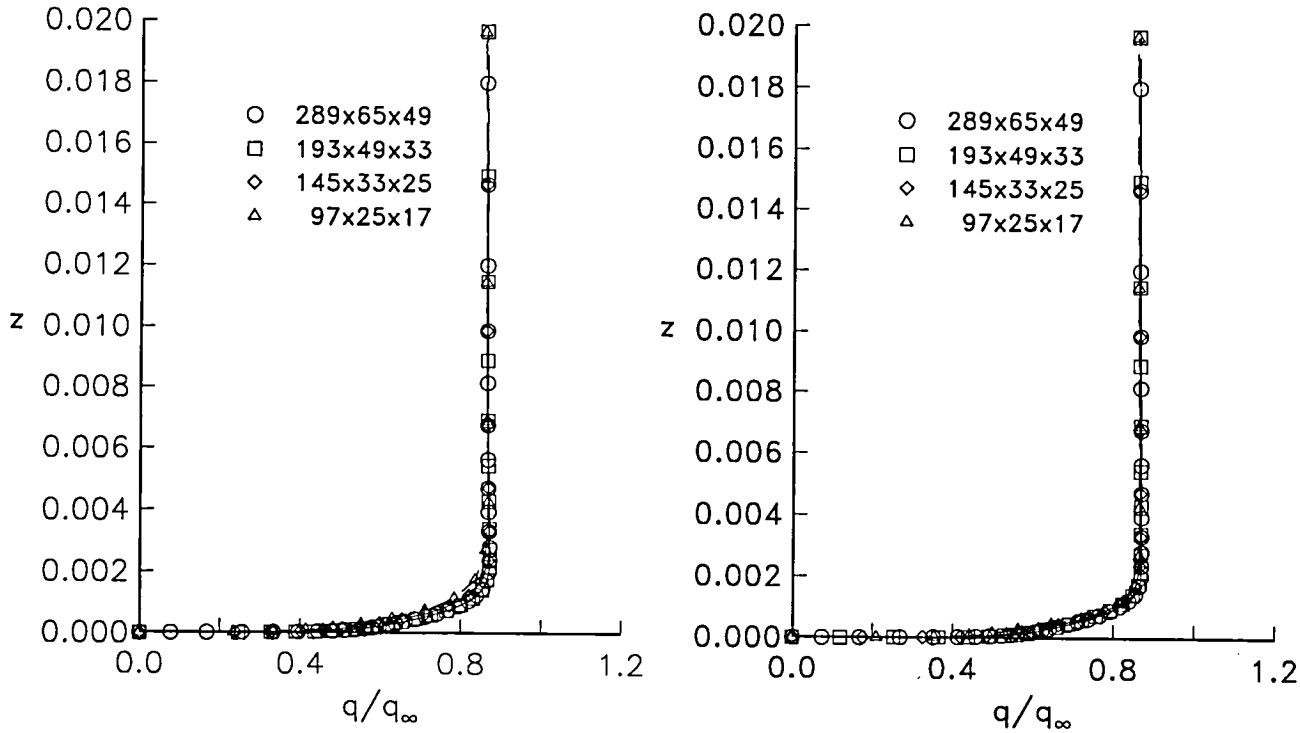

(a) TLNS3D—standard.

(b) CFL3D—standard.

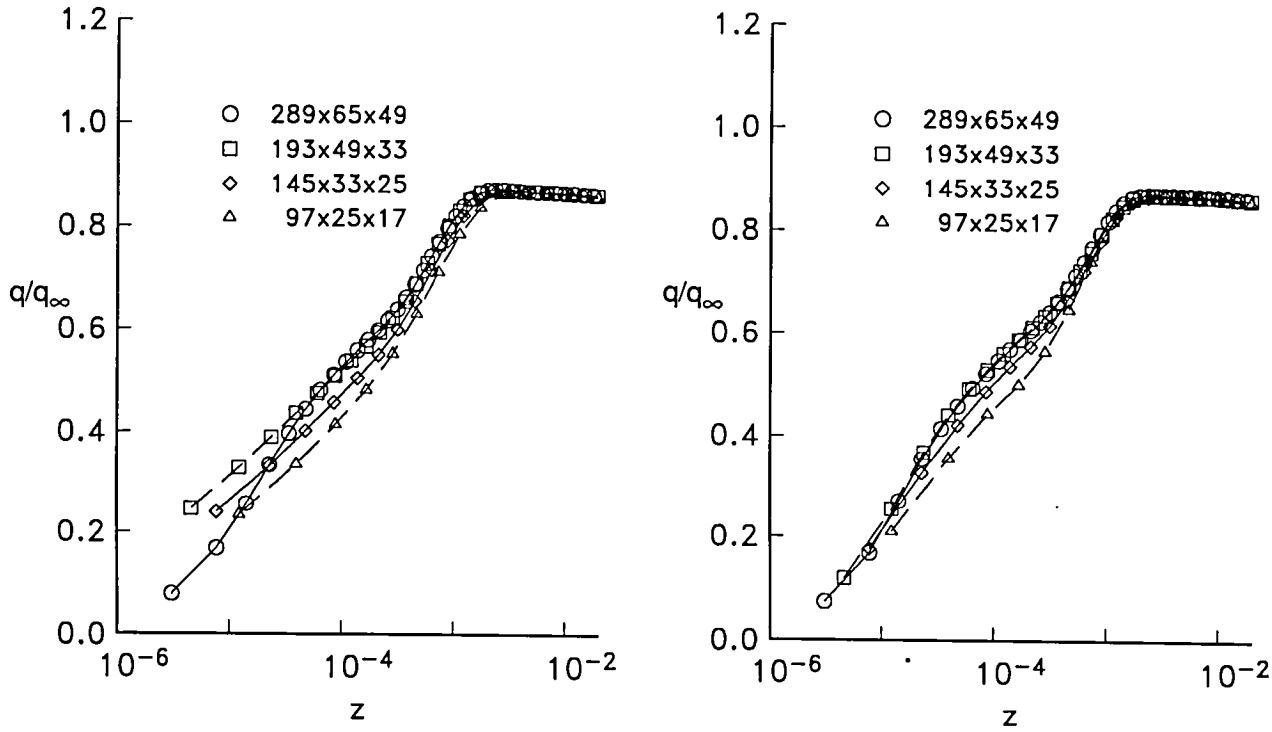

(c) TLNS3D—semilog.

(d) CFL3D—semilog.

Figure 51. Effect of grid refinement on the lower-surface boundary-layer profiles for the Lockheed Wing B. $\eta = 0.8; \xi = 0.25$.

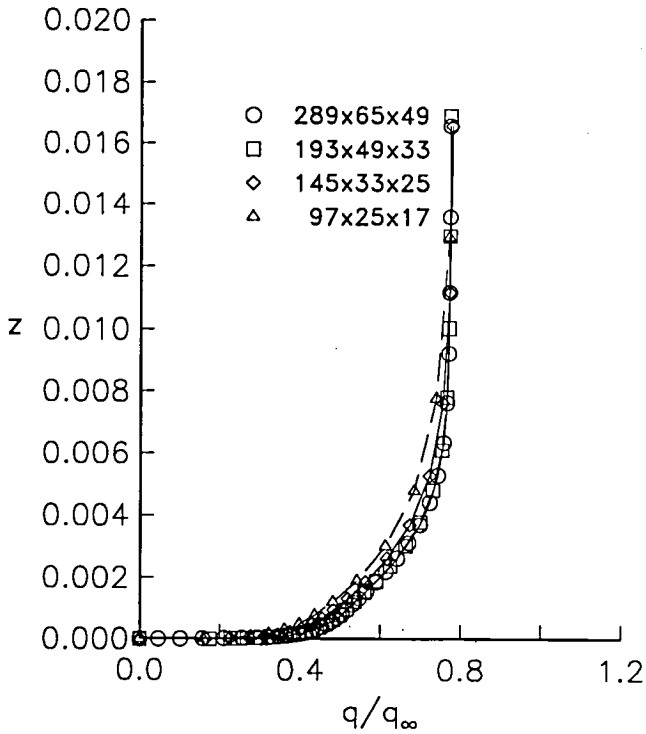

(a) TLNS3D—standard.

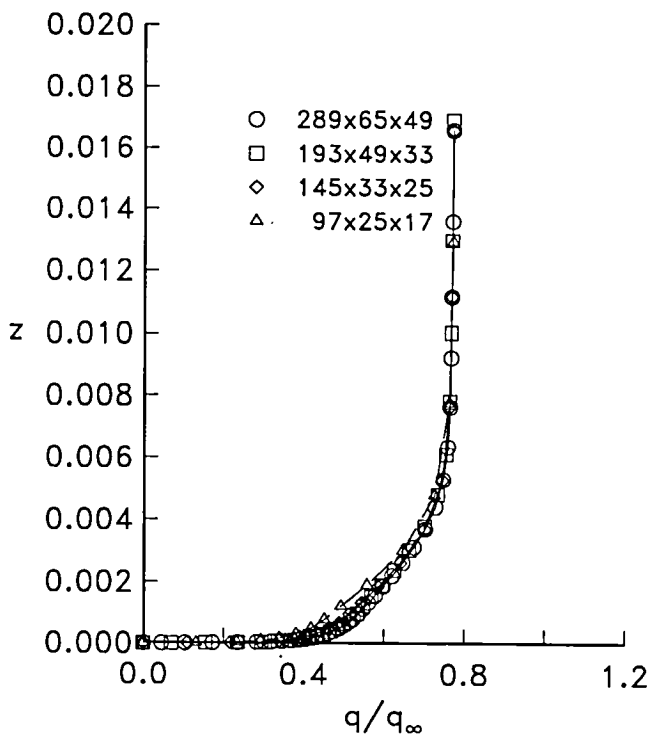

(b) CFL3D—standard.

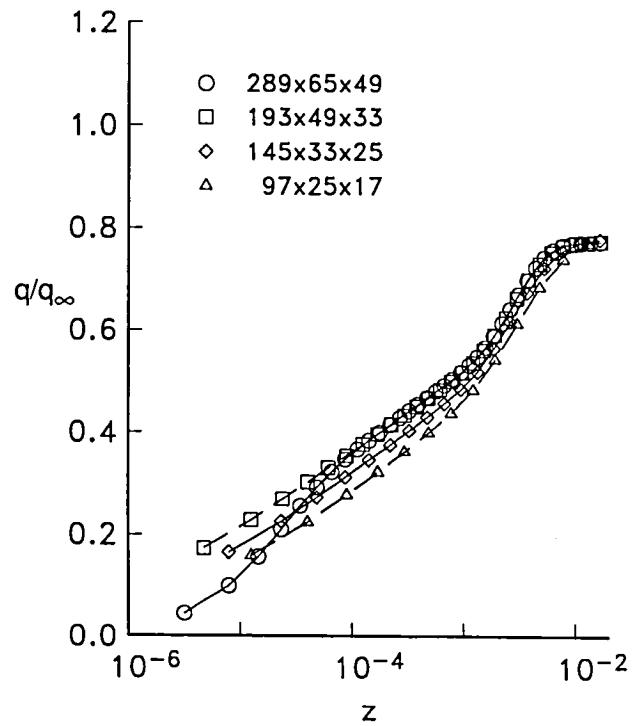

(c) TLNS3D—semilog.

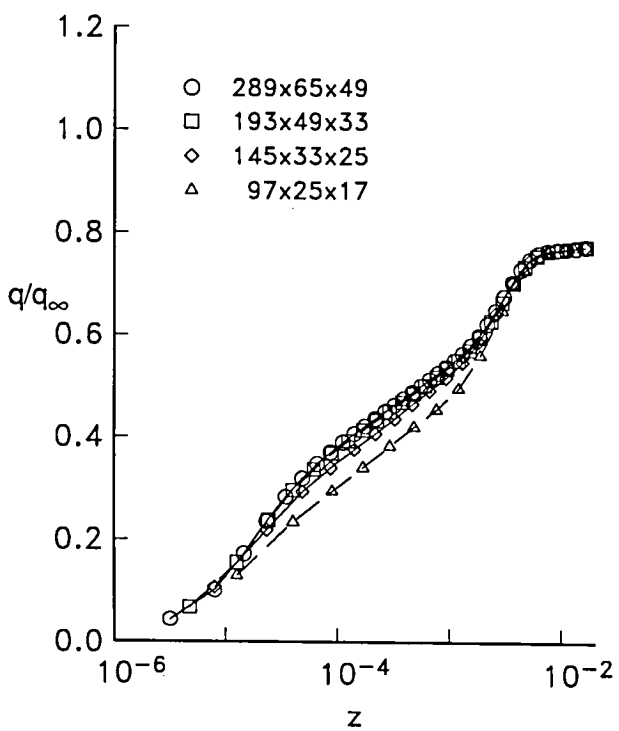

(d) CFL3D—semilog.

Figure 52. Effect of grid refinement on the lower-surface boundary-layer profiles for the Lockheed Wing B. $\eta = 0.8; \xi = 0.75$.

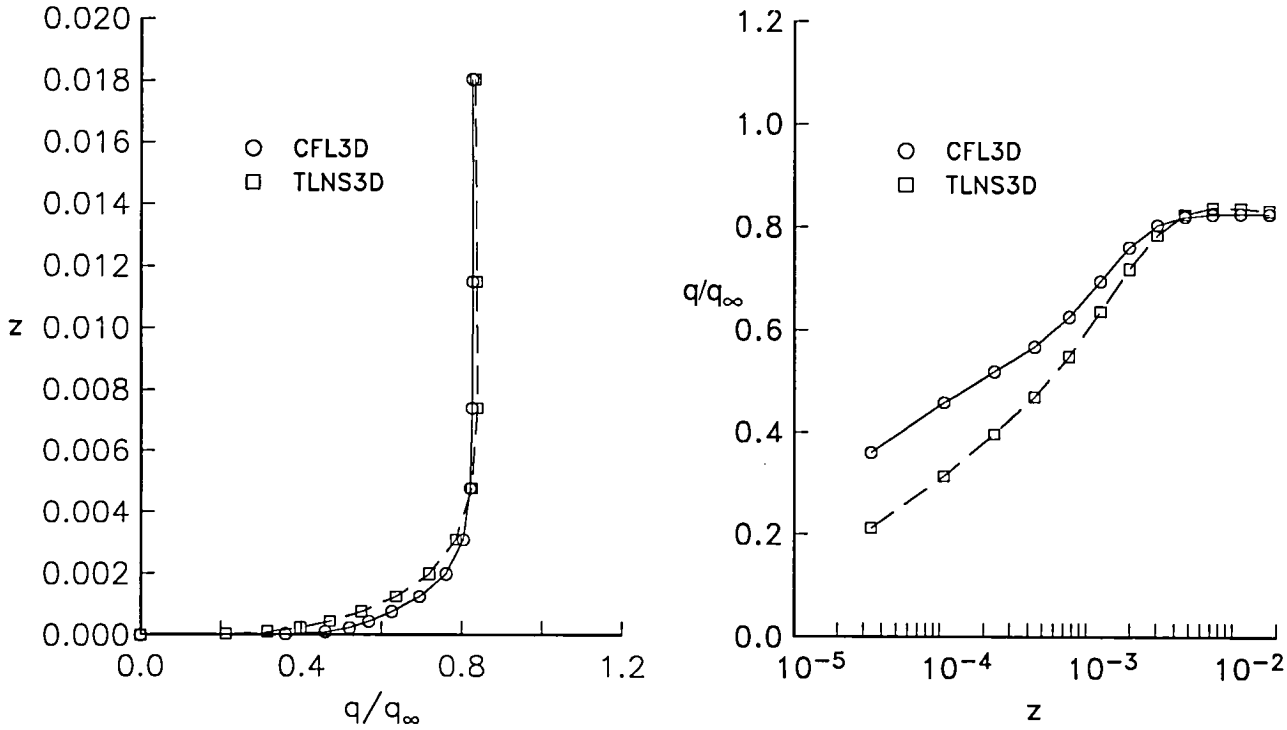

(a) $\eta = 0, \xi = 0.25$.

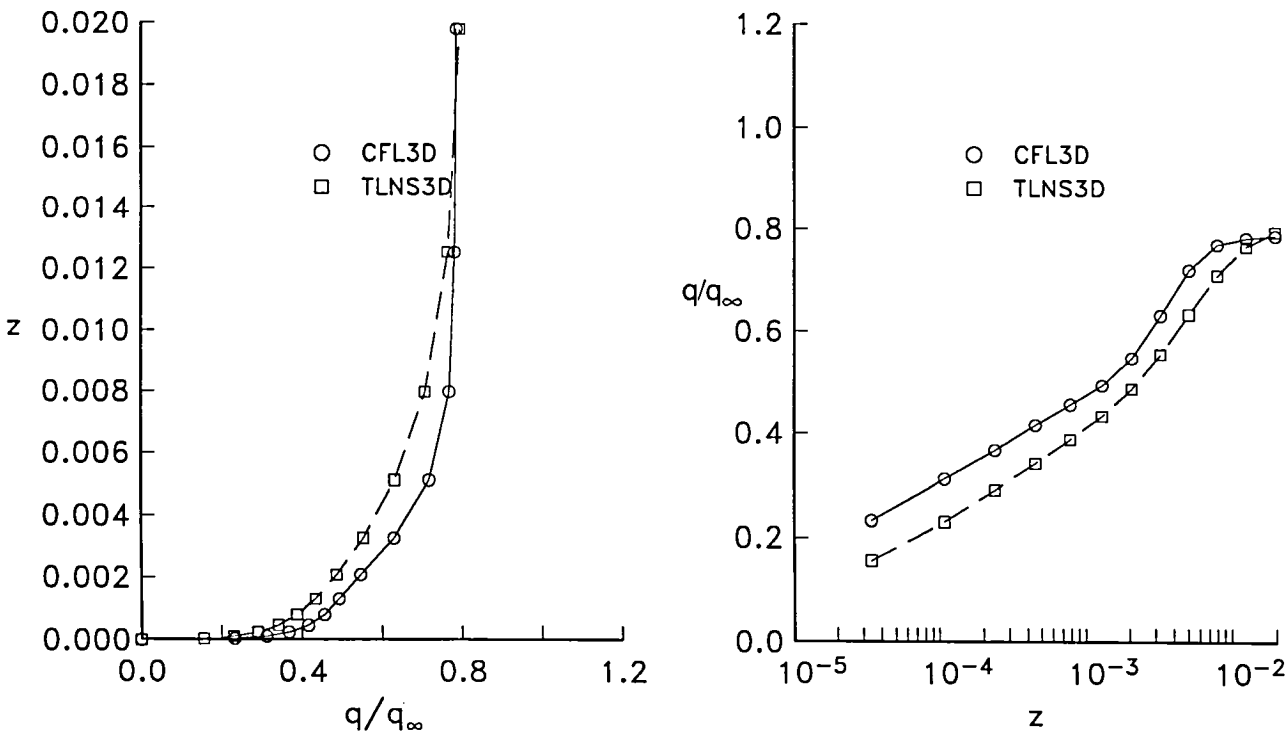

(b) $\eta = 0, \xi = 0.75$.

Figure 53. Lower-surface boundary-layer profiles for the Lockheed Wing B. $97 \times 25 \times 17$ grid.

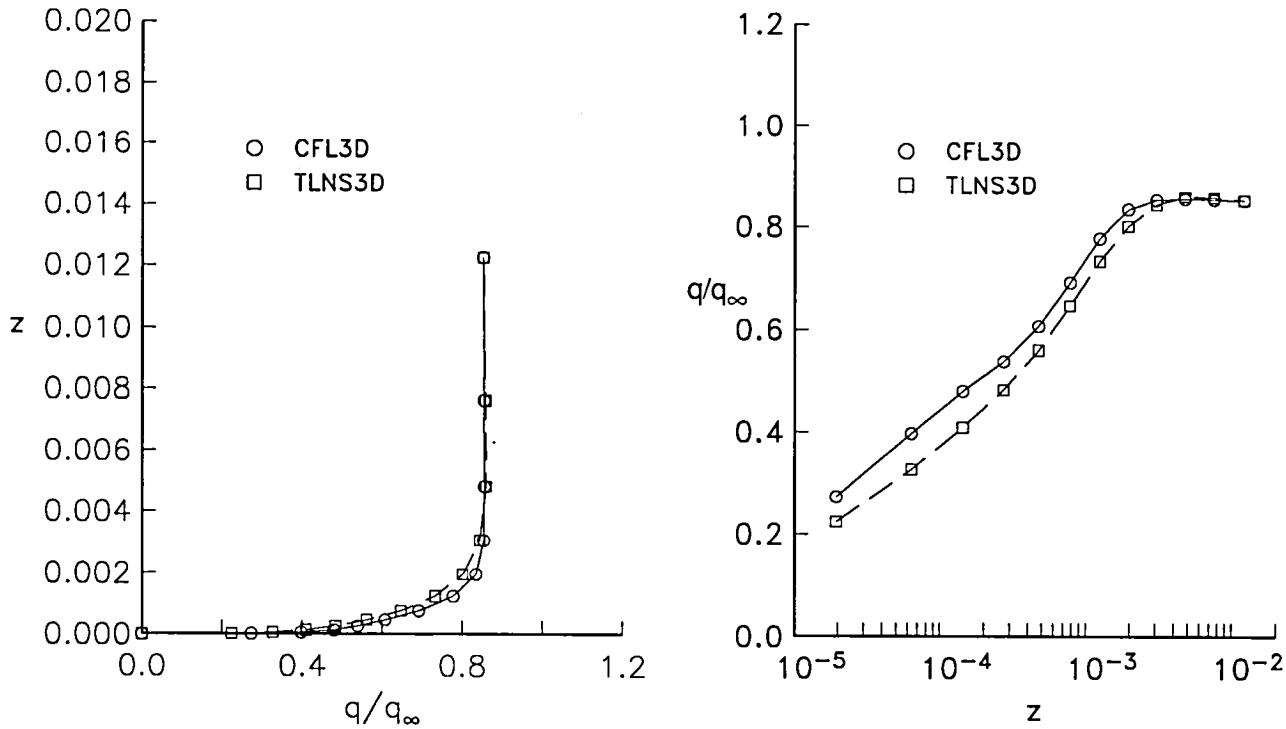

(c) $\eta = 0.5, \xi = 0.25$.

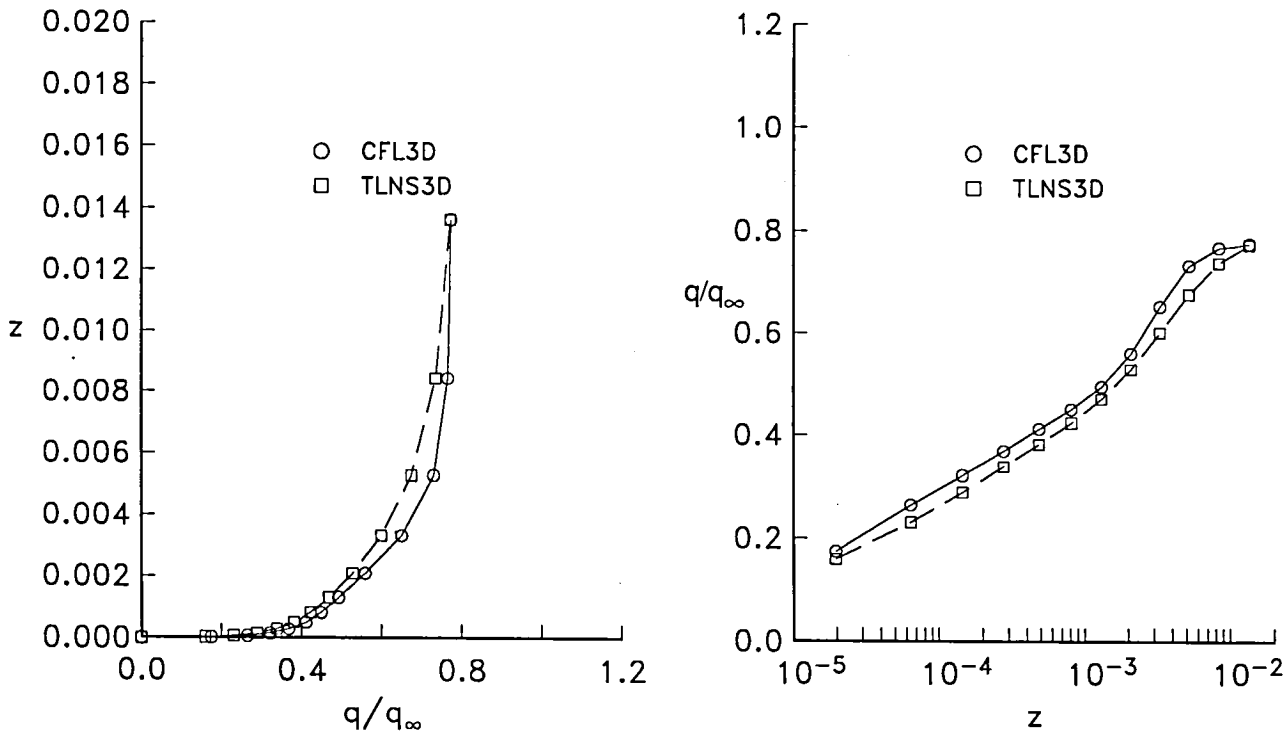

(d) $\eta = 0.5, \xi = 0.75$.

Figure 53. Continued.

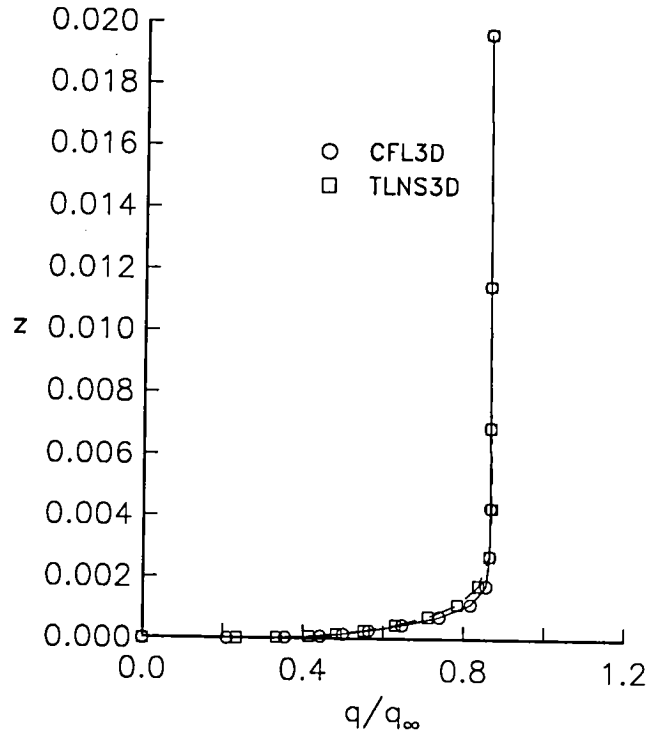

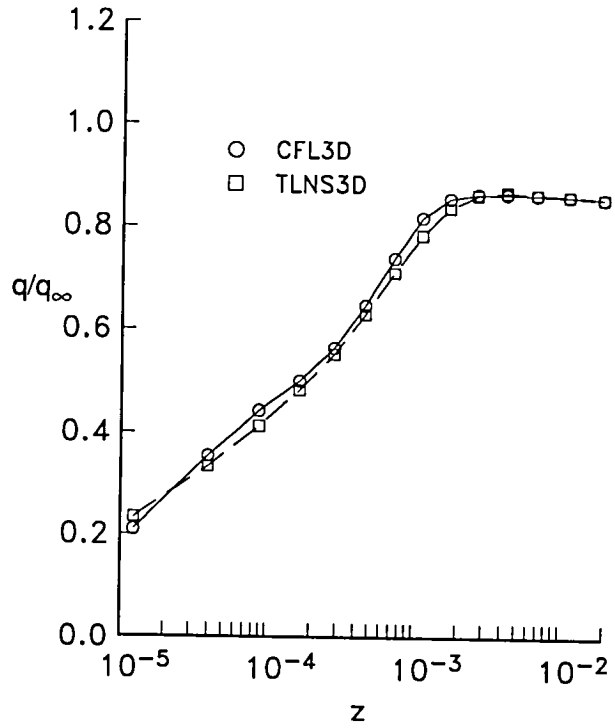

(e) $\eta = 0.8, \xi = 0.25$.

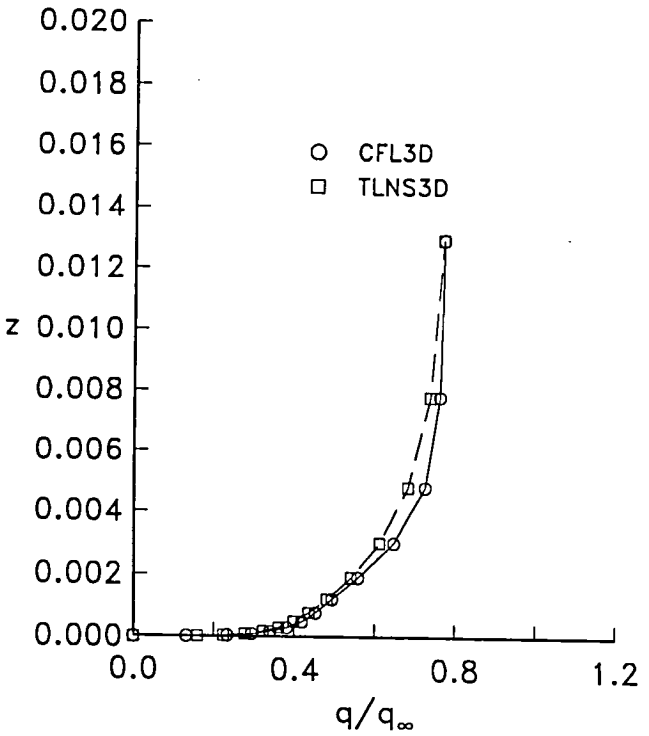

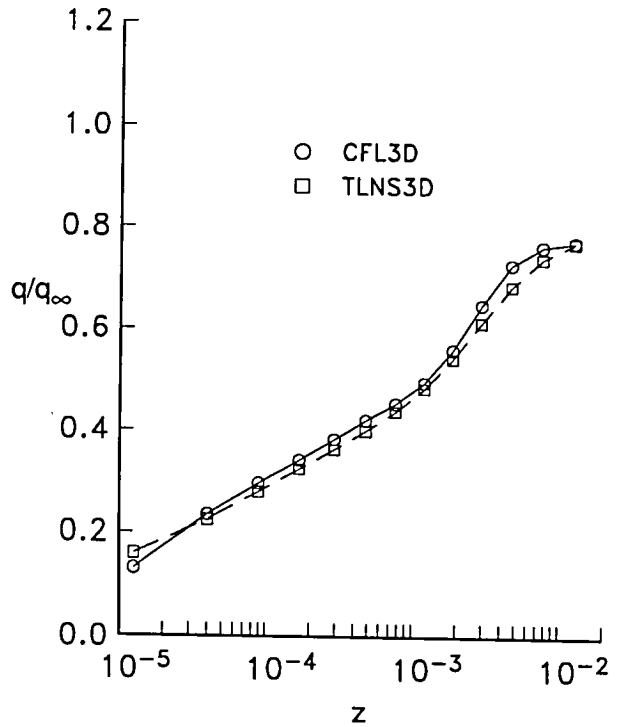

(f) $\eta = 0.8, \xi = 0.75$.

Figure 53. Concluded.

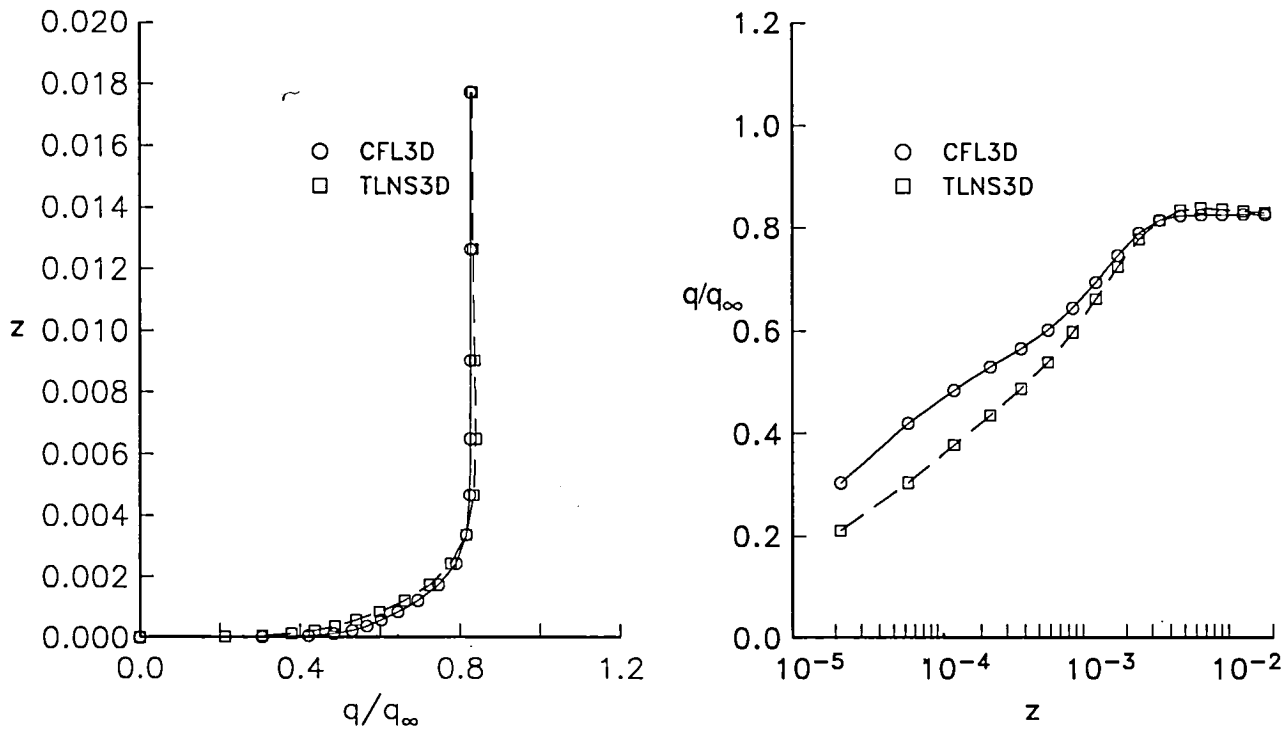

(a) $\eta = 0, \xi = 0.25$.

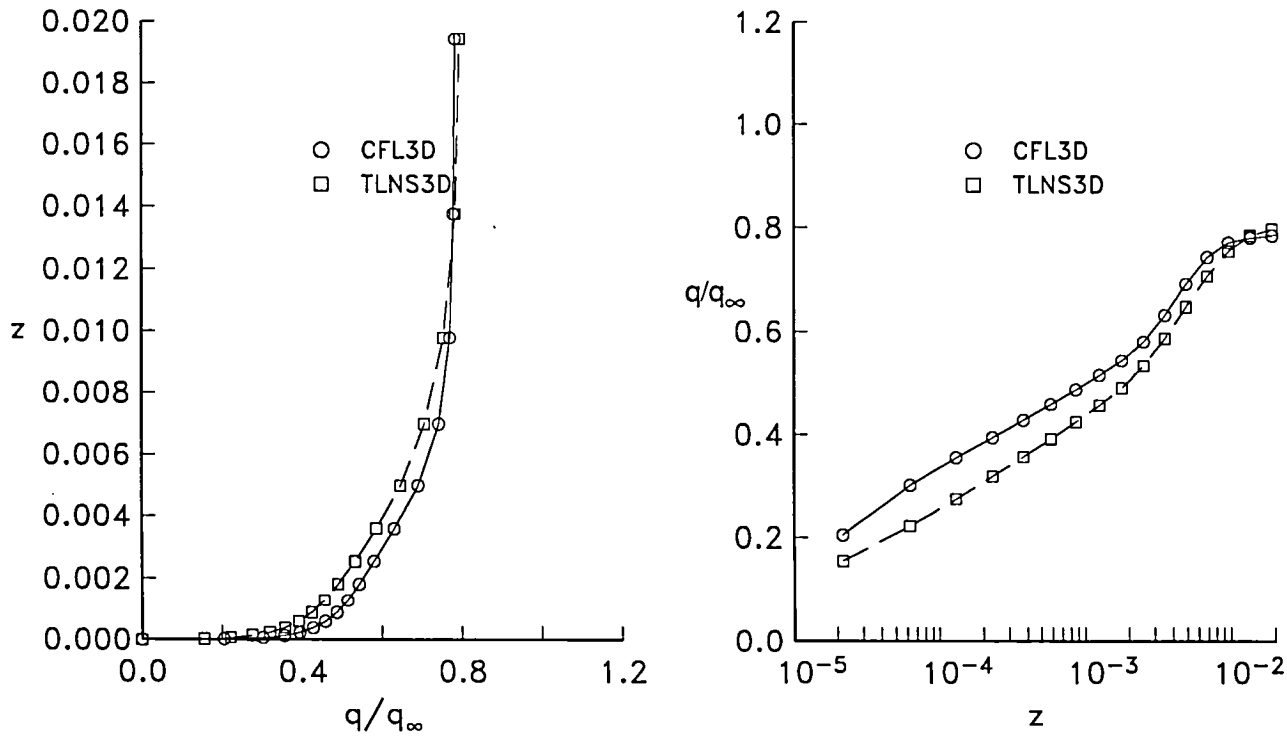

(b) $\eta = 0, \xi = 0.75$.

Figure 54. Lower-surface boundary-layer profiles for the Lockheed Wing B. $145 \times 33 \times 25$ grid.

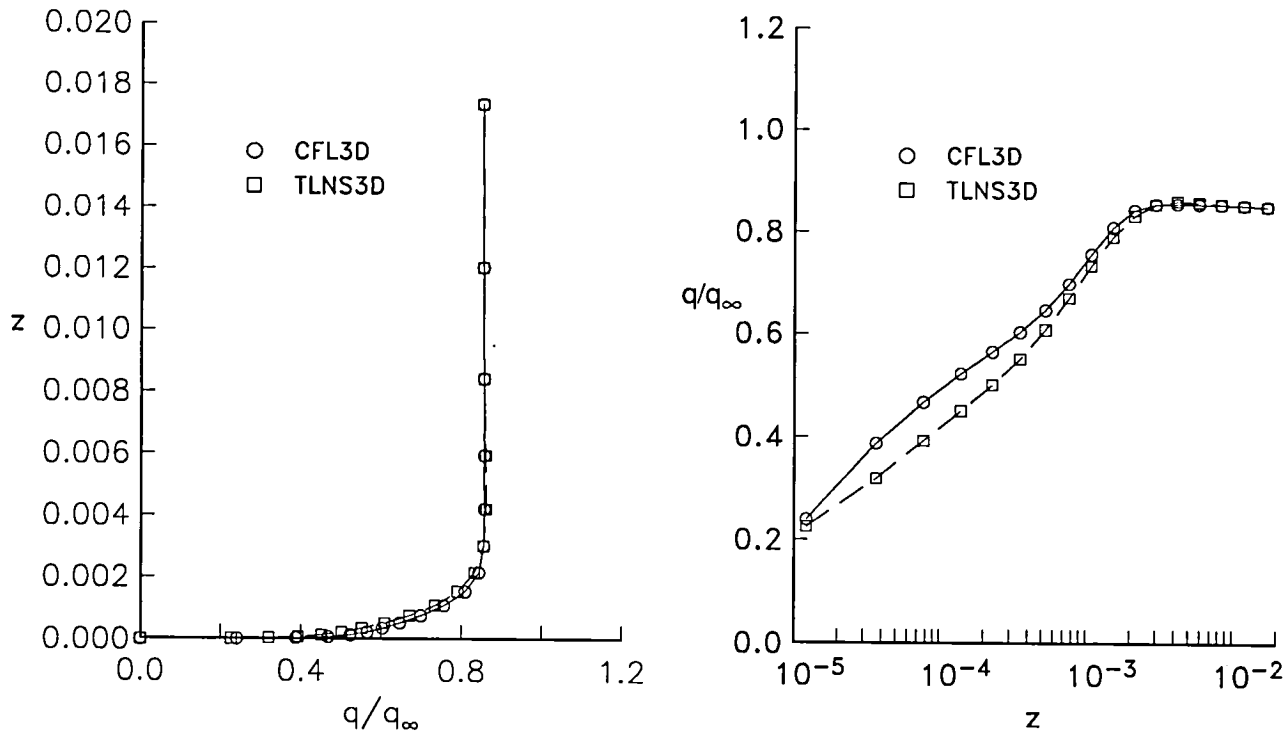

(c) $\eta = 0.5, \xi = 0.25$.

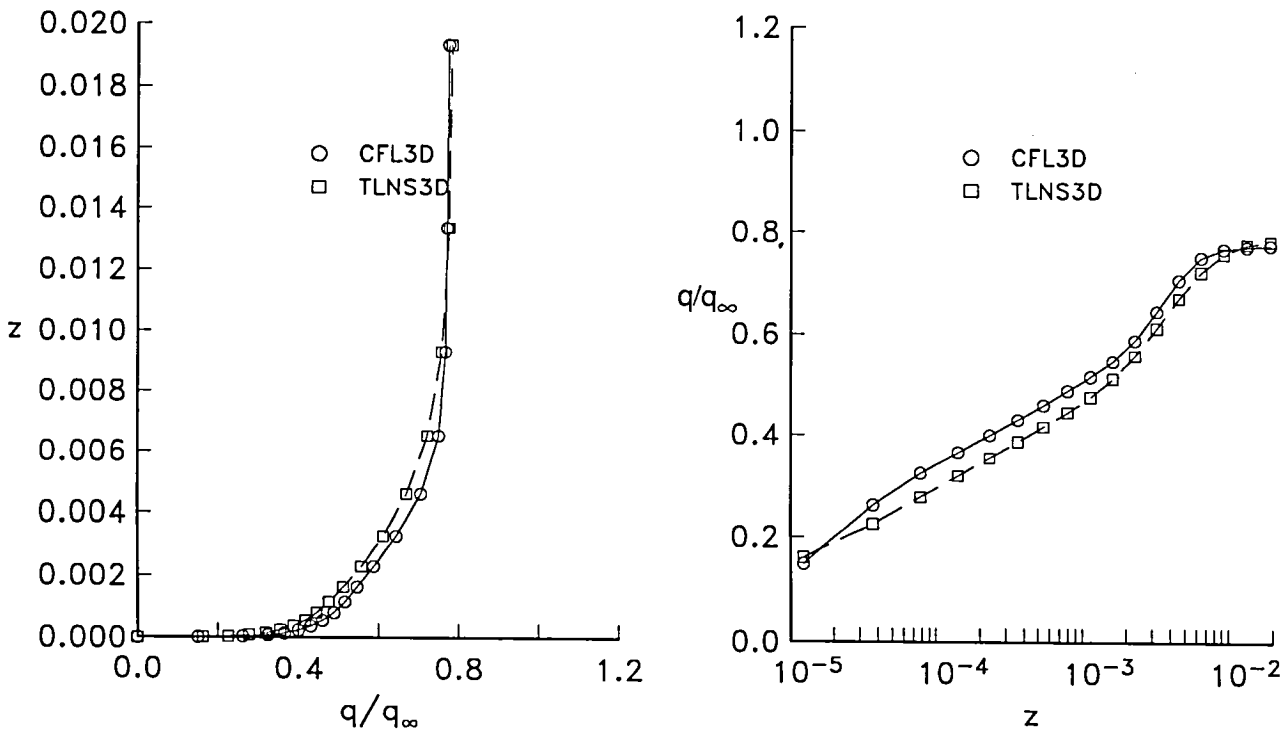

(d) $\eta = 0.5, \xi = 0.75$.

Figure 54. Continued.

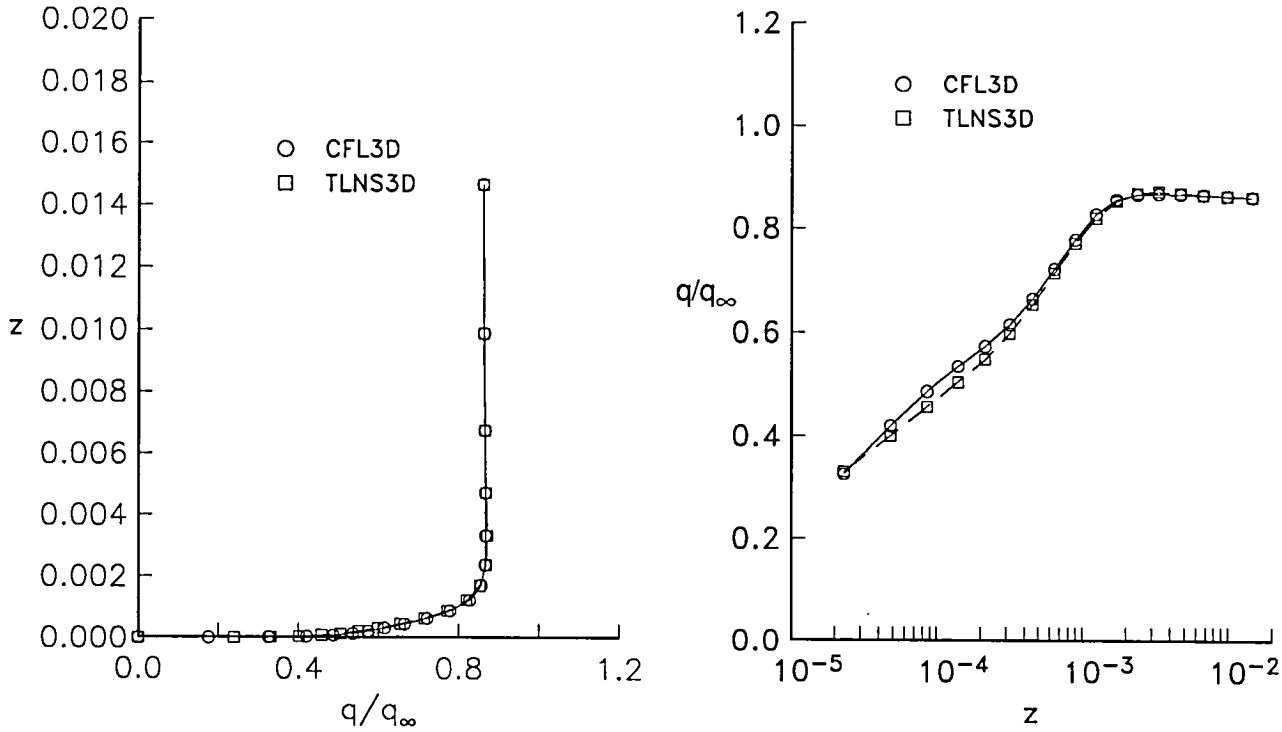

(e) $\eta = 0.8, \xi = 0.25$.

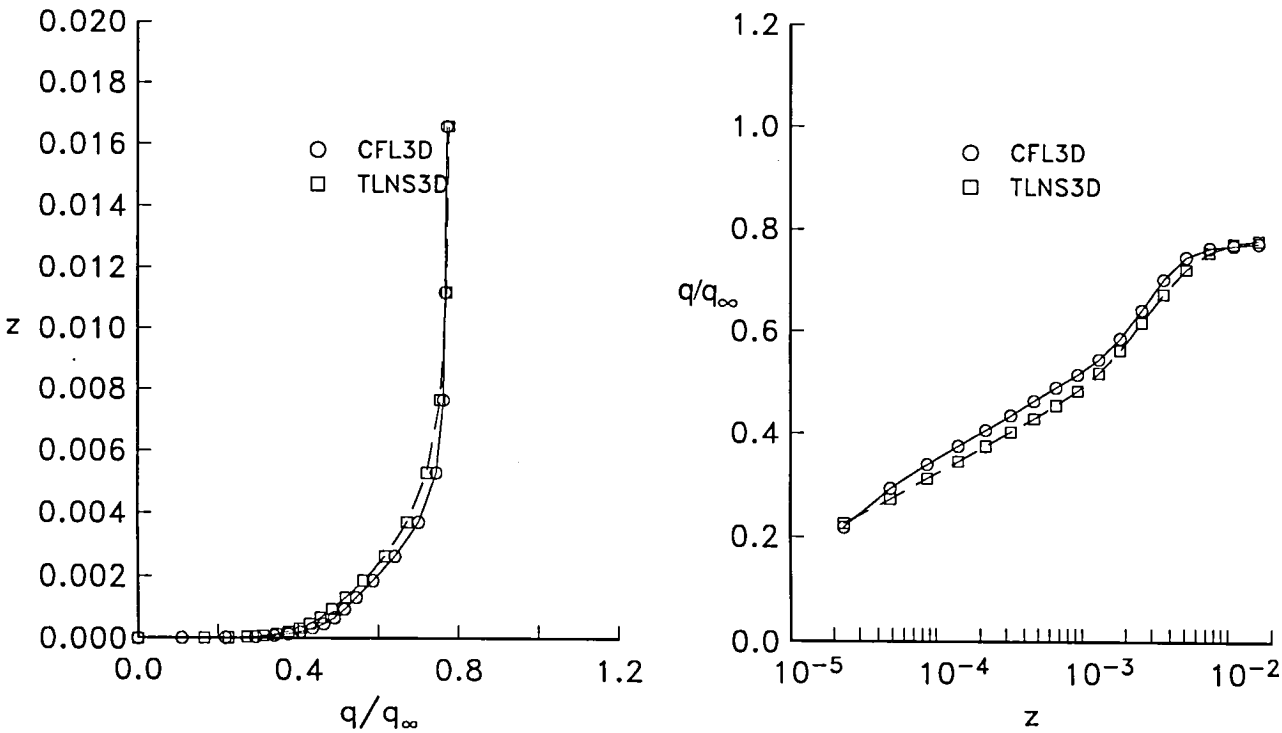

(f) $\eta = 0.8, \xi = 0.75$.

Figure 54. Concluded.

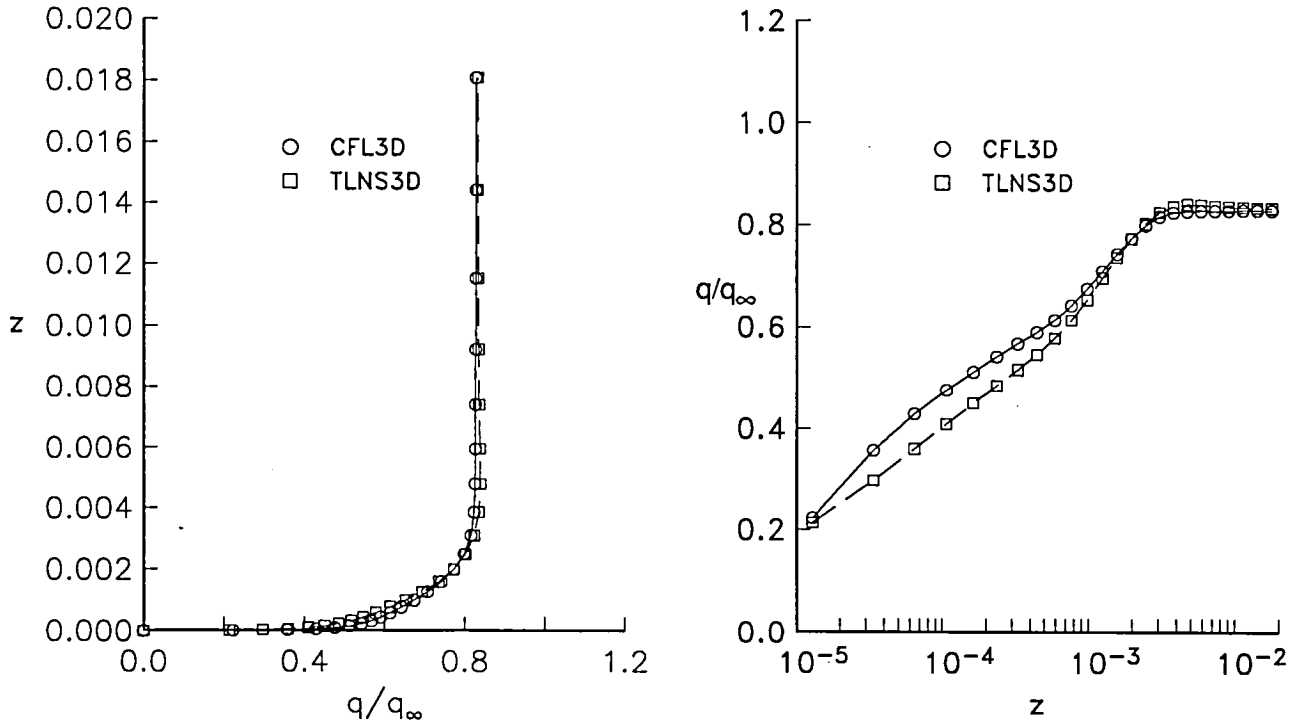

(a) $\eta = 0, \xi = 0.25$.

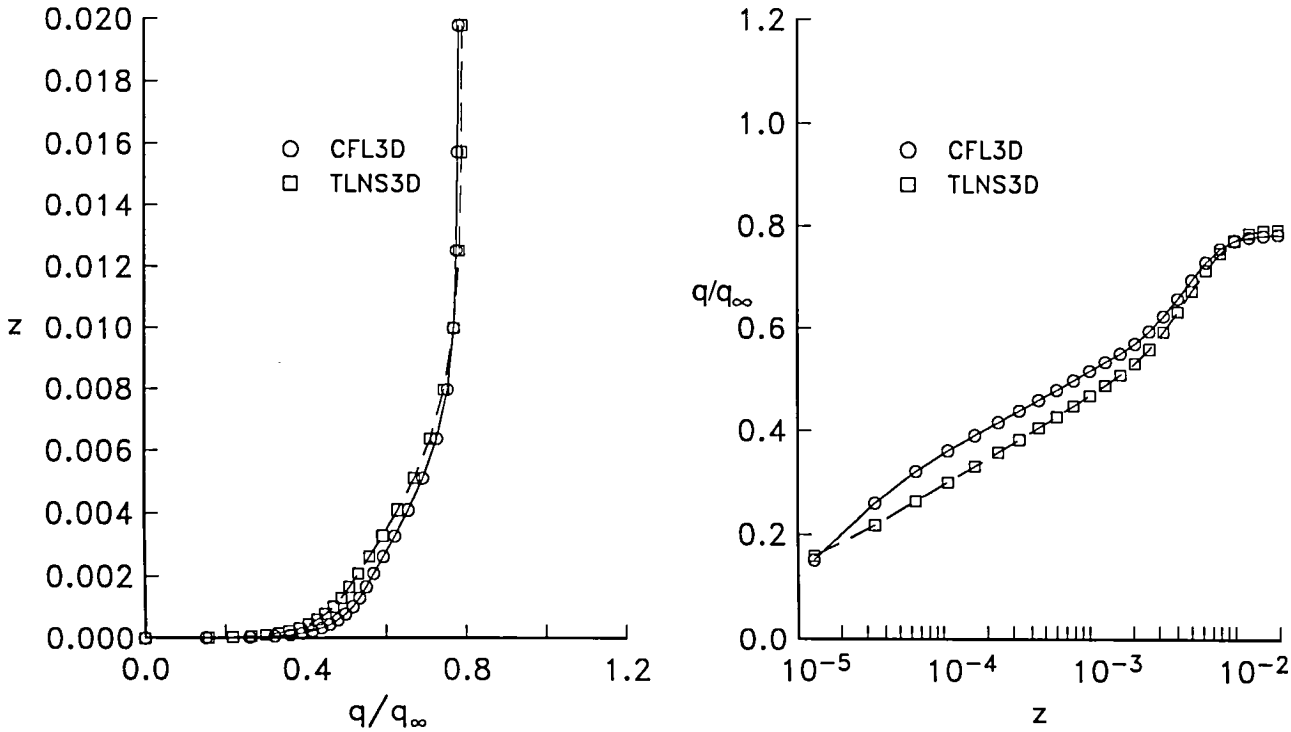

(b) $\eta = 0, \xi = 0.75$.

Figure 55. Lower-surface boundary-layer profiles for the Lockheed Wing B. $193 \times 49 \times 33$ grid.

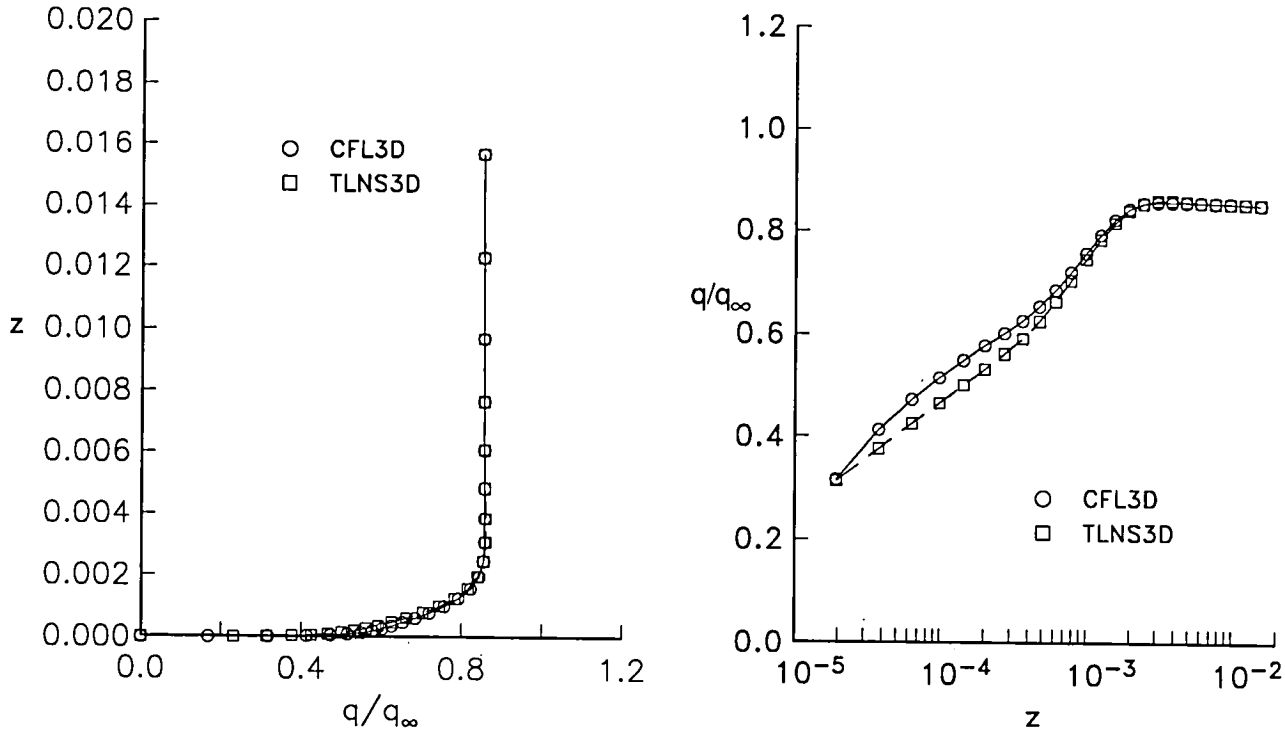

(c) $\eta = 0.5, \xi = 0.25$.

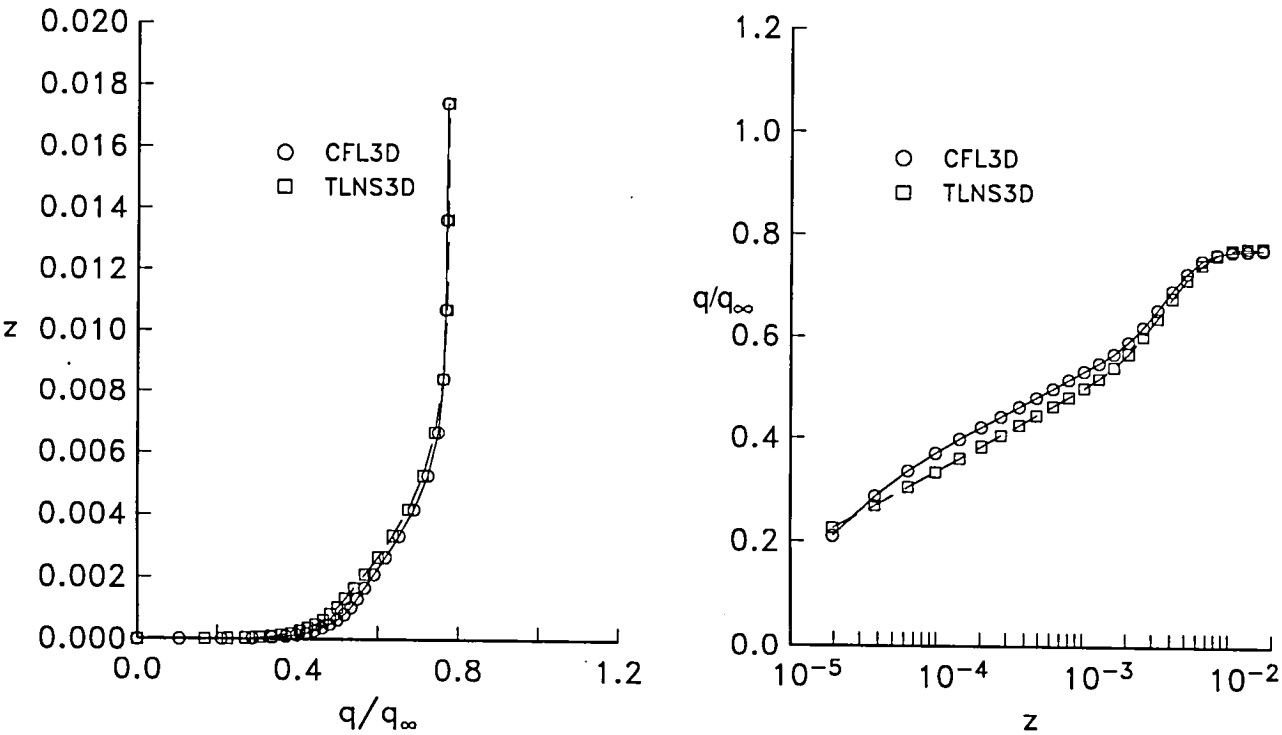

(d) $\eta = 0.5, \xi = 0.75$.

Figure 55. Continued.

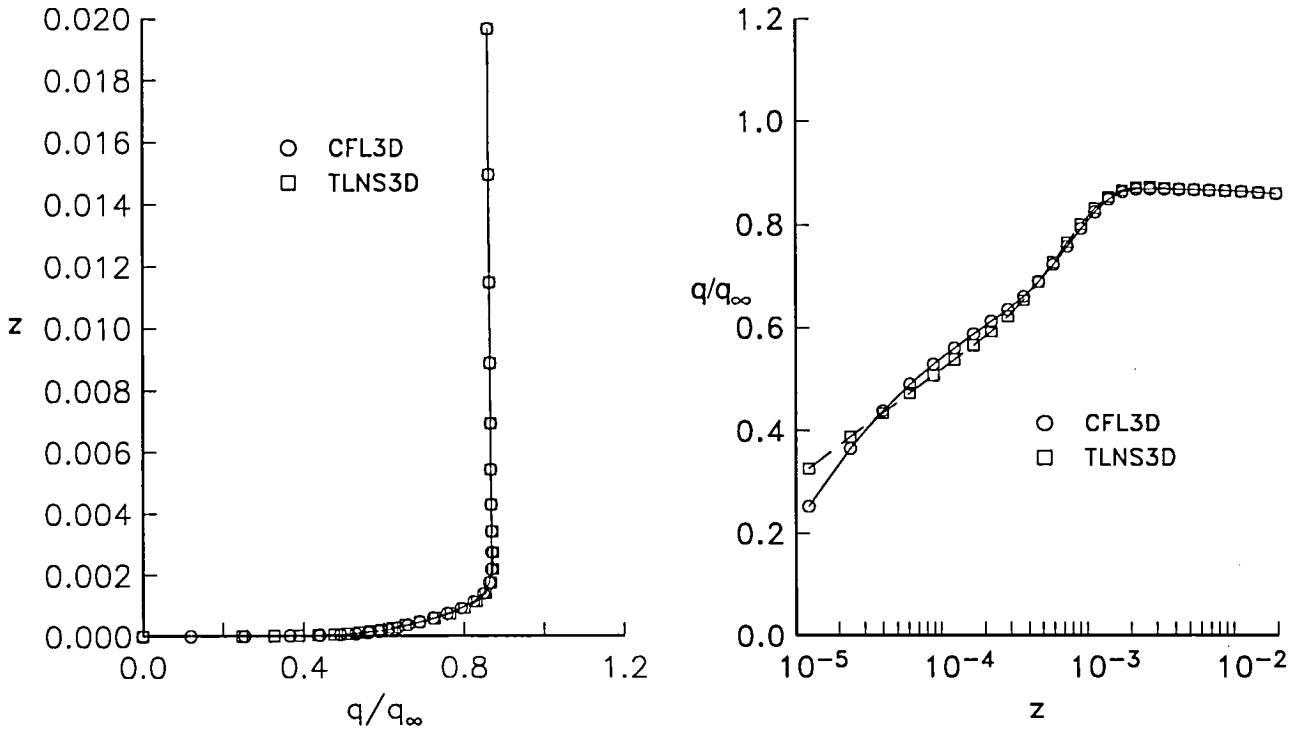

(e) $\eta = 0.8, \xi = 0.25$.

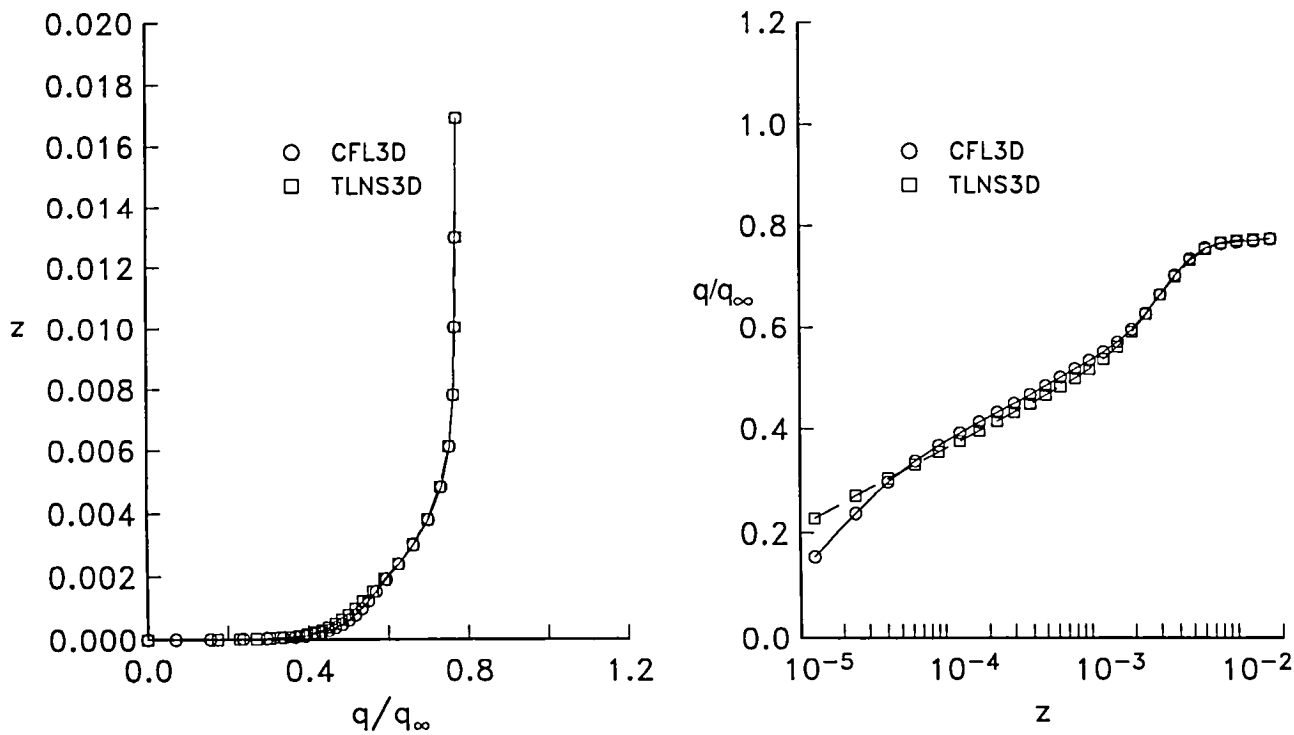

(f) $\eta = 0.8, \xi = 0.75$.

Figure 55. Concluded.

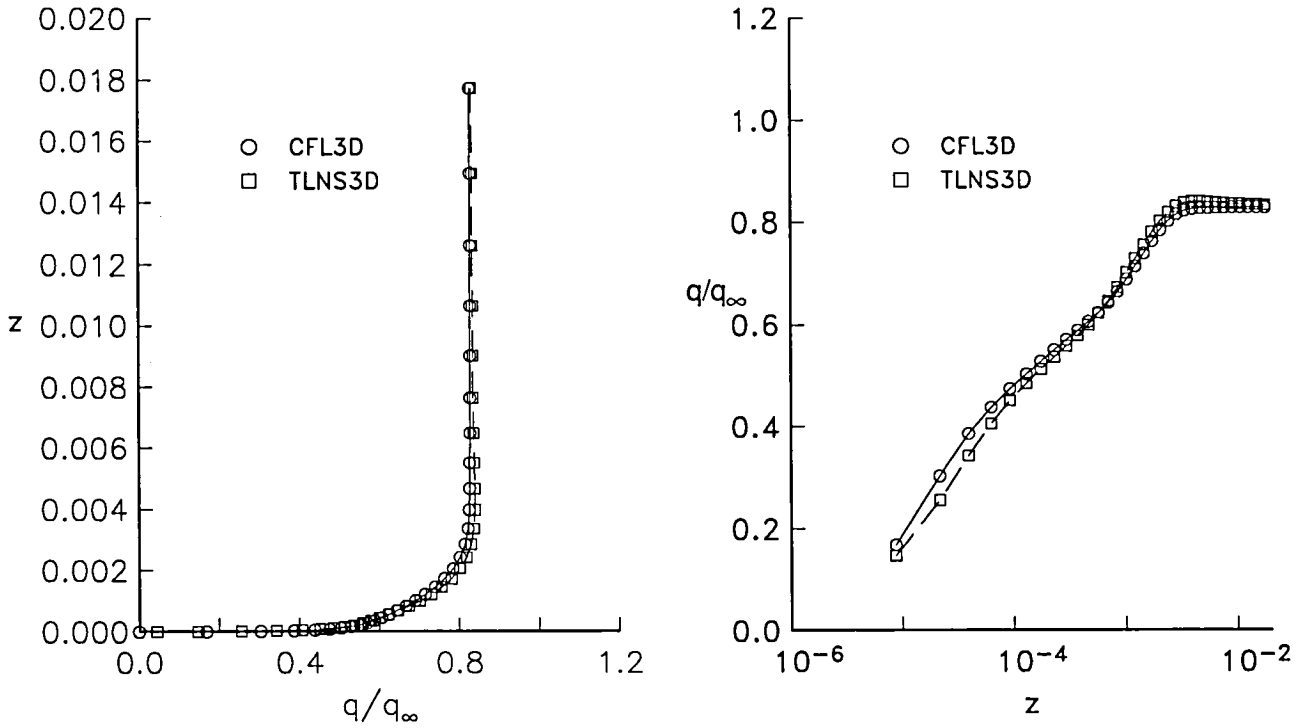

(a) $\eta = 0, \xi = 0.25$.

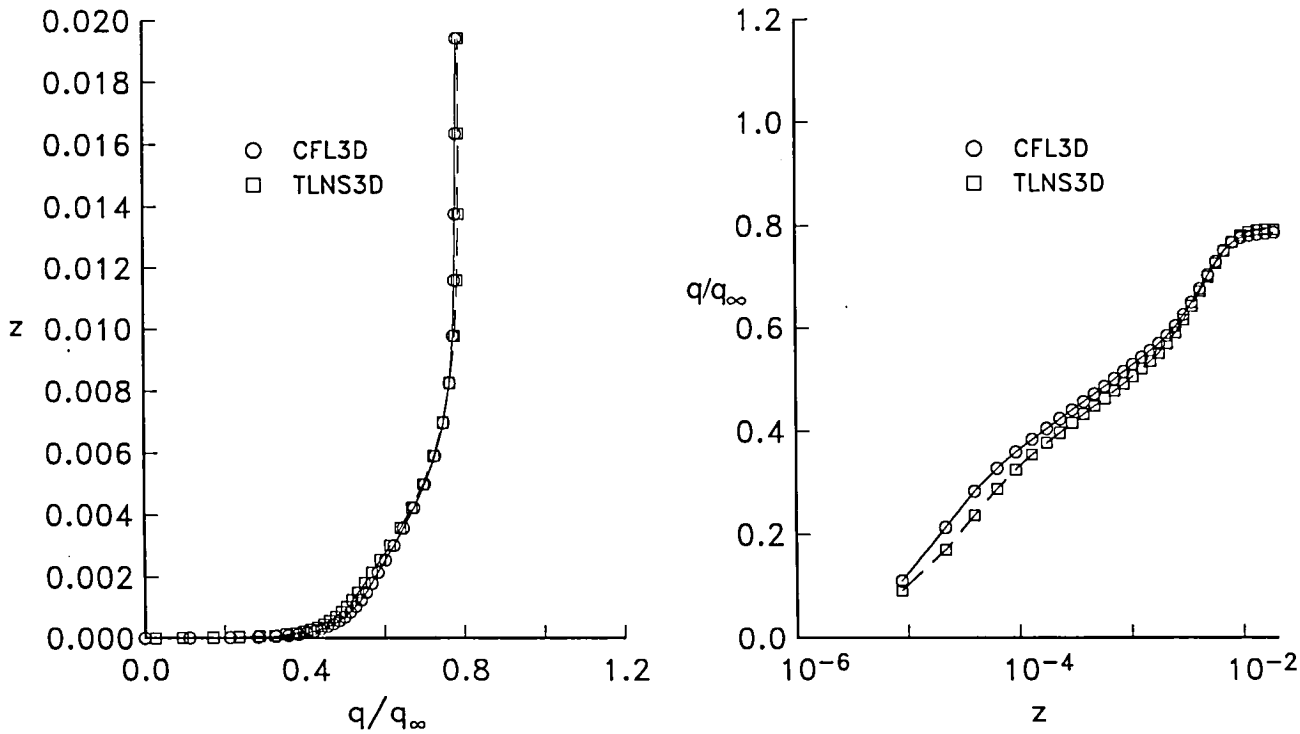

(b) $\eta = 0, \xi = 0.75$.

Figure 56. Lower-surface boundary-layer profiles for the Lockheed Wing B. 289 × 65 × 49 grid.

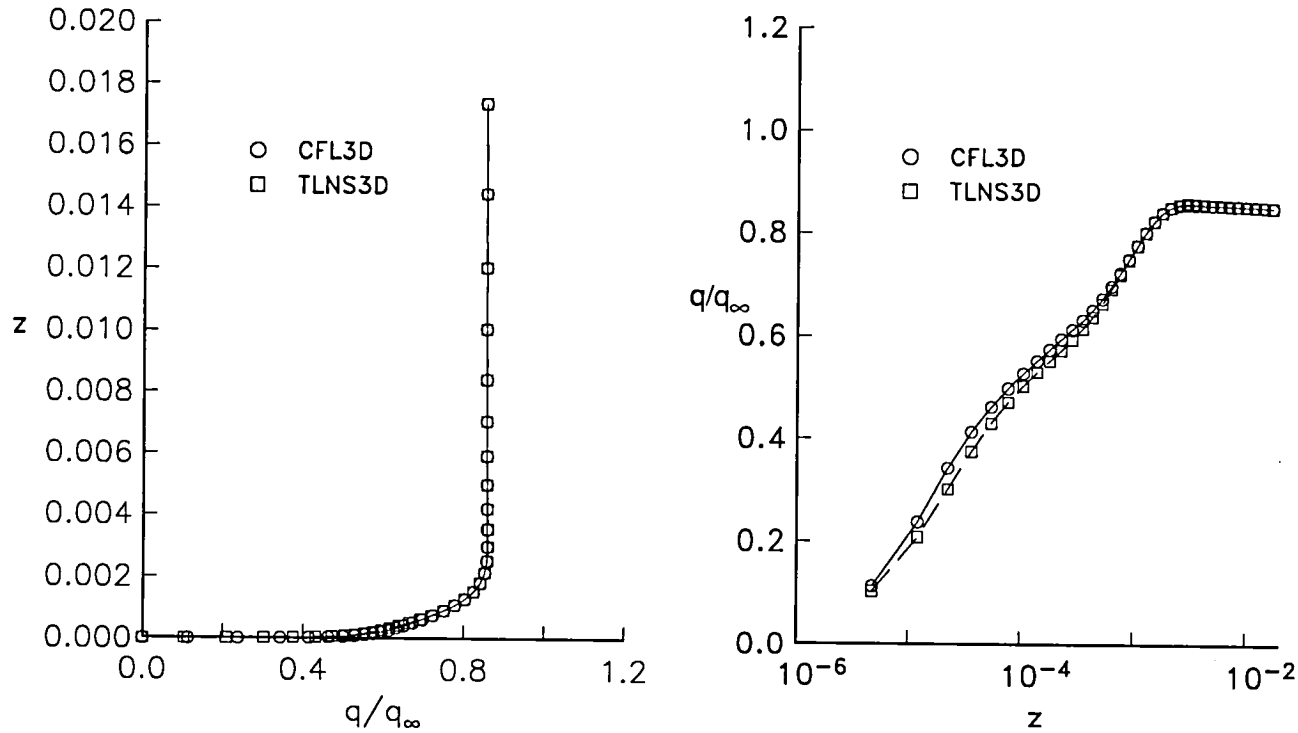

(c) $\eta = 0.5, \xi = 0.25$.

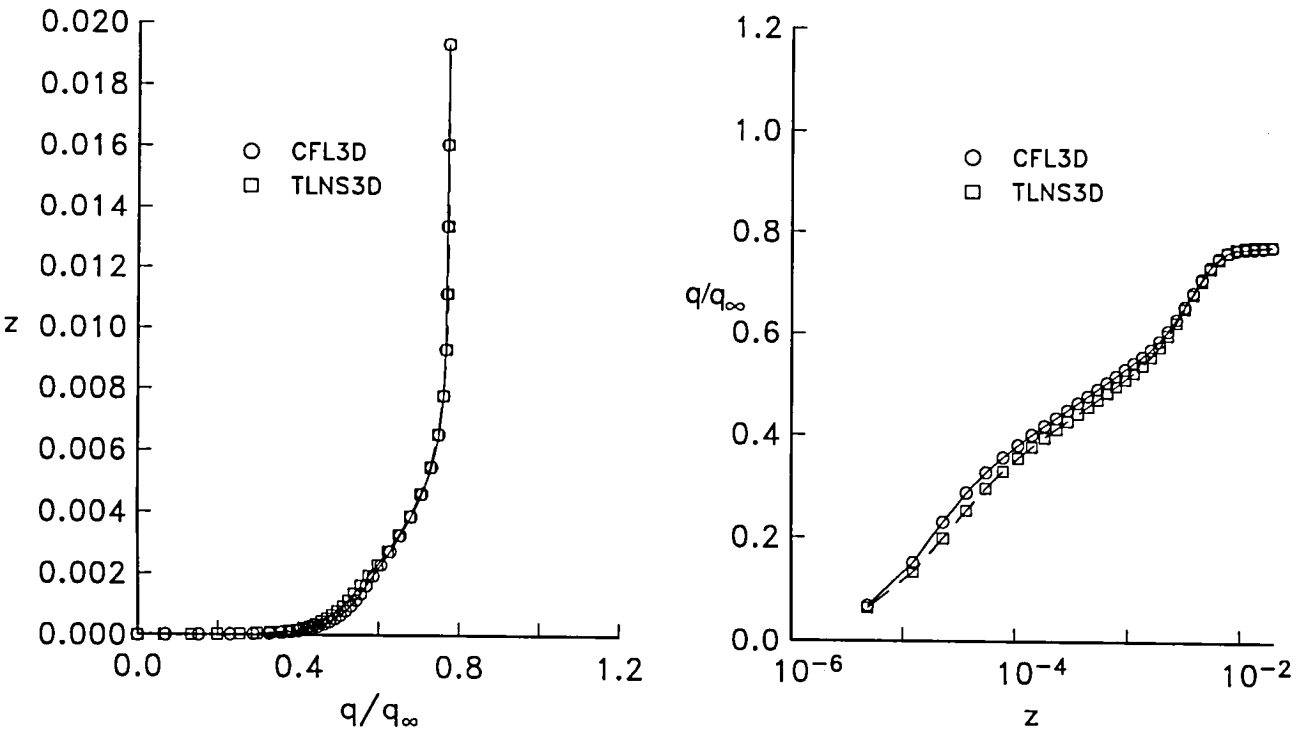

(d) $\eta = 0.5, \xi = 0.75$.

Figure 56. Continued.

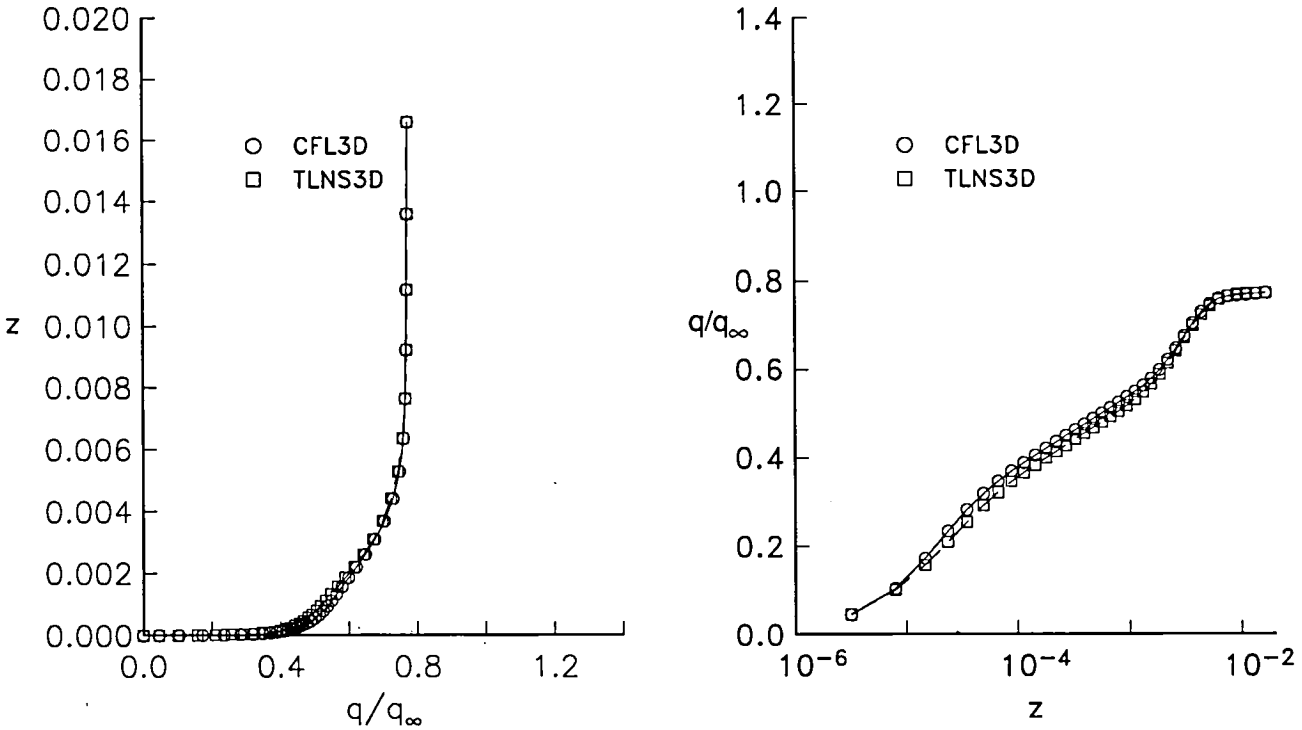

(e) $\eta = 0.8, \xi = 0.25$.

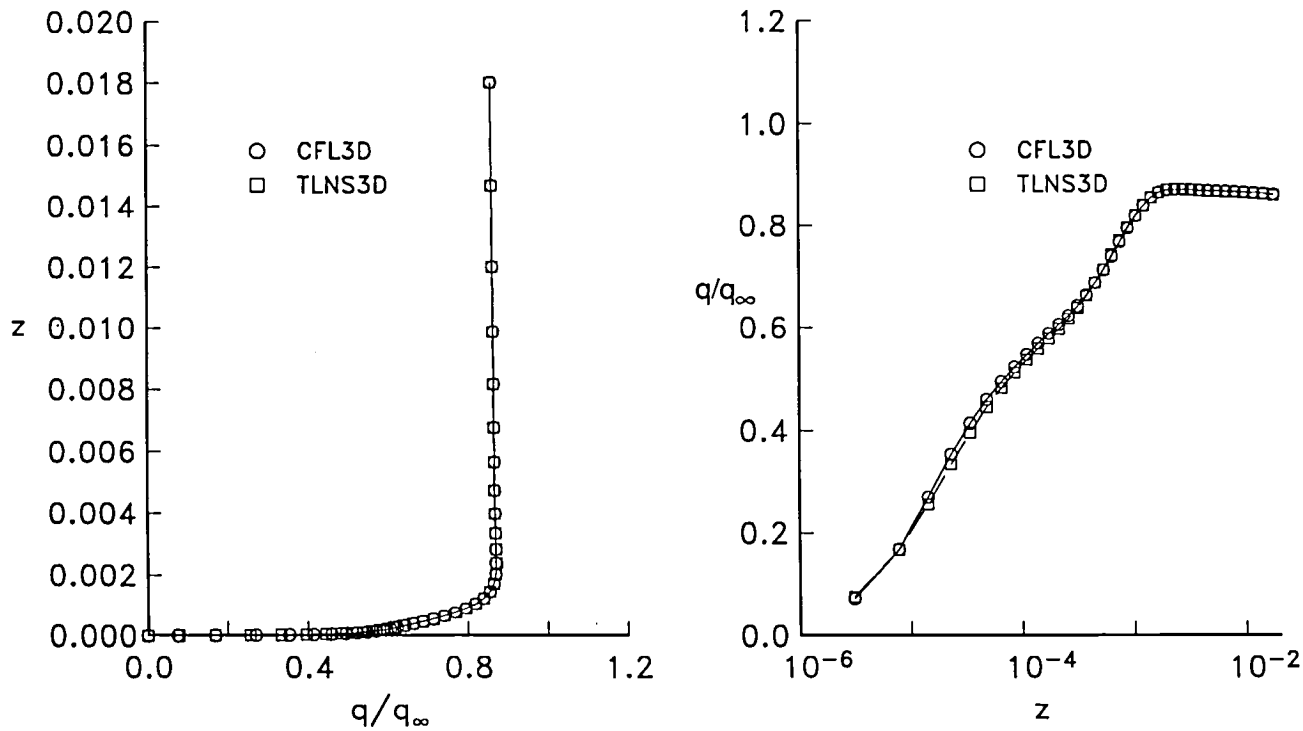

(f) $\eta = 0.8, \xi = 0.75$.

Figure 56. Concluded.

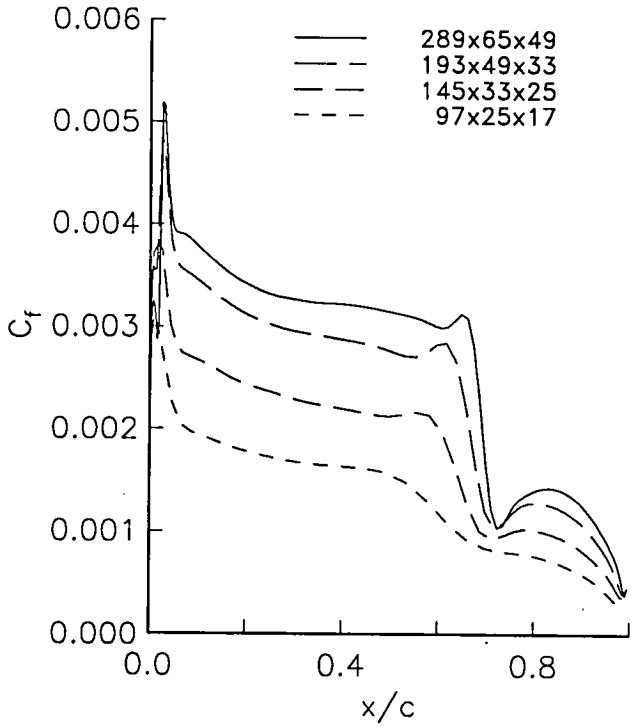

(a) Upper surface; TLNS3D.

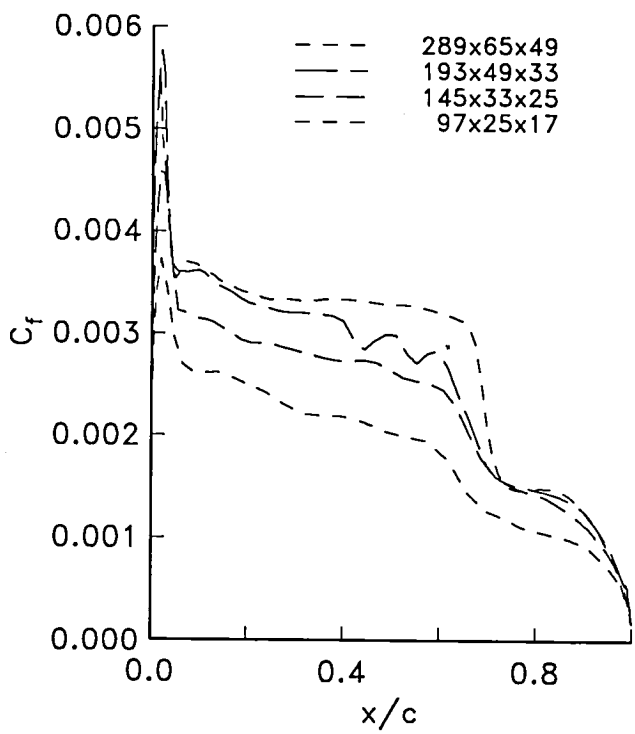

(b) Upper surface; CFL3D.

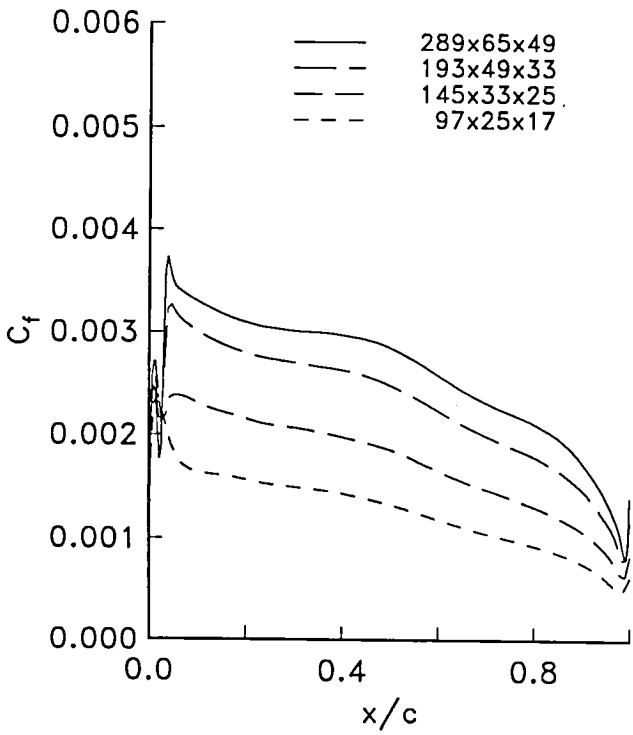

(c) Lower surface; TLNS3D.

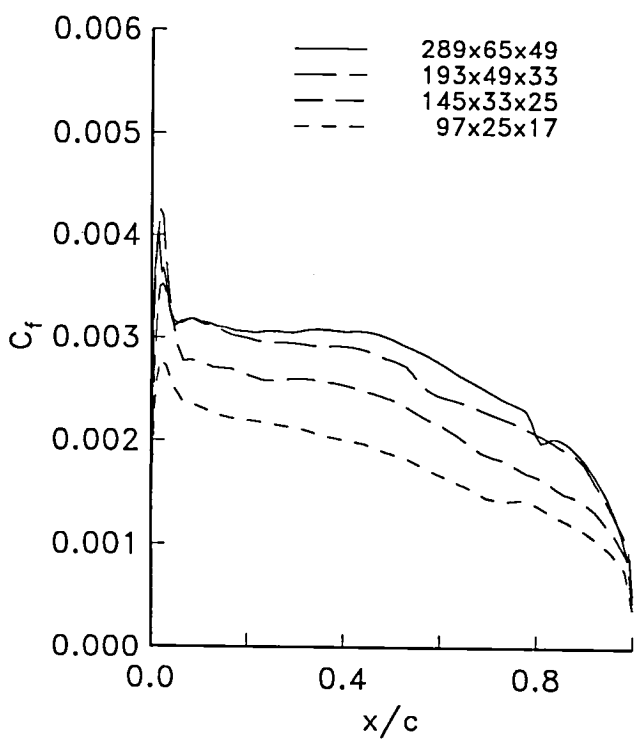

(d) Lower surface; CFL3D.

Figure 57. Effect of grid refinement on the symmetry plane skin friction for the ONERA M6 wing.

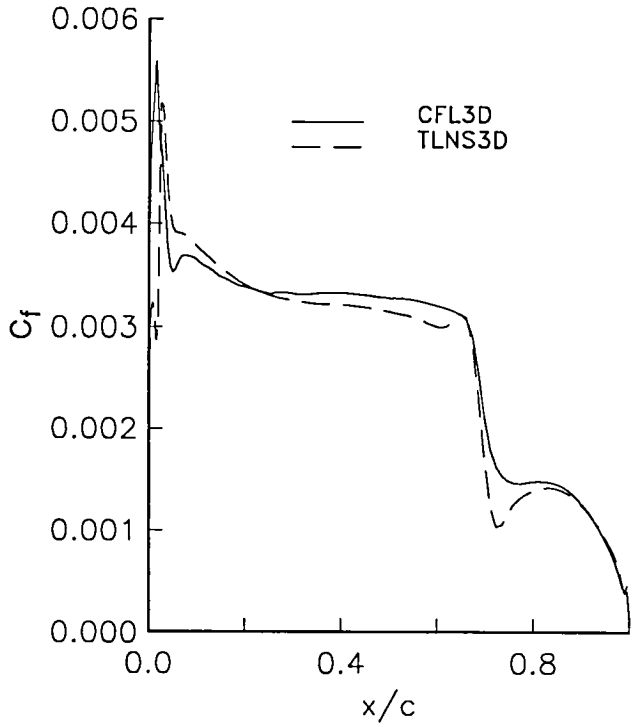

(a) Upper surface; 289 × 65 × 49.

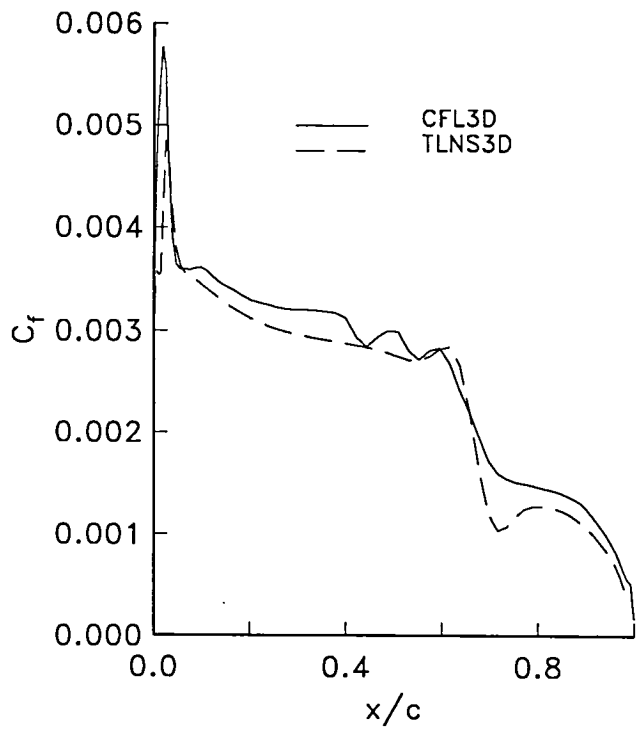

(b) Upper surface; 193 × 49 × 33.

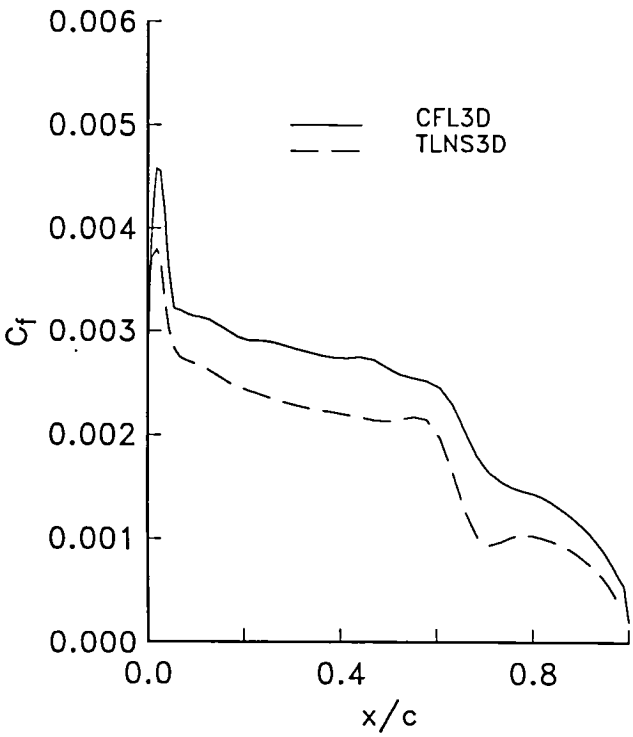

(c) Lower surface; 145 × 33 × 25.

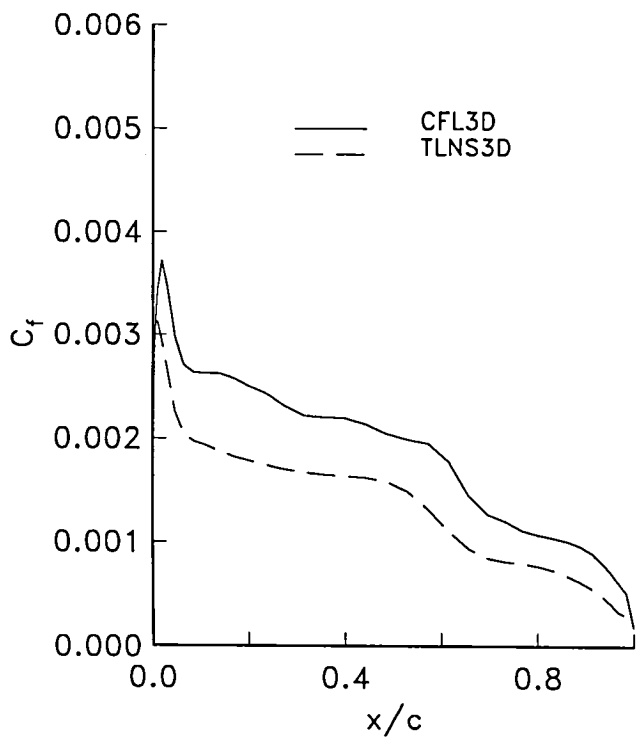

(d) Lower surface; 97 × 25 × 17.

Figure 58. Symmetry plane skin friction distributions using the same grid. ONERA M6 wing.

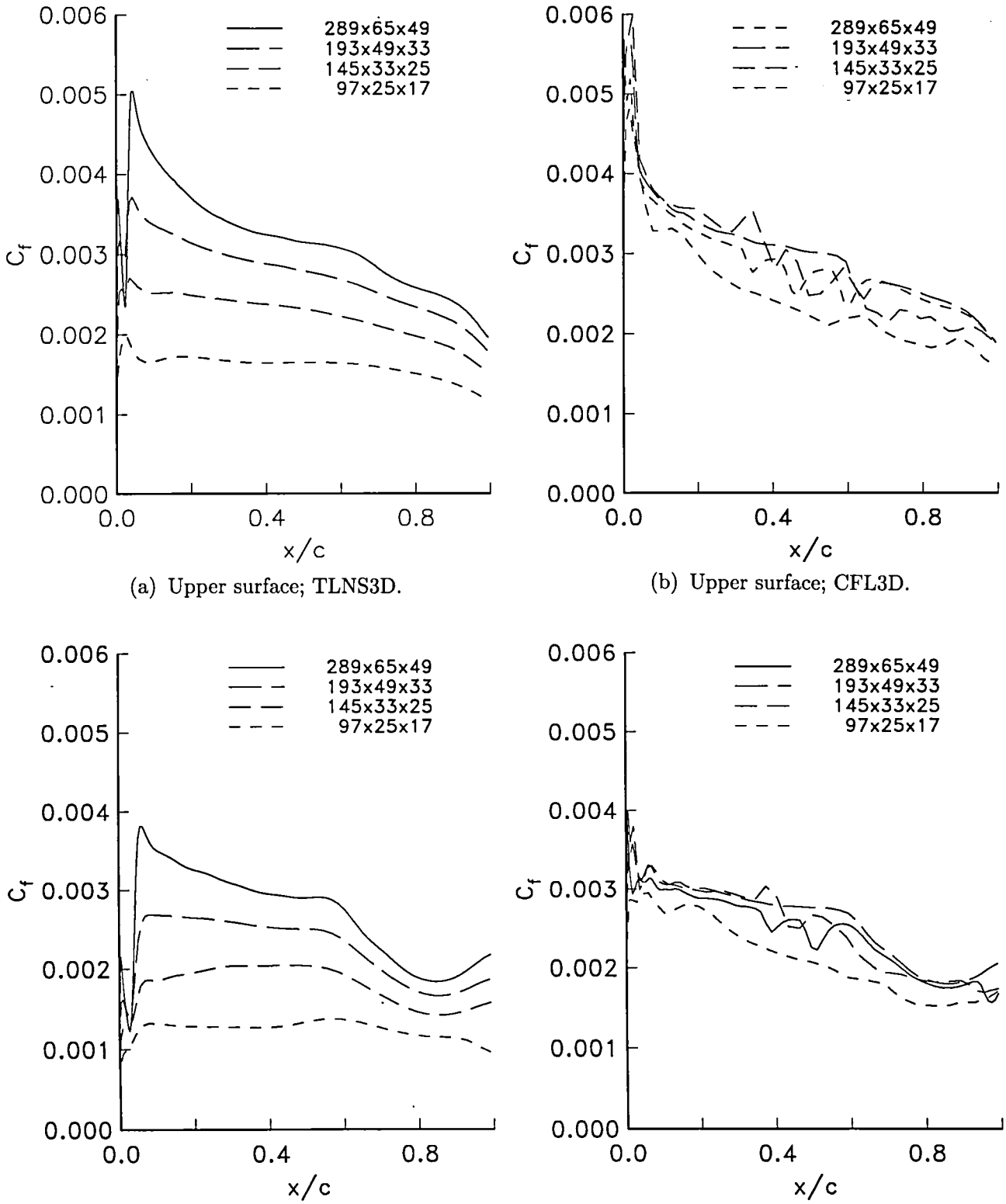

(a) Upper surface; TLNS3D.

(b) Upper surface; CFL3D.

(c) Lower surface; TLNS3D.

(d) Lower surface; CFL3D.

Figure 59. Effect of grid refinement on the symmetry plane skin friction. Lockheed Wing B.

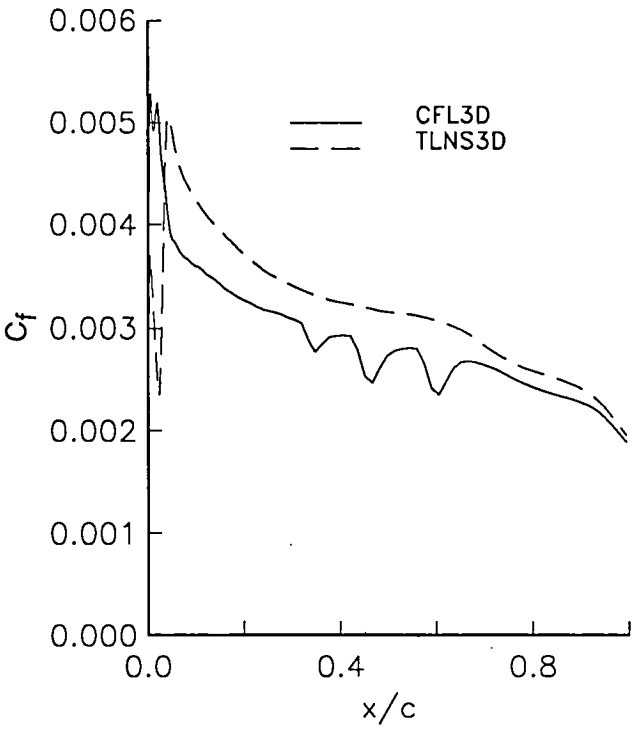

(a) Upper surface; 289 × 65 × 49.

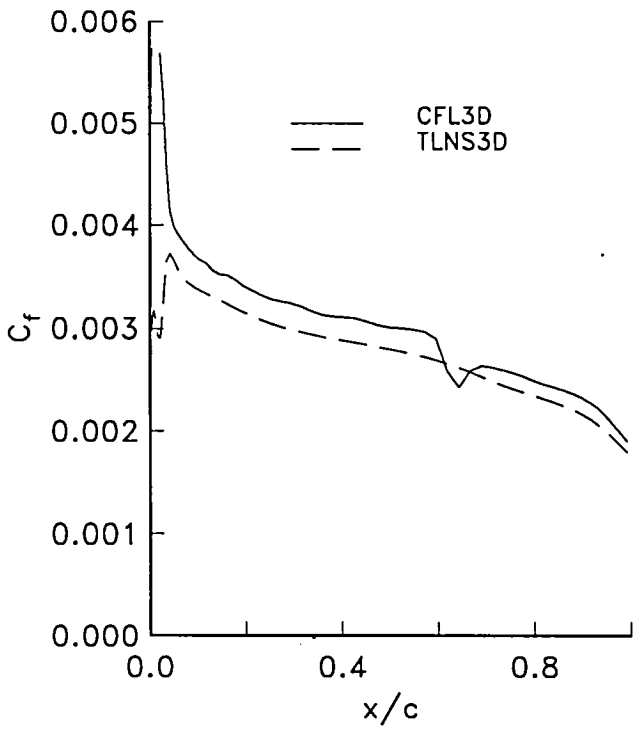

(b) Upper surface; 193 × 49 × 33.

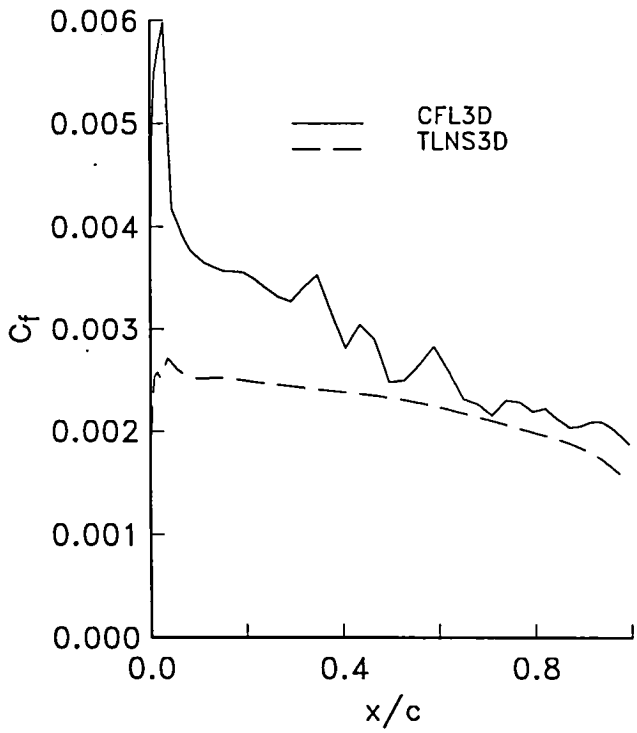

(c) Lower surface; 145 × 33 × 25.

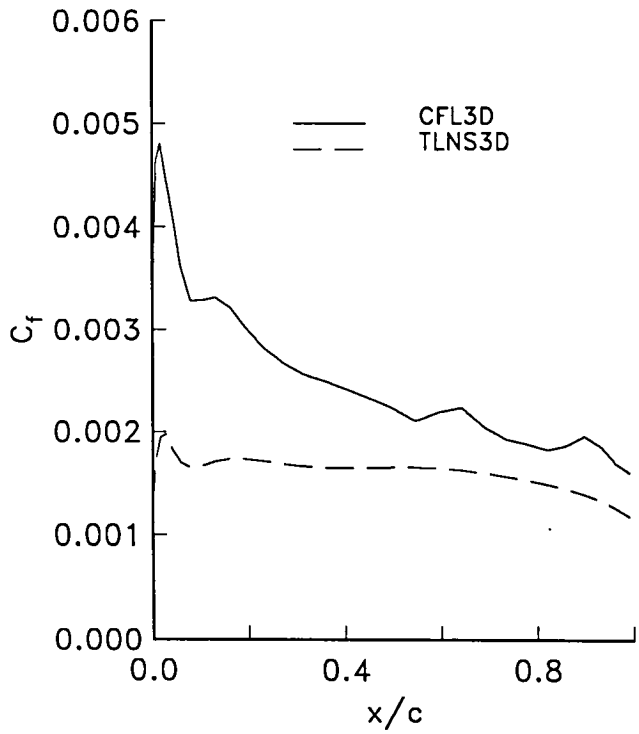

(d) Lower surface; 97 × 25 × 17.

Figure 60. Symmetry plane skin friction distributions using the same grid. Lockheed Wing B.

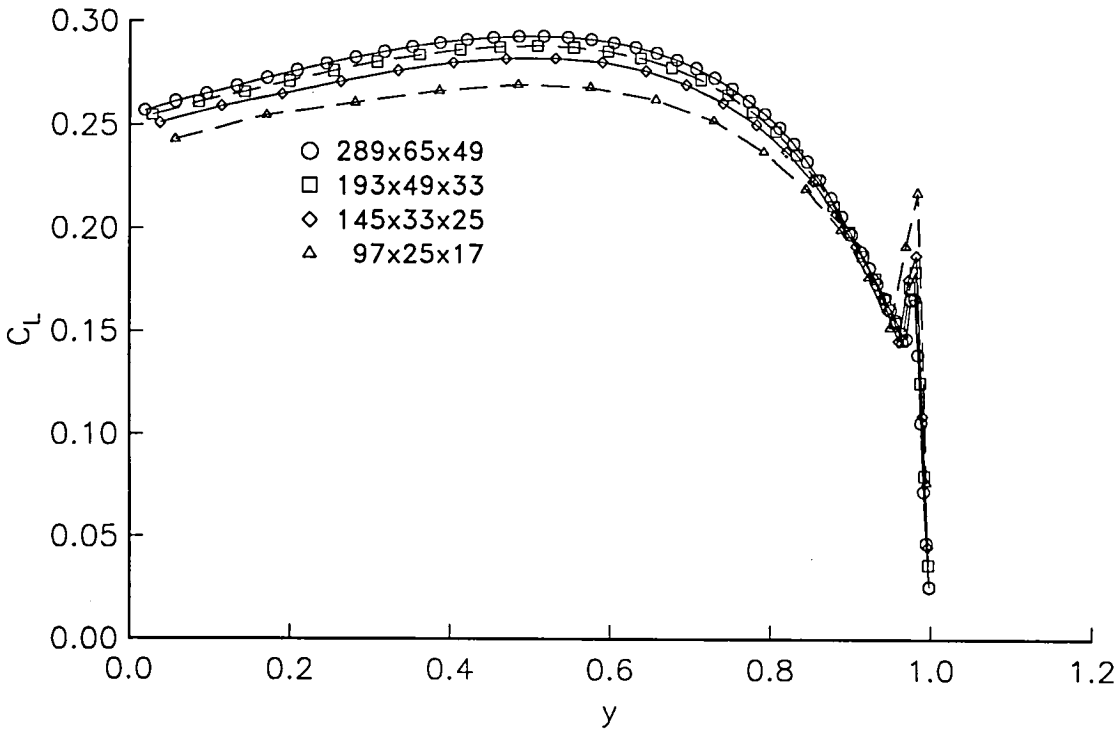

(a) TLNS3D.

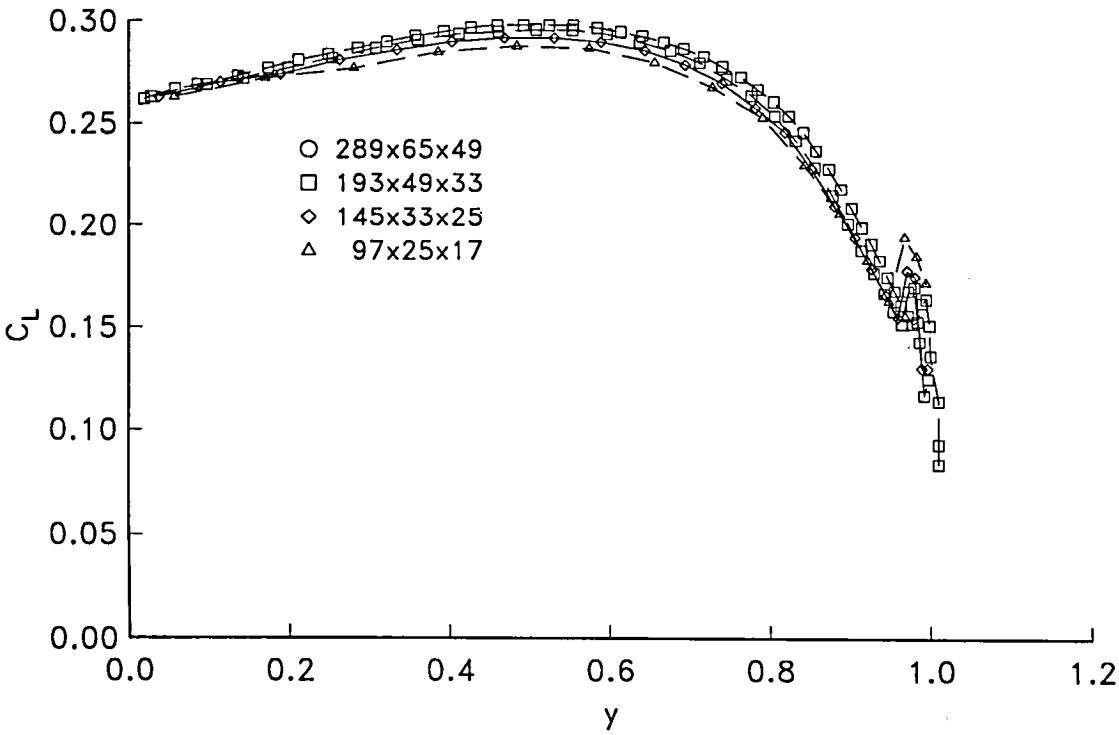

(b) CFL3D.

Figure 61. Effect of grid refinement on spanwise lift distributions. ONERA M6 wing.

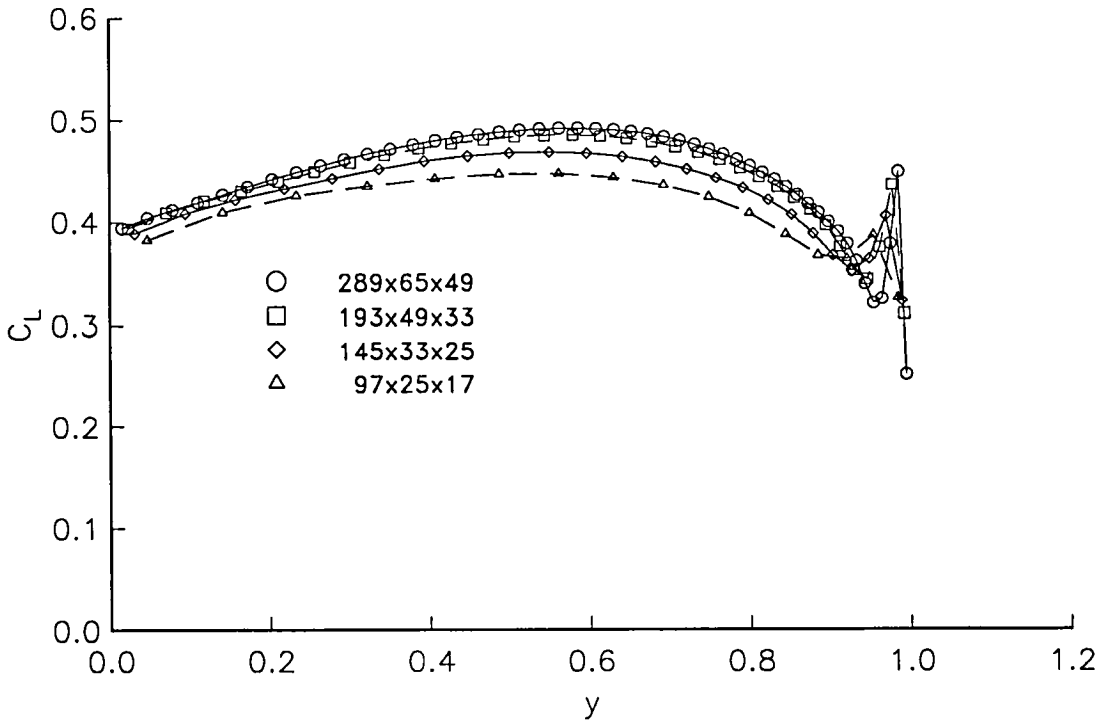

(a) TLNS3D.

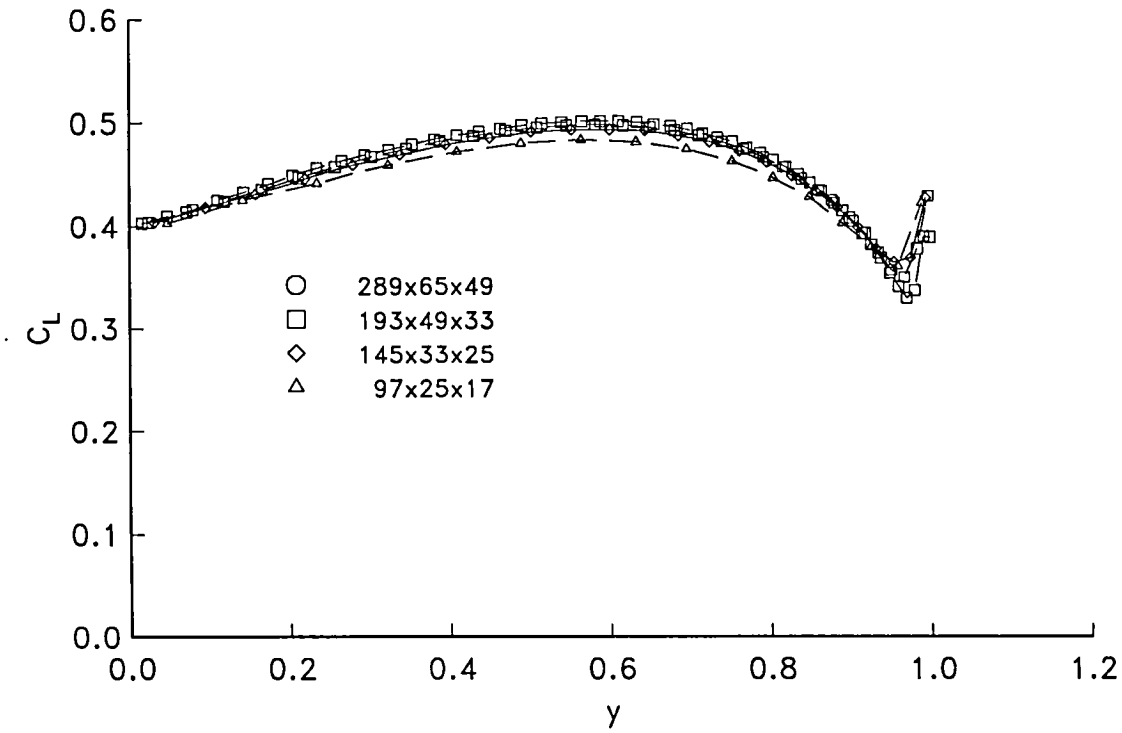

(b) CFL3D.

Figure 62. Effect of grid refinement on spanwise lift distributions. Lockheed Wing B.

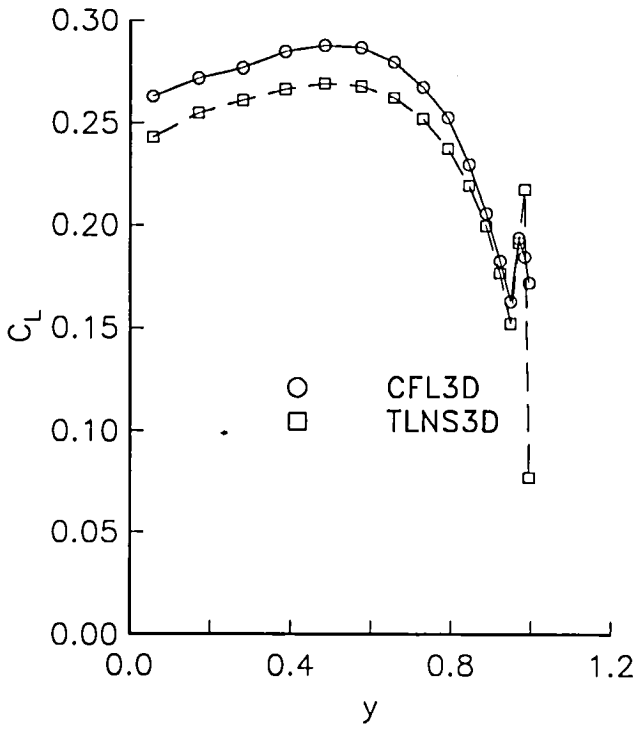

(a) $97 \times 27 \times 17$.

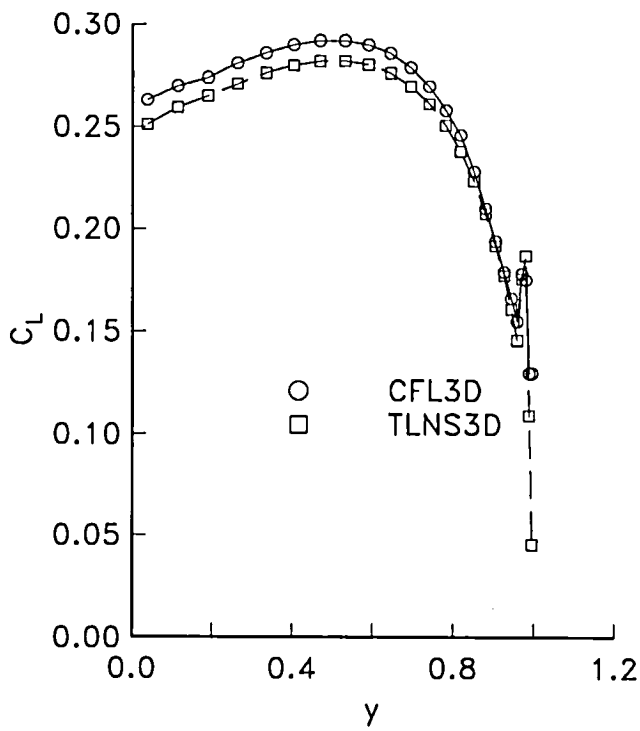

(b) $145 \times 33 \times 25$.

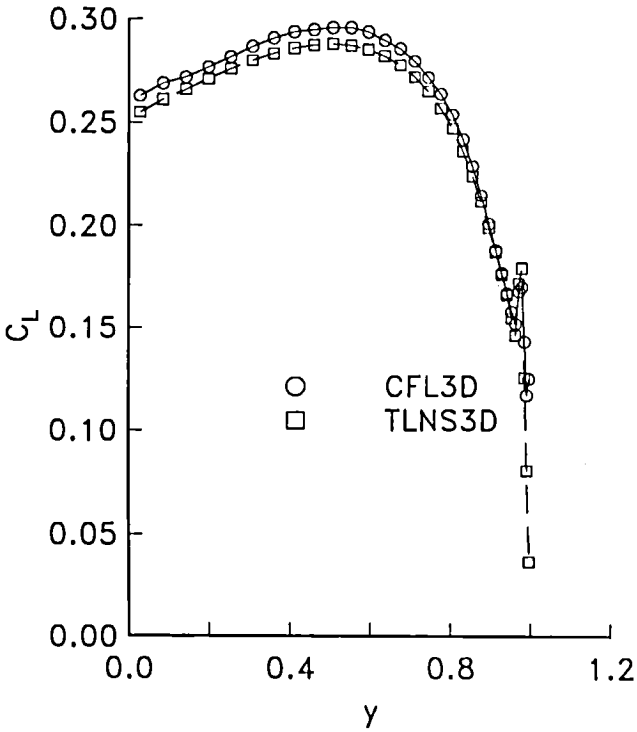

(c) $193 \times 49 \times 33$.

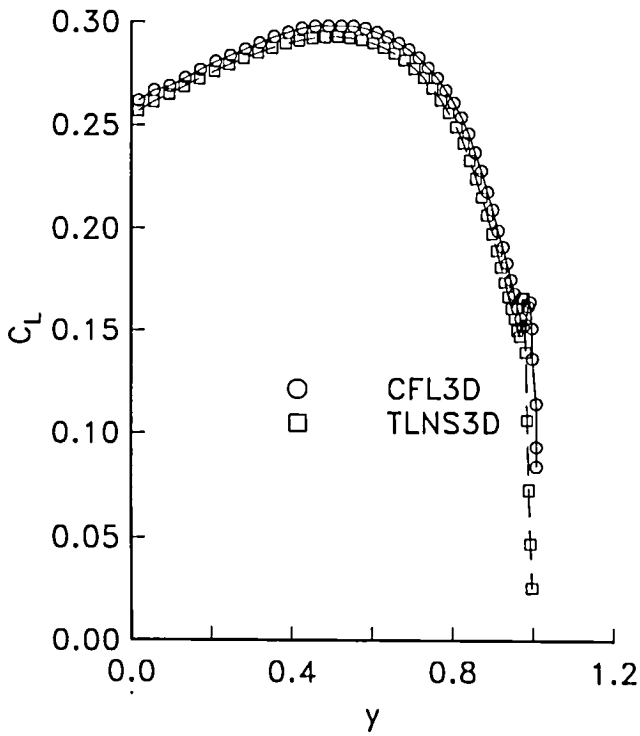

(d) $289 \times 65 \times 49$.

Figure 63. Spanwise lift distributions for the ONERA M6 wing.

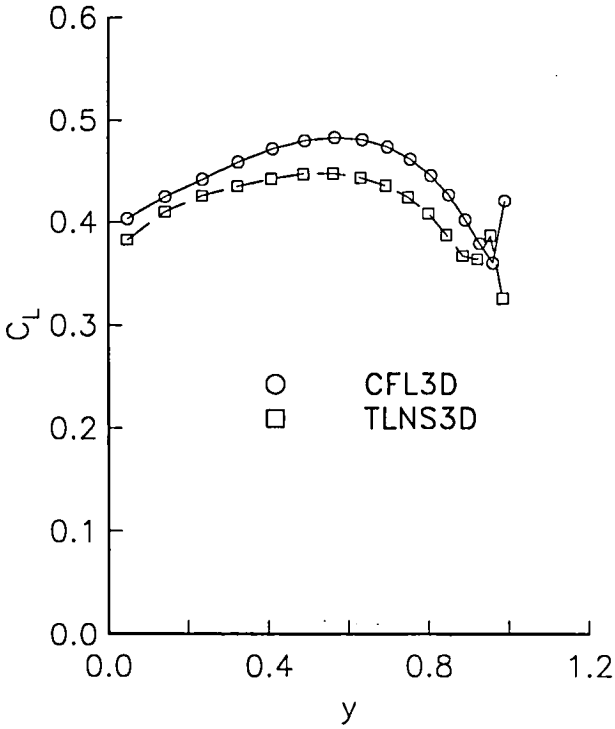

(a) $97 \times 27 \times 17$.

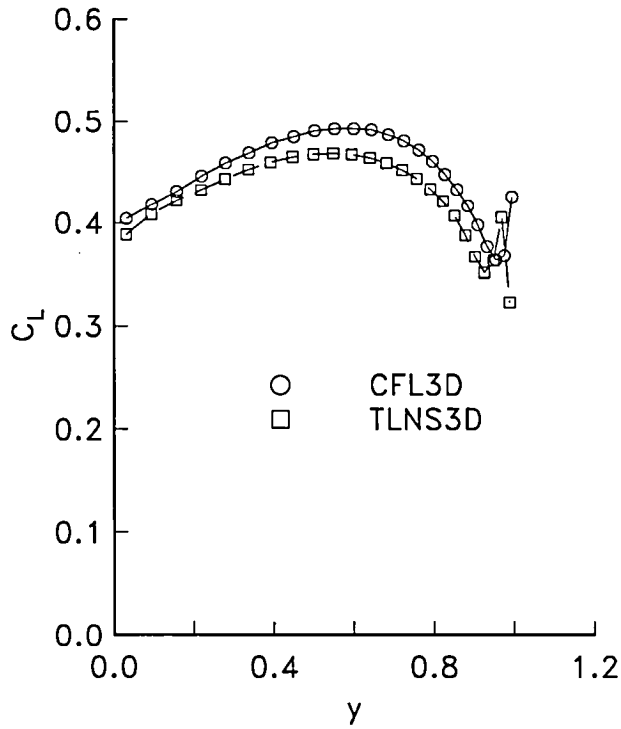

(b) $145 \times 33 \times 25$.

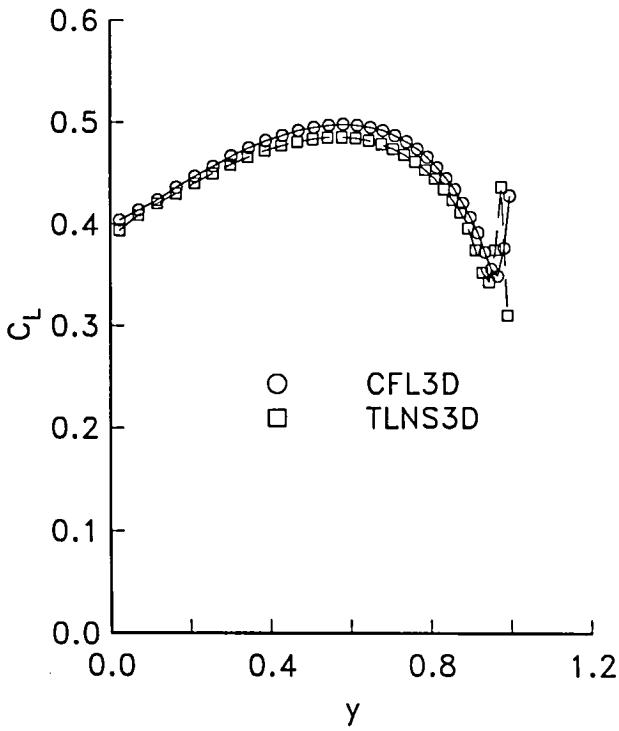

(c) $193 \times 49 \times 33$.

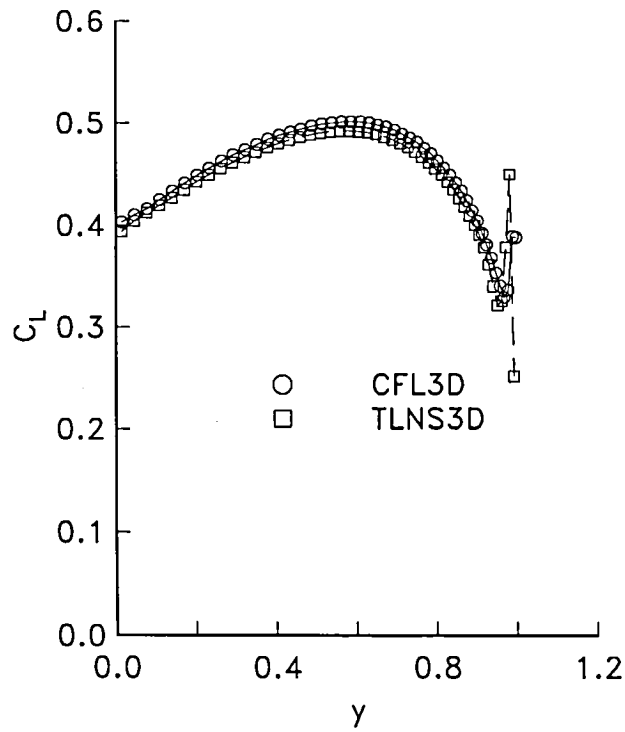

(d) $289 \times 65 \times 49$.

Figure 64. Spanwise lift distributions for the Lockheed Wing B.

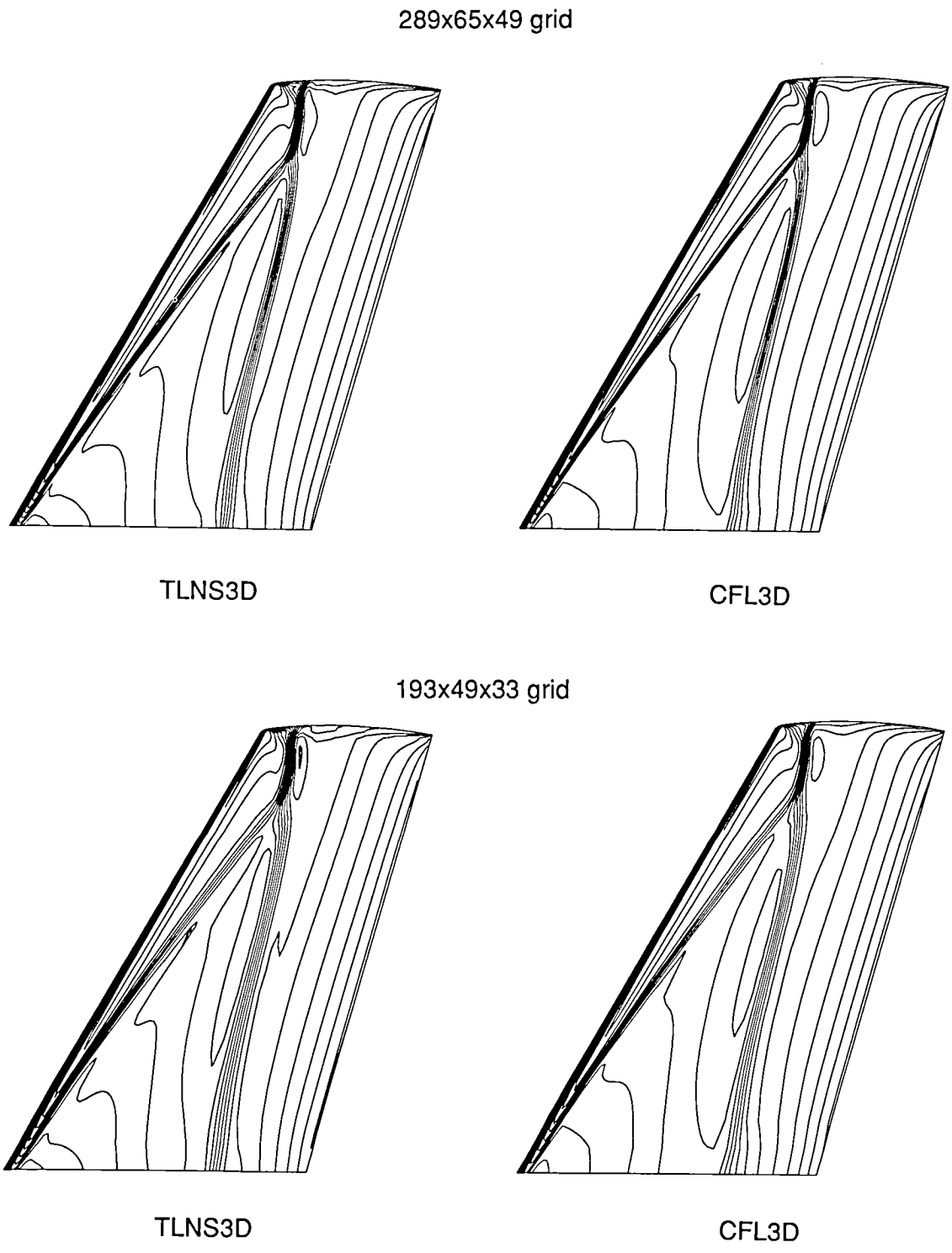

Figure 65. Upper surface pressure contours for ONERA M6 wing.

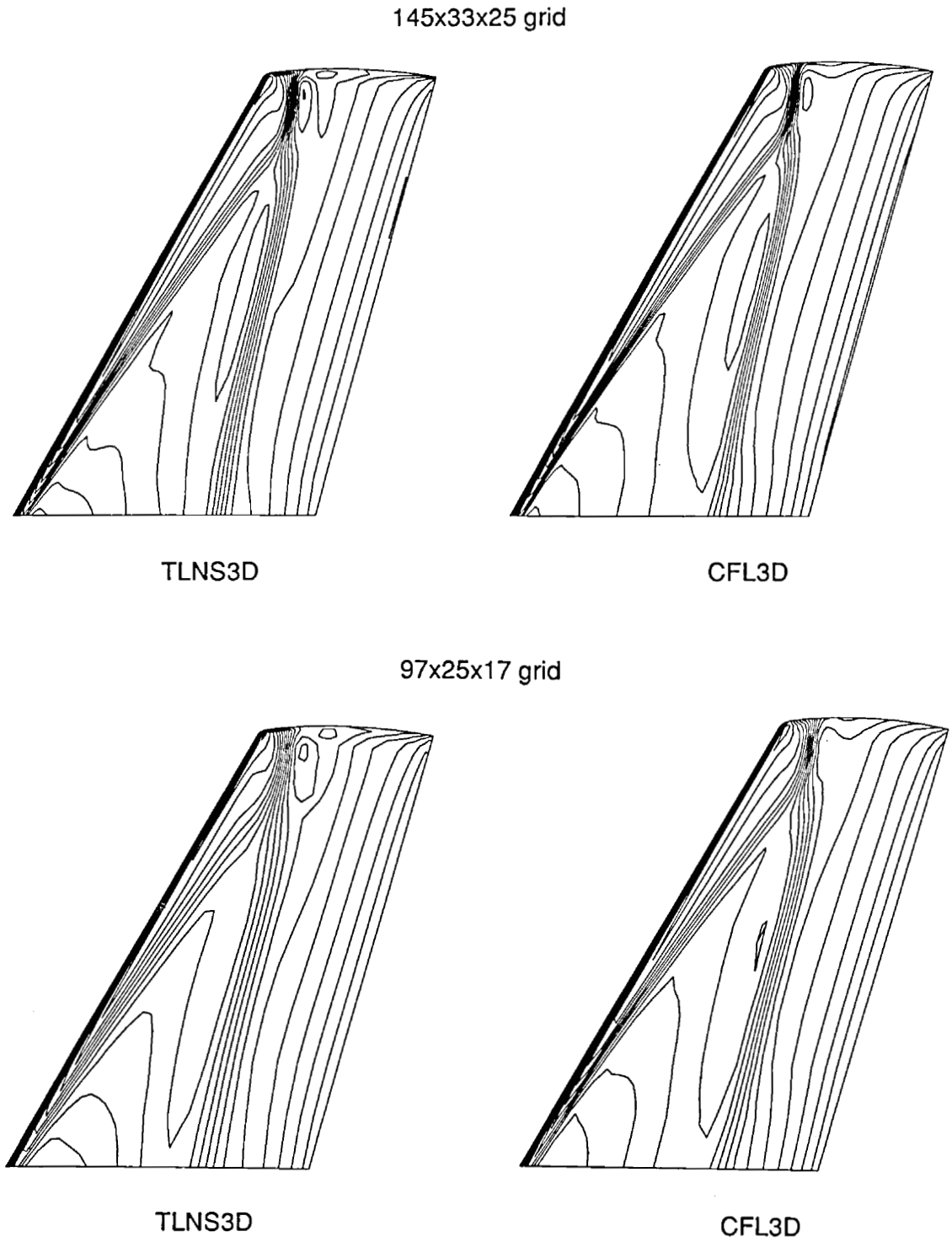

Figure 65. Concluded.

289x65x49 grid

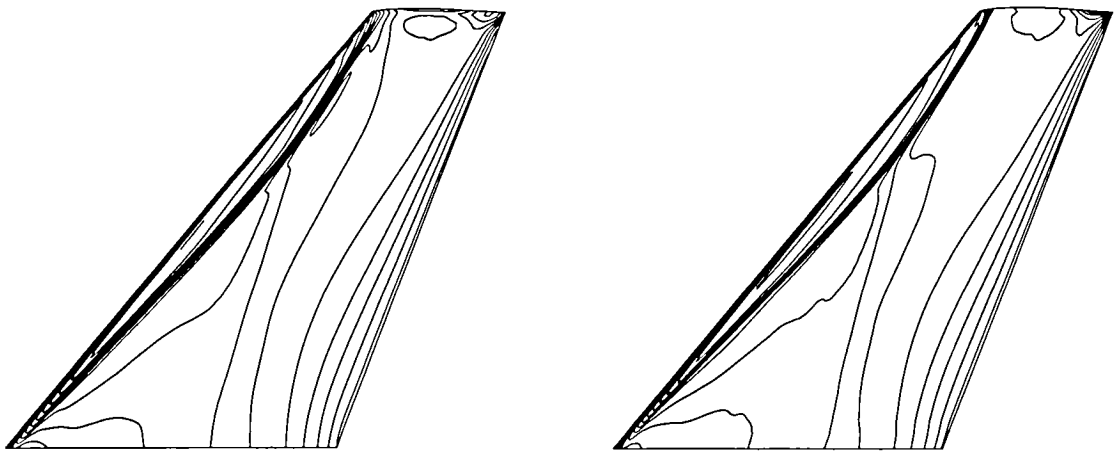

TLNS3D CFL3D

193x49x33 grid

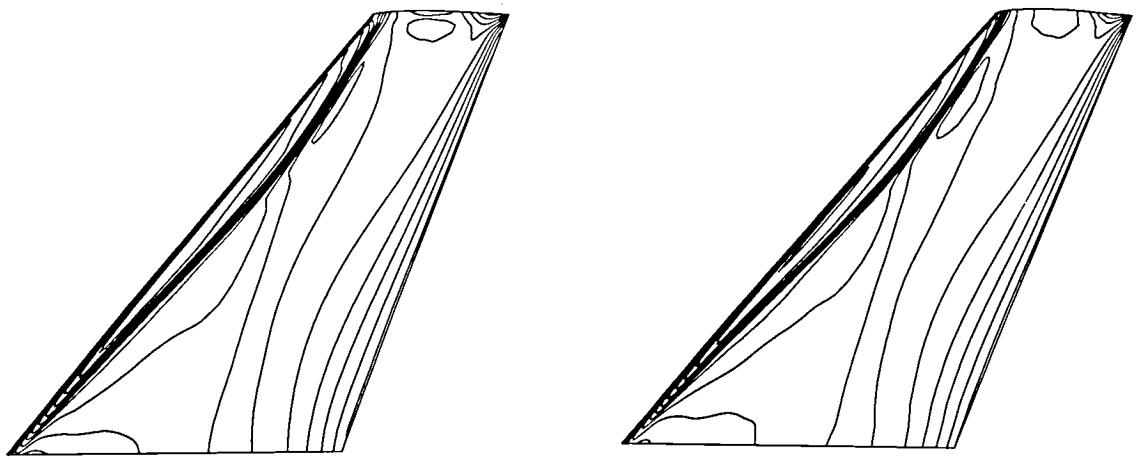

TLNS3D CFL3D

Figure 66. Upper surface pressure contours for Lockheed Wing B.

145x33x25 grid

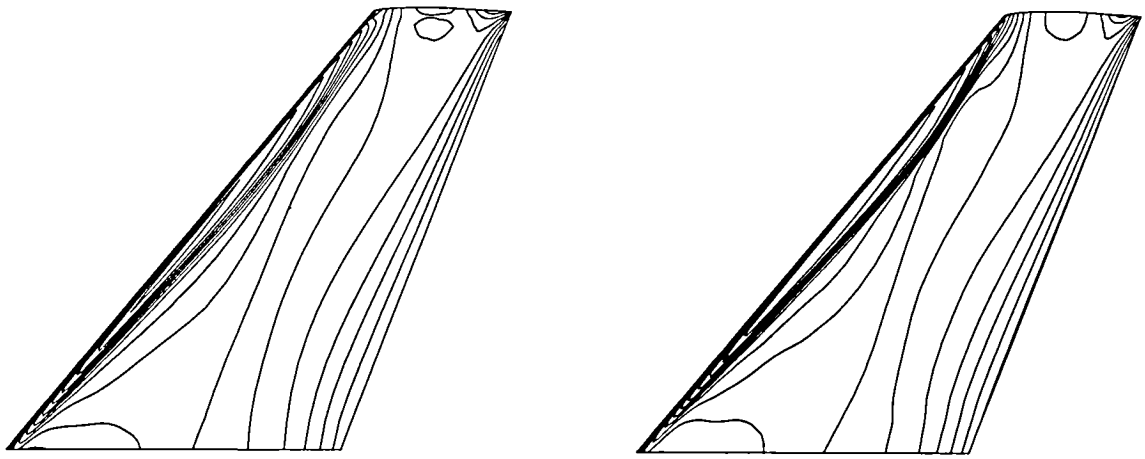

TLNS3D CFL3D

97x25x17 grid

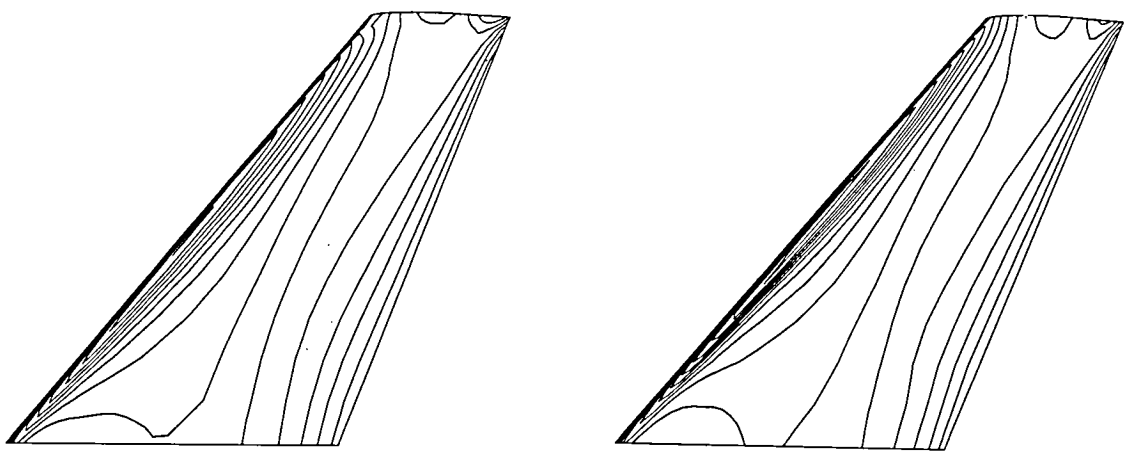

TLNS3D CFL3D

Figure 66. Concluded.

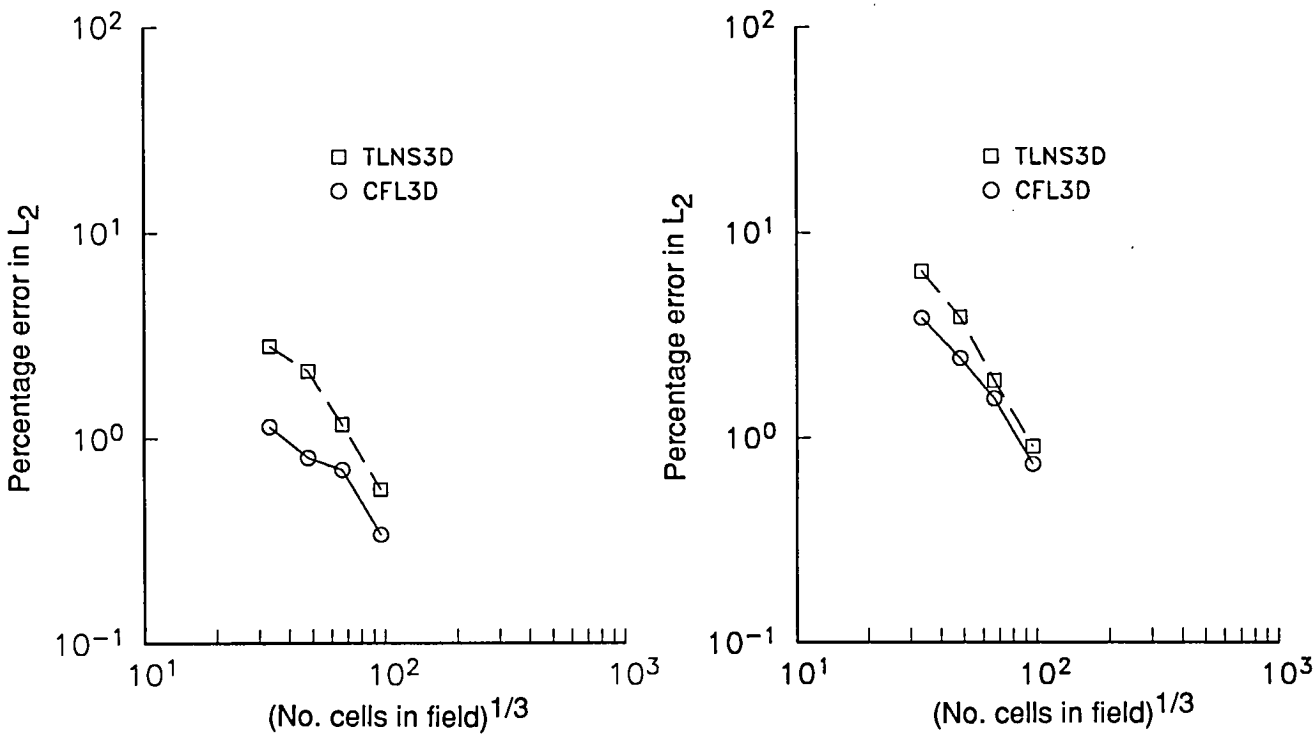

(a) ONERA M6 wing.

(b) Lockheed Wing B.

Figure 67. L_2 spatial error norm.

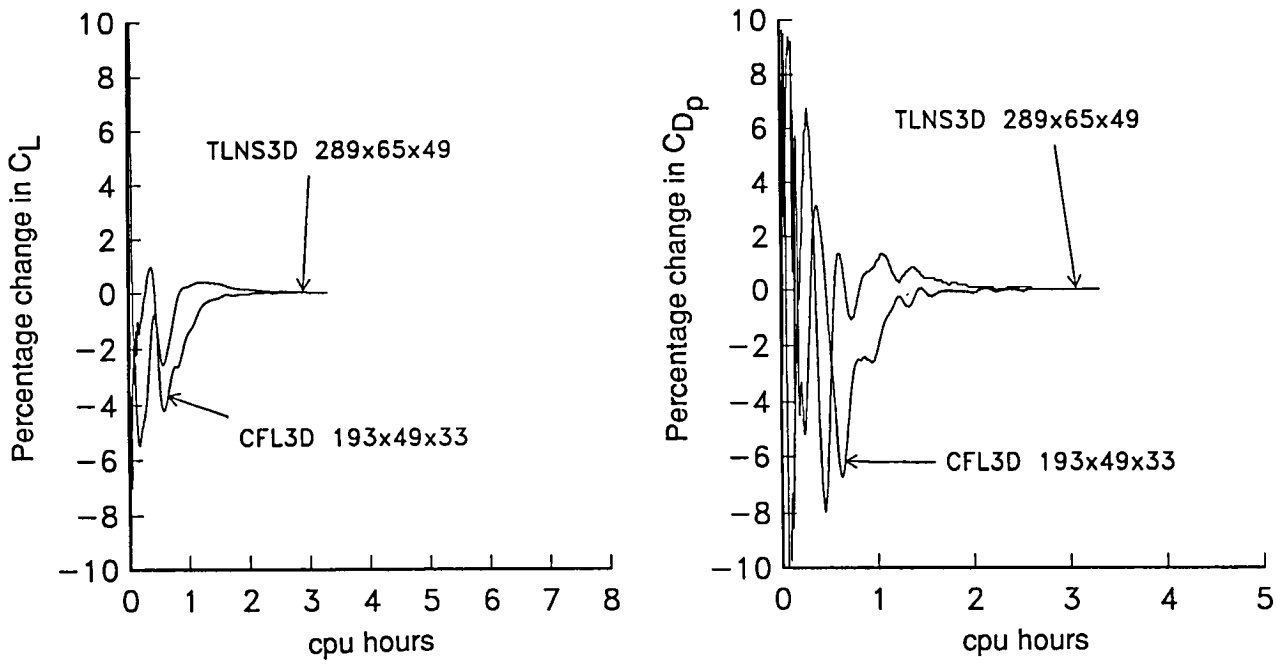

(a) Lift history.

(b) Pressure drag history.

Figure 68. Relative efficiency of the ONERA M6 wing.

NASA
National Aeronautics and Space Administration

Report Documentation Page

1. Report No.	2. Government Accession No.	3. Recipient's Catalog No.
NASA TP-3061		

4. Title and Subtitle	5. Report Date
Relative Efficiency and Accuracy of Two Navier-Stokes Codes for Simulating Attached Transonic Flow Over Wings	February 1991
	6. Performing Organization Code
7. Author(s)	8. Performing Organization Report No.
Daryl L. Bonhaus and Stephen F. Wornom	L-16811
9. Performing Organization Name and Address	10. Work Unit No.
NASA Langley Research Center Hampton, VA 23665-5225	505-62-31-06
	11. Contract or Grant No.
12. Sponsoring Agency Name and Address	13. Type of Report and Period Covered
National Aeronautics and Space Administration Washington, DC 20546-0001	Technical Paper
	14. Sponsoring Agency Code

15. Supplementary Notes

16. Abstract

In the present study, two codes that solve the three-dimensional thin-layer Navier-Stokes equations are used to compute the steady-state flow for two test cases representing typical finite wings at transonic conditions. Several grids of *C-O* topology and varying point densities are used to determine the effects of grid refinement. After a description of each code and test case, standards for determining code efficiency and accuracy are defined and applied to determine the relative performance of the two codes in predicting turbulent transonic wing flows. Computed surface pressure distributions are compared with experimental data.

17. Key Words (Suggested by Authors(s))	18. Distribution Statement
Thin-layer Navier-Stokes equations Transonic flow	Unclassified—Unlimited Subject Category 02

19. Security Classif. (of this report)	20. Security Classif. (of this page)	21. No. of Pages	22. Price
Unclassified	Unclassified	123	A06

NASA FORM 1626 OCT 86

NASA-Langley, 1991

For sale by the National Technical Information Service, Springfield, Virginia 22161-2171

National Aeronautics and
Space Administration
Code NTT-4

Washington, D.C.
20546-0001

BULK RATE
POSTAGE & FEES PAID
NASA
Permit No. G-27

Official Business
Penalty for Private Use, $300

NASA

POSTMASTER: If Undeliverable (Section 158 Postal Manual) Do Not Return

DO NOT REMOVE SLIP FROM MATERIAL

Delete your name from this slip when returning material to the library.

NAME	DATE	MS
~~E. Gartenberg~~	~~6/94~~	~~267~~
Kenneth Jones	1/10/95	286

NASA Langley (Rev. Dec. 1991) RIAD N-75